A Compressed Sensing Framework for Biological Microscopy

Marcio Marim

DOCTORAL SCHOOL
Edite de Paris, France

P h D T H E S I S

to obtain the title of

Doctor of Philosophy

of the Télécom ParisTech - Institut Télécom
Specialty : Signal & Image Processing

defended by

Marcio Marim

A Compressed Sensing Framework for Biological Microscopy

in collaboration with Institut Pasteur,
Quantitative Image Analysis Unit

defended on April 8, 2011

Jury:

Reviewers:	Rémi Gribonval	-	INRIA Rennes
	Michael Liebling	-	UC Santa Barbara
Examiners:	Eric Moulines	-	Télécom ParisTech
	Jean-Luc Starck	-	CEA Saclay
Advisors:	Elsa Angelini	-	Télécom ParisTech
	Jean-Christophe Olivo-Marin	-	Institut Pasteur
Invited:	Michael Atlan	-	ESPCI Paris

ÉCOLE DOCTORALE
Edite de Paris - Paris, France

T H È S E

présentée pour obtenir le grade de

Docteur

de Télécom ParisTech - Institut Télécom
Specialty : Traitement du Signal et des Images

présentée par

Marcio Marim

A Compressed Sensing Framework for Biological Microscopy

en collaboration avec l'Institut Pasteur,
Unité d'Analyse d'Images Quantitative

soutenue le 8 Avril 2011

Jury:

Rapporteurs:	Rémi Gribonval	-	INRIA Rennes
	Michael Liebling	-	UC Santa Barbara
Examinateur:	Eric Moulines	-	Télécom ParisTech
	Jean-Luc Starck	-	CEA Saclay
Directeurs:	Elsa Angelini	-	Télécom ParisTech
	Jean-Christophe Olivo-Marin	-	Institut Pasteur
Invité:	Michael Atlan	-	ESPCI Paris

Acknowledgments

First, I would like to thank my thesis advisor and head of the Quantitative Image Analysis Unit of Institut Pasteur, Jean Christophe Olivo-Marin. I have been in his laboratory during my master internship and he has proposed to me this Ph.D. project. His understanding, encouragement, support and guidance have made the present thesis possible. I am deeply grateful to my co-adviser, Elsa Angelini, associate professor of Computer Science at the department of Signal and Image Processing of Télécom ParisTech. I would like to thank her involvement in the work, valuable comments, suggestions, and support all along my thesis. Not to mention all the working days prior to submission of articles.

I wish to express my sincere thanks to the jury members, Jean-Christophe Olivo-Marin, Elsa Angelini, Michael Liebling, assistant professor in the department of Electrical and Computer Engineering from UC Santa Barbara, Rémi Gribonval, senior researcher at the IRISA group from INRIA Rennes, Eric Moulines, professor of the department of Signal and Image Processing of Télécom ParisTech, Jean-Luc Starck, researcher at Astrophysics service of the CEA-Saclay, and Michael Atlan, researcher at the Institut Langevin from ESPCI ParisTech.

I am greatly indebted to Michael Atlan. He has worked with me in some of my research subjects, shared his knowledge, and provided me with his great help, and valuable ideas. I wish to express my warm thanks tos Christophe Zimmer from the Computational Imaging and Modeling Group of Institut Pasteur, who co-advised my master internship.

I would also like to thank my colleagues from the laboratory, Fabrice de Chaumont, Alexandre Dufour, Vannary Hardy, Stéphane Dallongeville, François Orieux, Praveen Pankajakshan, Sorin Pop, Nicolas Hervé, Yoann Le Montagner, Marie-Anne Lin and former collaborators, Nicolas Chenouard, Bo Zhang, Mathieu Baudin, Clovis Tauber and Sylvain Berlemont, for their encouragement, warm helps, and discussions during the last three years. Some of them became real friends and I thank them for providing a nice working ambience and amazing chess games during the coffee breaks.

This research was funded by the Direction Générale de l'Armement (DGA), CNRS, and Institut Pasteur, and I would like to acknowledge them.

Last but certainly not least, I owe my loving thanks to Joana Treger for her continuous support, encouragement and love.

Abstract

Compressed sensing (CS) is a new sampling theory that was recently introduced for efficient acquisition of compressible signals. In this thesis, we have studied practical applications of the Fourier-based CS sampling theory for biological microscopy imaging, with two main contributions: **(i) Image denoising:** microscopic images suffer from complex artifacts associated with noise and non-perfect illumination conditions. In fluorescence microscopy, noise and photobleaching degrade the quality of the image. In this work, we have exploited the CS theory as an image denoising tool, using multiple random undersampling in the Fourier domain and the Total Variation as a spatial sparsity prior. Compounding of images reconstructed from multiple sets of random measurements enforce spatial coherence of meaningful signal components and decorrelate noisy components. We have studied the relation between signal sparsity and noise reduction performance under different noise conditions. We have demonstrated on simulated and practical experiments on fluorescence microscopy that the proposed denoising framework provide images with similar or increased signal-to-noise ratio (SNR) compared to state of the art denoising methods while relying on a limited number of samples. If Fourier-domain image point acquisitions were feasible, the proposed denoising could be used as a fast acquisition scheme which would enable to reduce exposition times, and reduce the photobleaching effects. **(ii) Compressed digital holographic microscopy:** high data throughput is becoming increasingly important in microscopy, with high-resolution cameras (i.e. large numbers of samples per acquisition) and long observation times. The compressed sensing theory provides a framework to reconstruct images from fewer samples than traditional acquisition approaches. However, the very few measurements must be spread over a large field of view, which is difficult to achieve in conventional microscopy. In a first experiment, we have proposed a computational scheme to perform fast temporal acquisitions of sequences of Fourier amplitude measures in optical Fourier imaging and estimate the missing phase information from spectra interpolation between few in-between complete keyframes. This approach was evaluated for high-frame rate imaging of moving cells. In a second experiment, we have implemented a real CS acquisition scheme for digital holographic microscopy, acquiring a diffraction map of the optical field and recovering high quality images from as little as 7% of random measurements. The CS acquisition setup was successfully extended to high speed low-light single-shot off-axis holography.

Keywords: Compressed sensing, inverse problems, total variation, Fourier sampling, sparsity, denoising, biological imaging, microscopy, digital holography.

Résumé

La technique d'acquisition compressée (*compressed sensing, CS*) est une nouvelle théorie pour l'échantillonnage qui fût introduite afin de permettre l'acquisition efficace de signaux compressibles. Dans cette thèse, nous avons étudié des applications pratiques de cette technique d'échantillonnage, où les acquisitions sont réalisées dans le domaine de Fourier, menant aux deux principales contributions suivantes : **(i) Débruitage d'image :** Les images microscopiques présentent souvent des dégradations dûs à des artefacts complexes, associés à du bruit ou encore des mauvaises conditions d'éclairage. En microscopie à fluorescence, le bruit et le photoblanchiment altèrent la qualité de l'image. Notre travail a consisté à exploiter la théorie d'acquisition compressée comme un outil de débruitage d'image. Nous avons utilisé plusieurs acquisitions aléatoires dans le domaine de Fourier, et la variation totale comme un *a priori* sur la parcimonie spatiale. La composition des différentes images de reconstruction correspondant aux différents ensembles de mesures aléatoires renforce la cohérence spatiale de composants du signal significatifs et permet de décorréler les composants bruités. Nous avons étudié les relations entre la parcimonie d'un signal et les statistiques et la performance pour la réduction du bruit sous différentes conditions initiales de bruitage. Nous avons montré que la technique proposée, basée sur un *a priori* sur la parcimonie du signal et sur des échantillonnages aléatoires dans le domaine de Fourier, permet d'obtenir des images avec un rapport signal/bruit (SNR) au pire égal à celui obtenu avec les méthodes de débruitage classiques, tout en utilisant un nombre limité d'échantillons. Sous réserve de pouvoir acquérir l'image dans le domaine de Fourier, le schéma de débruitage proposé fournirait une méthode d'acquisition rapide nécessitant un temps d'exposition moindre, réduisant les effets de photoblanchiment. **(ii) Acquisition compressée en microscopie holographique :** En microscopie, les données en sortie deviennent considérables, impliquant notamment l'utilisation de capteurs haute-définition (i.e. beaucoup d'échantillons par acquisition) et l'augmentation des temps d'acquisition. La théorie de l'acquisition compressée fournit des outils pour la reconstruction d'images, nécessitant moins d'échantillons que les approches classiques. Cependant, les quelques mesures nécessaires doivent être prises dans un domaine incohérent au domaine spatiale, ce qui est difficile à réaliser en microscopie conventionnelle. Nous avons tout d'abord proposé un schéma de calcul permettant l'acquisition de séquences temporelles de mesures d'amplitude dans le domaine de Fourier, et l'estimation de l'information manquante sur la phase par interpolation de spectre de quelques acquisitions complètes d'images. Cette approche a été mise en pratique dans le contexte de l'imagerie rapide, utilisée pour des cellules en mouvement. Dans un deuxième temps nous avons implanté un schéma d'acquisition compressée pratique, conçu pour l'holographie numérique. Ce schéma permet de mesurer une figure de diffraction du champ optique et reconstruire images de haute qualité à partir de seulement 7% de mesures aléatoires. L'expérience d'acquisition compressée a été étendue avec succès à l'holographie compressée rapide à acquisition

unique et dans des conditions d'éclairage faible.

Keywords: Acquisition compressée, problèmes inverses, variation totale, parcimonie, échantillonnage dans le domaine de Fourier, débruitage, imagerie biologique, microscopie, holographie numérique.

Contents

Acknowledgments i
Abstract iii
Résumé v
Table of Contents x
Table of Figures xvi
Table of Tables xvii
Notations and Definitions xix

General Introduction **1**

I A Denoising Framework for Biological Microscopy **5**

1 Introduction **7**
1.1 Microscopic Imaging: Signal and Noise Models 8
1.1.1 White Gaussian Noise 10
1.1.2 Poisson Noise 10
1.1.3 Microscopic Image Formation Model 11
1.1.4 Image Estimation: Error and Similarity Measures 12
1.2 Image Representation, Norms and Sampling 15
1.2.1 The Fourier Transform 16
1.2.2 Image Transform and Sparsity 18
1.2.3 Sparsifying Transforms 19
1.2.4 Total Variation Measures on Images 23
1.2.5 Two-Dimensional Sampling Theory 25
1.3 Compressed Sensing Theory 26
1.3.1 Signal Sparsity 27
1.3.2 Sensing Matrix and Incoherence 30

1.3.3 CS Image Recovery Algorithms 32
1.4 Image Denoising with Sparsity Constraints 36
1.4.1 Denoising via Wavelet Thresholding 37
1.4.2 Denoising by Total Variation Minimization 41
1.4.3 Non-Local Means 43

2 A Denoising Framework Based on Image Sparsity and Random Fourier-based Sampling 47
2.1 Denoising Approaches and Fluorescence Microscopy 48
2.2 Denoising Methods 50
2.2.1 Reconstruction from Noisy Measurements 50
2.2.2 The Noise Model and Image Sparsity Measures 51
2.2.3 The Sampling Pattern for Denoising 53
2.2.4 Denoising and Scalability 56
2.3 Algorithms for Multiple Reconstructions 58
2.3.1 Algorithm Workflow 58
2.4 Images Fusion by Averaging 61
2.4.1 Simulations on Pure Noise Signal 61
2.4.2 Results with Averaging 62
2.5 Images Fusion by Non-Local Averaging 64
2.5.1 Results with Non-Local Averaging 68
2.6 Conclusion 71

II CS-based Biological Imaging Methods 75

3 Introduction 77
3.1 High-Resolution and High-Throughput Data Acquisition 78
3.2 Intelligent Acquisition Systems in Microscopy 79
3.2.1 Intelligent Acquisition and Learning of Fluorescence Microscope Data Models 80
3.2.2 Controlled Light Exposure Microscopy 81
3.3 Existing Compressed Sensing Acquisitions Systems 82
3.3.1 MRI 83
3.3.2 Single Pixel Camera 84

3.3.3 Astronomy . . . 85
3.3.4 Coded Aperture . . . 86
3.3.5 Optics and Holography . . . 87

4 Temporal Compressed Sensing With Random Fourier Measurements 89
4.1 CS in Microscopy with Random Fourier Measurements . . . 90
4.2 Displacements and Phase . . . 92
4.3 Fourier Phase Estimation . . . 96
4.4 Image Reconstruction and Algorithm . . . 98
4.4.1 Algorithm Adaptation . . . 100
4.5 Results and Error Propagation . . . 100
4.6 Conclusion . . . 101

5 Compressed Digital Holographic Microscopy 105
5.1 Introduction . . . 106
5.2 An Overview of Digital Holographic Microscopy . . . 107
5.2.1 Digital Holography Principles . . . 108
5.2.2 Inline or Off-Axis Holography . . . 109
5.2.3 Image Reconstruction from the Hologram . . . 111
5.2.4 From Fresnel to Fourier Domains . . . 113
5.3 Coupling DHM With Compressed Sensing . . . 114
5.3.1 CS Reconstruction from Fresnel Measurements . . . 115
5.3.2 Incoherent Sampling of Hologram Coefficients . . . 117
5.4 Experiments and Results . . . 119
5.4.1 Compressed DHM Setup for USAF Imaging . . . 120
5.4.2 USAF Image Reconstruction . . . 121
5.4.3 Compressed DHM Setup for Biological Imaging . . . 121
5.4.4 Biological Image Reconstruction . . . 123
5.4.5 Effect of Undersampling on CS Reconstructions . . . 125
5.5 Conclusion . . . 125

6 One-Shot Off-Axis Compressed DHM in Low Light Conditions 127
6.1 Introduction . . . 128
6.2 One-Shot Holography Setup . . . 129

6.3 Image Reconstruction With Bounded Support 131
6.4 Noise Robustness and Results 133
6.5 Conclusion 134

Conclusion **137**

List of Publications **141**

A Random and Radial Undersampling in Holography With an Programable Camera **143**
A.1 Introduction 144
A.2 The Acquisition System 145
A.2.1 The Holographic Setup 145
A.2.2 The Programmable CMOS Camera 147
A.2.3 Preliminary Experiences 148
A.3 The Image Reconstruction 148
A.4 Results 151
A.5 Conclusion 151

Appendix **143**

B Reducing Photobleaching on Fluorescence Microscopy **155**
B.1 Introduction 156
B.1.1 Fluorescence Microscopy 157
B.1.2 Photobleaching and Photodamage 159
B.2 Methods 160
B.2.1 Reconstruction from Noisy Measurements 160
B.2.2 The Recovery Algorithm 162
B.3 CS and Scalability 164
B.4 Photobleaching 166
B.5 Conclusion 169

Bibliography **171**

List of Figures

1.1 Histogram of a Poisson noise for different parameter values. 11
1.2 Image formation model: Gaussian and Poisson noise simulations. . . 13
1.3 Aliasing. 25
1.4 Signal sparsity. Left: S-sparse signal with $S = 8$, or 8 time-values being non-zero. Right: Nearly S-sparse signal, with 8 strong coefficients and several small coefficients. 27
1.5 Example of sparse representation of a signal (top) using a simple dictionary (middle), and its respective coefficients (bottom). 28
1.6 Original megapixel image with pixel values in the range [0,255] and its wavelet transform coefficients. 29
1.7 Image sparsity illustrated in a two-dimensional spatial domain. Top left: original image. Top right: sparse representation domain (using the gradient of the signal). Bottom: intensity profiles from corresponding blue lines in the spatial and gradient domains. 30
1.8 Example of noisy fluorescence microscopy image. 36
1.9 Hard- and soft-thresholding functions applied to each wavelet coefficient. 40

2.1 (a) Microscopic image with simulated noise such as (2.6). The sparsifying transformation ∇x applied to (b) noise-free image (compressible signal of interest), (d) simulated Gaussian noise component and (f) simulated Poisson noise component are illustrated in (c), (e) and (g) respectively. 54
2.2 Spatial distributions in the Fourier domain with M = 0.1N (a) Random, (c) Radial and (b,d) are the correspondent frequency histograms. 55
2.3 Circle of probability for the uniform distribution. 56

2.4 Average microscopic image recovered with six different numbers of measurements (i.e. 6 scales). Scales varies from a compression ratio exponentially increasing from M= 30% to M= 0.3%. 57

2.5 Denoising scheme with K acquisitions over T/K ms and K independent reconstructions. 59

2.6 Denoising scheme with a single shorter acquisition and K reconstructions using different sampling matrices Φ_i. 60

2.7 Left: Gaussian noise image (with mean $\mu = 3.99$ and standard deviation $\sigma_1 = 3.01$). Center: an individual noise reconstruction. Right: Reconstructed image obtained by averaging 20 images recovered with different sets of measurements Φ_i for ($i = 1...20$) with $\mu = 3.99$ and $\sigma_2 = 0.75$ (10% of measurements). 61

2.8 Left: Poisson noise image (with mean $\mu = 4.17$ and standard deviation $\sigma_1 = 4.1$). Center: an individual noise reconstruction. Right: Reconstructed image obtained by averaging 20 images recovered with different sets of measurements Φ_i for ($i = 1...20$) with $\mu = 4.17$ and $\sigma_2 = 2.09$ (10% of measurements). 62

2.9 (a) Drosophila cells imaged by fluorescence microscopy with exposure time $t = 10ms$. (b) Denoised image with the first CS scheme (10 reconstructions of 10 short-exposure time images as in (a) with M=10%N). (c) Noise residual comparing (b) to (d). (d) Image acquired with exposure time equal to $t = 100ms$. (e) Denoised image with the second CS scheme (10 reconstructions from (d) with M=10%N). (f) Noise residual comparing (e) to (d). (g) Denoised image with the first CS scheme (4 reconstructions of 4 short-exposure time images, with M=10%N) 65

2.10 (a) Lymphocytes imaged by fluorescent microscopy, SNR= 8.14. Denoised images by (b) scalar TV filtering (SNR= 11.2), (c) adaptive TV filtering (SNR= 12.5) and (d) by CS 2nd scheme, using 10 reconstructions (SNR= 14.28) with M=10%N. (e)(f)(g) Noise residuals for each method comparing (a) to (b-d)$\| \hat{x} - x \|_{\ell_2}$. 66

2.10 Green and red channels; fluorescence microscopy image of hair follicle. (a)(f) Original noisy image. (b)(g) One single CS reconstruction. (c)(h) Multiple CS with averaging (2.12). (d)(i) NL-means filtering of the noisy image. (e)(j) Multiple CS with NL-means 2.15. 70

2.11 Fluorescence microscopy image of cells. (a) Image exposed 10 ms. (b) Multiple CS with averaging (2.12). (c) NL-means from one single CS reconstruction (d) NL-means from the image exposed 10 ms. (e) Multiple CS with NL-means (2.15). (f) Reference image exposed 200 ms. (g-j) SSIM index maps for images (b-e) in comparison to the reference image. 73

3.1 A diagram of the method proposed by Jackson et al.. The "model building" module constructs a model from the microscope data, and the "intelligent acquisition" module determines what acquisitions to make to efficiently improve on this model. Figure extracted from [Jackson 2009] 80

3.2 Confocal image of auto-fluorescence of pollen grain in the absence and presence of CLEM. Top panel shows the illumination image (left) and confocal image (right) in the absence of CLEM. Bottom panel shows the illumination image (left), detected image (middle) and CLEM image (right). Figure extracted from [Hoebe 2007] 82

3.3 Figure extracted from [Lustig 2007]. Reconstruction from 5-fold accelerated acquisition of first-pass contrast enhanced abdominal angiography. 85

3.4 Figure extracted from [Baraniuk 2007] 86

4.1 Example of diffraction phenomenon at a circular aperture. 91

4.2 Object movement on an image sequence. 93

4.3 Image sequence, $t = 0$ (a) and $t = 1$ (b) and global movement (c) computed as the difference of pixels intensities between the two consecutive frames. 94

4.4 Fourier phases from frames (a) $t = 0$ (b) $t = 1$ and (c) the difference between the phases of the two consecutive frames (d) and a profile for a line passing through the center of the image in (c). 95

4.5 Recovery algorithm and acquisition system. 97

4.6 MSE propagation for the CS reconstructed image in Fig. 4.7. 101

4.7 Top: Phase contrast microscopy image sequence of amebas, $x_{\Delta k+j\Delta t}$ at $\Delta k + j\Delta t = \{5, 75, 135\}$, $\Delta k = 10$. Middle: CS reconstructions $\hat{x}_{\Delta k+j\Delta t}$ with 5% of measurements ($M = 5\%N$). Bottom: Residual $\|\hat{x}_{\Delta k+j\Delta t} - x_{\Delta k+j\Delta t}\|_{\ell_2}$. 102

5.1 A general setup of inline holography imaging. 107

5.2 Off-axis holographic setup. 110

5.3 Radiation field propagation, from full coherence for a detector plane at $z = 0$ to complete incoherence at plane at $z \to \infty$. Fresnel and Fourier diffraction domains are defined according to the distance between the object and the detector plane. 114

5.4 CS reconstruction scheme. 116

5.5 Sketch of the digital holographic microscopy experimental image acquisition setup. 120

5.6 (a) Standard holography experiment, as described in Eq. (5.6). (b) CS reconstruction, using 7% of the Fresnel coefficients. (c) Gradient of (a). (d) Residual from (a) and (b). (e), (f) Magnified views from (a) and (b). 122

5.7 Sketch of the holographic microscopy experimental image acquisition setup. 123

5.8 Mouse cerebral blood flow (CBF) imaged by digital holographic microscopy (a) Standard holographic reconstruction, as described in (5.7). (b) CS exact recovery, using 7% of the Fresnel coefficients acquired with holography, as described in (5.12). (c) CS recovery with denoising, as described in (5.13). (d-f) Magnified views from (a-c). (g) Gradient of (a). (h) Residual from |(a)-(b)|. (i) Residual from |(a)-(c)|. 124

5.9 (a) Standard holographic reconstruction, as described in (5.7). (b) CS exact recovery, using 4% of the Fresnel coefficients acquired with holography, as described in (5.12). (c) Residual from |(a)-(b)|. (d) Structural Similarity between images (a) and (b) SSIM=0.1355 (top) and SSIM=0.1653 (bottom). Here, the CS reconstruction is not satisfactory due to the number of samples being too low. 126

6.1 Sketch of the experimental one-shot holographic acquisition setup. . 129

6.2 Compressed holographic reconstruction of E_o without support constraint (a). Reconstruction with TV minimization over the region $\mathcal{R}$ (b). In both cases, $\langle n \rangle = 2.4\,\mathrm{e}$ ($D = 0$) and $M/N = 9\%$. Magnified views over 330×330 pixels (c,d) of (a,b). 132

6.3 (a-c) Amount of digital counts in the object channel averaged over N pixels, for three different attenuations levels : $D = 0$ (a), $D = 0.5$ (b), $D = 1$ (c). The LO beam (reference beam) is turned off. The optical field E impinges onto the detector (i) and is blocked (ii) sequentially by the optical chopper, from one frame to the next. The horizontal axis represents the frame number, the vertical axis is the average number of counts per pixels. (d-f) Standard holographic reconstructions at $D = 0$ (d), $D = 0.5$ (e), $D = 1$ (f). (g-i) CS reconstructions at $D = 0$ with $M/N = 9\%$ (g), at $D = 0.5$ with $M/N = 13\%$ (h), and at $D = 1$ with $M/N = 19\%$ (i). 135

A.1 Holographic setup with intelligent CMOS. 146

A.2 Photo of the holographic setup with intelligent CMOS. 146

A.3 Programmable CMOS camera. 148

A.4 US Air Force (USAF) target. 149

A.5 Fresnel hologram measured with CMOS. 150

A.6 Random pattern from undersampling. 151

A.7 Radial pattern from undersampling. 152

A.8 Conventional digital holography and CS reconstruction with radial and random sampling from only 15% of measurements. 153

B.1 Fluorescence photochemistry diagram. 157

B.2 Image sequence of fluoresceine. Images are exposed 20 milliseconds each (200 frames). 159

B.3 Photobleaching and SNR profiles of the image sequence of fluoresceine. 160

B.4 Photobleaching curve of the image sequence of fluoresceine and SNR of accumulated frames (SNR vs. exposure time). 160

B.5 TV versus number of images (Lymphocytes) recovered and combined for the 10 scales represented in Figure B.6. 163

B.6 TV versus scales for recovered images of Lymphocytes. Scales vary from a compression ratio exponentially increasing from $M = 30\%$ to $M = 0.3\%$. 163

B.7 Fluorescence microscopic image of Lymphocytes. Results from the same image recovered with six different numbers of measurements (i.e. 6 scales). Scales vary from a compression ratio exponentially increasing from $M = 30\%$ to $M = 0.3\%$. 165

B.8 Top: Pure noise signal extracted from a background patch of a microscopic image, recovered with six scales, (i.e. six different sizes of sample measurements). Scales vary exponentially from $M = 30\%$ to $M = 0.3\%$. Bottom: relaxing the constrain $\delta_{bottom} > \delta_{top}$. 166

B.9 Left: Pure noise image extracted from a microscopic image background. Right: Result obtained averaging 20 images recovered with different sets of measurements Φ_i for $(i = 1...20)$. 166

B.10 Fluorescein images. Top: Six samples from the sequence of 200 images tagged with fluorescein. These images were acquired at $t = \{0, 500, 1000, 1500, 2000\}\ ms$. Bottom: Supposed photobleaching resulted from 200 image acquisitions using CS denoising. 167

B.11 SNR curves, we use a set of 150 fluorescein images acquired each 10 ms. The green line correspond to the SNR of images recovered with CS using the scheme proposed in Section B.2.2 and the blue line correspond to the SNR of the original set of images. 168

B.12 Photobleaching curves, represented by the mean fluorescence intensity vs. time for original images of fluorescein (blue) and for images denoised with our proposed scheme (green). The red line corresponds to the exponential model fitted to the original data, setting specific values of B and k in Equation (B.6). 168

List of Tables

2.1 Signal-to-noise ratio (SNR) and contrast-to-noise ratio (CNR) results for the first denoising scheme and for the image on Figure 2.9a. . . . 64
2.2 Signal-to-noise ratio (SNR) and contrast-to-noise ratio (CNR) results for the second denoising scheme proposed and for image on Figure 2.9d. 64
2.3 SNR, CNR measures for the green and red channel. 68
2.4 MSE, PSNR and SSIM measures. 71

4.1 Modifications of the ℓ_1-magic reconstruction. 100

5.1 Main differences between NESTA and our approach. 119

Notations and Definitions

2D	Two-Dimensional
3D	Three-Dimensional
CCD	Charge-Coupled Device
CG	Conjugate Gradient
CMOS	Complementary Metal-Oxide-Semiconductor
CNR	Contrast-to-Noise Ratio
CS	Compressed Sensing or Compressed Sampling
DFT	Discrete Fourier Transform
DHM	Digital Holographic Microscopy
EM-CCD	Electron-Multiplying CCD
FFT	Fast Fourier Transform
GFP	Green Fluorescent Protein
IDFT	Inverse Discrete Fourier Transform
iff	if and only if
MAP	Maximum A Posteriori
ML	Maximum Likelihood
MPG	Mixed-Poisson-Gaussian
MSE	Mean Squared Error
SNR	Signal-to-Noise Ratio
SSIM	Structural Similarity
s.t.	Subject to
TV	Total Variation
UWT	Undecimated Wavelet Transform

General Introduction

Microscopy is an essential tool for biological research, as it enables to study cellular and sub-cellular processes with the proper resolution. The search for methods aiming at optimizing the image acquisition in microscopy constitutes nowadays a very active research field. These methods try to fulfill different expectations. They can for instance try to increase the image resolution or the frame-rate, focus on using fewer pixels during measurement, be non-invasive, label-free, or aim at measuring only the most relevant part of a scene. Such improvements usually result from new physical systems, but may also happen from a new mathematics-based methods.

In this thesis we propose a framework which combines new acquisition protocols and mathematical imagery. The acquisition is tuned for the image reconstruction to take into account the acquisition model and a new sampling theory (compressed sensing). The goals are to improve the frame rates, to better preserve samples and photons while providing an image reconstruction scheme able to discriminate noise and signal. The theoretical basis of compressed sensing was introduced by David Donoho, Emmanuel Candès, Justin Romberg and Terence Tao [Candès 2004b, Candès 2004a, Donoho 2006b]. Its applications are nowadays among the most competitive research topics on image processing (including medical and biological imaging). Its principles are the following: after performing a transform (typically, the Fourier transform) on a compressible signal and then making a very limited number of acquisitions of transformed coefficients, each containing a small piece of information about the whole signal, it is then possible to reconstruct almost exactly the original signal. It is a much more efficient scheme than traditional sampling techniques, which are based on the Shannon-Nyquist criterion and require a large number of samples [Shannon 1948, Shannon 1949].

This thesis contributes mainly to two aspects of image processing and optical microscopic imaging. The two main contributions have been organized into two parts of the thesis document as follows.

The first part presents a denoising framework based on random and incoherent undersampling of Fourier coefficients and spatial sparsity for image reconstruction. Random and incoherent undersampling allow to capture the image information in a way that helps to separate the true signal from the noise. In addition, the sparsity introduces a regularization which enforces noise removal while preserving the signal structure. This framework was mainly inspired by the sparse coding theory [Olshausen 1997] and the unstructured sampling of compressed sensing [Donoho 2006b, Candès 2004b]. First, we review important concepts on signal and noise modeling, sampling theory, image denoising methods and compressed sensing theory. We then detail our contribution for fluorescence image denoising and present experimental results on biological microscopic data. The denoising approach combines random undersampling in the Fourier domain and total variation minimization and provides high denoising performances for biological microscopic images. We end the first part with a presentation of an improved version with better denoising performances that uses a non-local merging approach to combine multiple reconstructions.

The second part is dedicated to intelligent image acquisition and reconstruction. We focus on improving the acquisition to obtain an optimal ratio between number of measurements and data throughput. In this second part, we start by introducing the existing work about intelligent microscopy acquisition systems and also the existing devices employing compressed sensing. Our initial implementation of compressed acquisitions is then described. This work proposes to acquire complex-valued Fourier coefficients by measuring optically the Fourier magnitude and then estimating the Fourier phase with interpolation between keyframes. We extend this work by designing an microscopy acquisition scheme successfully combining compressed sensing and digital holographic microscopy (DHM). The main idea is to gather off-axis, frequency-shifting (for accurate phase-shifting) digital holography to obtain quadrature-resolved random measurements of an optical field in a diffraction plane with a total variation minimization algorithm to reconstruct the image.

Finally, we propose an improved DHM acquisition scheme. It employs high speed low-light single-shot off-axis holography and a total variation minimization with spatial support constraint to reconstruct the image. We present results consisting in an experimental demonstration of accurate image reconstruction from very few low-light (i.e. high noise level) holographic measurements. The reconstruction algorithm

is improved by using a total variation minimization restricted to the spatial support of the output image. The spatial support constraint enhances the image quality and reduces the number of measurements.

Part I

A Denoising Framework for Biological Microscopy

Chapter 1

Introduction

Microscopy imaging have seen recently the introduction of several new acquisition techniques, allowing to observe smaller biological samples with increasing image quality and screening speed [Vermot 2008, Liebling 2006]. In general, microscopic images are acquired with a digital sensor such as CCD camera, enabling digital storage, post-processing, quantitative display and interpretation. Microscopic image processing is typically required to enhance the extraction of information about the screened biological specimen. In biology, digital image processing has become an integral part of microscopy screening protocols, and has been used to extract quantitative information about cellular processes.

Recent developments in microscopic imaging techniques, allowing to observe specimens with a nano-metric precision, have led to rapid discoveries in biology, medicine and related fields. In this context, digital image processing is not only a natural extension to microscopic imaging but is proving to be essential to the success of the exploitation of new generations of microscopes.

Despite great progresses in microscopic image processing, image acquisitions in optical microscopy remain corrupted by high-level noise components and rely on weak signals acquired from the specimens (e.g. fluorescence). Noise, arising from a variety of sources, is inherent to all electronic image sensors, but is particularly critical in microscopic imaging. Ensuring that the signal level is adequate relative to the noise level to allow the capture of accurate image information, remains a challenging problem. This chapter proposes a review of the noise sources contributing to microscopic image degradation and present recent important denoising techniques, based on sparsity constraints of the image content. We therefore also introduce the theoretical basis of sparse representations, and signal compressibility. This thesis has focused on the exploitation of compressed-sensing (CS) image reconstruction for image denoising and acquisition. We introduce in this Chapter Fourier-based signal decomposition and properties of Fourier-based measures with respect to the

CS theory.

Contents

1.1 Microscopic Imaging: Signal and Noise Models 8
1.1.1 White Gaussian Noise 10
1.1.2 Poisson Noise 10
1.1.3 Microscopic Image Formation Model 11
1.1.4 Image Estimation: Error and Similarity Measures 12
1.2 Image Representation, Norms and Sampling 15
1.2.1 The Fourier Transform 16
1.2.2 Image Transform and Sparsity 18
1.2.3 Sparsifying Transforms 19
1.2.4 Total Variation Measures on Images 23
1.2.5 Two-Dimensional Sampling Theory 25
1.3 Compressed Sensing Theory 26
1.3.1 Signal Sparsity 27
1.3.2 Sensing Matrix and Incoherence 30
1.3.3 CS Image Recovery Algorithms 32
1.4 Image Denoising with Sparsity Constraints 36
1.4.1 Denoising via Wavelet Thresholding 37
1.4.2 Denoising by Total Variation Minimization 41
1.4.3 Non-Local Means 43

1.1 Microscopic Imaging: Signal and Noise Models

For algorithm design, image models must distinguish the "noise" from the "true signal" components. The noise component includes the artifacts disturbing the observation of the pure signal of interest. Images acquired in microscopy are affected by a large number of sources of distortions due to the spatial spread of the transfer function of the optical system, the thermal motion of electrons in the electronic circuits of the acquisition systems and the quantum nature of photons and electrons.

In a typical digital image sensor, for each incident photon hitting the photodetector element, one electron is liberated. The resultant charge in each pixel is linearly proportional to the number of incident photons. The charge in each pixel will also

increase due to the accumulation of electrons during the exposure time. The charge is converted to a proportional voltage with or without amplification and finally quantified by an analog-to-digital converter. In the detection process several noise sources are involved and will corrupt the measured signal and its precision.

In digital microscopy, images are mainly contaminated by dark noise, photon noise (or shot noise) and readout noise components. The **dark noise** is also called Johnson-Nyquist noise. It corresponds to the electronic noise generated by the thermal agitation of the electrons. More precisely, the kinetic vibration of silicon atoms in the sensor substrate liberates electrons even when no incident photon is present. The resulting charge contributes to the final signal intensity. Secondary sources of the dark noise involve external radiation from nearby sources such as an indoor illumination. The dark noise N_d follows a Poisson distribution, i.e., $N_d \sim \mathcal{P}(\lambda_d)$, where λ_d represents the average dark flux. In practice, high-quality sensors typically have a cooler to reduce the dark noise.

The **photon noise** is also called shot noise, which is typically generated from statistical quantum fluctuations of the number of photons sensed at a given exposure level. Due to the stochastic nature of the photon emission, the photon noise is inherent in all optical signals. Supposing the average photon flux to be λ, the measured photon number N_p follows a Poisson distribution with intensity parameter λ, i.e., $N_p \sim \mathcal{P}(\lambda)$. If the photon flux is high enough, N_p will be asymptotically normally distributed with both the mean and the variance equal to λ.

The **readout noise** is mainly generated by the imperfectness of the output amplifier during the process of converting the charge into a voltage signal. This noise is usually described by a normal distribution, i.e., $N_r \sim \mathcal{N}(\mu, \sigma^2)$. In some cases, the readout noise may depends on the frequency of the sensor. We note that the temperature can also have an effect on the amount of noise produced by an image sensor due to leakage effects. There are other sources of noise such as quantization noise and speckle. Here, we will mainly consider and model the dark, photon and readout noise components since the other sources are negligible.

For electronic sensors, the signal-to-noise ratio (SNR) characterizes the quality of a measurement and determines the ultimate performance of the screening system. With a CCD or CMOS image sensor, the SNR value specifically represents the ratio of the measured light signal and the combined noise components, which consist of undesirable signals arising in the electronic system, and the inherent natural

variation of the incident photon flux. Since the sensor collects charge over an array of discrete physical locations, the signal-to-noise ratio may be thought of as the relative signal magnitude, compared to the measurement uncertainty, on a per-pixel basis.

In this section we discuss common models of microscopic signal involving the main sources of noise present in microscopy imaging. We note that all sources of noise can be modeled as Gaussian noise, Poisson noise or a mixture of both distributions. In the following subsections the Gaussian and Poisson distributions are detailed.

1.1.1 White Gaussian Noise

A white Gaussian noise is a statistical signal, with independent temporal values drawn from zero-mean and constant variance Gaussian pdfs. The power spectral density of a white Gaussian noise is equal throughout the frequency spectrum. The term "white", originated from the fact that white light contains equal energy over the visible frequency band.

The Gaussian distribution or normal distribution in probability theory and statistics is usually denoted by $\mathcal{N}(\mu, \sigma^2)$ where the parameters μ and σ^2 are the mean intensity and the variance of the distribution. The Gaussian distribution is described by the probability density function

$$\mathcal{P}(x) = \frac{1}{\sqrt{2\pi\sigma^2}} e^{-\frac{(x-\mu)^2}{2\sigma^2}}. \tag{1.1}$$

A white Gaussian noise has $\mu = 0$. An illustration of a Gaussian noise is provided in Fig. 1.2c.

1.1.2 Poisson Noise

The quantum nature of photon emission leads to fluctuations in the counting process of photons measured by the image detector. The emission of a photon during a small time interval is modeled as a random event occurring with a fixed probability and which is independent of the number of photons already emitted. The number of photons received N_p can then be modeled by a Poisson law $\mathcal{P}_\lambda(N_p)$ of parameter λ:

$$\mathcal{P}_\lambda(N_p) = \frac{\lambda^{N_p} e^{-\lambda}}{N_p!} \tag{1.2}$$

A process described by a Poisson distribution has a variance $\text{Var}[N_p] = \lambda$ equal to its mean $E[N_p] = \lambda$ where the symbols $E[R]$ and $\text{Var}[R]$ correspond to the expectation and the variance of a random variable R. Thus, the greater the intensity, the higher the noise level. When the average count λ increases, the distribution of the number of photons N_p can be approximated by a normal distribution with mean and variance $\lambda : N_p \, \mathcal{N}(\lambda, \lambda)$. Finally, each photon received is converted into a photo-electron with a probability η_q called the "quantum" efficiency of the detector.

The presence of a Poisson noise in microscopy images means that each pixel value fluctuates about its mean λ with a standard deviation $\sigma = \sqrt{\lambda}$. In Fig. 1.1 we illustrate two histograms of poisson noise distributions (simulated on the image in Fig. 1.2a). The first histogram is for a low average count $\lambda = 5$ and the second histogram is for $\lambda = 128$. The second histogram illustrates very well the Gaussian-like distribution when the average count increases.

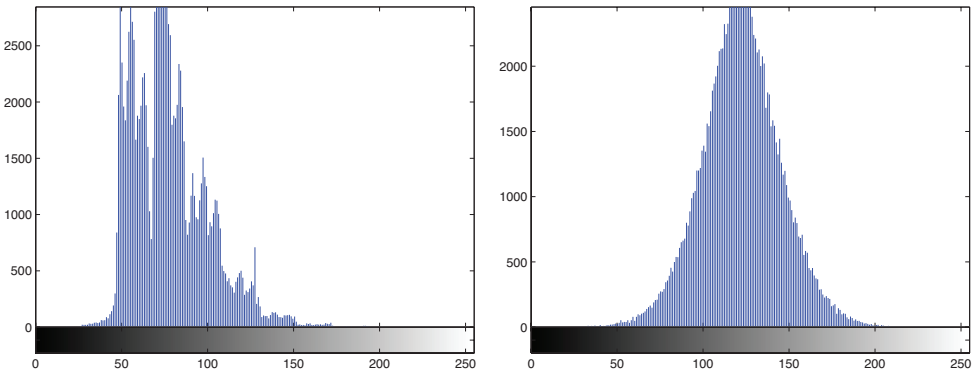

(a) $\lambda = 5$ (b) $\lambda = 128$

Figure 1.1: Histogram of a Poisson noise for different parameter values.

1.1.3 Microscopic Image Formation Model

Microscopic images are normally contaminated by photon, dark and readout noises. As N_p and N_d are independent Poisson variables, $N_p + N_d$ is also Poisson distributed. The readout noise N_r is usually described by a Gaussian distribution, hence, the global noise model can be described by Mixed-Poisson-Gaussian (MPG) process. The observation model commonly adopted for the final detected signal x can be

written as:

$$x(a,b) = \zeta U(A(a,b) + \lambda_B) + V, \quad \text{where } U \sim \mathcal{P}_\lambda(N_p),\ V \sim \mathcal{N}(\mu, \sigma^2) \tag{1.3}$$

where $U = N_p + N_d$, $V = N_r$ and ζ is the overall gain of the detector, $A(a,b)$ is the object intensity, λ_B is the mean intensity of the background, U is a Poisson variable with parameter λ modeling the photon counting and dark noise, and V is a normal distribution with mean intensity μ and standard deviation σ modeling the readout noise, U and V are two random process assumed mutually independent.

In Fig. 1.2, we illustrate the image formation model where the final image corresponds to a noise-free image corrupted with a mixture of Gaussian and Poisson noise. We note that the Poisson noise in Fig. 1.2d, contrarily to the Gaussian noise in Fig. 1.2c, is image-dependent as it originates from fluctuations in the counting process of photons.

1.1.4 Image Estimation: Error and Similarity Measures

When working with signal estimation, restoration, reconstruction or denoising, it is essential to be able to quantify the effect of the processing tasks in estimating the true signal component. This is generally described as quantifying the difference between the originally observed signal and the estimated signal. This difference is commonly called a data fidelity measure or a measure of error. The goal of a signal fidelity measure is to compare two images by providing a quantitative score that describes the degree of similarity/fidelity or, conversely, the level of error/distortion between them. As an alternative, the estimated image can be evaluated independent of the content of the observed samples, by quantifying its visual quality.

We have used in this work different measures to quantify and compare our method to other denoising approaches, including the mean-squared error (MSE), the structural similarity index measure (SSIM) [Wang 2009], the signal-to-noise ratio (SNR) and the contrast-to-noise ratio (CNR).

MSE and SSIM measures fall in the category of error measures while the SNR and the CNR fall in the category of image quality measures.

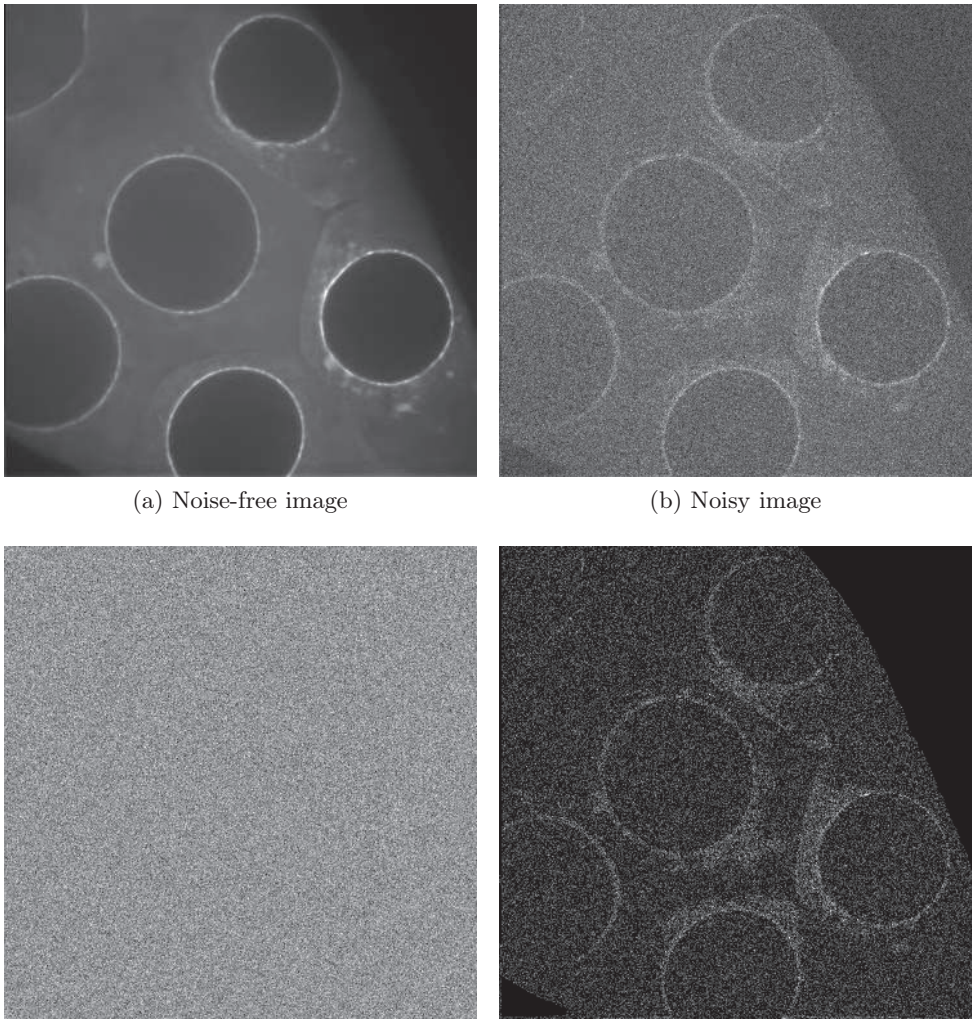

(a) Noise-free image (b) Noisy image

(c) Gaussian noise, $\mu = 20, \sigma = 10$ (d) Poisson noise, $\lambda = 10$

Figure 1.2: Image formation model: Gaussian and Poisson noise simulations.

Mean-Squared Error. The mean-squared error (MSE) remains the standard criterion for the assessment of signal fidelity given an original observation. This is a global measure for comparing signals and is a powerful tool for variational estimation methods, being derivable. Suppose a finite-length signal $\mathbf{x} = x_i | i = 1, 2, ..., N$ and $\hat{x}$ being an estimator of x, the MSE measures the average of the quadratic distance between the original and estimated signals and can be defined as:

$$\mathrm{MSE}(\hat{\mathbf{x}}|\mathbf{x}) = \mathrm{E}[(\hat{\mathbf{x}} - \mathbf{x})^2] \tag{1.4}$$

or,

$$\text{MSE}(\hat{\mathbf{x}}|\mathbf{x}) = \frac{1}{N}\sum_{i=1}^{N}(\hat{\text{x}}_i - \text{x}_i)^2 \tag{1.5}$$

It can also be viewed as a measure of the energy of the removed noise component when used to estimate denoising efficiency. We note two important properties (i) it is robust to outliers and (ii) when removing a zero-mean white Gaussian noise, it is expected that $E[R^2] = \sigma^2$ for $\mathcal{N}(0, \sigma)$.

Structural Similarity Index Measure For many applications the MSE exhibits low performance when dealing with perceptual signals such as images. The structural similarity index measure (SSIM) is a fidelity measure which takes into account the structural information in the image [Wang 2004, Wang 2009]. The index depends on local patch brightness measures, the similarity of local patch contrasts, and the similarity of local patch structures. These local similarities can be simply computed using basic statistics, as:

$$\begin{aligned}\text{SSIM}(\hat{\mathbf{x}}, \mathbf{x}) &= L(\hat{\mathbf{x}}, \mathbf{x}) \cdot C(\hat{\mathbf{x}}, \mathbf{x}) \cdot S(\hat{\mathbf{x}}, \mathbf{x}) \\ &= \left(\frac{2\mu_{\hat{\mathbf{x}}}\mu_{\mathbf{x}} + K_1}{\mu_{\hat{\mathbf{x}}}^2 + \mu_{\mathbf{x}}^2 + K_1}\right) \cdot \left(\frac{2\sigma_{\hat{\mathbf{x}}}\sigma_{\mathbf{x}} + K_2}{\sigma_{\hat{\mathbf{x}}}^2 + \sigma_{\mathbf{x}}^2 + K_2}\right) \cdot \left(\frac{\sigma_{\hat{\mathbf{x}}\mathbf{x}} + K_3}{\sigma_{\hat{\mathbf{x}}}\sigma_{\mathbf{x}} + K_3}\right),\end{aligned} \tag{1.6}$$

where $\mu_{\hat{\mathbf{x}}}$ and $\mu_{\mathbf{x}}$ are the local means of $\hat{\mathbf{x}}$, $\mathbf{x}$, $\sigma_{\hat{\mathbf{x}}}$ and $\sigma_{\mathbf{x}}$ are the local standard deviations and $\sigma_{\hat{\mathbf{x}}\mathbf{x}}$ the cross correlations. The SSIM index is computed locally within a sliding window that moves pixel-by-pixel across the image, resulting in a SSIM map. The SSIM is symmetric ($\text{SSIM}(\hat{\mathbf{x}}, \mathbf{x}) = \text{SSIM}(\mathbf{x}, \hat{\mathbf{x}})$) and bounded $-1 \leq \text{SSIM}(\hat{\mathbf{x}}, \mathbf{x}) \leq 1$ with $\text{SSIM}(\hat{\mathbf{x}}, \mathbf{x}) = 1$ if $\hat{\mathbf{x}} = \mathbf{x}$.

Peak Signal-to-Noise Ratio The peak signal-to-noise ratio (PSNR) gives the ratio between the power peak of the signal (i.e. the maximum possible pixel value) and the power of the corrupting noise:

$$\text{PSNR}(\hat{\mathbf{x}}|\mathbf{x}) = 10 \cdot \log_{10} \frac{R^2}{\text{MSE}(\hat{\mathbf{x}}|\mathbf{x})} \tag{1.7}$$

where R represents the dynamic range of pixel intensities. However, this measure requires the knowledge of the uncorrupted signal which in practice is not always the case.

Signal-to-Noise Ratio Since the true uncorrupted signal is often not known, the denoising performances are commonly evaluated via the signal-to-noise ratio (SNR) measurement exploiting an underlying noise model. The SNR of the images can be estimated from the noise model of (1.4) as:

$$\mathrm{SNR}(\hat{\mathbf{x}}) = \frac{\zeta A}{\sqrt{\zeta^2(A + \lambda_B) + \sigma^2}} \tag{1.8}$$

In our context, the mixed *Poisson-Gaussian* noise parameters $(\zeta, \lambda_B, \mu, \sigma)$ are estimated using cumulant method, matching the first four cumulants of $\hat{x}$ with the k-statistics of the samples in a uniform image region [Rose 2002]. This exploits the property that the k-statistics are the minimum variance unbiased estimators for cumulants.

Contrast-to-Noise Ratio. The contrast-to-noise ratio (CNR) is also an interesting measure of image quality. Indeed, when using a regularization term for the optimization of the image reconstruction process, the CNR determines if the sharpness of the object contours is compromised by the noise reduction. In other words, a denoised image having high CNR guarantees that noise and high-frequency details (such as sharp edges) were well discriminated by the regularization term. The CNR measure can be computed as:

$$\mathrm{CNR} = \frac{|\hat{\mathbf{x}}_{\Re_1} - \hat{\mathbf{x}}_{\Re_2}|}{\sigma}$$

where $\hat{\mathbf{x}}_{\Re_1}$ and $\hat{\mathbf{x}}_{\Re_2}$ are signal intensities on the region $\Re_1$ and $\Re_2$, which correspond to an object of interest and the surrounding background, and σ is the standard deviation of the noise distribution model.

1.2 Image Representation, Norms and Sampling

In this section, we describe mathematical models for image representations and measurements of information content via signal norms. We first introduce the basic tools to the representation of images in a frequency domain such as the Fourier domain. The Fourier domain is of central importance in our work since we have used random sampling in this domain. The following subsections will describe sparse and compact image representations commonly used for image denoising, compressed

sensing, dictionary learning and image compression. We mainly focus on sparse representations for image denoising and compressed sensing.

1.2.1 The Fourier Transform

The Fourier transform is a powerful tool in linear system analysis and is everywhere in physics and mathematics. It decomposes a signal over oscillatory waveforms that reveal its spectral content. In the work presented in this thesis, the Fourier transform and its link with optics will be recalled and discussed several times in the next chapters. One of the most remarkable and useful properties of a converging lens is its inherent ability to perform two-dimensional Fourier transforms of the image of the observed illuminated object. This complicated analog operation can be performed using a coherent optical setup which takes advantage of the basic laws of propagation and diffraction of light.

Mathematically, the Fourier analysis allows to represent any finite energy function $x(t)$ as a sum of sinusoidal waves $e^{i\omega t}$, also called the inverse Fourier transform:

$$x(t) = \frac{1}{2\pi} \int_{-\infty}^{+\infty} X(\omega) e^{i\omega t} d\omega. \tag{1.9}$$

In this decomposition, the Fourier transform $X(\omega)$ describes which frequencies are present in the original function $x(t)$, being defined as:

$$X(\omega) = \frac{1}{2\pi} \int_{-\infty}^{+\infty} x(t) e^{-i\omega t} dt. \tag{1.10}$$

In the discrete case and for 2-dimensional signals, such as for digital images, the discrete Fourier transform (DFT) is expressed as:

$$\begin{aligned} X(\omega, \nu) &= \mathcal{F}\{x(a,b)\} \; : \; \mathbb{C}^N \rightarrow \mathbb{C}^N \\ X(\omega, \nu) &= \frac{1}{\sqrt{N}} \sum_{a=0}^{n-1} \sum_{b=0}^{n-1} x(a,b) e^{-2\pi i \left(\omega \frac{a}{n} + \nu \frac{b}{n}\right)} \end{aligned} \tag{1.11}$$

where $N = n \times n$ is the total number of pixels.

The embedded structure of the DFT leads to fast Fourier transform (FFT) algorithms, which compute discrete Fourier coefficients with complexity $O(NlogN)$ instead of N^2 for an image of size N^2. This is very important in the image processing domain where N is often very large.

1.2.1.1 The 1D Fourier Transform as a Decomposition

When dealing with linear systems it is useful to decompose a complex signal (e.g. an image with complex features) into simpler inputs, calculate the response of the system to each of these inputs, and superpose the individual responses to build up the total response. Fourier analysis provides the basic tools for such decomposition. Over discrete signals, the Fourier transform can be seen as a decomposition in a discrete orthogonal exponential basis $\{e^{2\pi ikn/N}\}$, for $0 \leq k \leq N$ of $\mathbb{C}^N$. This decomposition has properties similar to the Fourier transform on functions, such as hermitian symmetry and evenness/oddness of real and imaginary components.

Notice that the DFT can be computed using a Vandermonde matrix in the form:

$$\mathcal{V} = \begin{bmatrix} \omega_N^{0\cdot 0} & \omega_N^{0\cdot 1} & \cdots & \omega_N^{0\cdot(N-1)} \\ \omega_N^{1\cdot 0} & \omega_N^{1\cdot 1} & \cdots & \omega_N^{1\cdot(N-1)} \\ \vdots & \vdots & \ddots & \vdots \\ \omega_N^{(N-1)\cdot 0} & \omega_N^{(N-1)\cdot 1} & \cdots & \omega_N^{(N-1)\cdot(N-1)} \end{bmatrix}$$

where

$$\omega_N = \frac{1}{\sqrt{N}} e^{-2\pi i/N} \tag{1.12}$$

Then, the DFT can be written as:

$$\begin{bmatrix} X_0 \\ \vdots \\ X_{N-1} \end{bmatrix} = \begin{bmatrix} \omega_N^{0\cdot 0} & \cdots & \omega_N^{0\cdot(N-1)} \\ \vdots & \ddots & \vdots \\ \omega_N^{(N-1)\cdot 0} & \cdots & \omega_N^{(N-1)\cdot(N-1)} \end{bmatrix} \begin{bmatrix} x_0 \\ \vdots \\ x_{N-1} \end{bmatrix}$$

or

$$\mathbf{F} = \mathcal{V}\mathbf{f}$$

and the inverse Fourier transform is given by the inverse of the matrix $\mathcal{W}$ [Turner 1966]. We observe here that each Fourier coefficients F_i are therefore generated from a linear combination of all the points from the input signal f_i. This will become a crucial property of the Fourier transform for the exploitation of Fourier-based measurements of sparse spatial signals.

1.2.2 Image Transform and Sparsity

Signals can be decomposed on sets of basis functions, for multiple purposes, such as spectral analysis, compression and denoising. For a finite-length signal $\mathbf{x} \in \mathbb{R}^N$ the projection on the basis $\Psi \in \mathbb{R}^{N \times N}$ generates a vector of projection coefficients $\mathbf{c} \in \mathbb{R}^N$ such that $\mathbf{x} = \Psi\mathbf{c}$. This means that we can write $\mathbf{x}$ as a linear combination of N atoms from a dictionary Ψ.

$$\mathbf{x} = \sum_{i=1}^{N} \psi_i c_i \tag{1.13}$$

If the projection basis functions Ψ form an orthogonal basis, the inverse transform $\Psi^T \in \mathbb{R}^{N \times N}$ can be used to compute the projection coefficients.

Well-known image transforms include the Fourier transform, wavelet transforms or the discrete cosine transform. Besides spectral analysis performed with Fourier basis functions, image transform usually targets a compact representation of the original signal with few non-zero coefficients. The transform is then called sparsifying. Choosing the appropriate sparsifying basis functions is a key step towards an efficient sparse representation and applies to compressed sensing. The assumption that natural signals, such as images, admit a sparse decomposition over a particular dictionary leads to efficient algorithms for handling such data. In recent years, dictionaries composed by a union of transforms were proposed to optimize the sparsity of the decomposition of a given signal or image [Fadili 2006, Aharon 2005]. For compression, the use of orthonormal basis is important to define a representation where the signal is well approximated with few non-zero coefficients. This is less important for signal estimation from noisy measures. All these applications are closely related to approximation theory. Enforcing sparsity representations of images has been used in denoising and compression since Donoho and Johnstone's initial works in the early 1990s [Donoho 1994, Donoho 1995b, Donoho 1998], where sparse signals in the wavelet domain were denoised by assuming that the noiseless version of the signal is sparse. In the past few years, many applications have employed sparse signal decompositions for signal denoising [Elad 2006], compression [Mallat 2009], enhancement [Yu 2010], super-resolution [Yang 2010a, Yu 2009], inpainting [Fadili 2009] and deconvolution [Fadili 2006]. These processing tasks all rely on the assumption that the noise components are decomposed in separate components from the true signal,

and with lower-intensity coefficients. Image decomposition on wavelet basis, along with optimization of the dictionary of wavelet functions, remains computationally costly. As an alternative, direct spatial norms have been proposed to measure the sparsity of the image content in terms of homogeneous objects and background.

1.2.3 Sparsifying Transforms

Identification of suitable sparsifying transforms typically requires the optimization of a non-linear approximation of the original signal from selected projection coefficients, associated with a subset of projection functions selected from a dictionary. A dictionary is a collection of parameterized waveforms $\mathcal{D} = (\psi_\gamma)_{\gamma\in\Gamma}$. The waveforms ψ_γ are discrete-time signals called atoms. Depending on the dictionary, the parameter γ can have the interpretation of indexing the frequency, in which case the dictionary is a frequency or Fourier dictionary, of indexing the time-scale jointly, in which case the dictionary is a time-scale dictionary, or of indexing the time-frequency jointly, in which case the dictionary is a time-frequency dictionary. Usually dictionaries are complete or overcomplete, containing exactly N atoms, or more than N atoms. One could also have continuum dictionaries containing an infinity of atoms and undercomplete dictionaries for special purposes, containing fewer than N atoms. The past decade has seen great successes in studying the optimization of signal representation. Beyond the Fourier domain, where signals are represented by a superposition of sinusoids of different frequencies, a large range of dictionaries suited for the sparsification of natural signals and images have been proposed, such as wavelets, curvelets, Gabor dictionaries, wavelet packets, steerable pyramids, and much more. For a given signal x, a transform provides a decomposition of the signal and a reconstruction from the linear combination of a set of atoms (projection functions) selected in a subset Γ of a dictionary $\mathcal{D}$ as:

$$x = \sum_{\gamma\in\Gamma} \alpha_\gamma \psi_\gamma \tag{1.14}$$

Sparsity of the signal decomposition is measured by the ℓ_p norm of the projection coefficients:

$$\| \alpha_\gamma \|_{\ell_p} = \left\{ \sum |\alpha_\gamma|^p \right\}^{1/p} \tag{1.15}$$

The transform is characterized as sparsifying if the ℓ_p-norm of the projection

coefficients (for $p = 0, 1$) is small compared to the signal ℓ_p-norm so that only a small subset of m coefficients is required to provide an accurate reconstruction of the original signal, as:

$$x = \sum_{i=1}^{m} \alpha_\gamma \psi_\gamma + r_m \tag{1.16}$$

where r_m is the residual, corresponding to the error made by preserving only m coefficients, and is small for efficient sparsifying transforms.

The problem of selecting the subset of m coefficients bears two levels of nonlinearity. The first level of nonlinearity is the selection of a subset of m coefficients from a larger set of N projections, usually based on the magnitude of the coefficients, given a family of basis functions. The second level of nonlinearity replaces a single family of basis functions with a more general system which is not necessarily minimal (for example, a redundant system or a dictionary of functions). Selection of an optimal set of m coefficients in this setting is much more complicated than with a single basis. However, the importance of redundant systems arises in both theoretical questions and in practical applications.

Sparsifying transforms have played an important role in the past decade, notably for denoising, compression and compressed sensing. The assumption that natural signals, such as images, admit a sparse decomposition over a redundant dictionary have lead to efficient algorithms for handling such sources of data. Sparsifying transforms allow to project a signal in a low-dimensional or compact domain and provide very strong prior information for image restoration.

Most of the new image dictionaries are overcomplete, and are made from a collection of transforms such as Fourier and wavelets dictionaries, to handle piecewise smooth and textured objects. In these cases, the decomposition (1.14) is non-unique. Several methods have been proposed to identify signal-specific optimal decompositions, including matching pursuit (MP) and orthogonal matching pursuit (OMP). Instead of exploiting pre-defined dictionaries as described above, Aharon et al. have introduced the K-SVD algorithm [Aharon 2005], to learn a dictionary that leads to sparse representations on some training signals.

Searching Sparse Representations

It is useful to determine whether a signal has a sparse representation in a given dictionary or union of basis [Gribonval 2003]. However, it is generally difficult to know if the sparse representation of a signal is optimal [Gribonval 2005, Gribonval 2007]. If an orthonormal basis Ψ is used, then a signal x has a unique representation $c = \Psi^{-1}x$ and we can learn whether x is S-sparse in c simply by inspecting this vector. When Ψ is a frame (i.e. a basis with redundant projection functions), there are infinitely many representations c for x. Several algorithms have been proposed to obtain sparse representations for a signal x in a frame Ψ. We review in this section the main ones.

ℓ_0-norm Minimization

The most intuitive algorithm proceeds by finding the sparsest representation of a signal x in a pre-defined basis Ψ. It can be estimated by computing the ℓ_0 pseudo-norm of the coefficients, defined as the total number of non-zero coefficients of the resultant vector such as $\| \alpha_\gamma \|_{\ell_0} = \sum \alpha_\gamma^0$. The problem can be expressed as:

$$\hat{\alpha_\gamma} = \arg \min_{\alpha_\gamma \in \mathbb{R}^N} \| \alpha_\gamma \|_{\ell_0} \text{ subject to } \Psi\alpha_\gamma = \mathbf{x} \tag{1.17}$$

This algorithm will find the sparsest representation of x. However, the computational complexity is combinatorial and requires an exhaustive search of all possible vectors x. For large scale signals this problem becomes intractable.

ℓ_1-norm Minimization

As proposed by Chen, Donoho and Saunders [Chen 1998], a convex relaxation of the problem (1.17) can be used by replacing the ℓ_0 pseudo-norm by the ℓ_1-norm, defined as $\| \alpha_\gamma \|_{\ell_1} = \sum |\alpha_\gamma|$. The problem can be expressed as:

$$\hat{\alpha_\gamma} = \arg \min_{\alpha_\gamma \in \mathbb{R}^N} \| \alpha_\gamma \|_{\ell_1} \text{ subject to } \Psi\alpha_\gamma = \mathbf{x} \tag{1.18}$$

This algorithm is known as the Basis Pursuit (BP) and is detailed in the subsection 1.2.3.1. Thanks to the convex relaxation, this algorithm can be implemented as a linear program, making its computational complexity polynomial in the signal length.

1.2.3.1 Basis Pursuit and Linear Programming

The principle of basis pursuit (BP) is to find a representation of the signal whose coefficients have minimal ℓ_1 norm and is very close to the compressed sensing principle. Formally, one solves the problem

$$\hat{\alpha_\gamma} = \arg \min_{\alpha_\gamma \in \mathbb{R}^N} \| \alpha_\gamma \|_{\ell_1} \text{ subject to } \Psi\alpha_\gamma = \mathbf{x}$$

Instead of using of a standard quadratic norm which would provide a convex problem, this algorithm replaces the ℓ_2 norm with the ℓ_1 norm. This apparently slight change has major consequences. Solving the quadratic optimization problem with linear equality constraints involves essentially just the solution of a system of linear equations. In contrast, BP requires the solution of a convex, non-quadratic optimization problem, which involves considerably more effort and sophistication.

This problem becomes feasible by using linear programming (LP) techniques and a solution can be obtained by solving an equivalent linear program [Bloomfield 1983].

Greedy Algorithms

The greedy algorithms came as an alternative to optimization-based algorithms to find sparse representations. The main idea behind these algorithms is to perform iterations to select columns of Ψ with the greater correlation with the relevant signal f.

The matching pursuit algorithm (MP) [Mallat 1993] proceeds iteratively by finding the function Ψ within the dictionary most correlated to the signal residual, which is obtained by subtracting the contribution of previously selected Ψ from the original signal. The algorithm is defined as Algorithm 1.

While the MP algorithm is computationally efficient and often features good performance, there are specific cases in which a dictionary of basis functions Ψ can be constructed that defeat the algorithm by preventing convergence. Such a flaw is manifested, for example, when the algorithm selects a cycle of functions Ψ that are highly coherent to correct for an overcompensation made by a certain Ψ.

Matching pursuit approximations are improved by orthogonalizing the directions of the projections [Davis 1994, Pati 1993]. The resulting orthogonal matching pursuit (OMP) converges with a finite number of iterations. This orthogonalization was introduced by Mallat and Zhang together with the nonorthogonal pursuit algorithm.

Algorithm 1 Matching pursuit

Input: Sparsifying basis Ψ and signal x
Output: List of coefficients c and ψ

Initialize: $i = 1, \mathbf{r} \leftarrow \mathbf{x}, \hat{c}_0 = 0$
while criterion on $\mathrm{x} \neq \Psi c$ **do**
  $\mathbf{b} \leftarrow \Psi^T \mathbf{r}_i$; ▷ form residual signal estimate
  $\hat{c}_i \leftarrow \hat{c}_{i-1} + \mathcal{T}(\mathbf{b}, 1)$; ▷ update largest magnitude coefficient
  $r_{i+1} \leftarrow \mathbf{r}_i - \Psi\mathcal{T}(\mathbf{b}, 1)$; ▷ update measurement residual
  $i \leftarrow i + 1$;
end while
return $\hat{\mathrm{x}} \leftarrow \Psi c_i$

The algorithm is modified as shown in Algorithm 2, where we let Ψ_Ω denote the restriction of the dictionary Ψ to the functions corresponding to the index set $\Omega \subseteq 1, ..., N$. The residual is obtained by subtracting the projection of the signal x into the span of the previously selected functions. While OMP does not suffer the aforementioned flaw, it is penalized in its computational complexity by the calculation of the pseudoinverse of the matrix composed of the selected Ψ_Ω functions.

Algorithm 2 Orthogonal Matching pursuit

Input: Sparsifying basis Ψ and signal x
Output: List of coefficients c and ψ

Initialize: $i = 1, \mathbf{r} \leftarrow \mathbf{x}, \hat{c}_0 = 0, \Omega = \emptyset$
while criterion on $\mathrm{x} \neq \Psi c$ **do**
  $\mathbf{b} \leftarrow \Psi^T \mathbf{r}_i$; ▷ form residual signal estimate
  $\Omega \leftarrow \Omega \cup \mathrm{supp}(\mathcal{T}(\mathbf{b}, 1))$; ▷ add index of residual's largest magnitude entry to signal support
  $\hat{c}_i|_\Omega \leftarrow \Psi_\Omega^\dagger \mathbf{x}, \hat{c}_i|_\Omega \leftarrow 0$; ▷ form signal estimate
  $r_{i+1} \leftarrow \mathbf{r}_i - \Psi\mathcal{T}(\mathbf{b}, 1)$; ▷ update measurement residual
  $i \leftarrow i + 1$;
end while
return $\hat{\mathrm{x}} \leftarrow \Psi c_i$

1.2.4 Total Variation Measures on Images

The total variation (TV) measure was introduced as a spatial sparsity measure of images in [Rudin 1994, Rudin 1992, Chambolle 1997]. For digital images, it measures the total amplitude of pixels variations, and is calculated by approximating

the signal derivative by finite differences over the sampling distance, such as:

$$\mathrm{TV}(x) = \sum_{a,b} \sqrt{\{x_{(a+1,b)} - x_{(a,b)}\}^2 + \{x_{(a,b+1)} - x_{(a,b)}\}^2} \tag{1.19}$$

The total variation thus measures the total amplitude of the oscillations of x. We say that the discrete signal has a bounded variation if $\| x \|_{TV}$ is bounded by a constant independent of the spatial resolution N. Looking in more details at the transform which produces the TV coefficients, it corresponds to the ℓ_2-norm of a particular operation on the image [Candès 2005d], based on the computation of horizontal ∇_a and vertical ∇_b gradients and combination of these operators into a complex-valued image: $\nabla_a + i\nabla_b$. The TV coefficients are the ℓ_2-norm of this transformed image (computed locally for each pixel) and the CS framework minimizes the global ℓ_1-norm of these TV coefficients over the whole image. Such a transform corresponds to the decomposition of the image onto Heavisides basis functions, the support of which is adaptive (similarly to the *Basis Pursuit* framework for decompositions on dictionaries of projection functions [Chen 1998]) and defined by the localization of high-gradient values in the image (i.e. edge maps).

The TV value depends on the length of the image level sets, and is therefore very sensitive to the presence of image noise, while being very simple to compute. It therefore plays a very important role in image processing for denoising (TV filtering) and variational segmentation. The total variation can be used a sparsity constraint suited for piecewise regular images as it provides an intuitive and precise mathematical framework to characterize the piecewise regularity of objects in an image. More broadly, it can be used to compute approximation errors, to evaluate the risk when removing noise components from an image, and to analyze the distortion rate of image transform codes.

As we will see, the compressed-sensing framework relies on sparsity constraints enforced on a reconstructed image. To provide additional computational efficiency, it relies on a specific sampling of the image information in a domain incoherent with the sparsity domain.

1.2.5 Two-Dimensional Sampling Theory

The sampling theorem by C.E. Shannon in 1949 places restrictions on the frequency content of the time/space function signal x. It states that in order to recover the signal x exactly it is recommended to sample at a rate greater than twice its highest frequency component. For example to sample an analog signal having a maximum frequency of $2KHz$ requires sampling at greater than $4KHz$ to preserve and recover the waveform exactly. The consequences of sampling a signal at a rate below its highest frequency component results in a phenomenon known as aliasing due to spectrum overlap. This phenomenon is roughly illustrated in Fig. 1.3, showing that sampling the function represented by the red curve with low frequency can result in the representation of the blue curve, which gives a completely erroneous representation.

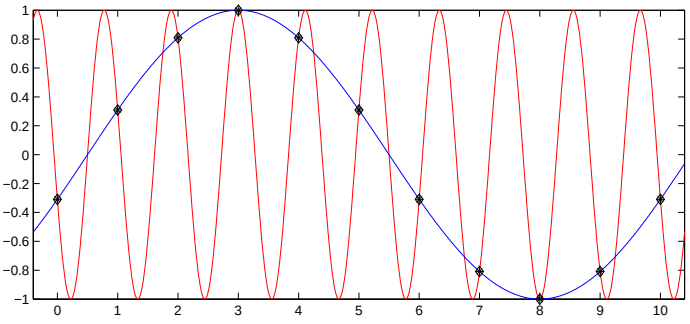

Figure 1.3: Aliasing.

Imaging a scene with a photography digital camera for example involves the measurement of thousands or millions of pixels, otherwise, to correctly display the finest details of the scene. Respecting such sampling density may become rapidly expensive in terms of acquisition time, design of large captors, storage size and transmission bandwidth.

In reality, with rapid advancement in data acquisition technologies (i.e. analog-to-digital and digital-to-analog converters) and in high-resolution sensor devices such as CCD and CMOS captors, hundred of images are produced per second with a resolution up to 10^6 pixels per image. The frame rate of a camera is normally limited by its resolution. Moreover, the huge amount of data produced becomes difficult to process and to analyze.

From a mathematical point of view, we define a two-dimensional signal as an array $\mathbf{x}[n, m]$, with values sampled on a signal of finite energy $\mathbf{x}(a, b)$ at discrete spatial positions $[n, m]$ in the plane. We further assume that the signal is band-limited (i.e. with a zero power spectrum for frequencies $\nu > B$) If samples are taken sufficiently close to each other, the sampled image $\mathbf{x}[n, m]$ is an accurate representation of the original image $\mathbf{x}(a, b)$, which can be reconstructed accurately by interpolation of $\mathbf{x}[n, m]$. More precisely, the sampling theorem states that the original image can be fully recovered if it is sampled at a rate $\nu \geq 2B$. The value $\nu = 2B$ is called the Nyquist frequency. The sampling theorem therefore sets the equivalence, under specific conditions, between the knowledge of a continuous signal $\mathbf{x}(a, b)$, known for all (a, b) and a set of samples $\mathbf{x}[n, m]$. The conditions are: samples $[n, m]$ must be regularly spaced and with intervals smaller than $\frac{1}{2B}$. A bandlimited signal has an infinite support. Sampling on a finite number of samples implicitly assumes that the signal is periodic (so that full knowledge of it can be acquired with a finite set of measures), and therefore replicates the spectrum in the Fourier domain, at intervals of ν. Reconstruction of the original image $\mathbf{x}(a, b)$ from the samples $\mathbf{x}[n, m]$ can be done by masking the Fourier transform with the rectangle function defined on the frequency support $[-B, B]$. The Fourier transform of the rectangle function is the sinc function, and therefore corresponds to the interpolating function to be used to reconstruct the original image, as:

$$\mathbf{x}(a, b) = \sum_{n,m} \text{sinc}(a - n, b - m)x[n, m] \tag{1.20}$$

The compressed sensing introduced a novel framework to the sampling theory, enabling to reconstruct some images from the acquisition of much less samples than required by the Nyquist sampling frequency, under some specific constraints regarding the content of the image, that will be discussed in the paragraph introducing the CS.

1.3 Compressed Sensing Theory

Compressed sensing provides a mathematical framework for the reconstruction of sparse signals (i.e. compressible signals) from few measures acquired in a domain incoherent with the sparsity domain. The main theoretical findings in this recent field

have mostly focused on defining the minimum number of incoherent measurements necessary to reconstruct an accurate representation of the original signal with a high probability and the nonlinear optimization methods suited for the reconstruction process. Another equally important field of research focuses on the design of novel sensing devices based on the CS sampling scheme, which is not a trivial problem to solve. While current researches spend many efforts on performing faster reconstruction of original signals from compressed measurements, we were interested in this work in the acquisition process to achieve compressed sensing acquisitions of microscopic images.

1.3.1 Signal Sparsity

A discrete signal is considered sparse when it has a large number of zero coefficients in some basis. We define a S-sparse signal $x \in \mathbb{R}^N$ in the basis Ψ if there exists a vector $c \in \mathbb{R}^N$ with only $S \ll N$ nonzero entries such that $x = \Psi c$. We call the set of indices corresponding to the nonzero entries the support of c and denote it by $\text{supp}(c)$.

An example of a S-sparse signal is illustrated in Figure 1.4 (left). Natural signals measuring discrete events or natural images with smooth and homogeneous objects can be considered approximately sparse in some spatial basis and can be accurately approximated with a small set of coefficients as illustrated in Figure 1.4 (right).

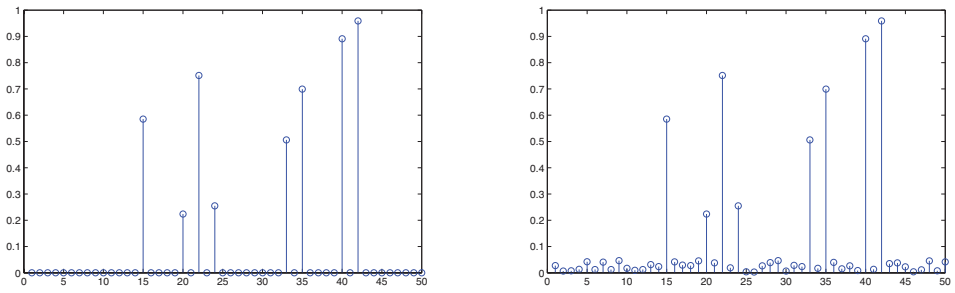

Figure 1.4: Signal sparsity. Left: S-sparse signal with $S = 8$, or 8 time-values being non-zero. Right: Nearly S-sparse signal, with 8 strong coefficients and several small coefficients.

Sparsity of a signal might not be trivially observed on the direct spatial observation, but rather identified with the use of appropriate projection basis functions. Consider the simple signal in Figure 1.5 (top), represented in blue. This signal can

be represented as a linear combination of Gaussian functions, represented in green scattered line. A single Gaussian basis function is illustrated in Figure 1.5 (middle). We can observe the sparse representation of the original signal on Gaussian basis functions, composed by six elements (bottom). This example illustrates the upmost importance of the choice of the sparsity basis.

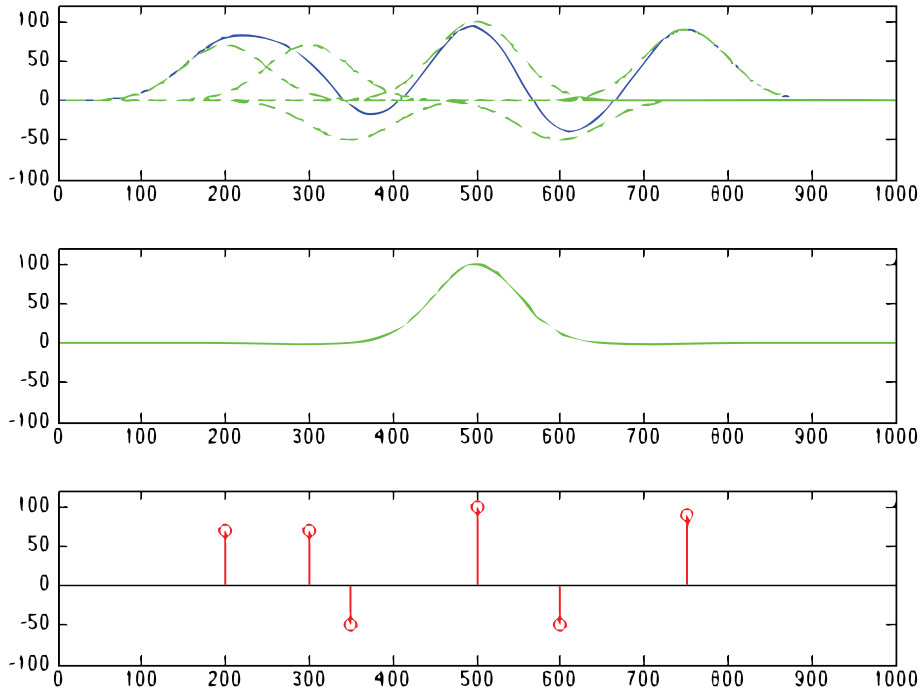

Figure 1.5: Example of sparse representation of a signal (top) using a simple dictionary (middle), and its respective coefficients (bottom).

In the general case [Chen 1998, Donoho 2001], we assume that we work with a signal that has a S-sparse representation in a set of basis functions $\Psi = \{\Psi_i\}_{i=1}^{N}$ if:

$$x = \sum_i c_i \Psi_i \qquad \text{with} \| \ c \ \|_{\ell_0} = S \tag{1.21}$$

Here Ψ_i represents a basis function and the ℓ_0-norm is defined as the number of nonzero coefficients of c.

Natural images typically have a compact representation when expressed in a wavelet-types of basis functions. For example, we show a drosophyla cell in figure 1.6a and its wavelet coefficients in figure 1.6b (magnification in figure 1.6c). The

wavelet coefficients offer a compact representation with most coefficients close to zero, and only few large coefficients that capture most of the information. This property is used for the JPEG-2000 compression [Taubman 2002].

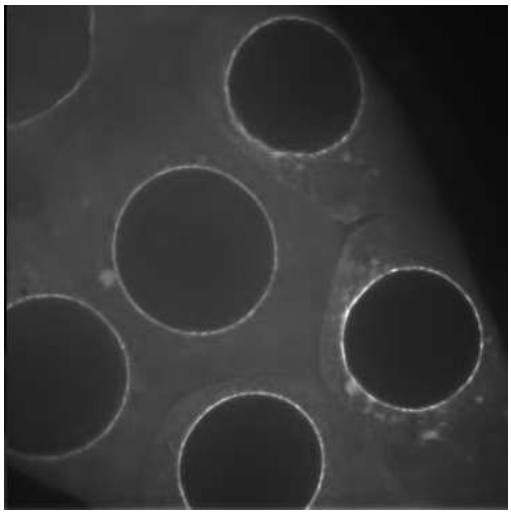

(a) Drosophyla cell.

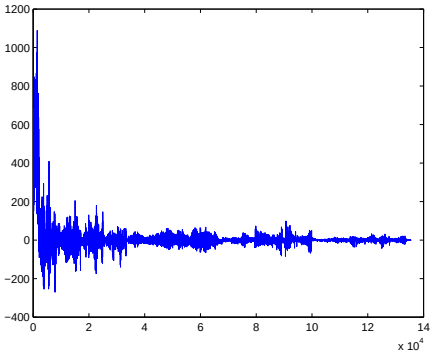

(b) Wavelet coefficients.

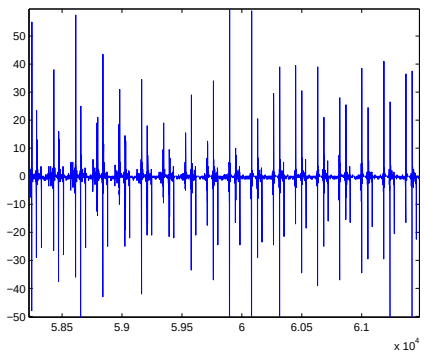

(c) Magnification in the wavelet coefficients.

Figure 1.6: Original megapixel image with pixel values in the range [0,255] and its wavelet transform coefficients.

In our framework we chosen the Total Variation (TV) as the sparsifying measure used in the CS reconstruction, corresponding to projections on image-specific Heavisides basis functions [Candès 2006b, Cohen 1999]. This measure is well-known in image processing and very popular in variational segmentation problems for its abil ity to limit high frequency components and to provide regularized piecewise smooth regions. This measure is also well suited for denoising where the goal is to restore an image with smooth objects and background. Minimization of the TV norm, intro-

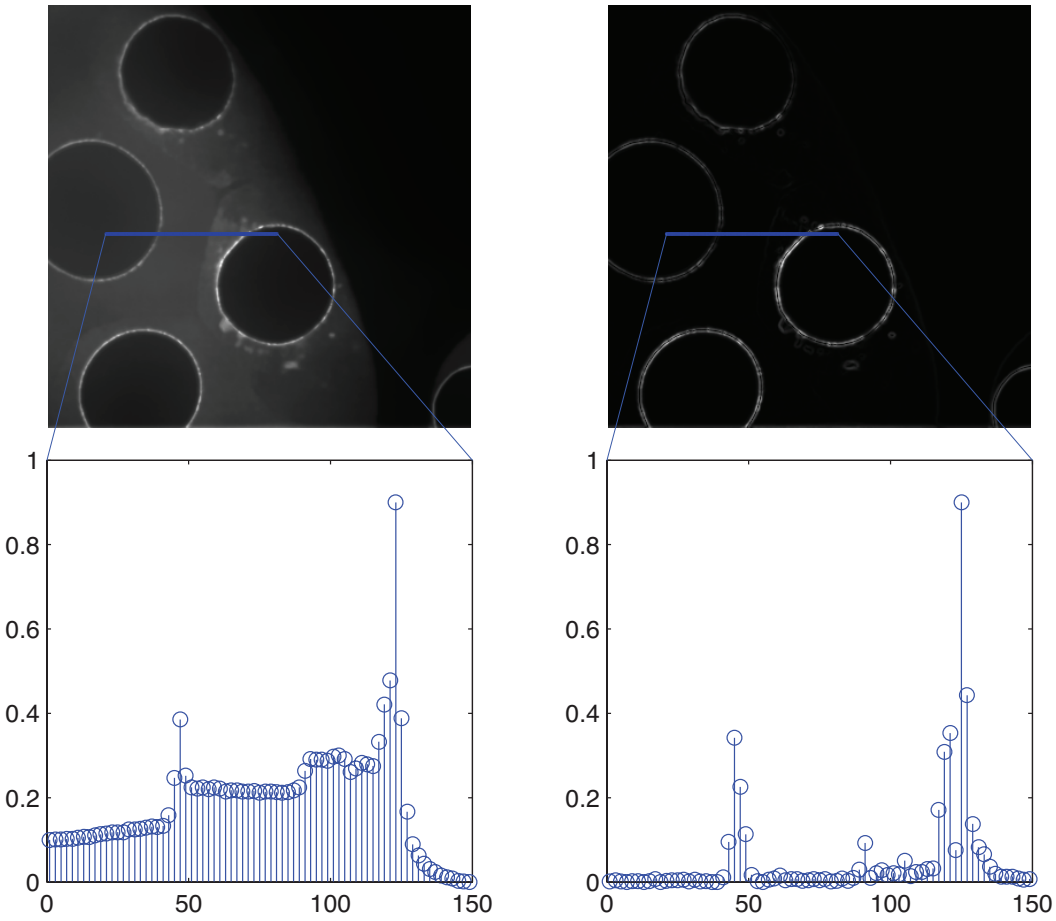

Figure 1.7: Image sparsity illustrated in a two-dimensional spatial domain. Top left: original image. Top right: sparse representation domain (using the gradient of the signal). Bottom: intensity profiles from corresponding blue lines in the spatial and gradient domains.

duced in [Chan 2001, Rudin 1992] for signal denoising, corresponds to a constraint on the number of discontinuities in an image, and the homogeneity of the regions. TV sparsity constraint for CS was introduced by Candès [Candès 2005d]. The TV constraint is well suited for biological images, where structures and background provide small gradient values while a finite set of edges provides high gradient values as illustrated in Figure 1.7 for drosophila ovocytes.

1.3.2 Sensing Matrix and Incoherence

In compressed sensing, we are constrained to perform image measures in a domain incoherent with the sparsifying domain. Intuitively, sampled measures must contain

dense information from the original image. If the signal is sparse in the basis defined by Ψ, its content must be spread in the measurement domain defined by Φ, so that the probability to sample zero values should be very small. The incoherence constraint has been formulated through several criteria for Φ and Ψ, based on mutual coherence measures [Candès 2006b, Donoho 2006a], or matrix properties such as the *Restricted Isometry Property* (RIP) condition introduced by Candès and Tao [Candès 2005e, Candès 2008]. The RIP condition is defined for Φ, an order k and constant $\delta_k \in (0, 1)$ as:

$$(1 - \delta_k) \| x \|^2 \leq \| \Phi x \|^2 \leq (1 + \delta_k) \| x \|^2 \tag{1.22}$$

with $x \in \mathbb{R}^N$, $\Phi x \in \mathbb{R}^M$ and $M \ll N$. The RIP condition enforces the sensing matrix satisfying the k-Restricted Isometry Property to act as a near isometry on all k-sparse vectors. More precisely, to ensure unique and stable reconstruction of k-sparse vectors, it is sufficient that Φ satisfies a $2k$-RIP condition. Candès and Tao [Candès 2005e, Candès 2008] have shown that whenever a matrix Φ satisfies this property, we can obtain accurate reconstructions of sparsely sampled sparse signals with high probabilities.

The two fundamental principles in compressed sensing are therefore to construct suitable sparse sensing matrices Φ, and recover the signal from few measurements efficiently, under some sparsity constraints in a domain incoherent with the sensing domain. Now the question arises on how to design a suitable sensing matrix Φ. To tackle this task, it is important to first take into account the fact that the incoherence between Φ and Ψ affects the number M of required measurements as:

$$M = C \cdot \mu^2(\Phi, \Psi) \cdot S \cdot \log N \tag{1.23}$$

where $\mu(\Phi, \Psi)$ is an incoherence measure, giving a rough characterization of the degree of similarity between the sparsity and measurement systems, and can be computed as:

$$\mu(\Phi, \Psi) = \max_{i,j} |\langle \Phi_i, \Psi_j \rangle| \quad \text{for} \quad \begin{aligned} &\| \Phi_i \|_2 \simeq 1 \\ &\| \Psi_j \|_2 \simeq 1 \end{aligned} \tag{1.24}$$

The definition of the number of required measurements M in (1.23) provides some insights on how the choice of the sensing modality (Φ) and the signal model (Ψ) affect the efficiency of the CS sampling scheme.

In the work presented in this thesis, we chose to perform Fourier-based acquisitions based to the intrinsic frequency-content of the image information in optics and the fact that random acquisitions in the Fourier domain, encoded by a matrix with 1s and 0s at random frequency locations, verifies the incoherence property when combined with TV spatial constraints [Candès 2008]. The Fourier transform being an orthogonal linear transform, sub-sampling of its coefficients does not provide enough information to accurately reconstruct the original signal. The key component of the CS sampling framework is to propose the formulation of an optimal reconstruction of the original signal, given some a-priori constraints on its spatial sparsity. This prior information reduces the number of degrees of freedom of x making signal reconstruction possible and accurate with high probability. We note that greater spatial sparsity of the observed image provides a larger support of its frequency content leading to less measurements required and a better fit of the a priori constraint during image reconstruction.

1.3.3 CS Image Recovery Algorithms

Before reviewing specific CS reconstruction algorithms, we provide a short review some quadratically constrained ℓ_1-minimization problems. We can start with the basis pursuit problem formulated as:

$$(\mathrm{BP}_\varepsilon) \qquad \min_{\alpha_\gamma \in \mathbb{R}^2} \| \alpha_\gamma \|_{\ell_1} \quad \text{subject to} \quad \| \mathbf{x} - \Psi\alpha_\gamma \|_{\ell_2} \leq \varepsilon \tag{1.25}$$

where ε quantifies the uncertainty about the reconstruction of x when considering that the projection coefficients are noisy. Generally, ε can be estimated, which makes this formulation often preferred. A second commonly used approach considers solving the problem in the Lagrangian form, such as:

$$(\mathrm{QP}_\lambda) \qquad \min_{\alpha_\gamma \in \mathbb{R}^2} \| \alpha_\gamma \|_{\ell_1} + \frac{1}{2} \| \mathbf{x} - \Psi\alpha_\gamma \|_{\ell_2}^2 \tag{1.26}$$

which is also known as the basis pursuit denoising problem (BPDN) [Chen 1998]. This problem is popular in signal and image processing because of its loose interpre-

tation as a maximum a *posteriori* estimate of $\mathbf{x}$ in a Bayesian setting. In statistics, the same problem is known as the lasso [Tibshirani 1996]:

$$(\mathrm{LS}_\tau) \qquad \min_{\alpha_\gamma \in \mathbb{R}^2} \| \mathbf{x} - \Psi\alpha_\gamma \|_{\ell_2} \quad \text{subject to} \quad \| \alpha_\gamma \|_{\ell_1} \leq \tau \tag{1.27}$$

These three problems are equivalent provided that $\varepsilon, \lambda, \tau$ obey some special relationships. With the exception of the case where the matrix Ψ is orthogonal, this functional dependence is hard to compute [Berg 2008]. Usually, it is more natural to determine an appropriate ε rather than an appropriate λ or τ, so that the BP algorithm provides significant advantage over the BPDN and the lasso ones.

As detailed in the next chapter, the CS image reconstruction problem shares some great similarities with the previous optimization problems. The quadratic data fidelity term $\mathbf{x} = \Psi\alpha_\gamma$ or its relaxed version is replaced by $\Phi\mathbf{x} = \Phi\hat{\mathbf{x}}$ and the sparsity constraint $\| \alpha_\gamma \|_{\ell_1}$ is replaced by $\| \Psi\hat{\mathbf{x}} \|_{\ell_1}$ or in our case $\| \hat{\mathbf{x}} \|_{TV}$.

In this work we have used two algorithms to solve the ℓ_1-minimization problem for image reconstructions. The ℓ_1-magic [Candès 2006c, Candès 2006e] was used in the denoising framework to perform image reconstructions. In the second part, for compressed holographic microscopy, the algorithm NESTA [Becker 2009] was used for image reconstruction. The choice of the algorithms was performed based on optimal computational times, given similar image quality performance. We would like to emphasize though that the improvement or analysis of the existent algorithms available to solve the CS reconstruction problem, with Fourier-based measures and TV constraints is out of the scope of this thesis.

1.3.3.1 ℓ_1-magic

ℓ_1-magic was proposed in [Candès 2005a, Candès 2004b] by Candès *et al.* to recover sparse signals via convex programming. More specifically, we used this algorithm to solve quadratic data fidelity minimization with relaxed and unrelaxed constraints.

The algorithm consists in recasting the problem (1.18) as a second-order cone program (SOCP) [Alizadeh 2003] or a linear program (LP) if f is real, and uses a modern interior point solver [Nesterov 1994]. Although primal-dual techniques exist for solving second-order cone programs (see [Chan 1999, Alizadeh 2003]), their implementation is not quite as straightforward as in the LP case. The ℓ_1-magic algorithm implements each of the SOCP recovery problems using a log-barrier method.

The log-barrier method [Boyd 2004] is conceptually more straightforward than the primal-dual method, but consists again in solving a series of Newton steps. Note that solving the problem (1.18), if Φ is the identity matrix, reduces to the standard Rudin-Osher-Fatemi image restoration problem [Rudin 1992].

1.3.3.2 NESTA

NESTA was proposed in [Becker 2009] by Becker *et al.* and is able to efficiently solve the problem (1.18). This algorithm is based on Nesterov's work [Nesterov 2007] minimizing non-smooth functions, with an improved gradient descent method to derive first-order approximations which achieve a convergence rate proved to be optimal. As suggested by Nesterov's work, the main idea of NESTA is a subtle averaging of sequences of iterates, which has been shown to improve the convergence properties of standard gradient-descent algorithms.

In our case, NESTA provides an iterative algorithm which solves both the ℓ_1 and the TV minimization problem. It works by producing a decreasing sequence of iterates converging to the solution. At each step, the new guessed iterate solution is expressed as a linear combination of two terms. At the current point, the first term makes the iterate evolve in the exact opposite direction than the objective function gradient. Whereas the aim of the second term is to somehow keep track of the previous gradient directions. Moreover, it has been proved in [Nesterov 2007] that this second additional term helps to improve the convergence properties of the algorithm. Both terms constitute a solution to a quadratic optimization subproblem, which can be described analytically. In addition, if the property $\Phi\Phi^* = \mathrm{Id}$ holds (which means that the rows of Φ form an orthonormal family), then all matrix inverts in the analytical solutions of the quadratic subproblems can be simplified. This property results in a very fast computation of the optimal solution. The overall algorithmic complexity of each NESTA iteration is $\mathcal{O}(N + \mathcal{C}_\Phi)$, where $\mathcal{C}_\Phi$ stands for the complexity of a Φ or Φ^* application. When Φ is a subset of the rows of the Fourier transform matrix, the property $\Phi\Phi^* = \mathrm{Id}$ holds, $\mathcal{C}_\Phi = \mathcal{O}(N \log(N))$ and the computational cost of each NESTA step becomes then affordable.

NESTA is a first-order method for sparse recovery using an averaging of sequences of iterates to improve the convergence properties of standard gradient-descent algorithms. NESTA is based in the Nesterov work [Nesterov 1983, Nesterov 2004, Nesterov 2005] which proposed smoothing techniques with improved

gradient method to derive first-order methods.

Nesterov proposed an algorithm to minimize any smooth function f on the convex set Q_p

$$\min_{x \in Q_p} f(x)$$

where Q_p is the primal feasible set. Assuming that f is differentiable and $\nabla f(x)$ is Lipschitz, obeying:

$$\| \nabla f(x) - \nabla f(y) \|_{\ell_2} \leq L \| x - y \|_{\ell_2}$$

where L is an upper bound on the Lipschitz constant. Based on theses assumptions, the algorithm minimizes f over Q_p by iteratively estimating three sequences xk, yk and zk while smoothing the feasible set Q_p.

Initialize x_0. For $k \geq 0$,

1. Compute $\nabla f(x_k)$
2. Compute y_k:
   $y_k = \arg\min_{x \in Q_p} \frac{L}{2} \| x - x_k \|_{\ell_2}^2 + \langle \nabla f(x_k), x - x_k \rangle$
3. Compute z_k:
   $z_k = \arg\min_{x \in Q_p} \frac{L}{\sigma_p} p_p(x) + \sum_{i=0}^{k} \alpha_i \langle \nabla f(x_k), x - x_k \rangle$
4. Update x_k:
   $x_k = \tau_k z_k + (1 + \tau_k) y_k$

Stop when a given criterion is valid.

for $\alpha_k = 1/2(k+1)$ and $\tau_k = 2/(k+3)$ (see [Nesterov 2005]). A standard first-order would stop in step two and replacing x_k by y_{k-1}. We note that y_k is the current guess of the optimal solution at the iteration k. The Nesterov's approach propose to compute z_k which keeps a memory of all previous iterations by computing a weighted sum of the previous gradients such as $\sum_{i=0}^{k} \alpha_i \langle \nabla f(x_k), x - x_k \rangle$. It also makes use of a prox-function $p_p(x)$ for the primal feasible set Q_p, which is strongly convex with parameter σ_p [Ben-Tal 2001]. Nesterov has also enlarged this framework to deal with non-smooth convex functions [Nesterov 2005]. Becker *et al.* have extended the Nesterov method with NESTA, which can solve recovery problems from incomplete measurements, such as compressed sensing.

When using the relaxed data fidelity constraint, the CS is able to handle noisy measurements in $\mathbf{x}$ and therefore operate as a denoising operator in the estimation of $\hat{\mathbf{x}}$ thanks to the TV constraint. We have studied this property of the CS in this thesis, and therefore provide a short review of sparsity-based denoising approaches in the following paragraphs.

1.4 Image Denoising with Sparsity Constraints

In microscopy, image acquisition is often performed in low-light conditions, where each photon detected by the captor is expensive and precious. However the important signal is generally noisy making it difficult for biologists to analyze and extract information about the specimen.

An example of noisy image in fluorescence microscopy is displayed in figure 1.8. In this noisy image we can see that the light intensities from the membranes around the cell nucleus are confused with the noise intensity and are difficult to observe.

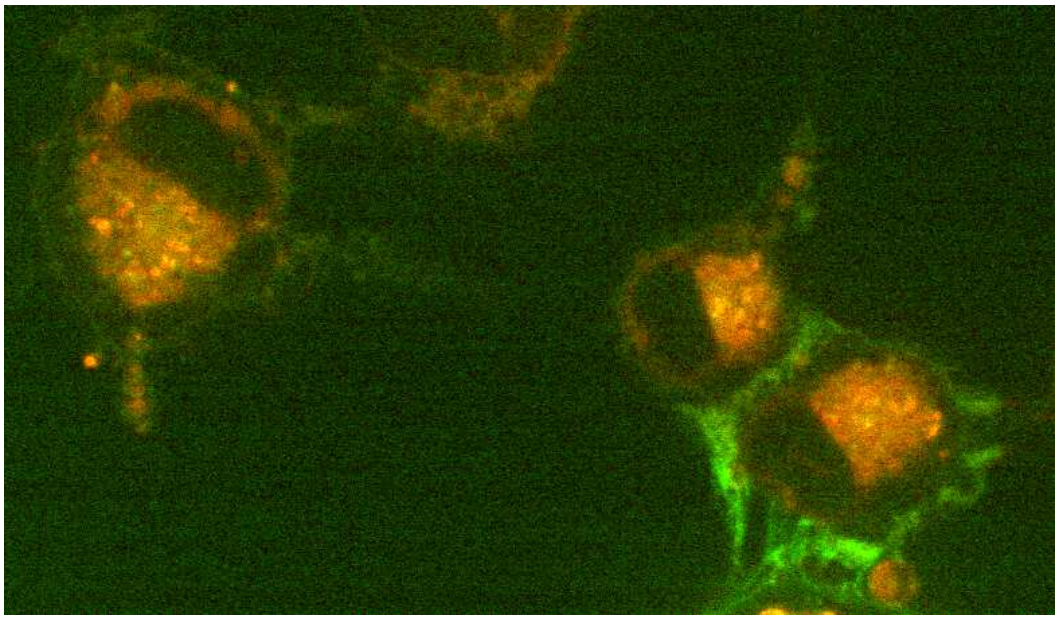

Figure 1.8: Example of noisy fluorescence microscopy image.

A host of image denoising methods, well suited for piecewise smooth images, have been developed such as Non-Local Means (NL-means) [Buades 2005], Total Variation Filtering (TV) [Rudin 1992], non-linear isotropic and anisotropic diffusion [Weickert 1998]. There are also methods which exploit the decomposition of the data

onto wavelets, ridglets or curvelets basis functions and shrink the coefficients (i.e. thresholding) to eliminate noise components [DeVore 1992, Donoho 1995d]. These approaches work by adaptively thresholding the wavelet coefficients that correspond to undesired frequency components. Recently, efficient denoising methods were also developed based on sparsity and redundant representations over learned dictionaries [Elad 2006], denoising image while simultaneously training a dictionary using the K-SVD algorithm [Aharon 2005], or based on sparse code shrinkage and maximum likelihood estimation of non-gaussian variables [Hyvärinen 1999].

In this section we present some *state of the art* denoising methods, relying on various formulations of image sparsity content in terms of object contours. In this context, a regularization parameter h, which measures the spatial extent of the low-pass filtering applied to the image is used and tuned to depend on a noise level estimator such as the noise variance σ^2. A simple image denoising framework can be defined as the decomposition of the observation into a noise-free signal (signal of interest) component and a noise component,as:

$$x(a,b) = D_h(x(a,b)) + n(a,b) \tag{1.28}$$

where $x(a,b)$ is the noisy observed signal, D_h is the denoising operator and $n(a,b)$ corresponds to an additive noise component. After denoising, the noise component can be estimated as the residue:

$$n(a,b) = x(a,b) - D_h(x(a,b)) \tag{1.29}$$

which energy is typically constrained to be minimal, to avoid the inclusion of structured signal components.

1.4.1 Denoising via Wavelet Thresholding

Denoising by thresholding in the wavelet domain has been developed principally by Donoho et al. [Donoho 1994, Donoho 1995c, Donoho 1995b, Donoho 1995a, Donoho 1998].

The basic idea behind wavelet thresholding for denoising is to apply a well-adapted wavelet threshold $\mathcal{W}$ to the noisy image x and suppose that $\mathcal{W}$ encodes efficiently the noise-free signal by keeping only the most important coefficients of $\mathcal{W}(x)$ to perform efficient denoising. Assume that the observed noisy data corre-

sponds to:

$$x(a,b) = o(a,b) + n(a,b) \tag{1.30}$$

where $o(a,b)$ is the noise-free signal and $n(a,b)$ is the noise. Let $\mathcal{W}(\cdot)$ and $\mathcal{W}^{-1}(\cdot)$ denote the forward and inverse wavelet transform operators. We intend to apply the wavelet shrinkage denoise in $x(a,b)$ in order to recover $\hat{o}(a,b)$ as an estimate of $o(a,b)$. The wavelet estimation procedure has three main steps:

- Transform the observations $x(a,b)$ by applying a discrete wavelet transformation. The result is a sequence of wavelet coefficients $w[i], i = 1, ...n$.
- Estimate the threshold λ and use this estimator to shrink the wavelet coefficients.
- Invert the wavelet transform with the thresholded coefficients, recovering the estimator $\hat{o}$ of the true signal o.

The three steps can be expressed as:

$$\begin{aligned} w &= \mathcal{W}(x) \\ w_T &= D(w) \\ \hat{o} &= \mathcal{W}^{-1}(w_T) \end{aligned}$$

Selection of the threshold value and the shrinkage operator defining D are key components of the efficiency of the denoising.In this context, several thresholding approaches of wavelet coefficients were proposed. In [Donoho 1994, Donoho 1998], the authors introduced the *RiskShrink* with the minimax threshold and the *VisuShrink* with the universal threshold. These papers discussed both hard- and soft-thresholds in a general context that included ideal denoising in both the wavelet and Fourier domains. In [Donoho 1995c], the *SureShrink* denoising was introduced with the SURE threshold, the *WaveJS* James-Stein threshold, and the *LPJS* James-Stein threshold but in the Fourier domain instead of the wavelet domain. We now provide a short overview of hard- and soft-thresholding operators, and universal, minimax and SURE thresholds selection.

Hard Thresholding. Let $\mathcal{B} = \{a\}$ be an orthonormal wavelet basis [Mallat 1998] and $w_{\mathcal{B}}[i]$ the i-coefficient of the wavelet transformation. One approach of wavelet

denoising is to use a projection operator approximating the best projection, which is called *hard thresholding*, and keep only coefficient greater than a certain threshold λ,

$$w_{\mathcal{B}}[i] = \begin{cases} w_{\mathcal{B}}[i] & \text{if } |w_{\mathcal{B}}[i]| > \lambda \\ 0 & \text{if } |w_{\mathcal{B}}[i]| \leq \lambda \end{cases}$$

This approach is based on the fact that if $\mathcal{B}$ is well chosen, the noise-free data is represented by large wavelet coefficients, whereas the noise is distributed across small coefficients, which are cancelled by thresholding. The performance of this approach depends on the ability of approximating x by a small set of large coefficients. This is the case for wavelets that are well adapted to encode localized discontinuities such as edges.

Soft Thresholding. In practice, a great amount of details and edges lead to coefficients lower than the chosen threshold, while inversely, the noise can produce coefficients greater than λ. Thresholding these coefficients generates Gibbs-like phenomenons and oscillations near the edges during the reconstruction. In [Donoho 1995b], Donoho proposed a *soft thresholding* shrinkage operator to improve the visual quality of the reconstruction,

$$w_{\mathcal{B}}[i] = \begin{cases} \frac{w_{\mathcal{B}}[i] - \operatorname{sgn}(w_{\mathcal{B}}[i])\lambda}{w_{\mathcal{B}}[i])} & \text{if } |w_{\mathcal{B}}[i]| \geq \lambda \\ 0 & \text{if } |w_{\mathcal{B}}[i]| < \lambda \end{cases}$$

Soft thresholding takes advantage of the continuity of the shrinkage function to better preserve the local structure of the wavelet coefficients, and reduce the Gibbs oscillations. In addition, soft thresholding still attenuates all small coefficients, as an ideal denoising operator.

The threshold λ must be chosen larger than the maximum noise coefficients to ensure good noise suppression and lower than the minimum signal coefficients to preserve the original image. In practice λ will depend on the noise type and noise statistics. For example, it can be shown that the maximum wavelet coefficient intensity of a n-points white noise sequence with standard deviation σ has a high probability of being smaller than $\sigma\sqrt{2\log n}$ [Donoho 1994, Mallat 1998]. In practice, this λ value is too high and cancels too many coefficients not produced by the noise.

In figure 1.9 we illustrate the visual results of soft and hard thresholding applied on the same image.

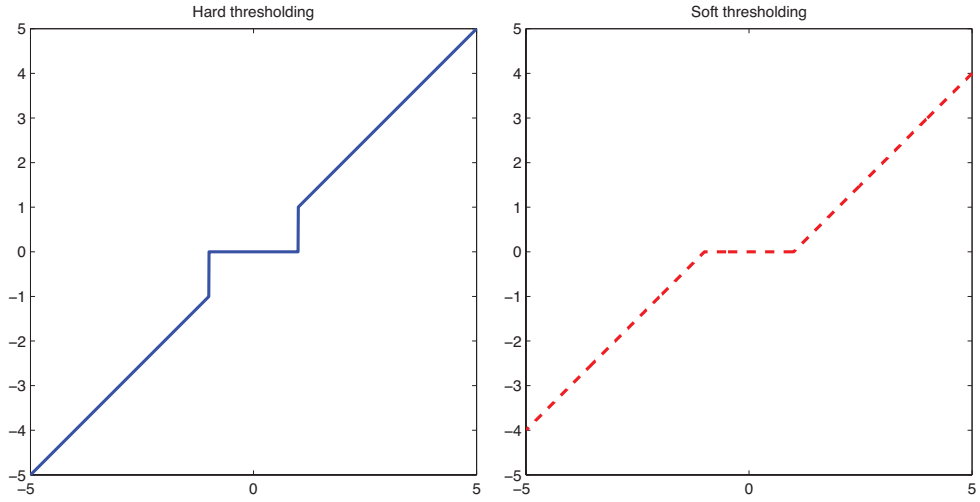

(a) (b)

Figure 1.9: Hard- and soft-thresholding functions applied to each wavelet coefficient.

Generic thresholds, such as the minimax threshold or the universal threshold [Donoho 1994], that depend only on n, can be used in a three-step denoising procedure already described. However, if we prefer to use a data-adaptive threshold, $\lambda = d(U)$, such as the threshold selected by Stein's unbiased risk estimator (SURE) [Donoho 1995c], we must use a four-step procedure for wavelet shrinkage denoising:

$$\begin{aligned} w &= \mathcal{W}(f) \\ \lambda &= d(w) \\ w_T &= D(w, \lambda) \\ \hat{o} &= \mathcal{W}^{-1}(w_T) \end{aligned}$$

The estimation $\hat{o}$ from $D(w, \lambda)$ has a risk $r(D, o) = E\| \hat{o} - o \|^2$ which corresponds to the expectation of the error measure. The oracle risk corresponds to an hypothetical optimal selection of the coefficients minimizing the following risk:

$$r(D, o) = \sum_i \min(|o_i|^2, \sigma^2) \tag{1.31}$$

This risk assumes that we know the value of the true signal values o_i. Based on this

modeling of the estimation risk via wavelet coefficients shrinkage, and especially the minimization of the maximal (minimax) risk, other optimal thresholds were defined.

Considering the hard- and soft-thresholding discussed above, by using the universal threshold $\lambda = \sigma\sqrt{2\log n}$ we can asymptotically approach the "oracle" risk [Donoho 1994]. The universal threshold has a good asymptotic minimax properties and also removes noise with high probability, ensuring good visual quality of reconstructed signals. Such denoising performance is based on probabilistic modeling of the maximum estimation risk for identically distributed Gaussian random variables [Donoho 1994, Vidakovic 1999]. Donoho and Johnstone [Donoho 1995c] also proposed to select the threshold by minimizing the Stein's unbiased risk estimator (SURE) [Stein 1981]. The threshold λ^{sure} and the soft-thresholding rule are the core of a level-dependent procedure that Donoho and Johnstone called the *SureShrink*. If the wavelet representation at a particular level is not too sparse, a SURE threshold is used, based on the magnitude of the preserved coefficients. Otherwise, the universal threshold is selected.

Image denoising via wavelet thresholding remains widely used in numerous applications such medical images [Kalifa 2003] and astronomical images [Starck 1998]. This framework is currently enriched by research works dedicated to novel algorithms for the identification of optimal sparsifying transforms using decomposition functions and image norms suited for textural components [Peyre 2010].

1.4.2 Denoising by Total Variation Minimization

Image filtering and denoising using total variation (TV) minimization was introduced by Rudin, Osher and Fatemi in [Rudin 1992, Rudin 1994]. The proposed method assumes that an image is composed by a finite number of level sets and that the image is smooth or regular in each level with a finite number of discontinuities defining edges.

Given a noisy image $x(a,b) : \Omega \to \mathbb{R}$, where Ω is a bounded open subset of $\mathbb{R}^2$, the method aims to achieve the following decomposition,

$$x(a,b) = o(a,b) + n(a,b) \tag{1.32}$$

where $o(a,b)$ is the object signal and $n(a,b)$ is the noise. Then, the total variation

approach is defined as follows:

$$\hat{o}(a,b) = \arg \min_{o \in BV(\Omega)} \left\{ |o(a,b)|_{BV} + \lambda \| \, x(a,b) - o(a,b) \, \|_{\ell_2}^2 \right\} \tag{1.33}$$

for a Lagrange multiplier (regularization parameter) $\lambda > 0$, where $BV(\Omega)$ denotes the space of functions with bounded variation on Ω and,

$$|o(a,b)|_{BV} = \int_{\Omega} |\nabla o(a,b)| d\Omega, \tag{1.34}$$

denotes the BV semi-norm. We note that in this thesis we will refer to the TV-norm to as the ℓ_1-norm of the gradient of x. It is equivalent to equation (1.34) and is defined in the discrete case as:

$$|x(a,b)|_{TV} = \sum_{x \in \Omega} |\nabla x(a,b)|. \tag{1.35}$$

We call this variational problem the Rudin–Osher–Fatemi (ROF) model.

If the first term $|o(a,b)|_{BV}$ were replaced by $J_p(f) = \int_{\Omega} |\nabla o(a,b)|^p$ for any $p > 1$, it would lead to differentiability and strict convexity of the regularization constraint. The main reason for this effect is that for $p > 1$ the derivative of J_p corresponds to a non-degenerate elliptic differential operator of second order and thus has a smoothing effect in the optimality condition, whereas for total variation the operator is degenerated and affects only the level lines of the image. Hence, the TV minimization is well adapted to denoise piecewise smooth images.

The unconstrained problem (1.33) is naturally linked to the constrained problem:

$$\hat{o}(a,b) = \arg \min_{o \in BV(\Omega)} |o(a,b)|_{TV} \tag{1.36}$$

subject to the noise constraints:

$$\sum_{\Omega} |x(a,b) - o(a,b)|^2 = \sigma^2 \quad \text{and} \quad \sum_{\Omega} |x(a,b) - o(a,b)| < \varepsilon \tag{1.37}$$

The best estimation $\hat{o}(a,b)$ must have the minimum total variation with the minimum error $\sum_{\Omega} |x(a,b) - o(a,b)| < \varepsilon$, and where σ is chosen to correspond to the noise energy.

The unconstrained problem is often preferable, because the functional is strictly

convex, the minimum exists, is unique and computable [Chambolle 1997]. In the problem (1.33), the parameter λ controls the trade off between the regularity and fidelity terms. As λ gets smaller the weight of the regularity term increases. Therefore λ is related to the degree of filtering of the solution of the minimization problem.

Consider the solution for the problem (1.33) given the Lagrange multiplier value λ. The Euler Lagrange equation associated with the minimization problem [Rudin 1994], corresponds to:

$$(o(x) - x(x)) - \frac{1}{2\lambda}\text{curv}\{o(x)\} = 0 \tag{1.38}$$

Thus, the distance between the estimation and the original image is:

$$\hat{o}(x) - x(x) = \frac{1}{2\lambda}\text{curv}\{\hat{o}(x)\} \tag{1.39}$$

Since straight edges have small curvature, they are well preserved using TV minimization. However, if the Lagrange multiplier λ is too small, details and texture may be over smoothed.

1.4.3 Non-Local Means

Neighborhood filters have been originally proposed by Yaroslavsky *et al.* [Yaroslavsky 1985, Yaroslavsky 1996]. The main idea is to compute a filtered image $\hat{x}$ by taking an average of the noisy image x. The average is taken over pixels which have similar intensities, and not over pixels which are close in the image, as it is usual for a convolution. The value of the cleared image $\hat{x}$ at position a is defined by:

$$\hat{x}(a) = \frac{1}{C(a)}\int_{\Omega} K(a,b,x)x(b)db, \text{ where } C(a) = \int_{\Omega} K(a,b,x)db, \tag{1.40}$$

The choice of the kernel $K(a,b,x)$ determines the actual filter and $C(a)$ acts as a normalization to ensure that a constant function x is mapped to itself.

The continuous non-local patch-based functional for denoising and deblurring images was introduced by Kindermann *et al.* [Kindermann 2005]. This functional is built upon a new norm which measures the degree of similarities between patches

and takes the general form:

$$J(x) = \int_{\Omega\times\Omega} g\left(\frac{|x(a)-x(b)|^2}{h^2}\right) w(|a-b|)dadb \tag{1.41}$$

with an appropriate positive weight function w, a differentiable filter function $g : \mathbb{R}^+ \to \mathbb{R}$, and a parameter h. The non-local patch-based functional was extended by Boulanger *et al.* [Boulanger 2010].

The non-local means (NL-means) algorithm was introduced by Buades *et al.* [Buades 2005] for 2D image denoising and is a generalization of (1.41). The method takes advantage of the high degree of redundancy of natural images. It is based on the idea that any natural image has similar patches non-locally, and that any pixel of the image has similar pixels that are not necessarily located in a spatial neighborhood.

Similarly to patch-based approaches [Kindermann 2005, Lee 1998, Boulanger 2010], the weight involving pixels in the average does not depend on their spatial proximity but on the intensity similarity of their neighborhoods with the neighborhood of the pixel being filtered. The NL-means filtering can be viewed as a case of neighborhood filtering with infinite spatial kernel and where the similarity of the neighborhood intensities is replaced by a point-wise similarity.

Let $x(a)|a \in \Omega$ be the noisy image observation. The NL-means algorithm is defined by the following formula:

$$\mathrm{NL}\{x(a)\} = \frac{1}{C(a)} \int e^{-\frac{G_\beta \star |x(a+)-x(b+)|^2}{h^2}} x(a)da, \tag{1.42}$$

where G_β is a Gaussian kernel with standard deviation β, h is a filtering parameter and $C(a) = \int e^{-\frac{G_\beta \star |x(a+)-x(b+)|^2}{h^2}} da$.

In the discrete case, the denoised estimation of $x[a]|a \in \mathbb{R}^2$ is computed as a weighted average of all pixels in the image,

$$\mathrm{NL}\{x[a]\} = \sum_{b\in\mathbb{R}^2} w[a,b]x[b] \tag{1.43}$$

where the family of weights $\{w[a,b]\}_b$ take into account the similarity between the pixels a and b, satisfying the conditions $0 \leq w[a,b] \leq 1$ and $\sum_b w[a,b] = 1$.

The similarity between two pixels a and b depends on the similarity between the vectors $x[\mathcal{N}_a]$ and $x[\mathcal{N}_b]$, where $\mathcal{N}_k$ denotes a neighborhood of fixed size and centered at the pixel k. The similarity is computed as a gaussian weighted Euclidean distance $\| x[\mathcal{N}_a] - x[\mathcal{N}_b] \|^2_{2,\beta}$. The use of the Euclidean distance is well adapted to an additive white noise which alters the distance between windows in uniform way. Supposing an additive noise where σ^2 is the noise variance and o the original noise-free image, we have the following equality:

$$E\| x[\mathcal{N}_a] - x[\mathcal{N}_b] \|^2_{2,\beta} = \| o[\mathcal{N}_a] - o[\mathcal{N}_b] \|^2_{2,\beta} + 2\sigma^2 \tag{1.44}$$

This expectation shows that the Euclidean distance preserves the order of similarity between pixels, which means that the most similar pixels to a in x also are expected to be the most similar pixels of a in o. Finally, the weights are defined by

$$w[a,b] = \frac{1}{Z[a]} e^{-\frac{\|x[\mathcal{N}_a]-x[\mathcal{N}_b]\|^2_{2,\beta}}{h^2}} \tag{1.45}$$

and where $Z[a]$ is the equivalent normalizing term $Z[a] = \sum_a e^{-\frac{\|x[\mathcal{N}_a]-x[\mathcal{N}_b]\|^2_{2,a}}{h^2}}$ and h controls the decay of the weights as a function of the Euclidean distance.

TV filtering and non-local means filtering have been used successfully in a variety of denoising applications. In recent works it was applied to fluorescence microscopy in [Boulanger 2010, Yang 2010b], involving several improvements such as the adaptation of the neighborhood size and the measure of similarity to handle more sophisticated noise models.

Chapter 2

A Denoising Framework Based on Image Sparsity and Random Fourier-based Sampling

Noise level and photobleaching are cross-dependent problems in biological fluorescence microscopy. Indeed, observation of fluorescent molecules is challenged by photobleaching, a phenomenon whereby the fluorophores are degraded by the excitation light. One way to control this process is by reducing the intensity of the light or the time exposure, but it comes at the price of decreasing the signal-to-noise ratio (SNR). Although a host of denoising methods have been developed to increase the SNR, most are post-processing techniques and require full data acquisition.

In this chapter we detail a novel technique, based on compressed sensing (CS) that simultaneously enables reduction of exposure time or excitation light level and improvement of image SNR. Our CS-based method can simultaneously acquire and denoise data, based on statistical properties of the CS optimality, noise reconstruction characteristics and signal modeling applied to microscopy images with low SNR. The proposed approach is based on an experimental optimization combining sequential CS reconstructions in a multiscale framework to perform image denoising. Simulated and practical experiments on fluorescence image data demonstrate that thanks to CS denoising we obtain images with similar or increased SNR while still being able to reduce exposure times. Such results open the gate to new mathematical imaging protocols, offering the opportunity to reduce photobleaching and help biological applications based on fluorescence microscopy.

[0]Based upon: M. Marim, E. Angelini and J.-C. Olivo-Marin. *"A Compressed Sensing Approach for Biological Microscopy Image Denoising"*, SPARS'09, 2009. M. Marim, E. Angelini and J.-C. Olivo-Marin. *"Compressed Sensing in Biological Microscopy"*, Proc. SPIE Wavelets XIII, vol. 7446, pp. 744605, 2009. M. Marim, E. Angelini and J.-C. Olivo-Marin. *"Denoising in Fluorescence Microscopy Using Compressed Sensing with Multiple Reconstructions and Non-Local Merging"*, Int. Conference of the IEEE Engineering in Medicine and Biology Society, EMBS, 2010.

This chapter is divided in the following manner: in Section 2.1 we discuss previously derived denoising approaches for fluorescence microscopy, in Section 2.2 and 2.3 we introduce our CS denoising approach and its respective algorithm, in Section 2.4.2 and 2.5 we present experimental results and validation.

Contents

2.1 Denoising Approaches and Fluorescence Microscopy 48
2.2 Denoising Methods 50
2.2.1 Reconstruction from Noisy Measurements 50
2.2.2 The Noise Model and Image Sparsity Measures 51
2.2.3 The Sampling Pattern for Denoising 53
2.2.4 Denoising and Scalability 56
2.3 Algorithms for Multiple Reconstructions 58
2.3.1 Algorithm Workflow 58
2.4 Images Fusion by Averaging 61
2.4.1 Simulations on Pure Noise Signal 61
2.4.2 Results with Averaging 62
2.5 Images Fusion by Non-Local Averaging 64
2.5.1 Results with Non-Local Averaging 68
2.6 Conclusion 71

2.1 Denoising Approaches and Fluorescence Microscopy

In biological fluorescence microscopy, cellular components of interest in the specimen, such as proteins, are typically labeled with a fluorescent molecule called a fluorophore (green fluorescent protein (GFP), dyes, inorganic molecules) and can therefore be imaged with high specificity. Fluorophores lose their ability to fluoresce as they are illuminated through a process called photobleaching. In microscopy, observation of fluorescent molecules is challenged by photobleaching, as these molecules are slowly destroyed by the light exposure necessary to stimulate them into fluorescence. Loss of emission activity caused by photobleaching can be controlled by reducing the intensity or time-span of light exposure. Unfortunately, reducing the exposure time or intensity of the excitation also reduces the emission intensity but not the noise acquisition components, leading to a decrease of the SNR. Regarding

the noise, images acquired by a fluorescence microscope are contaminated by dark noise, photon noise (shot noise) and readout noise, which were described in section 1.1.

To improve the SNR, many denoising methods are available, well suited for piecewise smooth images, such as *Non-Local Means* (NL-means) [Buades 2005], *Total Variation Filtering* (TV) [Rudin 1992], non-linear isotropic and anisotropic diffusion [Weickert 1998]. Applying these methods to fluorescence microscopy corrupted with Gaussian noise typically require a pre-processing with a variance-stabilizing transform, as done for example in [Boulanger 2008]. A novel anisotropic-type for filtering was recently proposed in [Wang 2010] for two-photon fluorescence images. There are also methods which exploit the decomposition of the data onto wavelet-types of functions (including recent ridglets or curvelets basis functions) and shrink the coefficients to eliminate noise components [DeVore 1992, Donoho 1995d]. Recently, efficient denoising methods were also developed based on sparsity and redundant representations over learned dictionaries [Elad 2006], denoising image while simultaneously training a dictionary using the K-SVD algorithm [Aharon 2005], or based on sparse code shrinkage and maximum likelihood estimation of non-Gaussian variables [Hyvärinen 1999]. Wavelet shrinkage was used for example by [Olivo-Marin 2002] to denoise fluorescence images and count spot, or in [Zhang 2007, Delpretti 2008, Luisier 2010] using variance stabilizing transforms prior to image decomposition and wavelet shrinkage.

In this chapter we propose an application of compressed sensing to fluorescence microscopy images, enabling the reconstruction of high SNR images. Our framework is based on the CS ability to efficiently reconstruct sparse signals with under-sampled acquisition rates, significantly below the Shannon/Nyquist theoretical bound. Similarly to some recent experiments for CS-based MRI reconstruction [Lustig 2007], the acquisition protocol consists in measuring the image signal on a random set of Fourier vectors [Candès 2006a] and constraining the *Total Variation* (TV) measure of the reconstructed image in the spatial domain. Sampling in the Fourier domain, provides incoherent measurements with the spatial domain for images with bounded variations (BV) (and small TV measures). Indeed, the CS framework introduced by Candès [Candès 2005d] provides theoretical results which show that if a signal is sparse (i.e. has a small number of non-zero coefficients) in some basis, then with high probability, uniform random projections of this signal onto an incoherent domain,

where the signal is not sparse, contains enough information to optimally reconstruct this signal. The incoherence property between some sparsity basis Ψ and some sampling basis Φ ensures that signals having sparse representations in Ψ must have a large support in the measurement domain described by Φ. Random selections of basis functions in Φ are typically suitable since random vectors are, with very high probability, incoherent with any sparsity-encoding basis functions from Ψ, defining orthogonal domains [Donoho 2006b].

Considering that a noisy signal $x + n$ has a sparse representation in some basis Ψ, we want to recover the signal $x \in \mathbb{R}^N$ from noisy measurements $y = \Phi(x + n)$ | $y \in \mathbb{R}^M$, the sampling matrix being Φ, with M $\ll$ N. The presence of noise in the acquired signal might alter its sparsity in the domain Ψ. By enforcing the reconstruction of sparse signals, CS offers a theoretical framework to remove non-sparse random noise components from corrupted observations. Indeed, removing noise from $x + n$ will rely on the efficacy of Ψ on representing the signal x sparsely and the inefficacy on representing the noise n [Donoho 2006a]. The choice of the basis function Ψ is very important and depends directly on the type of signal (or image) we want to recover and denoise using CS.

2.2 Denoising Methods

2.2.1 Reconstruction from Noisy Measurements

In the context of noisy measurements $y = \Phi(x+n)$, which is the case for microscopy images corrupted with acquisition noise, we wish to recover only the signal component $x \in \mathbb{R}^N$. If we make the assumptions that: (I) the noise energy is bounded by a known constant $\| n \|_{\ell_2} \leq \varepsilon$, (II) the transformed signal Ψx is sparse, and (III) $\Phi \in \mathbb{R}^{M \times N}$ is a random matrix sampling x in the Fourier domain, the true signal component x can be recovered nearly exactly using the following convex optimization:

$$\hat{x} = \arg \min_{x \in \mathbb{R}^N} \| \Psi x \|_{\ell_1} \text{ s.t. } \| y - \Phi x \|_{\ell_2} \leq \delta \tag{2.1}$$

for a small $\delta \geq \varepsilon$. In [Candès 2006c] it was shown that the solution $\hat{x}$ is guaranteed to be within $C\delta$ of the original signal.

$$\| \hat{x} - x \|_{\ell_2} \leq C\delta \qquad \text{with } C > 0 \tag{2.2}$$

We note here that this CS-based estimation framework, with noisy observations and sparsity constraints, guarantees that no false component of $x + n$ with significant energy is created, if $\| \Psi x \|_{\ell_1}$ is particularly high for additive random noise components. If Ψx corresponds to the TV-based spatial sparsity constraint,

$$\hat{x} = \arg \min_{x \in \mathbb{R}^N} \| x \|_{TV} \text{ s.t. } \| y - \Phi x \|_{\ell_2} \leq \delta \tag{2.3}$$

the image reconstruction leads to smooth edges, textures and removal of noise components, resulting in an error:

$$\| \hat{x} - x \|_{\ell_2} \leq \alpha + \beta \tag{2.4}$$

where α reflects the desired error (corresponding to noise removal) from the relaxation of the constrain δ in (2.1) and β reflects the undesired error from the edge smoothing effect. If TV represents x efficiently (i.e. Ψx is sparse) and n inefficiently (i.e. Ψn is non-sparse), i.e. $\| \Psi x \|_{TV} \ll \| \Psi n \|_{TV}$, the term β vanishes and $\alpha \to C\delta$.

2.2.2 The Noise Model and Image Sparsity Measures

In the context of microscopic images, noise models usually combine a mixture of Poisson and Gaussian components, and the observation model commonly adopted is the following:

$$\begin{aligned} x(a,b) = \quad & \zeta U_i(A(a,b) + \lambda_B) + V_i, \\ & \text{where } \; U_i \sim \mathcal{P}(\lambda_i), \;\; V_i \sim \mathcal{N}(\mu, \sigma^2) \end{aligned} \tag{2.5}$$

and ζ is the overall gain of the detector, $A(a,b)$ is the object intensity at pixels a, b, λ_B is the mean intensity of the background, U_i is a Poisson variable with parameter λ_i modeling the photon counting, and V_i is an additive noise component with a normal distribution with mean intensity μ and standard deviation σ. U_i and V_i are assumed mutually independent. An image with a noise simulated as described in (2.6) is illustrated in figure 2.1.

Indeed, both denoising approaches propose to perform a series of sparsity-based reconstructions from a set of randomly selected measures, and combine them into a

single denoising result. The only underlying assumption is that noise components on the restored images will be mutually uncorrelated (i.e. not similar for each reconstruction) while fluorescence signal components will be mutually correlated. This assumption holds in the general case only when assuming that the noise components are non-sparse (i.e. spread out over all pixels) and random, but not necessarily derived from a Gaussian distribution.

The Fourier transform of the noise component will add up to the Fourier transform of the signal component (the Fourier transform being linear). As a consequence, the noise component will promote changes in Fourier coefficients with most energy concentrated in the high frequencies, since the noise corresponds to fast spatial variations. On the other hand, the TV spatial constraint, which is non linear, will easily recognize and enhance low-frequency structural components while discriminating random high components. In other words, there is a high chance of sampling noisy Fourier coefficients but they have little chance to contribute to the reconstructed image because of the TV constraint, into which they do not add up but compete. The less sparse the noise component is compared to the true signal component, the more the TV constraint will discriminate them.

Robustness of the CS reconstruction to the presence of noise relies on the efficiency of the sparsity transform on representing well the signal of interest and on representing inefficiently the noise distribution. In the context of microscopic images, noise models usually combine Poisson and Gaussian components. We perform here an analysis of the sparsity of each noise component by adding a simulated mixture of Poisson and Gaussian (MPG) noise to a fluorescence microscopy image of drosophyla cell and applying the sparsifying transform to noise components independently, results to this experience are illustrated in Fig. 2.1. Fig. 2.1a is the noisy microscopy image, which is composed by a noise-free image 2.1b and a mixture of Gaussian 2.1d and Poisson noise 2.1f (simulated as described in equation (2.6)). 2.1c shows the magnitude of the gradient of the noise-free image (compressible signal of interest) while 2.1e shows the magnitude of the gradient of the Gaussian noise component and 2.1g for the Poisson noise component. The TV measure $\| x \|_{TV}$ correspond to the measure of sparsity which is approximatively the ℓ_1-norm of the gradient.

In both cases, the coefficients provided by the transformation are not sparse or strongly less sparse than in Fig. 2.1c (for the signal of interest). These results show

clearly that the sparsifying transform used does not encode efficiently the MPG noise, which is strongly suited for a denoising framework. Moreover we can observe that the signal of interest is very efficiently encoded by the transformation presenting the smaller TV measure 2.1c.

2.2.3 The Sampling Pattern for Denoising

In this subsection we deal with the Fourier sampling pattern adopted for the CS reconstruction. Since the goal is to perform an optimal denoising, the sampling pattern is of central importance. The design of the sampling matrix Φ can be based on different distributions, such as a independent and identically-distributed random uniform distribution, or a line-based radial distribution, which are illustrated in Figure 2.2.

Theoretically, the optimal sampling scheme would be the one which maximizes the incoherence between the sampling basis Φ and the sparsity basis Ψ. A fully random sampling often results in a high degree of incoherence and near-optimal solution. Indeed random distributions present some advantages such as simple mathematical proofs and satisfaction of the RIP conditions [Candès 2006a]. In practice, favoring low frequency measures lead to better denoising results since the noise corresponds essentially to high frequencies.

The Figure 2.2(b)-(d) displays the histograms of the spatial density of frequency measurements, characterized by the number of sampling points at a given distance from the $(0, 0)$ center frequency in Figure 2.2(a)-(c). The histogram 2.2b shows that for uniform random spatial distributions on a square, there are a majority of intermediate frequencies. On the other hand, the histogram 2.2d shows that for the radial distributions on a square, there are equal levels of low and intermediate frequencies while high frequencies have a minor density.

One interesting fact from Figure 2.2 is that when the sampling process is random, extreme high and low frequencies have the same low probabilities. These histograms can be modeled with the number of sample points contained on a circle of radius r ($0 \leq r \leq \sqrt{2}N/2$) and centered at $(0, 0)$. We then distinguish two different behaviors for r below and above $N/2$, as observed in Figure 2.2(b)-(d). For a uniform random distribution, we can define the following probability law of occurrences:

$$P(r) = \frac{(2\pi - 4\theta)r}{N^2} \tag{2.6}$$

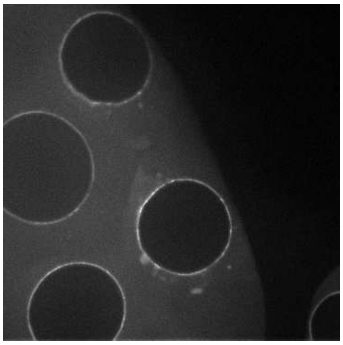

(a) Noisy image, $\| x \|_{TV} = 5.71\text{e+}06$

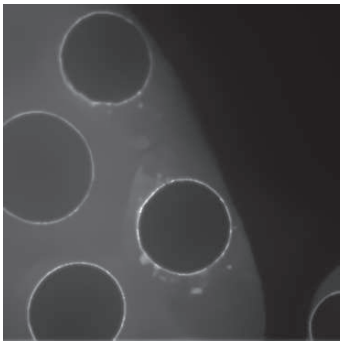

(b) Noise-free image, $\| x \|_{TV} = 4.61\text{e+}06$

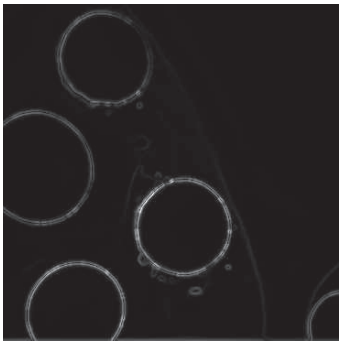

(c) $\| x \|_{TV} = 2.02\text{e+}04$

(d) Gaussian noise, $\| x \|_{TV} = 5.39\text{e+}05$

(e) $\| x \|_{TV} = 3.55\text{e+}05$

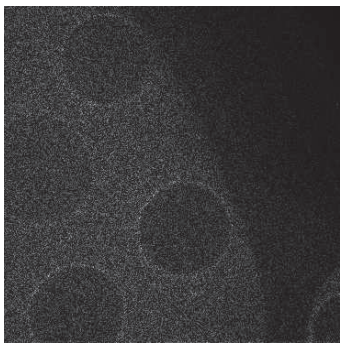

(f) Poisson noise, $\| x \|_{TV}$=5.63e+05

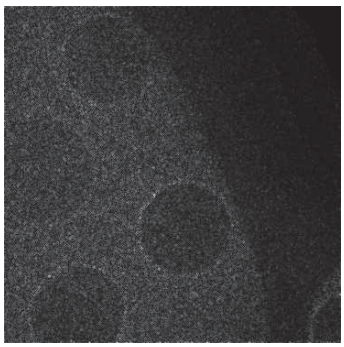

(g) $\| x \|_{TV} = 3.72\text{e+}05$

Figure 2.1: (a) Microscopic image with simulated noise such as (2.6). The sparsifying transformation ∇x applied to (b) noise-free image (compressible signal of interest), (d) simulated Gaussian noise component and (f) simulated Poisson noise component are illustrated in (c), (e) and (g) respectively.

where θ corresponds to the angle of the cone intersecting one of the four external parts of the circle (illustrated in Figure 2.3). When the radius of the circle is smaller than $N/2$, the circle is completely inside the image, then $\theta = 0$ and $P(r) = \frac{2\pi r}{N^2}$,

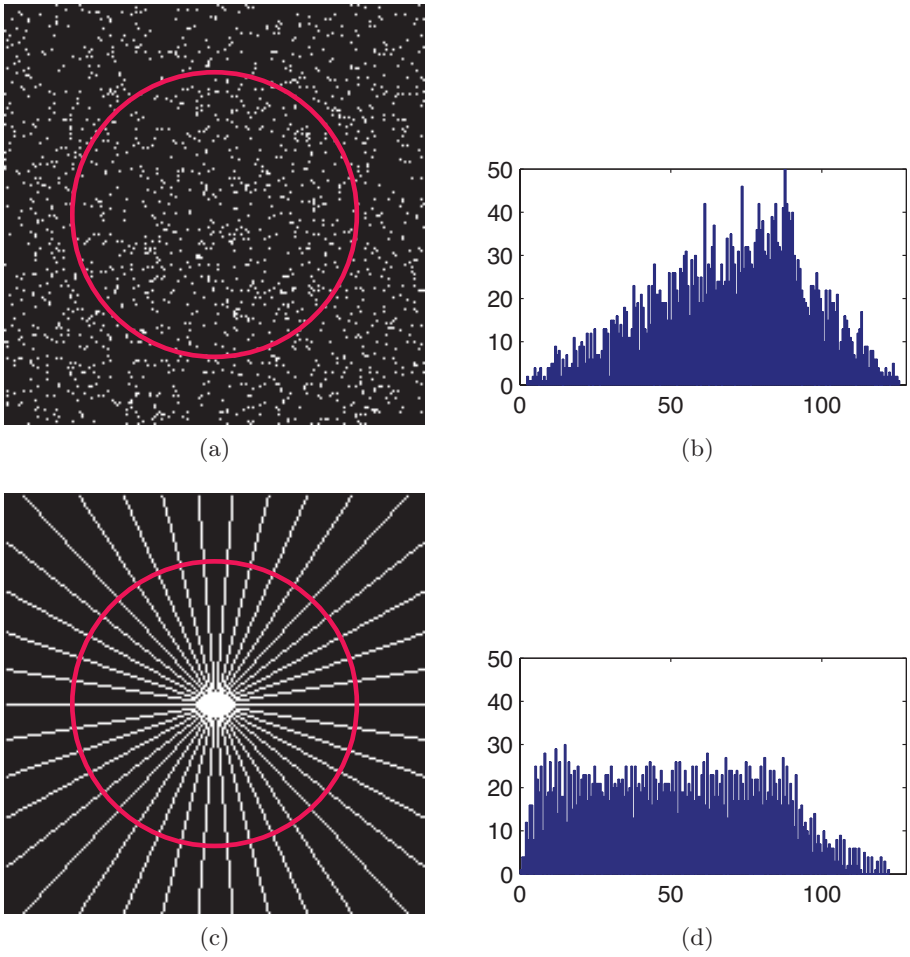

Figure 2.2: Spatial distributions in the Fourier domain with M = 0.1N (a) Random, (c) Radial and (b,d) are the correspondent frequency histograms.

otherwise $\theta > 0$ and can be computed as:

$$\theta = 2 \arctan\left(\frac{\sqrt{r^2 - n^2}}{n}\right) \tag{2.7}$$

and r is the distance to the center of the image, N^2 is the total number of pixels and $n = N/2$. For $r \leq N/2$ the probability of all possible pixels increases linearly with r. For $r > N/2$ the probability starts decreasing since the perimeter is not completely inside the image, as illustrated in Figure 2.2 and 2.3. For the radial distribution, the number of occurrences in a circle is constant for $r \leq N/2$ and depends on the number of lines n_l,

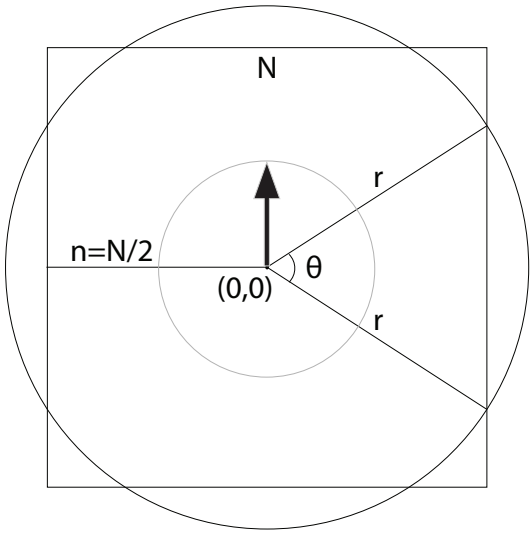

Figure 2.3: Circle of probability for the uniform distribution.

$$P(r) = \frac{(2\pi - 4\theta)}{2\pi} \frac{n_l}{N^2} \tag{2.8}$$

To perform our denoising we have the option to work with a set of random distributions or a set of rotated radial distributions. From (2.8) we can conclude that for a set of rotated radial distributions, low frequency samples are the same and the measurements are therefore redundant. Moreover, the small number of high frequency samples in the radial case constrains very loosely the CS reconstruction of high frequency details and noise. To combine multiple CS reconstructions, we want to achieve a good denoising performance. Indeed, sampling too few high-frequency components, leads to the risk with CS of creating patterns on the reconstructed image. Conversely, fully random sampling guarantees a better coverage of the high frequencies as illustrated in Figure 2.2b.

2.2.4 Denoising and Scalability

The degrees of freedom in the series of denoising experiments control the design of the sampling matrix Φ via the number of random measurements M and their location in the Fourier domain. The CS theoretical framework states that the more measurements are used in the Φ domain, the closer is the reconstructed signal to the original measured signal. In the context of denoising (rather than estimation) we have a dual constraint on the estimation of the true signal component and the risk of reconstructing noise components. Indeed, for a single CS experiment, the flu-

orescence signal will generate, from a set of random measures of structured Fourier values, a restored image with high values depicting a good estimation of the true signal. At the same time, purely random noise component will be interpreted, from a set of undifferentiated Fourier values, as a structured combination of oscillating components, extrapolated over the spatial domain into patches, under the regularizing TV effect (figure 2.7). Noise patches and fluorescence spatial localization will be directly related to M, the number of CS measurements acquired by Φ. We illustrate in Figure 2.4 how this number of measurements can be naturally viewed as a scale parameter where small scales enable more noise reconstruction. In the experiment on Figure 2.4, we observe that the noise component is more uncorrelated than the signal across scales while the signal component spatial resolution decreases.

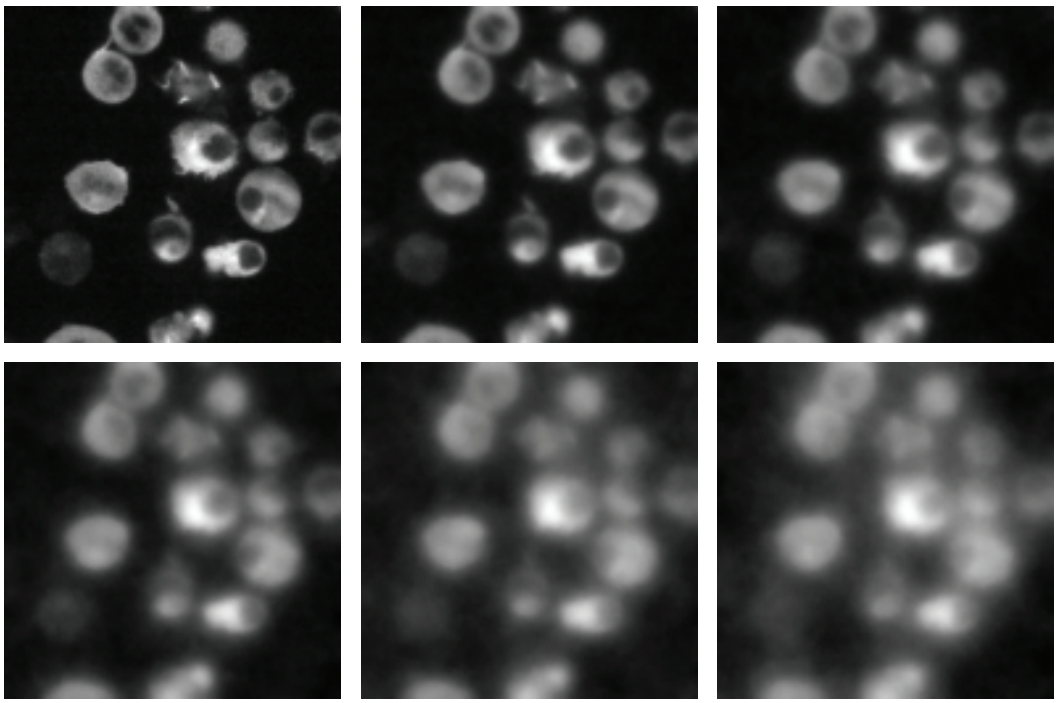

Figure 2.4: Average microscopic image recovered with six different numbers of measurements (i.e. 6 scales). Scales varies from a compression ratio exponentially increasing from M= 30% to M= 0.3%.

We can make a connection here with the family of multiscale transforms [Lindeberg 1994]. These transforms were theoretically defined as linear transforms with a scale parameter controlling the ability of the transform to simplify the signal. We know from the sparsity TV constraint that strong signals recovered by the CS

framework will correspond to strong underlying true signal components. Therefore, CS does not introduce false signal components and fits well in the framework of multiscale transforms, as illustrated in Figure 2.4. Moreover it appears that such multiscale CS approaches verify scale space properties such as simplification, homogeneity, isotropy as well as rotational and shift invariance.

2.3 Algorithms for Multiple Reconstructions

In this section we introduce our denoising framework based on random undersampling and sparsity maximization. The main idea is that using different random sampling matrices Φ (which select different sets of pixels to acquire), results in different reconstructed images. If the sparsifying transform is well adapted to represent the signal and not adapted to represent the noise, i.e. $\| \Psi x \|_{\ell_1} \ll \| \Psi n \|_{\ell_1}$, the signal reconstructed with different sampling matrices is much more correlated than the noise component. Roughly speaking, we can achieve good denoising performances when averaging reconstructions which have more variations in the noise representation than in the signal representation.

2.3.1 Algorithm Workflow

We propose a new paradigm for image acquisition in fluorescence microscopy based on multiple random undersampling and total variation minimization. We focus on utilizing dual sparse and redundant representations for fluorescence microscopic image denoising via two separate schemes. Assume that we observe an image over T *ms* and we will either make several observations with a single Φ measurement matrix or a single observation through a set of different Φ matrices.

A first strategy consists in acquiring K images $x_i + n_i$ exposed T/K *ms*, restoring each one independently (2.9) and combining the K restoration results into a single denoised image. This scheme exploits the fact that fluorescence signal Φx_i should be strongly correlated in all acquisitions, while noisy components Φn_i should not be.

$$\hat{x}_i = \arg\min_{x \in \mathbb{R}^N} \| x_i \|_{TV} \text{ s.t. } \| y_i - \Phi x_i \|_{\ell_2} \leq \delta \tag{2.9}$$

where $y_i = \Phi(x_i + n_i)$ for $i = 1...\text{K}$.

This first denoising scheme is illustrated in Figure 2.5, and includes the following steps:

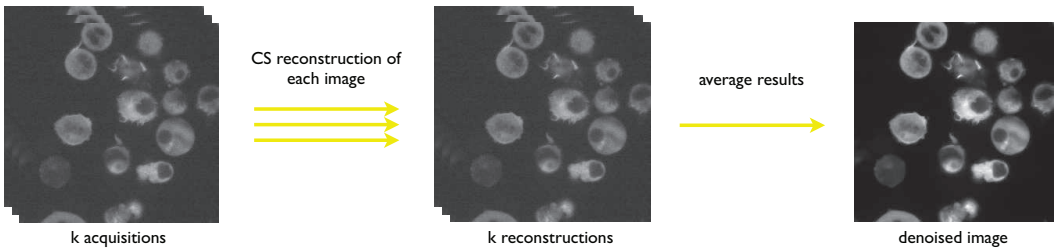

Figure 2.5: Denoising scheme with K acquisitions over T/K *ms* and K independent reconstructions.

- Acquisition of K images $x_i + n_i$ exposed T/K *ms*.
- Sparsity-based reconstruction of $\hat{x}_i$ images from noisy measurements $y_i = \Phi(x_i + n_i)$.
- Combination of reconstructed images $\hat{x}_i$ to generate a single denoised image $\hat{x}$ such as described in section 2.4.

A second denoising scheme is also proposed, which consists in determining the exposure time X necessary to obtain, with a set of combined restorations, a target SNR level, corresponding to the SNR measured on the image exposed T *ms*. This scheme provides the potential advantage of requiring a single shorter acquisition time, limiting degradation of the biological material due to phototoxicity and photobleaching. This second denoising scheme is illustrated in Figure 2.6 and includes the following steps:

- Acquisition of a single image exposed X *ms* (X < T).
- Sparsity-based reconstructions of the noisy image $x + n$ using N different random sampling matrices Φ_i, producing different sets of measurements $y_i = \Phi_i(x + n)$.
- Combination of the reconstructed images $\hat{x}_i$ to generate a single denoised image $\hat{x}$ such as described in section 2.4.

Combining CS reconstructions implies a sequence of CS reconstructions of a single noisy image acquisition $x + n$, using different sampling matrices Φ_i, as described below:

$$\hat{x}_i = \arg\min_{x \in \mathbb{R}^N} \| x \|_{TV} \text{ s.t. } \| y_i - \Phi_i x \|_{\ell_2} \leq \delta \tag{2.10}$$

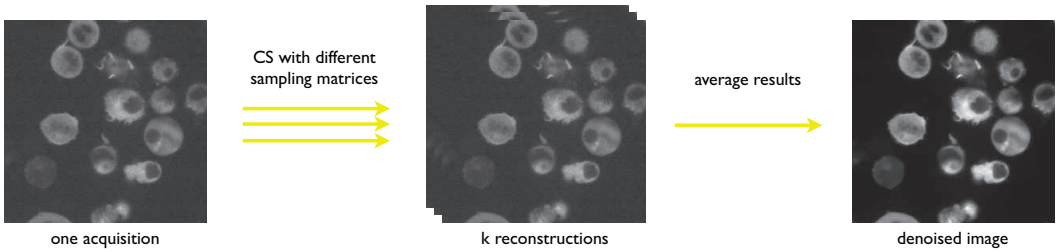

Figure 2.6: Denoising scheme with a single shorter acquisition and K reconstructions using different sampling matrices Φ_i.

for $i = 1...K$. We note that the value of K is an empirical estimation of the number of reconstructions for which the image SNR becomes constant.

The first approach (2.9) is more cell-friendly than the second (2.10) since smaller expositions leads to photo-damage reduction. The denoising performance is higher than the second approach (2.10). However, the first approach is acquisition-dependent requiring multiple under-exposed images and should be used in cases where the specimen must be preserved. The second approach offers a lower denoising performance (see results in tables 2.1 and 2.2) but much more flexibility by performing multiple reconstruction from only one acquisition. It is a post-processing method and is not specific to any acquisition.

Fusion Rule The last step of both algorithms involves the combination of the set of reconstructed images X such as:

$$\hat{x} = \text{fusion}_K(\hat{x}_i) \text{ for } i = 1, .., K \tag{2.11}$$

where fusion_K is a fusion method and $\hat{x}_i$ is the set of K image reconstructions.

To design the fusion rule we need to study the noise model 2.2.2 and the sampling pattern influences (2.2.3). We have proposed two different methods to combine multiple reconstructions which are detailed in 2.4 and 2.5.

2.4 Images Fusion by Averaging

In a first place, we proposed to average the set of x_i images to generate a single denoised image $\hat{x}$,

$$\hat{x} = \frac{1}{K} \sum_{i=1}^{K} \hat{x}_i \tag{2.12}$$

Each single reconstruction $\hat{x}_i$ is slightly different due to the differences in the sampling matrices Φ_i. Because of the random distribution of frequencies in Φ_i, the global frequency content of the $\hat{x}_i$ is similar and the images only differ in terms of details. Indeed, since $\| x \|_{TV}$ is sparse and $\| n \|_{TV}$ is non-sparse, noisy reconstructed patterns are uncorrelated for reconstructions using different sets of measures.

2.4.1 Simulations on Pure Noise Signal

Using a TV sparsity constraint, if the individual images reconstructed (figure 2.7b) from a simulated Gaussian noise 2.7a are averaged, the mean intensity results in a nearly homogeneous signal, as illustrated in Figure 2.7c. This result clearly justifies the averaging operator to combine images from multiple reconstructions and strengthen noise discrimination from images.

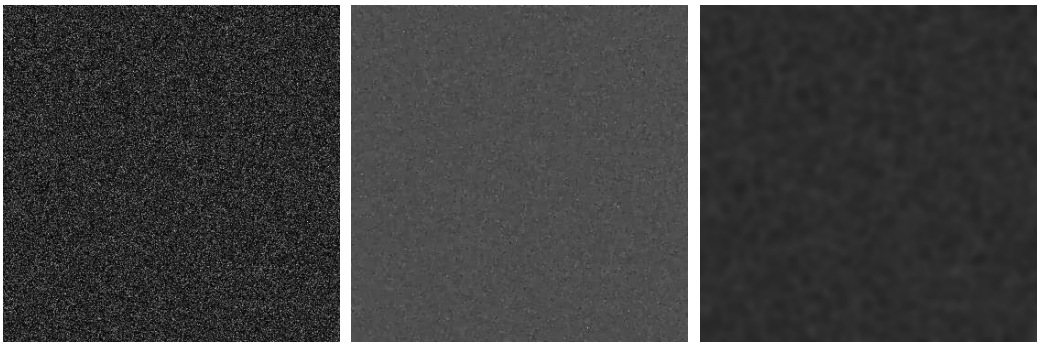

(a) Gaussian noise, $\mu = 3.99$ and $\sigma_1 = 3.01$

(b) Single reconstruction

(c) Average reconstructions, $\mu = 3.99$ and $\sigma_2 = 0.75$

Figure 2.7: Left: Gaussian noise image (with mean $\mu = 3.99$ and standard deviation $\sigma_1 = 3.01$). Center: an individual noise reconstruction. Right: Reconstructed image obtained by averaging 20 images recovered with different sets of measurements Φ_i for $(i = 1...20)$ with $\mu = 3.99$ and $\sigma_2 = 0.75$ (10% of measurements).

Theoretically the expected value of the standard deviation of K reconstructed images which are averaged is $\sigma_2 = \sigma_1/\sqrt{K}$, which is verified since $\sigma_1/\sqrt{K} = 3.01/\sqrt{20} = 0.67 \approx 0.75$.

The same experiment for a Poisson noise is illustrated in figure 2.8 and the same effect is observed. The resultant image is a nearly homogeneous image with smooth variations. In the Poisson noise case, the reduction of the standard deviation σ_2

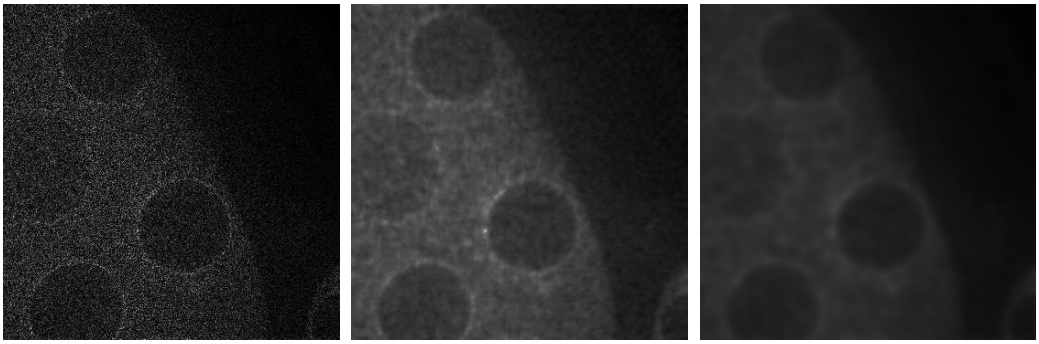

(a) Poisson noise, $\mu = 4.17$ and $\sigma_1 = 4.1$

(b) Single reconstruction

(c) Average reconstructions, $\mu = 4.17$ and $\sigma_2 = 2.09$

Figure 2.8: Left: Poisson noise image (with mean $\mu = 4.17$ and standard deviation $\sigma_1 = 4.1$). Center: an individual noise reconstruction. Right: Reconstructed image obtained by averaging 20 images recovered with different sets of measurements Φ_i for $(i = 1...20)$ with $\mu = 4.17$ and $\sigma_2 = 2.09$ (10% of measurements).

was not as strong compared to the Gaussian noise case. The reason is that the simulated Poisson noise depends on the object structures and light intensities. In the original image used to simulate the Poisson noise 2.1b, there is an important gap of intensities between the background and the drosophyla cell, increasing the standard deviation.

2.4.2 Results with Averaging

Here we present the results on drosophila cells imaged by fluorescence microscopy in two manners. The first one exploits a multiple acquisition of 10 images of the same sample where each image is exposed 10 milliseconds. The second acquisition is a single image exposed 100 milliseconds. The denoising approaches presented in (2.9) and (2.10) are evaluated and the results are in figure 2.9.

2.4.2.1 Denoising Evaluation

Denoising performances were evaluated via SNR measurements and image noise analysis. The SNR of the images can be estimated from the noise model as:

$$\mathrm{SNR} = \frac{\zeta A}{\sqrt{\zeta^2(A + \lambda_B) + \sigma^2}}$$

The mixed *Poisson-Gaussian* noise parameters $(\zeta, \lambda_B, \mu, \sigma)$ are estimated using cumulant method, matching the first four cumulants of I with the k-statistics of the samples in a uniform image region [Rose 2002]. This follows from the property that the k-statistics are the minimum variance unbiased estimators for cumulants.

The contrast-to-noise ratio (CNR) is estimated as:

$$\mathrm{CNR} = \frac{|x_{\Re_1} - x_{\Re_2}|}{\sigma}$$

where $x_{\Re_1}$ and $x_{\Re_2}$ are signal intensities in adjacent homogeneous regions $\Re_1$ and $\Re_2$, and σ is the standard deviation of the background additive noise.

2.4.2.2 Noise removal and recovered images

Results from the first scheme of denoising are illustrated in Figure 2.9b and detailed in Table 2.1 while results from the second scheme of denoising are illustrated in Figure 2.9e and are detailed in Table 2.2. In all experiments, important improvements of the SNR or the exposure time were achieved. For experiments on drosophila cells image (Figure 2.9) and lymphocytes image (Figure 2.10), the SNR was highly improved and details were very well preserved. The algorithm shows its efficacy and importance on microscopy applications, where photons detected are limited and image quality is usually degraded. The improvement can be provided in two different ways, either by fixing the desired SNR and reducing the exposure time, or by fixing the exposure time and improving the SNR, as illustrated by images in Figure 2.9 (b-e).

Note that by averaging four reconstructed images with the first scheme, the SNR is equivalent to the reference acquisition with exposure time of 100 milliseconds (see Table 2.1). If the goal is to obtain a SNR equivalent to the reference image, by using the first denoising scheme the time exposure is reduced from 100 to 40 milliseconds. Complementary results about improvements in photobleaching and denoising are presented in appendix B.

We have compared the denoising quality of the proposed method with regular *Total Variation* filtering. The algorithm used for this comparison was presented by Gilboa et al. in [Gilboa 2006]. This algorithm minimizes TV with two schemes:

Table 2.1: Signal-to-noise ratio (SNR) and contrast-to-noise ratio (CNR) results for the first denoising scheme and for the image on Figure 2.9a.

	Exposure Time	CNR	SNR
Ref:	100 ms	30.00	6.42
Acq:	10 ms	5.17	3.61
(4×) CS:	4 × 10 ms	34.20	6.89
(10×) CS:	10 × 10 ms	96.60	13.31

Table 2.2: Signal-to-noise ratio (SNR) and contrast-to-noise ratio (CNR) results for the second denoising scheme proposed and for image on Figure 2.9d.

	Exposure Time	CNR	SNR
Ref:	100 ms	30.00	6.42
(1×) CS:	100 ms	36.50	7.24
(10×) CS:	100 ms	90.23	11.02

(I) with global variance constraints (scalar fidelity term) and (II) with an adaptive variational scheme that controls the level of denoising by local variance constraints (adaptive fidelity term in order to preserve texture and small scale details). Noise residual images and SNR results are illustrated in Figure 2.10 and show that our proposed method is able to better discriminate the noise from the true signal component than direct TV minimization methods. This can be explained by the fact that our method provides TV minimization constraints combined with uncorrelated noise recovery constraints. Differences on each set of under-sampled random projections lead to better enhancement of true signal-measures and attenuation of noise-measures.

2.5 Images Fusion by Non-Local Averaging

In this section we describe a fusion method based on the nonlocal filtering to combine the set of images $\hat{x}_i$ obtained by Equation (2.10). The main difference between this method and the original denoising approaches is that the noisy image is not a single image but a vector of similar images. Here we exploit the idea that images present a high degree of spatial redundancy in terms of objects appearance and shapes, and consequently, the set of images $\hat{x}_i$ should present even more redundancy.

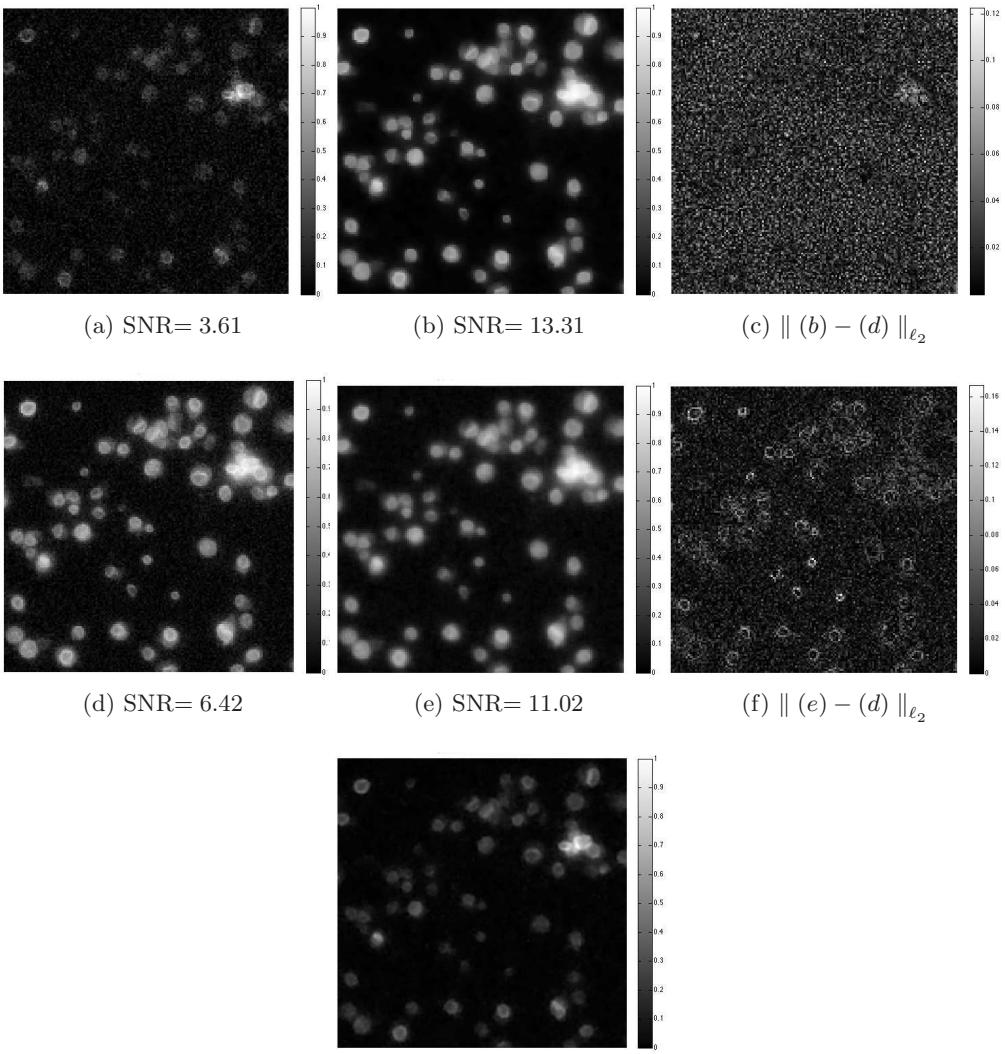

(a) SNR= 3.61 (b) SNR= 13.31 (c) $\| (b) - (d) \|_{\ell_2}$

(d) SNR= 6.42 (e) SNR= 11.02 (f) $\| (e) - (d) \|_{\ell_2}$

(g) SNR= 6.89

Figure 2.9: (a) Drosophila cells imaged by fluorescence microscopy with exposure time $t = 10ms$. (b) Denoised image with the first CS scheme (10 reconstructions of 10 short-exposure time images as in (a) with M=10%N). (c) Noise residual comparing (b) to (d). (d) Image acquired with exposure time equal to $t = 100ms$. (e) Denoised image with the second CS scheme (10 reconstructions from (d) with M=10%N). (f) Noise residual comparing (e) to (d). (g) Denoised image with the first CS scheme (4 reconstructions of 4 short-exposure time images, with M=10%N)

As discussed before, the reconstructed images $\hat{x}_i$ are slightly different, and most differences are high-frequency components.

The non-local fusion method does not make regularity assumptions on the orig-

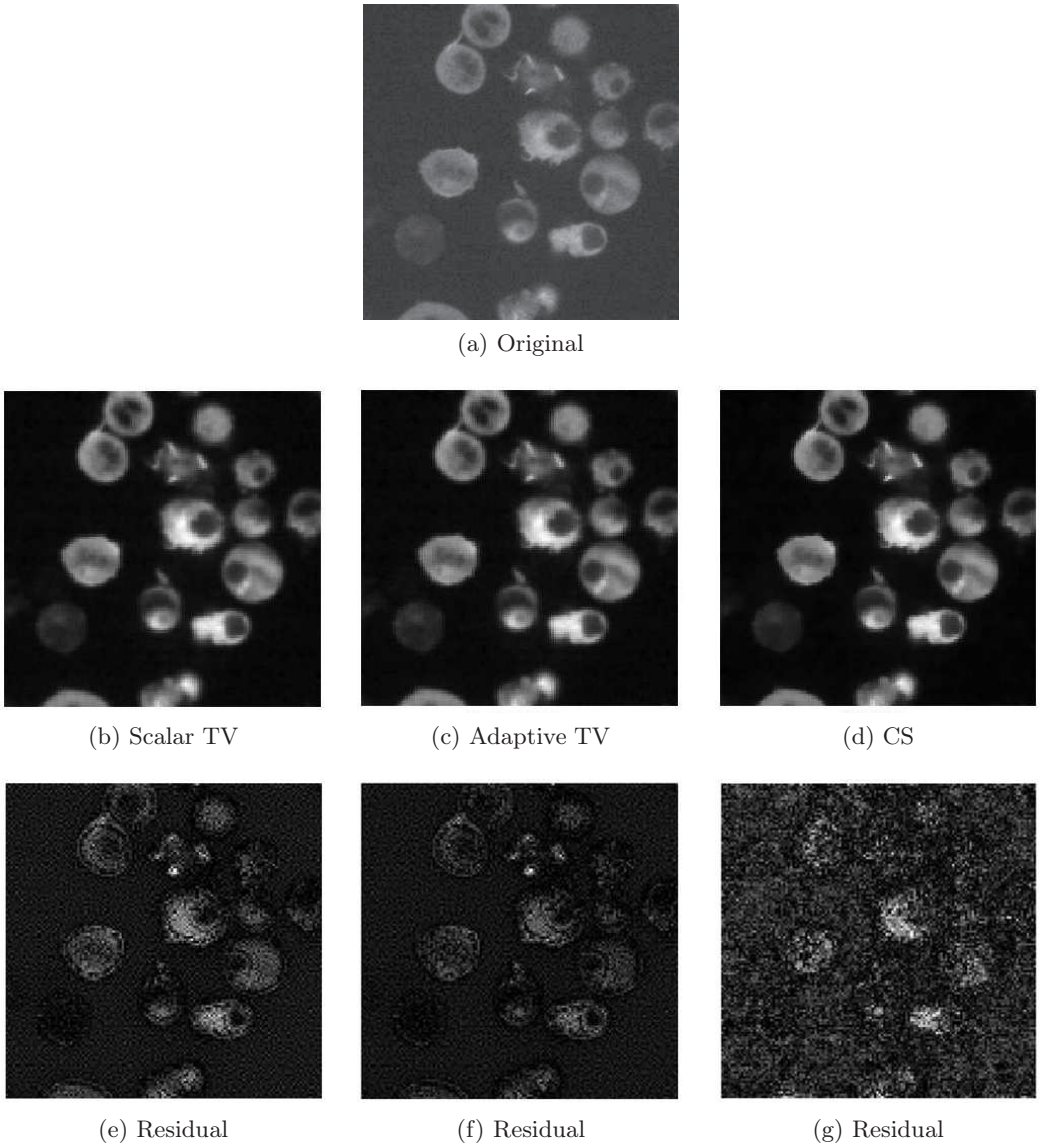

(a) Original

(b) Scalar TV (c) Adaptive TV (d) CS

(e) Residual (f) Residual (g) Residual

Figure 2.10: (a) Lymphocytes imaged by fluorescent microscopy, SNR= 8.14. Denoised images by (b) scalar TV filtering (SNR= 11.2), (c) adaptive TV filtering (SNR= 12.5) and (d) by CS 2nd scheme, using 10 reconstructions (SNR= 14.28) with M=10%N. (e)(f)(g) Noise residuals for each method comparing (a) to (b-d)$\| \hat{x} - x \|_{\ell_2}$.

inal image, allowing noise reduction and preserving fine structures, details, and texture. The basic assumption is that small patches on objects from an image have many similar patches in the same image and averaging similar patches should correct the noisy component. For NL-means, noise is assumed Gaussian. The algorithm

estimates the value of a pixel x as an average of the values of all the pixels belonging to patches with similar appearance to the neighborhood of x.

Consider a noisy image $v = \{v(i)|i \in \Omega\}$ defined on a discrete bounded domain $\Omega \subset \mathbb{R}^2$. Consider also a patch domain of fixed size $\mathcal{P}_i \subset \Omega$ where $v(\mathcal{P}_i)$ denotes a square patch centered at a pixel i. The estimated denoised image v_{NL} corresponds to a weighted average of all the pixels in the image:

$$v_{NL}(i) = \sum_{j \in \Omega} w(i,j) \cdot v(j) \tag{2.13}$$

where the weights $w(i,j)$ depend on the similarity between pixels i and j and are defined as:

$$w(i,j) = \frac{1}{C(i)} e^{-\frac{\|v(\mathcal{P}_i) - v(\mathcal{P}_j)\|_2^2}{h^2}}, \tag{2.14}$$

where $\| v(\mathcal{P}_i) - v(\mathcal{P}_j) \|_2^2$ is the Euclidean distance between pixels from the patches $v(\mathcal{P}_i)$ and $v(\mathcal{P}_j)$ and $C(i)$ is a normalizing constant

$$C(i) = \sum_j e^{-\frac{\|v(\mathcal{P}_i) - v(\mathcal{P}_j)\|_2^2}{h^2}},$$

enforcing two conditions (i) $0 \leq w(i,j) \leq 1$, (ii) $\sum_j w(i,j) = 1$.

To fuse multiple CS-reconstructed images, the search of similar patches in Equation (2.14) is performed only for the first image $\hat{x}_1$ and used for the entire set of images. Then, if the noisy image v is not a single image but a vector of similar images the final image is computed as a weighted average of all the pixels in the vector of images

$$\hat{x}_{NL}(i) = \frac{1}{K} \sum_{k=1}^{K} \sum_{j \in \Omega} w(i,j) \cdot \hat{x}_k(j), \tag{2.15}$$

with the condition $\frac{1}{K} \sum_{jk} w(i,j) = 1$. This method provides a much more discriminative combination of the set of images x_i than simple averaging, as initially proposed.

The simple averaging of $\hat{x}_i$ in (2.12) exploits only the local redundancy from the set of images but not from the different patches of one single image. Solving our proposed method in (2.15) allows to exploit the redundancy locally beyond all images $\hat{x}_i$ and also non-locally using similar patches from the same image.

2.5.1 Results with Non-Local Averaging

2.5.1.1 CS Recovery: Image of Hair Follicle

We applied our approach to a fluorescence microscopy image of hair follicle. The specimen is labeled with a green and a red marker. The total acquisition time is 15 seconds per image and the 3-dimensional stack has 65 frames (each channel). The results illustrated here concern the frame 31 of each channel taken from the 3D volume. Then each channel (red and green) is reconstructed independently as grayscale image.

In Figure 2.10 we show some reconstruction results of the noisy images from the green and red channels in Figures 2.10(a) and 2.10(f), with size 400×400 pixels. The Figures 2.10(b) and 2.10(g) correspond to one single CS reconstruction with 10% of measurements in the Fourier domain, such as described in chapter 2. In Figures 2.10(c) and 2.10(h) we display the denoised images by our previous work, solving the problem described in (2.12) and in 2.10(e) and 2.10(j) the denoised images with the improved method described in (2.15). For both methods, described in (2.12) and (2.15) with $K = 10$, we used the same sampling matrices with 10% of measurements in the Fourier domain. For comparison, Figures 2.10(d) and 2.10(i) display the noisy images denoised by the NL-means algorithm [Buades 2005], with variance $\sigma^2 = 20.4$ (2^8 gray levels). We note that the results for NL-means present many artifacts due to the noise characteristics.

Since there is no ground-truth such as a perfect noise-free image, the denoising performances were evaluated via signal-to-noise ratio (SNR) and contrast-to-noise ratio (CNR) measurements. The SNR and CNR measures are given for all methods in Table 2.3.

Image	SNR (dB)		CNR	
	green	red	green	red
Original	3.62	4.53	13.97	9.51
CS 1	10.45	5.14	89.42	10.89
CS-mean	18.32	7.74	106.71	20.72
NL-means	18.80	19.96	103.72	71.81
CS NL-means	20.29	22.37	121.78	71.09

Table 2.3: SNR, CNR measures for the green and red channel.

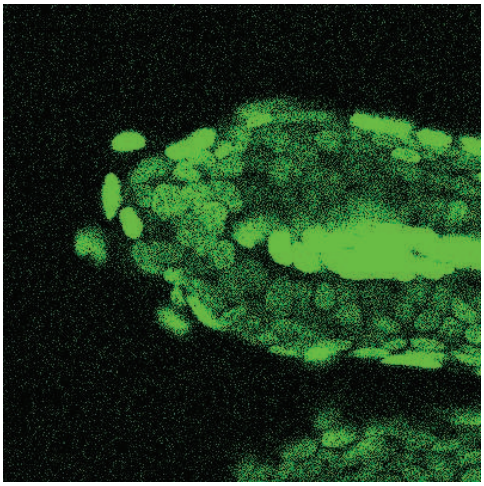

(a)

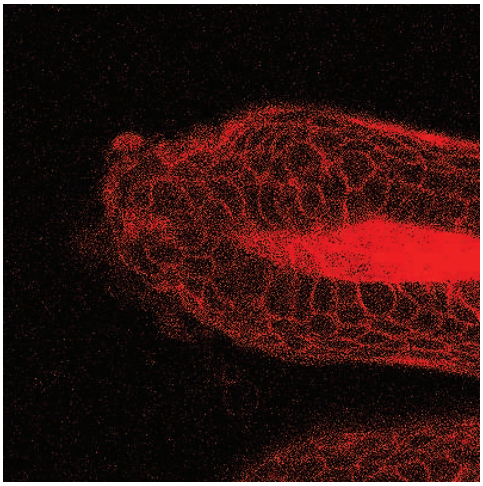

(f)

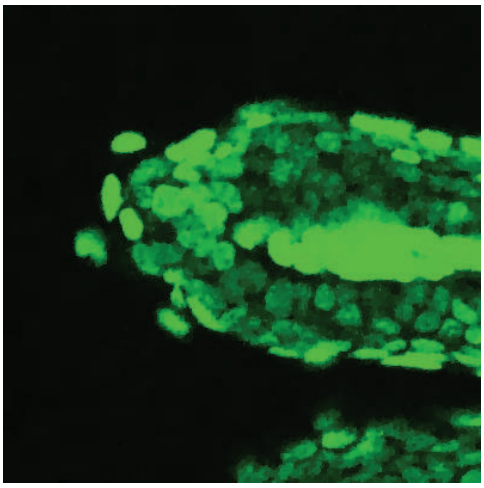

(b)

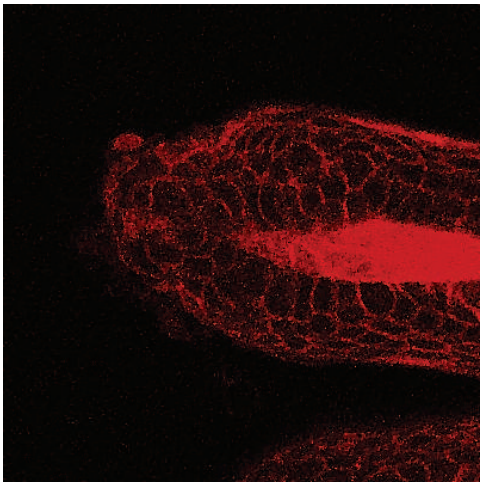

(g)

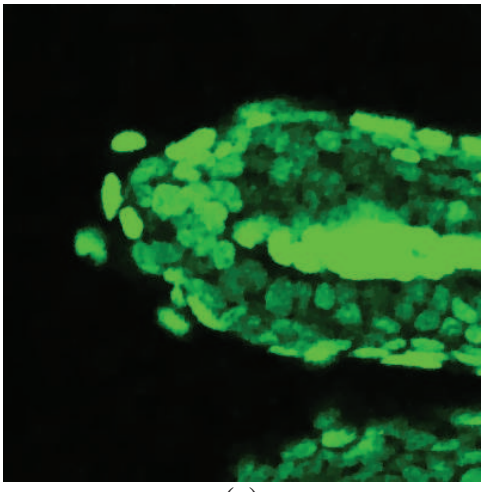

(c)

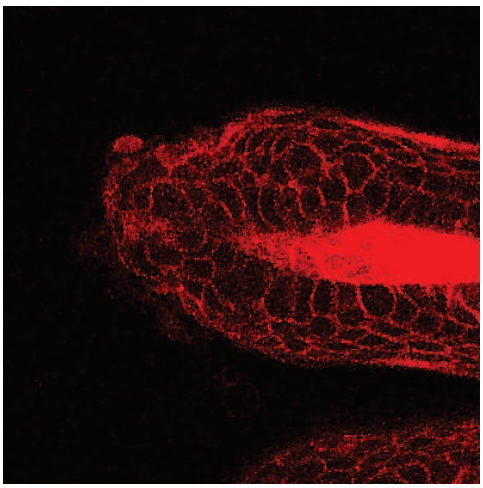

(h)

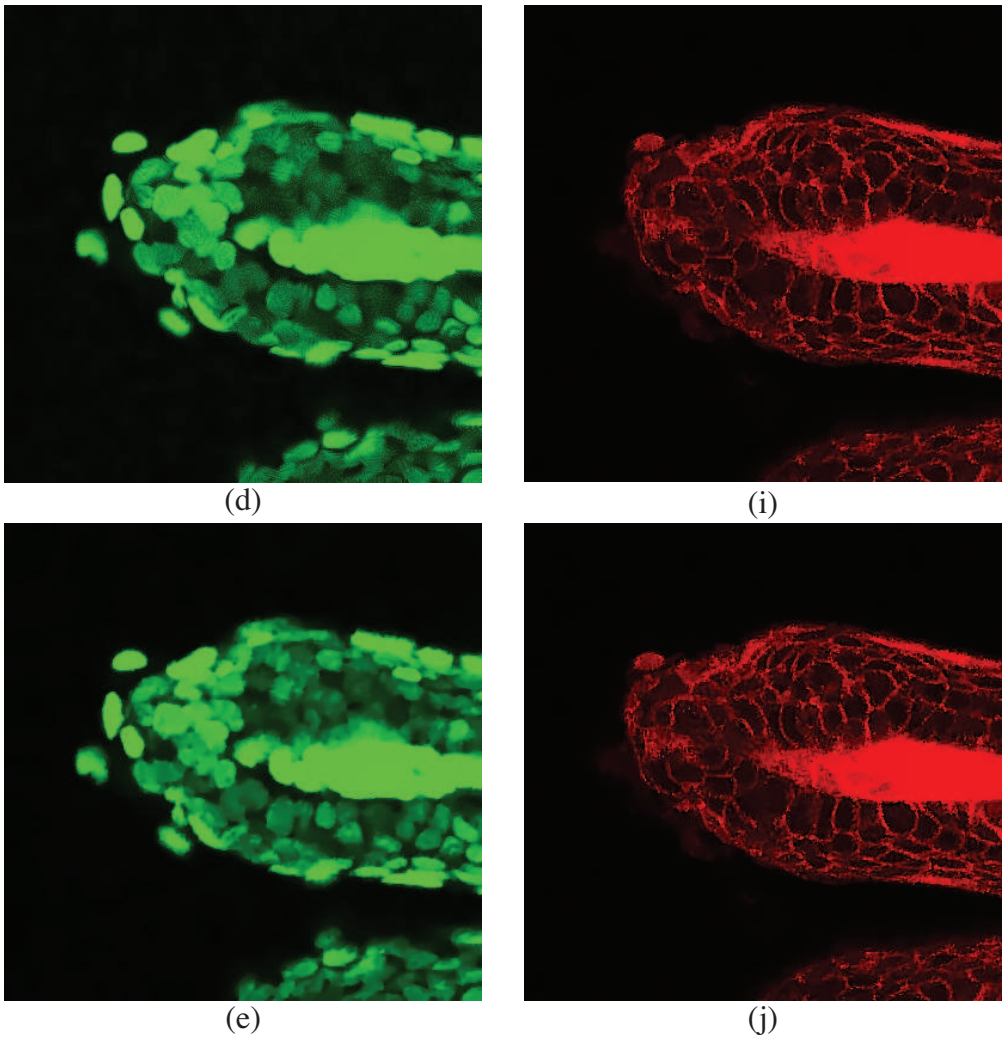

Figure 2.10: Green and red channels; fluorescence microscopy image of hair follicle. (a)(f) Original noisy image. (b)(g) One single CS reconstruction. (c)(h) Multiple CS with averaging (2.12). (d)(i) NL-means filtering of the noisy image. (e)(j) Multiple CS with NL-means 2.15.

2.5.1.2 CS Recovery: Image of Cells

In Figure 2.11 we show some results of our CS-based method from the noisy image of fluorescence microscopy image of cells with exposure time equals to 10 milliseconds (Figure 2.11(a)) with size 256×256 pixels. We compared the denoising results with a reference image of the same specimen acquired with a longer exposure time t = 200 ms, in Figure 2.11(f). In Figure 2.11(b) we display the denoised image solving the problem described in (2.12) and in Figure 2.11(e) the denoised image with the improved method described in (2.15). For both methods, described in (2.12) and

(2.15) with K = 10, we used the same CS sampling matrices, (2.9), with 10% of measurements in the Fourier domain.

For comparison, Figure 2.11(c) displays the denoised image from one single CS reconstruction $\hat{x}_1$ using the NL-means algorithm [Buades 2005], with variance $\sigma^2 = 11$ (2^8 gray levels), and Figure 2.11(d) displays the result from the NL-means applied to the noisy image in Figure 2.11(a). Images in Figure 2.11(g)-(j) display structural similarity (SSIM) index maps [Wang 2004], which is a fidelity measure better suited for extracting structural information from an image than the mean squared error (MSE). Measures of error such as the MSE, SSIM and PSNR are illustrated in Table 2.4. A SSIM = 1 corresponds to a maximum of similarity (minimum error). The values of MSE, PSNR and SSIM were computed using the reference image (Figure 2.11(f)).

Image	(b) CS-mean	(c) NL-means CS 1	(d) NL-means	(e) CS NL-means
MSE	94.98	92.28	42.78	42.18
PSNR	28.35 dB	28.47 dB	31.81 dB	31.87 dB
SSIM	0.883	0.885	0.930	0.938

Table 2.4: MSE, PSNR and SSIM measures.

2.6 Conclusion

We have introduced a denoising method exploiting multiple reconstructions with random undersampled Fourier projections and TV minimization. Our approach presents several advantages over traditional denoising methods by combining fast image acquisition, spatial smoothing constraints and denoising capabilities in a single framework. We also propose an improved approach of the CS-based denoising method exploiting a non-local merging scheme to combine multiple reconstructions instead of averaging. Experiments on fluorescence microscopy images of hair follicle demonstrate improvements of SNR and CNR values even with a very limited number of measurements, and experiments on fluorescence microscopy images of cells demonstrated improvements of PSNR, MSE and SSIM values. Our proposed method leads to a denoising performance equivalent or better than the NL-means method with the advantage of taking only 10% of measurements.

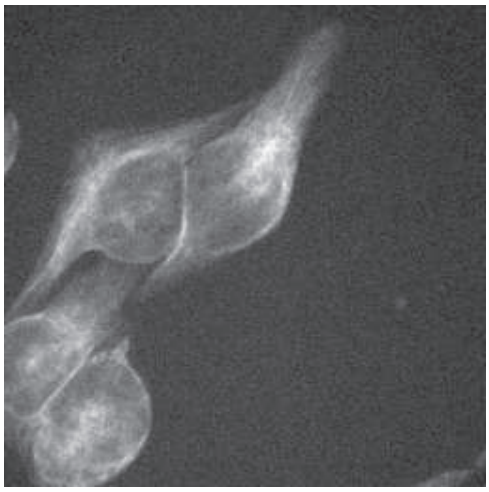

(a)

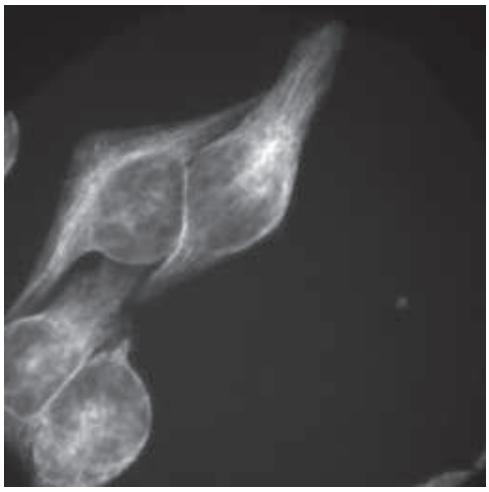

(f)

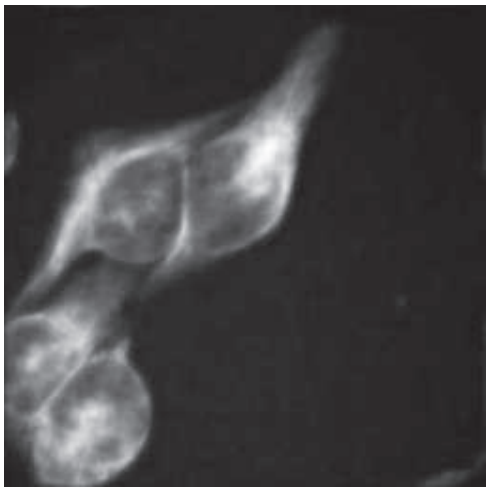

(b)

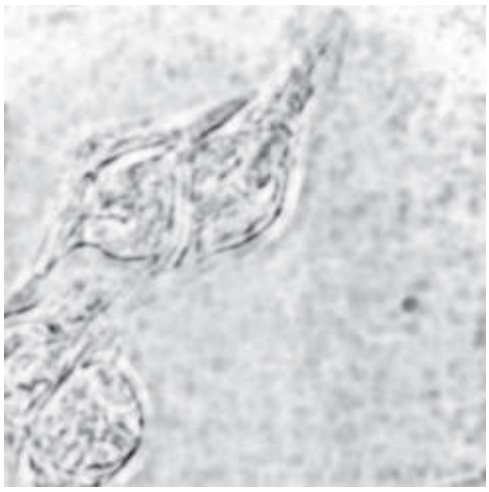

(g)

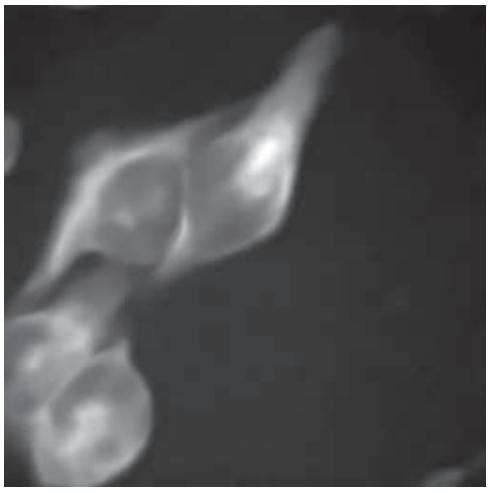

(c)

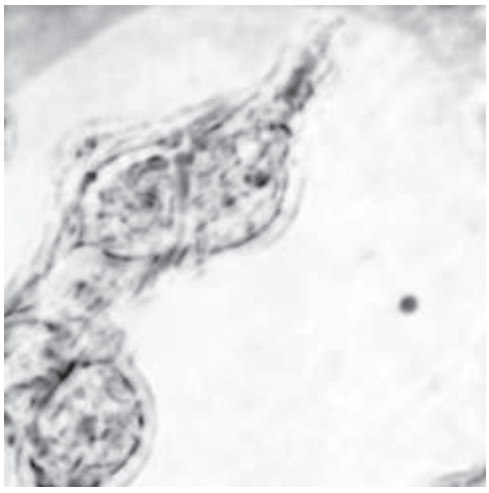

(h)

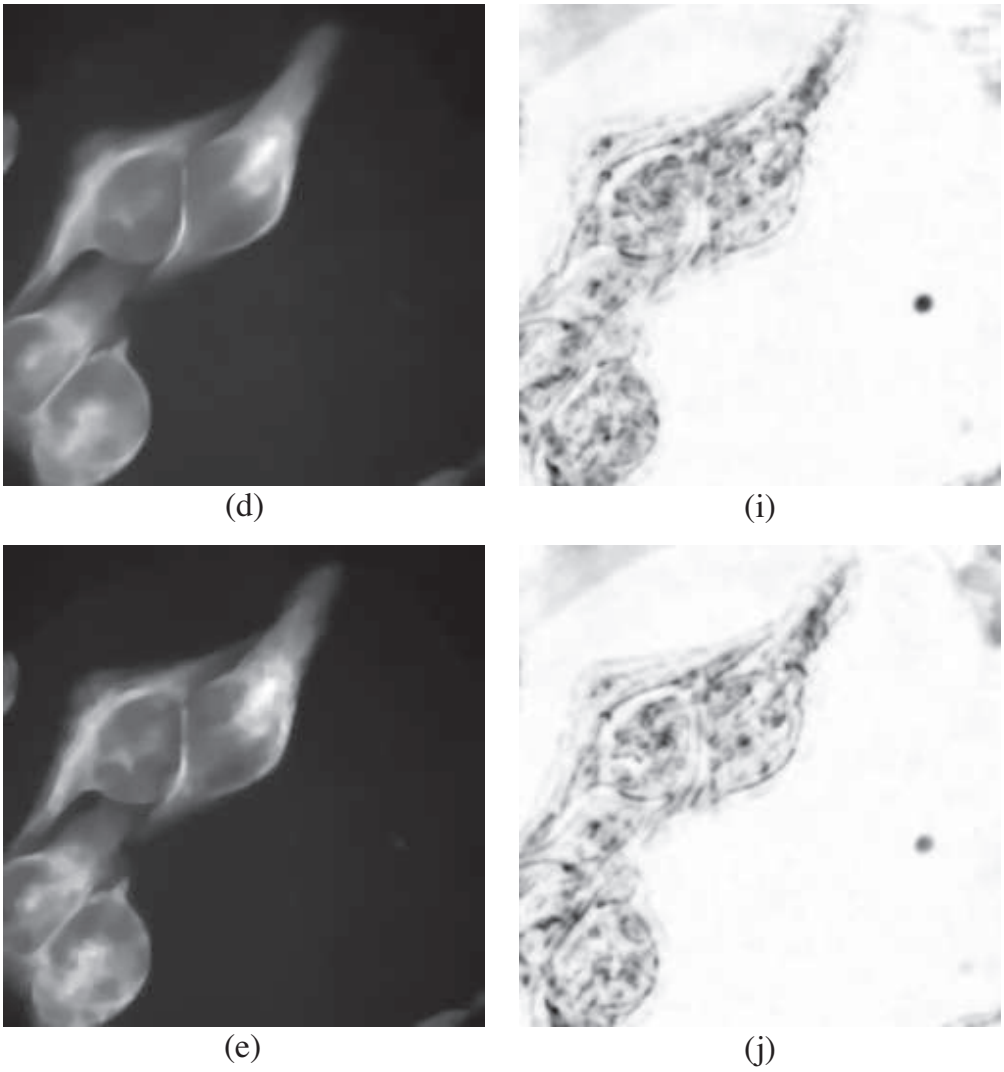

Figure 2.11: Fluorescence microscopy image of cells. (a) Image exposed 10 ms. (b) Multiple CS with averaging (2.12). (c) NL-means from one single CS reconstruction (d) NL-means from the image exposed 10 ms. (e) Multiple CS with NL-means (2.15). (f) Reference image exposed 200 ms. (g-j) SSIM index maps for images (b-e) in comparison to the reference image.

Part II

CS-based Biological Imaging Methods

Chapter 3

Introduction

Basically, optical or light microscopy involves passing visible light transmitted through or reflected from the sample through a single or multiple lenses to allow a magnified view of the sample. For most biologists, optical microscopy has become an essential tool [Herman 1993]. The simple reason is that cells are the basic units of life and their size are almost always bellow the upper limit of the resolution of the human eye. Microscopes make it possible to see inside the cells that make up all living organisms. Recent advances in microscopy, particularly the use of fluorescent probes to study cell function in living cells, are bringing microscopy back into the forefront of research in cell biology.

The latest microscopy imaging techniques offer sub-diffraction spatial resolution and real-time views of cellular phenomena. Confocal microscopy uses point illumination and a spatial pinhole to eliminate out-of-focus light in specimens that are thicker than the focal plane [Minsky 1988, Wilson 1988]. Photoactivated light microscopy (PALM) [Betzig 2006] and stochastic optical reconstruction microscopy (STORM) [Rust 2006] rely on the stochastic activation of single photoswitchable molecules to localize them with nanometric accuracy and reconstruct high-resolution images. Stimulated emission depletion microscopy (STED) is a fluorescence microscopy technique that uses non-linear de-excitation of fluorescent dyes to overcome the resolution limit imposed by diffraction [Hell 1994, Hell 1995]. Structured illumination uses patterned light to increase the resolution by measuring the fringes in the pattern created by the interference of the illumination pattern and the sample [Bailey 1993, Gustafsson 2000, Heintzmann 2006]. Otherwise-unobservable sample information can be deduced from the fringes and computationally restored with this latter technique.

Recent high-resolution microscopy techniques makes possible a wide range of applications in biology, however, there are still many limitations. We have been mostly interested in reducing the noise level which is present in all light microscopy

modalities and facilitate the high data throughput which can be time-expensive and invasive toward cells. In the first part of this thesis we proposed a denoising framework for biological microscopy. Here, we focus on the excessive high-throughput of high-resolution microscopy.

Contents

3.1 High-Resolution and High-Throughput Data Acquisition . 78
3.2 Intelligent Acquisition Systems in Microscopy 79
3.2.1 Intelligent Acquisition and Learning of Fluorescence Microscope Data Models 80
3.2.2 Controlled Light Exposure Microscopy 81
3.3 Existing Compressed Sensing Acquisitions Systems 82
3.3.1 MRI 83
3.3.2 Single Pixel Camera 84
3.3.3 Astronomy 85
3.3.4 Coded Aperture 86
3.3.5 Optics and Holography 87

3.1 High-Resolution and High-Throughput Data Acquisition

High-throughput data acquisition is a particularly relevant topic in biological microscopy, which tends more and more towards observations of a large number of biological samples over long periods of times. High-throughput applications lead to huge amount of data which makes visual inspection impractical. They also involve long exposure times causing photodamage or photobleaching. Therefore, the design of innovative and intelligent acquisition systems remains an essential field of research for high-throughput applications. Regarding the large amount of image data to acquire and store, solutions are to be seek within the field of intelligent signal sampling and compression. It has been recently suggested [Candès 2004b, Candès 2006a, Donoho 2006b] that efficient signal transform could be incorporated in new intelligent acquisition systems to encode the information contained in the images in a compact form. Indeed, exploiting a sampling or decomposition of the image signal on some basis functions that lead to a sparse rep-

resentation with a small number of non-zero coefficients enables to compress signal encoding by only keeping the most S energetic coefficients. In such case, sparsifying transforms enable low-loss or even lossless data compression. Compressed sensing theory falls in this category of approach, exploiting some sparsifying transform (e.g. wavelets, total variation, discrete cosine transform) during the acquisition process rather than as a post-processing step, prior to final storage of the signal, as described in a next chapter.

3.2 Intelligent Acquisition Systems in Microscopy

The ultimate goal in microscopy is to observe live cellular processes with a high spatial and temporal resolution, with low noise level, and for a period of time as long as possible while avoiding photodamage. Cellular processes can take place very fast and the movement of cellular components are generally complex and unintuitive. The main barrier to observe and understand such movements and behaviors is the inability to acquire image with high spatial and temporal resolution. In addition, the presence of noise and photodamage in such images add more difficulties to analyze and understand these processes. For example, the presence of noise degrades the image quality and the resolution, making it difficult to locate and track cell components.

Photobleaching and phototoxicity (photodamage) are also a great limitations of fluorescence live-cell microscopy since they degrade the image quality or can even change the cell behaviors through phototoxicity. A straightforward way to limit photodamage is to reduce the light dose for the excitation of fluorophores. When the amount of excited fluorophores is restricted the image quality is reduced due to the increment of noise level. Finally, the movement of cellular components can be complex and difficult to model which makes it a challenge difficult to face, but its accomplishment should promote great advances in cell biology.

In this sense, in the last few years, the field of intelligent acquisition systems has emerged in microscopy. We should define as intelligent acquisition any acquisition which takes into account prior information about the object of interest. Adding some prior information in the acquisition process can improve crucial problems such as resolution, noise and photobleaching.

3.2.1 Intelligent Acquisition and Learning of Fluorescence Microscope Data Models

In [Jackson 2009], a mathematical framework and algorithms were proposed to build accurate models of fluorescence microscope time series, as well as design intelligent acquisition systems based on these models. The authors propose to use an active learning approach to choose the acquisition regions having the most relevant information, resulting in a shorter acquisition time, as well as a reduction of the amount of photobleaching and phototoxicity incurred during acquisition. In other words, the acquisition is restricted to only those areas where the signal (not background) is present.

The motivations of this framework is that microscopy can be time-consuming and inconsistent. This works suggest to perform the analysis directly on the raw microscope data without the intermediary stage of a viewable image, which should improve the acquisition in terms of rapidity and photodamage. Intelligent acquisition suggests to automatically determine when to stop acquiring, avoiding the problem of acquiring more frames than necessary (which both wastes time and causes unnecessary photobleaching). It could also remove the risk of acquiring too few frames and thus not obtaining the desired information. With intelligent acquisition, the acquisition should be able to compute the optimal trade-off between temporal and spatial resolution, along with the best region to acquire, to build an accurate model as quickly as possible. A diagram of the method is illustrated in figure 3.1.

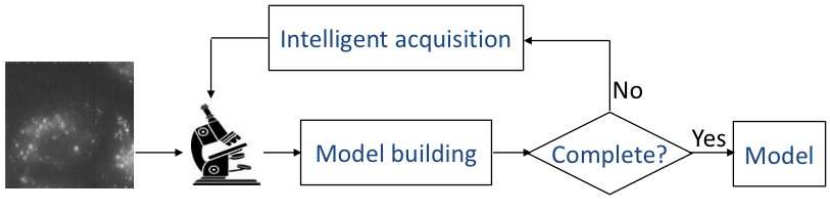

Figure 3.1: A diagram of the method proposed by Jackson et al.. The "model building" module constructs a model from the microscope data, and the "intelligent acquisition" module determines what acquisitions to make to efficiently improve on this model. Figure extracted from [Jackson 2009]

More generally, the problem of designing intelligent acquisition systems relates to the framework of active learning, which refers to any form of learning in which the learning program has some control over the inputs on which it trains. Assuming

that data acquisitions are expensive, the goal is to request the data that is most informative. The method proposes to model the motion of objects in a time series. They suggest to learn the dynamics of the objects, which can be described using the motion models. The cost of learning a model is a function of the time taken to learn it, and the phototoxicity and photobleaching incurred during acquisition. The idea of searching for the optimal acquisition strategy corresponds to choosing where to acquire, when to acquire, and when to stop acquiring. In addition to minimizing cost, the approach also needs to satisfy some physical constraints. Because it takes finite time to acquire each pixel, there is a trade-off between spatial resolution and temporal resolution. These global constraints make this approach not straightforward and difficult to use in practice.

3.2.2 Controlled Light Exposure Microscopy

The approach proposed in [Hoebe 2007] suggests to create a non-uniform illumination of the field of view allowing the adjustment of the light dose for excitation of fluorophores for every individual pixel leading to reduced photodamage without loss of image quality. Contrarily to the Jackson et al. approach, in the controlled light exposure microscopy (CLEM), the excitation is restricted to those areas where the signal is present and is based on two strategies. The first strategy of CLEM is to use significantly less excitation light in the background by limiting the time of illumination of all background pixels via a feed-back system. This strategy not only reduces excitation of the background that is in focus but also, and most importantly, fluorophores that are out-of-focus. The second strategy of CLEM is to stop the illumination when local fluorophore level is high (bright foreground). The resulting image has a lower SNR in the background (without signal) and a SNR in the bright foreground that is equal to the SNR of the weak foreground.

The approach is illustrated in figure 3.2; the top panel shows a conventional illumination and acquisition and the bottom shows the CLEM approach with the non-uniform illumination. The CLEM technique regulates laser illumination so that photobleaching is reduced and cell survival increased.

These approaches presented in the two subsections above allow photodamage reduction while keeping image quality, however, the acquisition processes are image-dependent and need a learning step during acquisition. To model restricted acquisition or control exposure they include a feedback loop during the acquisition.

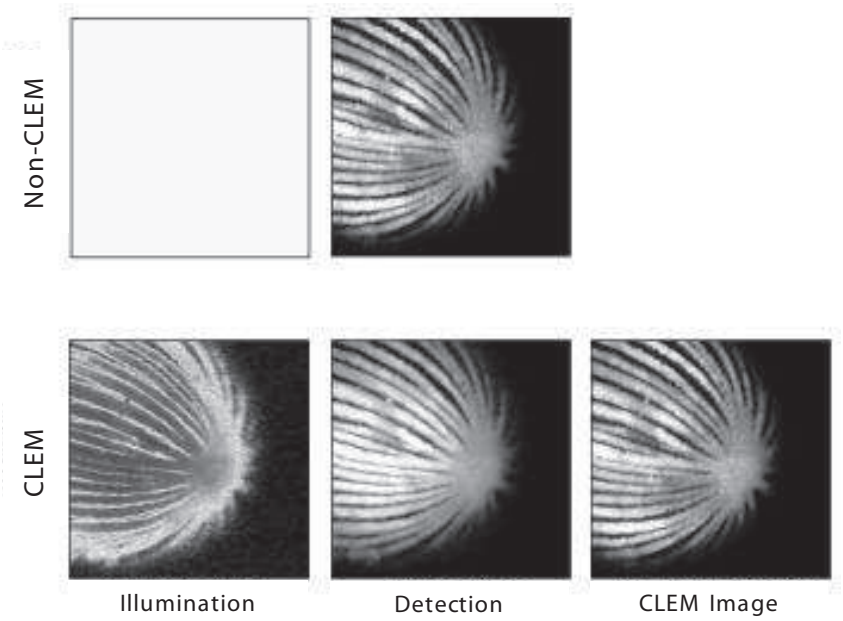

Figure 3.2: Confocal image of auto-fluorescence of pollen grain in the absence and presence of CLEM. Top panel shows the illumination image (left) and confocal image (right) in the absence of CLEM. Bottom panel shows the illumination image (left), detected image (middle) and CLEM image (right). Figure extracted from [Hoebe 2007]

Accordingly, the generalization of these approaches become difficult. In addition, noise level and temporal resolution limitations remains an open problem.

The compressed sensing approaches which we propose in the following chapters of this thesis compose a powerful framework for intelligent acquisition in microscopy. The remarkable advantage of our CS-based approach is that we perform a reduced number of linear measurements allowing to reduce photodamage, speed-up the acquisition while being robust to high noise levels. Indeed, the proposed CS reconstruction scheme achieve denoising performances comparable to state-of-art denoising techniques.

3.3 Existing Compressed Sensing Acquisitions Systems

The compressed sensing theory has revolutionized the field of signal processing in the last few years. However, the CS theory is difficult to apply since it depends on the acquisition setup which should acquire the data in a particular domain. Despite

significant progress in the theory and methods of CS, little headway has been made on real acquisition devices. Applying compressed sensing theory to practical imaging systems poses a key challenge where physical constraints typically make it infeasible to actually measure many of the random projections described in the literature, and therefore, innovative and sophisticated imaging systems must be carefully designed to effectively exploit CS theory.

Developing practical optical systems to exploit CS theory is a significant challenge being explored by investigators in the signal processing, optics, astronomy, and coding theory communities. In addition to implicitly placing hard constraints on the nature of the measurements which can be collected, such as nonnegativity of both the projection vectors and the measurements, practical CS imaging systems must also be robust and reasonably sized.

Globally, the large field of applications are compressive imaging, medical imaging, analog-to-information conversion, computational biology, geophysical data analysis, hyperspectral imaging, compressive radar, astronomy, communications, surface metrology, acoustic and time-frequency analysis, remote sensing, computer engineering, computer graphics, robotics and control, content based retrieval, optics and holography, physics and fault identification. And many other research fields should take advantage of this theory in the coming years. However, for instance there are a very small number of real devices using compressed sensing compared to the volume of research results about the theory.

Here, we will quickly describe some of these CS implementations. In the last part of this thesis, we will present some results on practical application of compressed sensing. The first one using digital holography in microscopy, and the second one using a simple holographic setup and a programable CMOS camera able to acquire only requested pixels (pixel random access and radial sampling were tested).

3.3.1 MRI

There are some real CS implementations such as the one proposed for Magnetic Resonance Imaging (MRI) [Lustig 2005, Lustig 2007], where the authors propose to acquire random radial lines in the frequency domain and to use a wavelet transform as sparsifying transform. In fact, the MRI scanners naturally acquire samples of the encoded image in spatial frequency, rather than direct pixel samples which made this application quite obvious and straightforward.

The authors exploit the sparsity which is implicit in MR images. Angiograms are already sparse in the pixel representation and more complicated images have a sparse representation in some transform domain (e.g. in terms of spatial finite-differences or their wavelet coefficients). The blood vessels are bright with a very low background signal. Angiograms are sparsified very well by both the wavelet transform and by finite-differences. The benefits underlined in this work is that CS allow to improve the field of view (FOV) with relative high resolution and the scan time should be small in the case of a real undersampling.

They present experimental verification of several implementations for 2D and 3D Cartesian imaging, showing that the sparsity of MR images can be exploited to significantly reduce scan time, or alternatively, improve the resolution of MR imagery. They demonstrated high acceleration in in-vivo experiments, in particular a 5-fold acceleration of first pass contrast enhanced MRA.

The figure 3.3 was extracted from [Lustig 2007] and illustrate a CS reconstruction and comparison to a reconstruction using a complete data set, a low-resolution image and a zero-fill wavelet reconstruction (zero-filling the missing k-space data and k-space density compensation).

3.3.2 Single Pixel Camera

In [Duarte 2008, Wakin 2006a, Baraniuk 2007] a single pixel camera is proposed to perform linear measurements, where a digital micromirror device (DMD) allow to acquire random combinations of pixels for each measurement. This work propose a prototype of sensor and some experiments show the ability to imaging at wavelengths where silicon is blind and should be considerably more complicated and expensive. Rather than measuring pixel samples of the scene under view, the single pixel camera measure inner products between the scene and a set of test functions. In practice, each measurement corresponds to a random sum of pixel values taken across the entire image.

The light-field is focused by biconvex lens not onto a CCD or CMOS sampling array but rather onto a DMD consisting of an array of N tiny mirrors. Each mirror corresponds to a pixel which can be independently oriented towards a biconvex lens collecting the light and focusing onto a single photon detector. For each measure, the DMD mirrors oriented to the second lens corresponds to a one at the pixel $\phi[x, y]$, and zero if oriented elsewhere.

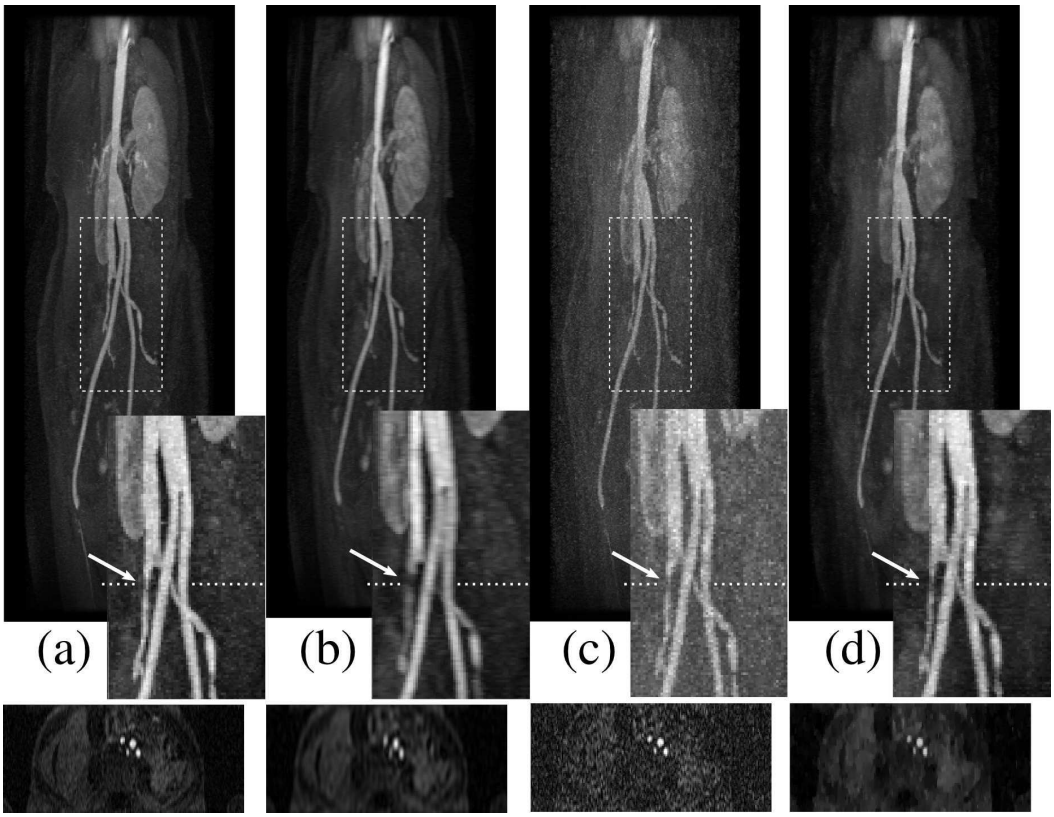

Figure 3.3: Figure extracted from [Lustig 2007]. Reconstruction from 5-fold accelerated acquisition of first-pass contrast enhanced abdominal angiography.

The most important advantages discussed by the authors of a such device is that it is simple, small and a cheap digital sensor which can operate in a broader spectral range than silicon-based cameras. The figure 3.4 is extracted from [Baraniuk 2007] to illustrate the device setup and a CS reconstruction.

3.3.3 Astronomy

There are many other works which investigate how compressed sensing should handle the acquisition for different applications. In astronomy, Bobin *et al.* [Bobin 2008] investigate how CS can provide new insights into astronomical data compression and how it paves the way for new conceptions in astronomical remote sensing. In this work, the CS is evoked as a method to reduce the amount of data to be transmitted from a spatial mission to the earth in the context of high-spatial resolution all-sky survey in the visible based on a scanning satellite.

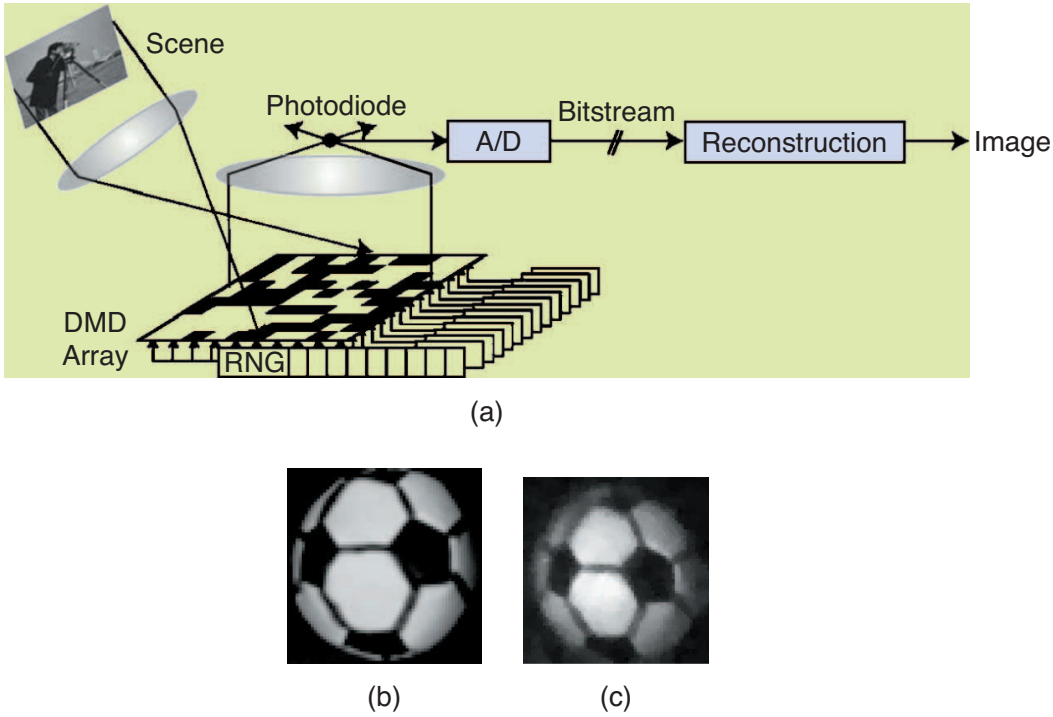

Figure 3.4: Figure extracted from [Baraniuk 2007]

In [Wiaux 2009], Wiaux *et al.* proposed a compressed sensing imaging technique for radio interferometry. Indeed, radio interferometry probes astrophysical signals through incomplete and noisy Fourier measurements, which is proved to be well adapted to capture enough information of compressible signals.

Both works proposed for astronomy remain a simulation and illustrate the potential of the approaches by studying reconstruction performances on simulations.

3.3.4 Coded Aperture

Some work was also dedicated to use coded aperture imaging for compressed sensing. The basic idea of coded aperture is to use a mask, i.e., an opaque rectangular plate with a specified pattern of openings, that allows significantly brighter observations with higher signal-to-noise ratio than those from conventional pinhole cameras. The mask used for compressed coded aperture is a downsampling operator which consists in partitioning the scene in blocks and measuring the total intensity in each block. This is sometimes referred to as integration downsampling. In [Marcia 2009] the authors propose a method which superimposes coded observations and uses wavelet-

based sparsity recovery algorithms to reconstruct the original subframes.

3.3.5 Optics and Holography

In [Denis 2009] an inline hologram reconstruction with sparsity constraints is proposed. The inline digital holograms are classically reconstructed using linear operators to model diffraction. In this work, the authors consider inverting the hologram formation model in Bayesian framework using a sparsity prior and a simple iterative algorithm for 3D image reconstruction.

An other work using holographic measurements is proposed in [Brady 2009]. In this paper, the authors underline the relationship between compressed sensing and the Gabor's invention of holography [Gabor 1948]. Indeed, the Gabor holography is a simple and near-incoherent encoder for compressed sensing, which means that performing holographic measurements corresponds to taking linear projections of a signal. In addition, the acquisition domain is a frequency domain and is incoherent to the direct spatial domain.

In this thesis, we have investigated the use of off-axis holographic measurements in a microscopy setup for CS acquisitions. We show that indeed, off-axis holographic measurements are well-adapted to compressed sensing acquisition and reconstruction, even in low-light conditions.

Chapter 4

Temporal Compressed Sensing With Random Fourier Measurements

In this chapter we describe a simulation study to demonstrate the feasibility of microscopy CS imaging. In conventional microscopy, only Fourier coefficients magnitudes are measurable. The main idea is to combine temporal sequences of optical Fourier transform (OFT) magnitude measurements with Fourier phase estimation by interpolation between complete keyframe acquisitions. For images with homogeneous objects and background, CS provides indeed a reconstruction framework from a set of random projections in the Fourier domain, while constraining bounded variations in the spatial domain. As with many other optical systems, in microscopy we can observe the magnitude of the Fourier coefficients. However, observing the phase of these coefficients can be a very expensive task. We propose a framework to exploit keyframes and phase interpolation along with a CS acquisition of OFT. Our experiments simulating the proposed microscopy image acquisition protocol confirm the feasibility of the CS computational framework to recover image sequences in microscopy with a very high frame rate while preserving high SNR levels. The results obtained with the technique presented in this chapter convinced us that we could get even better performance by associating compressed sensing with digital holography, which will be investigated in chapters 5 and 6.

Contents

4.1 CS in Microscopy with Random Fourier Measurements . . 90

4.2 Displacements and Phase 92

[0]Based upon: M. Marim, E. Angelini and J.-C. Olivo-Marin. *"Compressed Sensing in microscopy with random projections in the Fourier domain"*, IEEE International Conference on Image Processing, ICIP, pp. 2121-2124, 2009.

4.3 Fourier Phase Estimation 96
4.4 Image Reconstruction and Algorithm 98
4.4.1 Algorithm Adaptation 100
4.5 Results and Error Propagation 100
4.6 Conclusion 101

4.1 CS in Microscopy with Random Fourier Measurements

A major difficulty to exploit the CS framework in practical setups is the choice of the sampling basis functions and the architecture of the imaging system performing the measurements [Wakin 2006b]. The principal contribution presented in this chapter is a simulation of a CS-based image acquisition framework, for microscopy imaging. Similarly to recent experiments evaluating CS-based magnetic resonance image (MRI) acquisition protocols [Lustig 2007], we propose to sample image data in the Fourier domain and reconstruct the corresponding spatial image with suited sparsity constraints. We would like to use the undersampling capability of CS to improve acquisition speed and reduce the number of measures being performed.

In microscopy we have access to the object's diffraction pattern, which well approximates the amplitude of the Fourier transform of the object. The theory of light diffraction predicts that the diffraction pattern produced by a plane wave incident on an optical mask with a small aperture is described at an infinite distance by the Fourier transform of the mask, such as illustrated in figure 4.1. We note that the intensities observed in 4.1(b) are the magnitudes of the Fourier transform of the object without the phase information.

The diffraction pattern of an object can be observed optically using dedicated lenses [Goodman 1996]. However, the measured light intensity at the focal distance f of these lenses, contains only the magnitude (square of the amplitude) of the Fourier transform of the object being imaged. To recover the signal we would need to also know the phase of the Fourier coefficients. Knowing only the magnitude of the Fourier coefficients corresponds to knowing the autocorrelation of the object, which is not invertible and not unique.

In optics, phase information can be measured using interferometry or holography techniques [Atlan 2008, Liebling 2004], by acquiring at least three images, with dif-

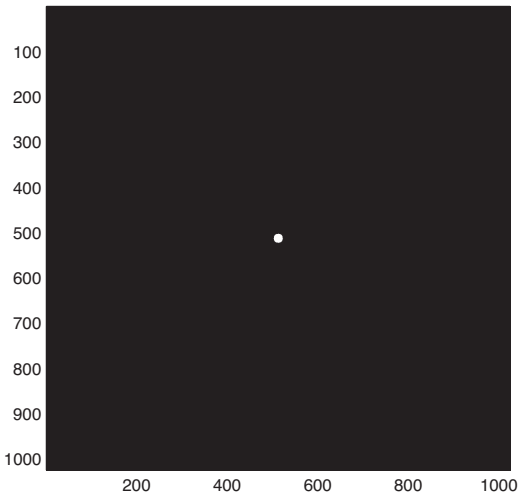

(a) Circular Aperture

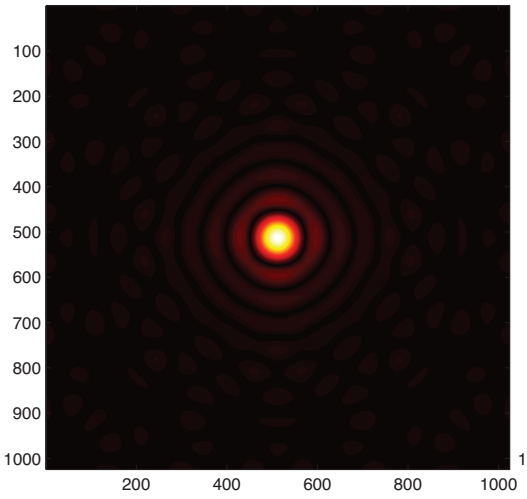

(b) Diffraction Pattern

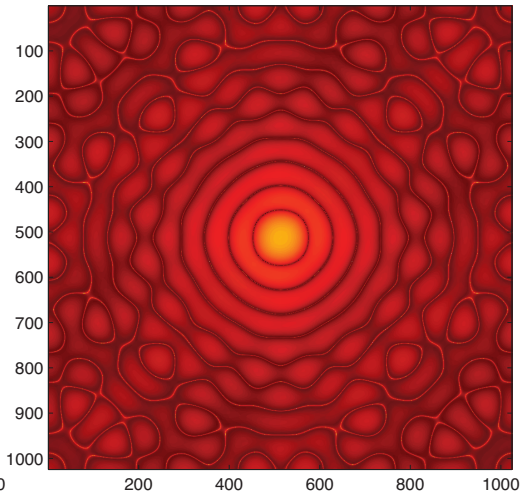

(c) Logarithmic Diffraction Pattern

Figure 4.1: Example of diffraction phenomenon at a circular aperture.

ferent phase-shifts and combining them to finally extract the phase [Goodman 1996]. Some numerical methods to achieve phase retrieval (PR) given just the magnitude of a Fourier transform of an object [Fienup 1982, Liebling 2003] were also investigated. A CS phase retrieval (CSPR) method based on incomplete magnitude measurements and ℓ_1-norm constraint has been proposed in [Moravec 2007]. However, this CSPR method requires a ℓ_1-norm constraint, which is not constant for microscopy image sequences.

Measuring a complex-valued signal such as $X = A(\omega, \nu)e^{j\phi(\omega,\nu)}$ with real-valued

sensors which are only able to measure the magnitude $A(\omega,\nu)^2$ is a challenge for many imaging systems such as wavefront sensing and interferometry. Indeed, the phase of the signal is as important as the amplitude. Recovering a spatial signal from its Fourier magnitude-only measurements is an ill-posed problem which is impossible to solve without some additional constraints on the spatial signal. As discussed in [Moravec 2007], phase retrieval constraints can involve positivity, explicit support, histogram shape, or sparsity.

In this chapter we present a method to interpolate the missing Fourier phase information between a subset of keyframes. For microscopy image sequences with high frame rates, we show that optical Fourier magnitude measurements combined with interpolated phase data are appropriate for CS recovery. Phase interpolation is adequate for high frame-rate images, since successive images present only small differences due to local motions of cells and show overall large redundancy.

We will first illustrate some results that demonstrate the potential of CS acquisition in microscopy. We then discuss the specific issues related to missing phase information in optical Fourier acquisitions. Finally, we detail our proposed computational framework to replace the missing phase information in the context of dynamic microscopy imaging.

4.2 Displacements and Phase

Suppose we have an initial image $x(a,b)$ with a single object as illustrated in Fig. 4.2. If the object is translated within the field of view, the phase of the Fourier transform $X(\omega,\nu)$ of the image is linearly shifted proportionally to the amplitude of the translation. The shift theorem from the Fourier transform properties, applied to a two-dimensional signal stats that a spatial displacement $\sqrt{\Delta_a^2+\Delta_b^2}$ produces a phase variation of [Goodman 1996]:

$$\begin{aligned} x(a,b) &\rightarrow X(\omega,\nu) \\ x(a-\Delta_a, b-\Delta_b) &\rightarrow e^{-2\pi i(\Delta_a\omega+\Delta_b\nu)}X(\omega,\nu) \end{aligned} \tag{4.1}$$

If we are able to estimate Δ_a and Δ_b (i.e. the amplitude of the displacement in each direction a and b), we can also estimate the Fourier phase variation. Unfortunately, in microscopy images, several objects move simultaneously and in different

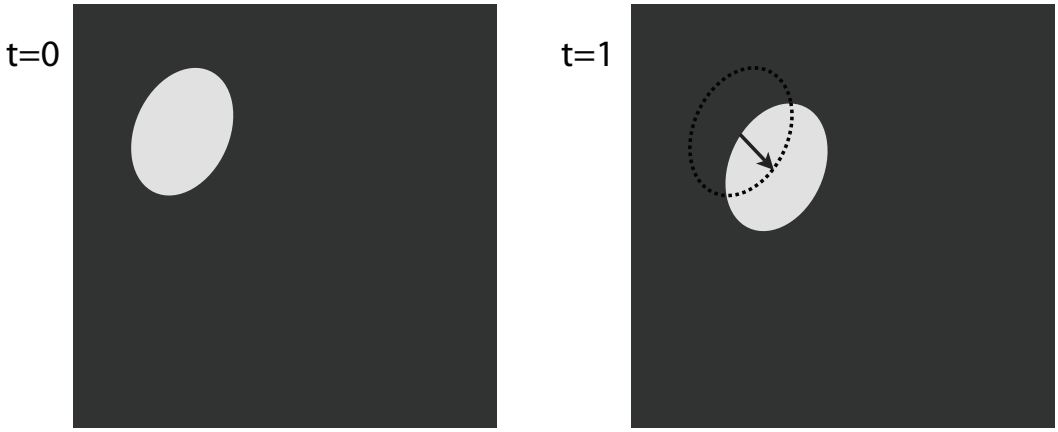

Figure 4.2: Object movement on an image sequence.

directions, so that simple phase correction can become difficult.

The phase variation between two consecutive frames depends on the moving objects and the amplitude of their displacement. A cell image can be considered as a linear combination of independent images. Suppose an image composed by a background and one simple object $x_t(a,b) = p(a,b) + o(a,b)$ the Fourier transform at the instant t is:

$$\begin{aligned} X(\omega,\nu) &= \mathcal{F}\{p(a,b)\} + \mathcal{F}\{o(a,b)\} \\ &= P(\omega,\nu) + O(\omega,\nu) \end{aligned} \tag{4.2}$$

Suppose that at the time $t+1$ the object $o(a,b) \in \mathbb{R}^2$ presents the same structures but shifted and that $p(a,b) \in \mathbb{R}^2$ is invariant. If we are able to estimate Δ_a and Δ_b, which corresponds to the shift of $o(a,b)$ in each direction a and b, then through the linearity of the Fourier transform we have:

$$\begin{aligned} X_{t+1}(\omega,\nu) &= \mathcal{F}\{p(a,b)\} + \mathcal{F}\{o(a-\Delta_a, b-\Delta_b)\} \\ &= P(\omega,\nu) + O(\omega,\nu)e^{-j2\pi(\Delta_a\omega+\Delta_b\nu)} \end{aligned} \tag{4.3}$$

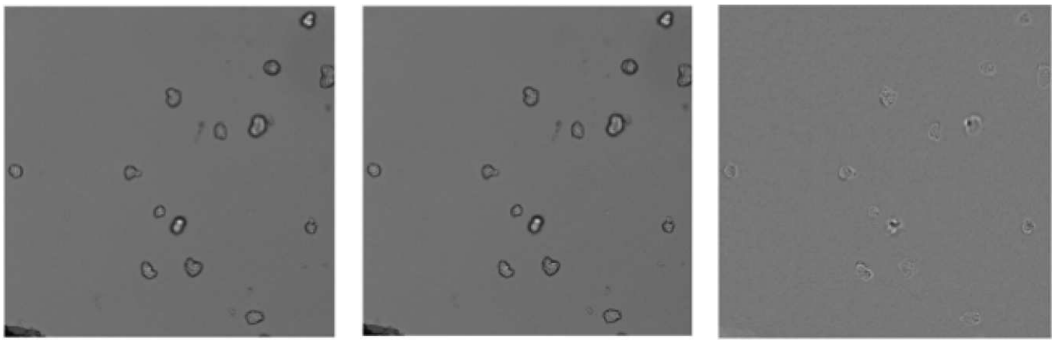

Figure 4.3: Image sequence, $t = 0$ (a) and $t = 1$ (b) and global movement (c) computed as the difference of pixels intensities between the two consecutive frames.

Then we can estimate the Fourier transform variation $\mathcal{G}_\varphi$ from (4.2) and (4.3):

$$\begin{aligned}
\mathcal{G}_\varphi &= \frac{X_{t+1}(\omega,\nu) - X_t(\omega,\nu)}{X_t(\omega,\nu)} \\
\mathcal{G}_\varphi &= \frac{P(\omega,\nu) + O(\omega,\nu)e^{-j2\pi(\Delta_a\omega+\Delta_b\nu)} - (P(\omega,\nu) + O(\omega,\nu))}{P(\omega,\nu) + O(\omega,\nu)} \\
\mathcal{G}_\varphi &= \frac{P(\omega,\nu) + O(\omega,\nu)e^{-j2\pi(\Delta_a\omega+\Delta_b\nu)}}{P(\omega,\nu) + O(\omega,\nu)} - 1
\end{aligned} \tag{4.4}$$

For high frame rate acquisition object displacements Δ_a and Δ_b are probably small compared to the image size. Accordingly, from Equation (4.4), if $\Delta_a \to 0$ and $\Delta_b \to 0$ the phase shift term $e^{-j2\pi(\Delta_a\omega+\Delta_b\nu)} \to 1$ and then $\mathcal{G}_\varphi \to 0$, which means that if displacements are small enough between consecutive frames the global phase variation $\mathcal{G}_\varphi \approx 0$.

To assess the validity of this assumption in dynamic microscopy imaging, we can look at two consecutive frames of an image sequence (Fig. 4.3a 4.3b). The global spatial movement can be computed as the difference of intensities between the image at $t = 0$ and the image at $t = 1$ (Fig. 4.3b). In Fig. 4.3c, which shows the phase difference between two consecutive frames, we can see that the global amplitude of the movements are very small between two consecutive frames. In Fig. 4.4c we show variations of the Fourier phases between these two frames. We can also see in Fig. 4.4 that most important changes in the Fourier phase data corresponds to the middle and high frequencies, which correspond essentially to noise information. It can also be observed in figure 4.4(d) which corresponds to the profile of a line

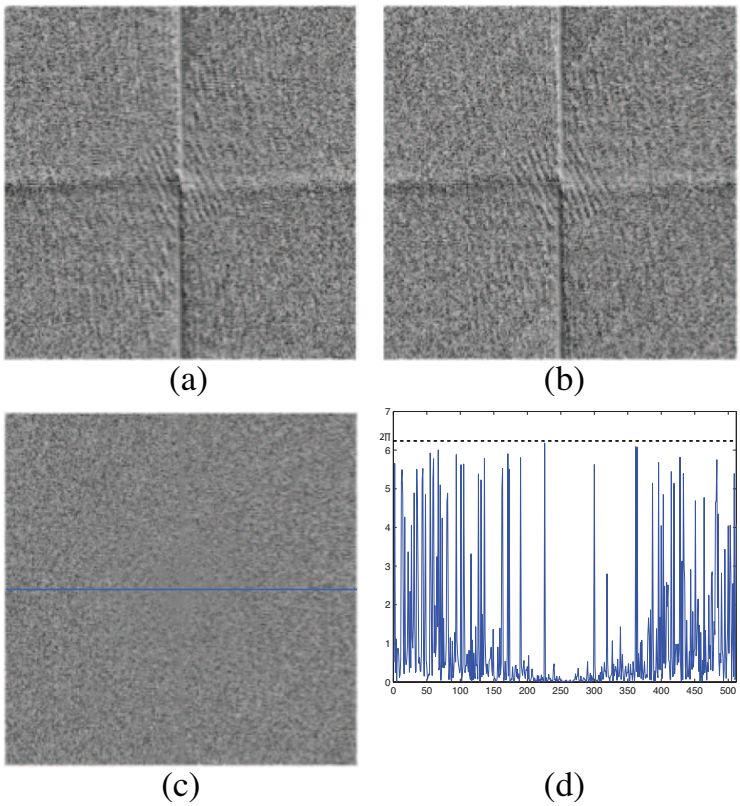

Figure 4.4: Fourier phases from frames (a) $t = 0$ (b) $t = 1$ and (c) the difference between the phases of the two consecutive frames (d) and a profile for a line passing through the center of the image in (c).

passing through the middle of the image 4.4(c).

4.3 Fourier Phase Estimation

As discussed in the introduction, to recover the original signal using CS we need both Fourier amplitude and phase information. Now, we consider that we are able to make M random measures of the Fourier amplitude at Δt intervals. We also assume that we acquire full keyframes each Δk frames of the sequence, with $K\Delta t < \Delta k$. Keyframes are used to limit the error propagation in the image sequence recovery, as illustrated in Section 4.5. Keyframes will also allow a linear Fourier phase interpolation between acquired keyframes. Each reconstruction exploits M amplitude measurements of Fourier coefficients and M corresponding phase values, estimated by interpolation of the phase between keyframes. This means that we propose an offline reconstruction of multiple frames between the keyframes which are fully acquired.

Given two keyframes $x_{\Delta k}(a,b)$ and $x_{2\Delta k}(a,b)$, with corresponding Fourier transforms $\mathcal{F}\{x_{\Delta k}(a,b)\} = X_{\Delta k}(\omega,\nu)$ and $\mathcal{F}\{x_{2\Delta k}(a,b)\} = X_{2\Delta k}(\omega,\nu)$, we make two hypothesis:

Hypothesis 1

The motion of objects from images $x_{\Delta k}(a,b)$ and $x_{2\Delta k}(a,b)$ induce a global linear shift of (Δ_a, Δ_b). This implicitly assures a global motion of all objects in one direction with constant speed from Δk to $2\Delta k$. Then, from the theorem (4.1):

$$X_{2\Delta k}(\omega,\nu) = X_{\Delta k}(\omega,\nu)e^{-2\pi i(\Delta_a\omega+\Delta_b\nu)}$$

Hypothesis 2

The shift (Δ_a, Δ_b) is derived from regular incremental displacements between frames $x_{\Delta k+j\Delta t}(a,b)$ and $x_{\Delta k+(j+1)\Delta t}(a,b)$ of amplitude $(\Delta_a/K+1, \Delta_b/K+1)$, for $j = 0,1,...,K-1$, $\Delta k + (K+1)\Delta t = 2\Delta k$ and $\Delta t = \frac{\Delta k}{K+1}$.

Then, the Fourier transform of a generic frame $x_{\Delta k+t}(a,b)$ for $0 < t < \Delta k$ can be

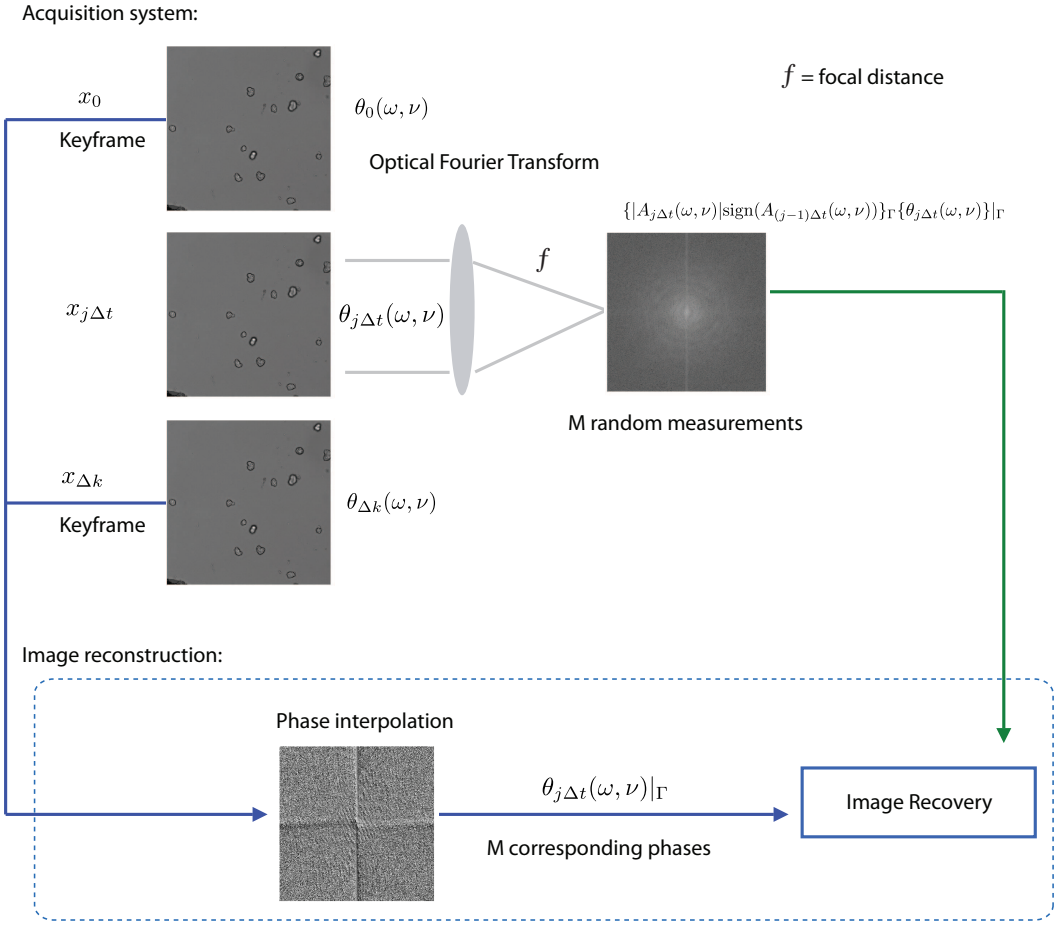

Figure 4.5: Recovery algorithm and acquisition system.

estimated with the following linear interpolation:

$$\begin{aligned}\mathcal{F}\{x_{\Delta k+j\Delta t}(a,b)\} &= \mathcal{F}\{x_{\Delta k}(a,b)\}e^{\frac{j}{K+1}\ln\{\frac{\mathcal{F}\{x_{\Delta k}(a,b)\}}{\mathcal{F}\{x_{2\Delta k}(a,b)\}}\}}\\ X_{\Delta k+j\Delta t}(\omega,\nu) &= X_{\Delta k}(\omega,\nu)e^{\frac{j}{K+1}\ln\{\frac{X_{\Delta k}(\omega,\nu)}{X_{2\Delta k}(\omega,\nu)}\}}\end{aligned} \tag{4.5}$$

and an estimation of the Fourier phase at a general $\Delta k + j\Delta t$ can be computed as:

$$\begin{aligned}\hat{\theta}_{\Delta k+j\Delta t}(\omega,\nu) &= \angle A_{\Delta k}(\omega,\nu)e^{i\theta_{\Delta k}(\omega,\nu)}e^{\frac{\Delta k+j\Delta t}{2\Delta k}\ln\{\frac{\mathcal{F}\{x_{\Delta k}(a,b)\}}{\mathcal{F}\{x_{2\Delta k}(a,b)\}}\}}\\ \hat{\theta}_{\Delta k+j\Delta t}(\omega,\nu) &= \theta_{\Delta k}(\omega,\nu)+\frac{\Delta k+j\Delta t}{2\Delta k}\ln\left\{\frac{A_{\Delta k}(\omega,\nu)e^{i\theta_{\Delta k}(\omega,\nu)}}{A_{2\Delta k}(\omega,\nu)e^{i\theta_{2\Delta k}(\omega,\nu)}}\right\}\end{aligned} \tag{4.6}$$

4.4 Image Reconstruction and Algorithm

The general image reconstruction formulation for uncompleted Fourier measurements and TV sparsity constraints is given by:

$$\hat{x} = \min_{x \in \mathbb{R}^N} \| x \|_{TV} \text{ s.t. } \| y - \Phi x \|_{\ell_2} \leq \delta \tag{4.7}$$

where $y \in \mathbb{C}^M$ are the Fourier measurements and each coefficient can be expressed in the form $A(\omega, \nu)e^{i\theta(\omega,\nu)}$.

We define Φ as a linear operator which selects uniformly a random subset of Fourier coefficients. In other words, $\Phi x(a, b)$ corresponds to sample a subset Γ of all Fourier coefficients $X(\omega, \nu)$, such as $\Phi x(a, b) = X(\omega, \nu)|_\Gamma$

Consider the case where $A(\omega, \nu)$ and $\theta(\omega, \nu)$ can be computed when a keyframe $x_{\Delta k}(a, b)$ is acquired and that only an incomplete set of magnitudes $A(\omega, \nu)^2|_\Gamma$ are acquired between two keyframes. The goal is to reconstruct $x(a, b)$ from $y(\omega, \nu) = \Phi\ x(a, b)$ where $y(\omega, \nu)$ is described in the next subsection.

Performing Amplitude Measurements

The first image and keyframes are fully acquired (each Δk frames) in the direct spatial domain such that we know exactly the image $x_{u\Delta k}(a, b)$ for $u = \{0, 1, 2...\}$. From the keyframes we extract:

- Fully acquisition of $x_{u\Delta k}(a, b)$.
- Compute the Fourier transform $X_{u\Delta k}(\omega, \nu)$.
- Extract from each complex Fourier coefficient $A(\omega, \nu)e^{i\theta(\omega,\nu)}$ the amplitude $A_{u\Delta k}$ and the phase $\theta_{u\Delta k}$,

$$A_{u\Delta k} = \sqrt{\text{Re}\{X_{u\Delta k}\}^2 + \text{Im}\{X_{u\Delta k}\}^2} \tag{4.8}$$

$$\theta_{u\Delta k} = \arctan\left\{\frac{\text{Im}\{X_{u\Delta k}\}}{\text{Re}\{X_{u\Delta k}\}}\right\} \tag{4.9}$$

Combining With Phase Estimation

The images between keyframes are acquired with a different scheme. In a simulated framework, the camera would be placed in the optical Fourier domain acquiring ran-

dom and incomplete measurements, corresponding to the magnitude of the Fourier coefficients A^2. Note that measuring A^2 the sign of A is lost. We suppose that the sign difference frame-to-frame is small, so that the signs of $A_{\Delta k+j\Delta t}$ are taken from $A_{\Delta k}$. For example, supposing that the image $x_{\Delta k}$ is well acquired, we estimate $x_{\Delta k+j\Delta t}$ by following the steps above:

- Acquisition of random sets of magnitude of Fourier coefficients, $A^2_{\Delta k+j\Delta t}$.
- Include the sign information from the last frame $A_{\Delta k+j\Delta t} = A_{\Delta k+j\Delta t} \cdot \text{sign}(A_{\Delta k+(j-1)\Delta t})$. We suppose that for high frame-rate images the sign of $A_{\Delta k}$ is a good estimation for the sign of $A_{\Delta k+j\Delta t}$.
- Include the interpolated phase information $\hat{\theta}_{\Delta k+j\Delta t}$ from (4.6).
- Define the measure:

$$y_{\Delta k+j\Delta t}(\omega,\nu) = \{|A_{\Delta k+j\Delta t}(\omega,\nu)| \cdot \text{sign}(A_{\Delta k+(j-1)\Delta t}(\omega,\nu))e^{i\hat{\theta}_{\Delta k+j\Delta t}(\omega,\nu)}\}|_\Gamma \tag{4.10}$$

- And finally, solve the problem:

$$\hat{x}_{\Delta k+j\Delta t} = \min_{x\in\mathbb{R}^N} \| x \|_{TV} \quad \text{s.t.} \quad \| y_{\Delta k+j\Delta t} - \Phi x \|_{\ell_2} \leq \delta \tag{4.11}$$

In our implementation, the problem (4.11) was solved by modifying the ℓ_1-magic toolbox (see modifications in table 4.1) proposed by Candès and Romberg and which can be found in http://www.acm.caltech.edu/l1magic/. The ℓ_1-magic toolbox was proposed in [Candès 2006c, Candès 2006e, Candès 2005c, Candès 2005d, Candès 2005e, Candès 2004a]. It solves the problem (4.11) by recasting it as second-order cone program (SOCP) in the form:

$$\begin{aligned} \min \sum t \quad \text{s.t.} \qquad & \| \Psi_{ij} x \|_2 \leq t, \quad i,j = 1,2,...,n \\ & \| \Phi x - y_t \|_2 \leq \delta \end{aligned} \tag{4.12}$$

Then, the SOCP is solved with a generic log-barrier algorithm following the implementation in [Boyd 2004]. The bottleneck of this solver is the calculation of

ℓ_1-magic	ℓ_1-modified
Perform random Fourier measurements:	
$y = \Phi x(a, b)$	$y_{\Delta k+j\Delta t} = \{\lvert A_{\Delta k+j\Delta t}\rvert \cdot \text{sign}(A_{\Delta k+(j-1)\Delta t}) e^{i\hat{\theta}_{\Delta k+j\Delta t}}\}\rvert_\Gamma$
Recast as a SOCP (4.12)	
Iterations of a log-barrier algorithm [Boyd 2004]	
Iterations of a Newton algorithm for log-barrier subproblems	
Solve a symmetric positive definite system $\Phi x = y$ via conjugate gradients (CG)	
Compute residual in CG: $r = y - \Phi x$;	Compute residual in CG: $r_A = y_A - \sqrt{\{\Phi x\}^2}$; $r_\theta = y_\theta - \angle \Phi x \lvert \text{mod}(\pi)$; $r = \alpha r_A + \beta r_\theta$; % for $\alpha > \beta$

Update criteria in CG:
if ($r <$ best_residual) **then**
best_x $\leftarrow \hat{x}$
best_residual $\leftarrow r$
end if	

Table 4.1: Modifications of the ℓ_1-magic reconstruction.

the Newton step where conjugate gradient (CG) iterates are used to approximately solve the system.

4.4.1 Algorithm Adaptation

In order to account for the fact that the phase values $\theta(\omega, \nu)$ are interpolated between keyframes while the amplitude values $A(\omega, \nu)$ are measured with a camera, we propose to weight differently their respective contribution in the data fidelity term of the reconstruction algorithm: For this purpose we have proposed a slightly modified algorithm to solve the problem (4.11). The modifications are detailed in Table 4.1.

4.5 Results and Error Propagation

Figure 4.7 illustrate the CS reconstruction results for a phase contrast microscopy sequence of 140 frames (228 $\times$ 228 pixels per frame, 14 keyframes and $\Delta k = 10$ frames). The recovery algorithm used only 5% of Fourier magnitude measurements and the full acquisition of one keyframe every 10 frames to interpolate the Fourier phase. As expected, phase estimation between keyframes introduces some recovery error. We use the Mean Squared Error (MSE) to estimate the recovery error, which

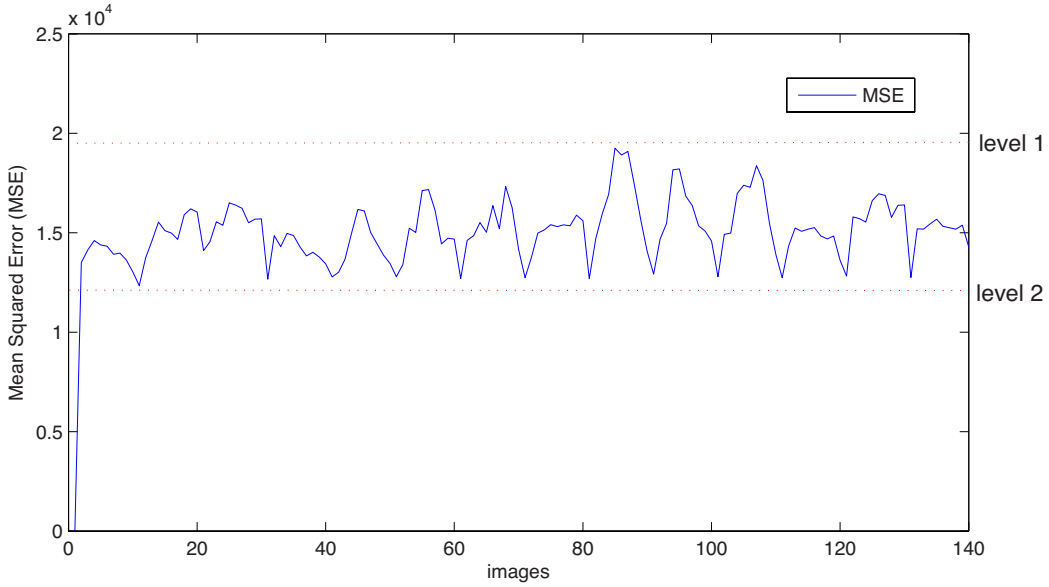

Figure 4.6: MSE propagation for the CS reconstructed image in Fig. 4.7.

is computed for each time $\Delta k + j\Delta t$ as:

$$\mathrm{MSE}_{\Delta k+j\Delta t} = \frac{1}{AB}\sum_{a=1}^{A}\sum_{b=1}^{B}\{\hat{x}_{\Delta k+j\Delta t}(a,b) - x_{\Delta k+j\Delta t}(a,b)\}^2 \tag{4.13}$$

where A and B are the width and the height of the image, $\hat{x}_{\Delta k+j\Delta t}(a,b)$ is the CS reconstructed image at $\Delta k + j\Delta t$ and $x_{\Delta k+j\Delta t}(a,b)$ the original image at $\Delta k + j\Delta t$.

In the Fig. 4.6 we can clearly identify two error bounds, level 1 and level 2. Level 1 corresponds to the maximum error introduced by the phase estimation, before it is reset when a keyframe is acquired. Level 2 corresponds to the residual error due to the CS regularization effect induced by the TV minimization, resulting in denoising. Both phase estimation errors and denoising effects can also be observed in Fig. 4.7 (bottom), which illustrates the residuals from each reconstruction.

4.6 Conclusion

In this chapter a CS-based dynamic image acquisition and recovery method was introduced combining Fourier magnitude measurements and Fourier phase estimation. We presented simulation results for a microscopy image sequence reconstruction demonstrating that our approach has several advantages over traditional acquisi-

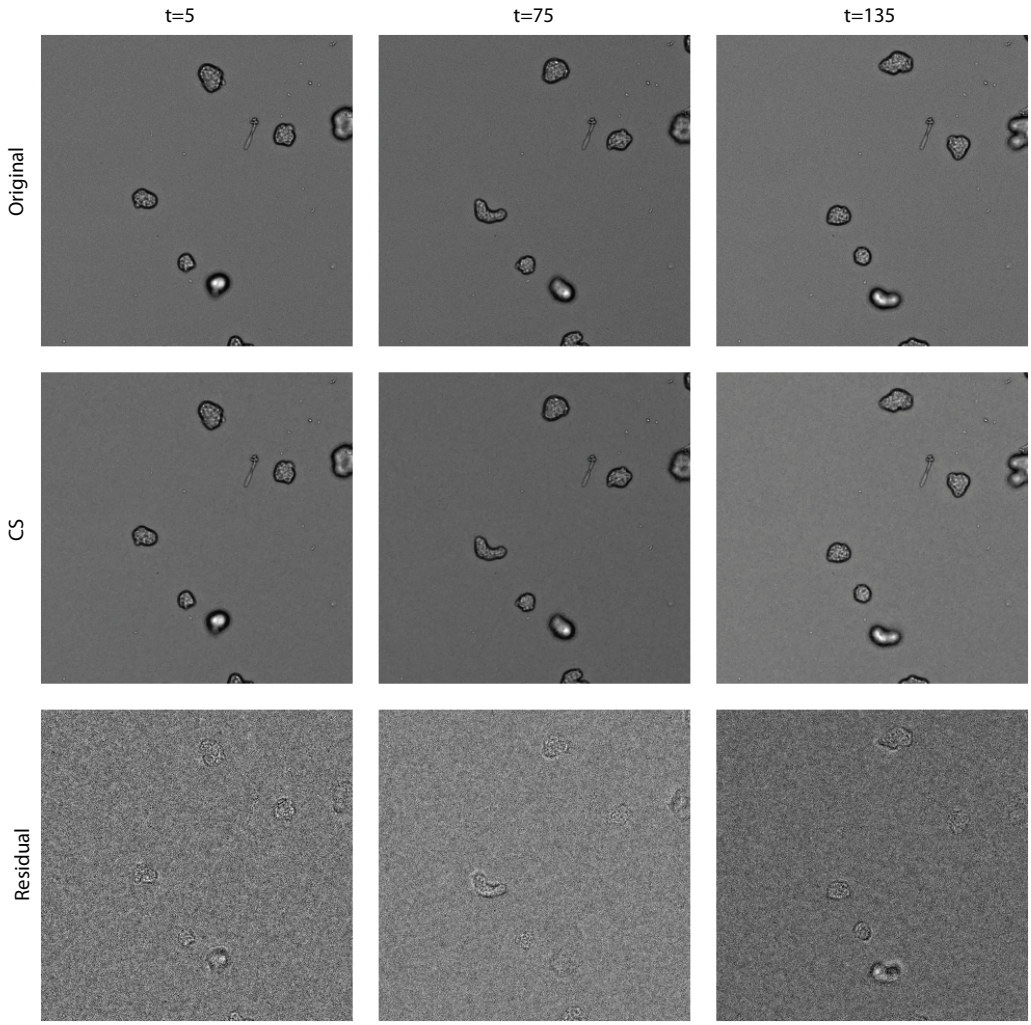

Figure 4.7: Top: Phase contrast microscopy image sequence of amebas, $x_{\Delta k+j\Delta t}$ at $\Delta k + j\Delta t = \{5, 75, 135\}$, $\Delta k = 10$. Middle: CS reconstructions $\hat{x}_{\Delta k+j\Delta t}$ with 5% of measurements ($M = 5\%N$). Bottom: Residual $\| \hat{x}_{\Delta k+j\Delta t} - x_{\Delta k+j\Delta t} \|_{\ell_2}$.

tion methods, since it can under-sample, recover and denoise images simultaneously. Our approach is limited to reconstruct microscopy image sequences with high frame rates, skipping Fourier phase measurements and opening the door to new microscopy acquisition schemes.

The approach is very difficult to implement in practice, the setup should be able to switch from the acquisition of a keyframe in the spatial domain and the acquisition in the Fourier domain. This could be obtained by creating two different optical pathways which is possible by using a beam splitter, one path for the acquisition in the spatial domain and the second path for the acquisition in the Fourier domain.

The work presented here incited us to find a practical acquisition scheme to test compressed sensing imaging using real Fourier-based measures. Therefore, we have worked on compressed holographic microscopy where the measurement process is based on off-axis digital holography. Digital holographic microscopy (DHM) enables to achieve measurements in the Fresnel domain and most important, it allows to measure not only the amplitude but also the phase of a complex signal (e.g. frequency coefficients). The main results on compressed sensing for DHM are presented in chapters 5 and 6.

Chapter 5

Compressed Digital Holographic Microscopy

This chapter reports an experimental microscopy acquisition scheme successfully combining compressed sensing imaging (CSI) and digital holography acquisition in off-axis and frequency-shifting conditions. Our approach combines a total variation minimization algorithm to reconstruct the image and digital holography to perform quadrature-resolved random measurements of an optical field in a diffraction plane. We show that digital microscopic holography is suited for compressed sensing since measurements are naturally taken as linear frequency-based projections of the original scene. We detail a CS-based imaging scheme for sparse images, acquiring a diffraction map of the optical field with holographic microscopy and measuring the signal from as little as 7% of measurements. We also demonstrate with practical experiments on holographic microscopy images of the USAF target (U.S. air force target) and of cerebral blood flow that our CS approach enables reconstruction from a very limited number of measurements while being robust to high noise levels. The results demonstrate how CS can lead to an elegant and effective way to reconstruct images, opening the door for new microscopy applications. The work presented here and in chapter 6 are joint works with the research team from the ESPCI ParisTech, headed by Michael Atlan.

Contents

5.1 Introduction 106

5.2 An Overview of Digital Holographic Microscopy 107

5.2.1 Digital Holography Principles 108

5.2.2 Inline or Off-Axis Holography 109

[0]Based upon: M. Marim, M. Atlan, E. Angelini and J.-C. Olivo-Marin. *"Compressed sensing with off-axis frequency-shifting holography"*, Optics Letters, vol. 35, pp. 871-873, 2010. M. Marim, M. Atlan, E. Angelini and J.-C. Olivo-Marin. *"Compressed Sensing for Digital Holographic Microscopy"*, IEEE International Symposium on Biomedical Imaging, ISBI, 2010.

5.2.3 Image Reconstruction from the Hologram 111
5.2.4 From Fresnel to Fourier Domains 113
5.3 Coupling DHM With Compressed Sensing 114
5.3.1 CS Reconstruction from Fresnel Measurements 115
5.3.2 Incoherent Sampling of Hologram Coefficients 117
5.4 Experiments and Results 119
5.4.1 Compressed DHM Setup for USAF Imaging 120
5.4.2 USAF Image Reconstruction 121
5.4.3 Compressed DHM Setup for Biological Imaging 121
5.4.4 Biological Image Reconstruction 123
5.4.5 Effect of Undersampling on CS Reconstructions 125
5.5 Conclusion 125

5.1 Introduction

Digital holographic microscopy (DHM) provides quantitative phase contrast imaging, high resolution via non-destructivity and multi-focus representation of microscopic specimens [Gross 2007]. In biology, this technique is suitable for marker-free analysis of living cells.

Holography presents several advantages over traditional imaging techniques providing high resolution three-dimensional recording of an object from a limited perspective, an image display that may be viewed from a variety of angles, a precise quantitative reproduction of the object being imaged and a translucent image that allows the viewer to both visualize deep and superficial structures simultaneously [Gross 2007]. In addition, it is a non-invasive technique, avoiding photo-toxicity contrary to fluorescence imaging techniques. This is an active field of research for biological imaging applications [Aizu 1999, Atlan 2006, Rappaz 2005].

This chapter addresses the sensing problem in DHM by increasing the detection throughput via the concept of an actual compressed sensing implementation. This method is image-content independent and does not need any feedback loop during the acquisition. The main idea presented here is to combine off-axis, frequency-shifting (for accurate phase-shifting) digital holographic microscopy [Atlan 2007] to perform quadrature-resolved random measurements of an optical field in a diffraction

plane and the use of a total variation minimization algorithm to reconstruct the image.

5.2 An Overview of Digital Holographic Microscopy

In this section we briefly discuss the main principles of holography and underline two different types of holography acquisition. Holography is an imaging technique initially proposed by Dennis Gabor in 1948 [Gabor 1948]. It can be defined as a two-step lensless imaging process which requires a wavefront reconstruction. Gabor discovered that by combining a reference light-coherent wave with the diffracted or scattered wave from an object, it was possible to record both the amplitude and the phase of the diffracted wavefront. In spite of the fact that the recording media (holographic film or digital sensors) can only measure light intensities, the amplitude and phase information can be measured with holography. In figure 5.1 we illustrated the classic Gabor inline setup for holographic imaging. The term digital holography (DH) specifies that the hologram is acquired with a digital sensor like a CCD or CMOS camera.

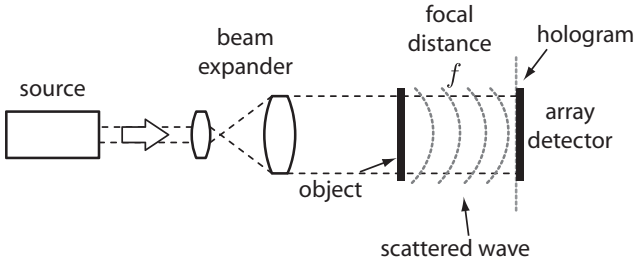

Figure 5.1: A general setup of inline holography imaging.

There are two basic types of diffraction situations, the near-field and far-field diffraction depending on the distance between the object and the observation planes. These two types of diffraction are called Fresnel and Fraunhofer diffraction respectively. The Fraunhofer diffraction pattern is mathematically identical to the Fourier transform, within certain approximations, thus we will refer to Fraunhofer holography as Fourier holography. For a Fourier hologram the light from each point on the object interferes with the reference beam, which is assumed to be planar, to create a sinusoidal fringe with a vectorial spatial frequency that is unique to that object point.

The Fresnel or "near-field" diffraction occurs when a wave passes through an aperture and diffracts in the near field, in this case waves are spherical. The diffraction pattern depends on the distance between the object and the detection planes. When the distance between the two planes increases, outgoing diffracted waves become planar and Fourier or "far-field" diffraction occurs.

The physical difference between a Fresnel and Fourier holographic setup relies in the average curvature difference between the reference and the object waves, hence, the distance between the object plane and the acquisition plane. For both cases, the acquisition plane contains frequency-based multiplexed information about the original object [Goodman 1996, Hildebrand 1970]. In the Fresnel case, the distance between the illuminated object plane and the acquisition plane is smaller than in the Fourier case. As a consequence the information is more spatially incoherent in the Fourier case than the Fresnel configuration. We will discuss later on how this will affect our CS-based image reconstruction, and why the Fourier case enables compressed sensing. In subsections 5.2.3.2 and 5.2.3.1 we detail more precisely the difference between Fresnel and Fourier diffraction with regards to holography.

5.2.1 Digital Holography Principles

In electromagnetic theory, the electromagnetic wave propagates such that both the magnetic field oscillations, and the electric field oscillations are perpendicular to the direction of the propagating waves. The electromagnetic wave transports energy like any wave and the total energy is shared between the electric and the magnetic field. In digital holography, we identify the electric field wave as the optical field.

The optical field which is measured in holography is the result of the interferences between the object field (signal of interest) and a reference optical field. The image of interest can then be computed in a post-processing step since the relation between the detected diffraction pattern and the object is known (via a Fourier or Fresnel transformation).

Consider that E_r and E_o are the reference and object optical fields respectively, a, b are the spatial coordinates and z is the traveled distance between the object and the camera (array detector in figure 5.2). The intensity distribution of the diffraction pattern (interferences between the reference wave and the object wave)

in the detection plane (measured by the CCD camera) corresponds to:

$$\begin{aligned} I(a,b,z) &= |E_o(a,b,z) + E_r(a,b,z)|^2 \\ &= |E_o(a,b,z)|^2 + |E_r(a,b,z)|^2 \\ &\quad + E_o(a,b,z)E_r^*(a,b,z) + E_r(a,b,z)E_o^*(a,b,z) \end{aligned} \tag{5.1}$$

where * represents the complex conjugate term.

The third and fourth conjugate terms are proportional to the object field and will generate virtual images of the object field, which are called twin-images. The superposing twin-images disturb the observation of the real object. The second term in equation (5.2) is called the zero-order intensity, which comes from the reference optical field. Similarly to the twin-images, the superposition of the zero-order intensity to the object intensity perturbs the observation of the real object.

5.2.2 Inline or Off-Axis Holography

Since the invention of holography by Gabor in 1948, removal of the unwanted twin-images has remained a persistent area of research [Goodman 1996]. The results of Gabor's original in-line experiment (see figure 5.1) were marred by the presence of the twin-image and the so called zero-order intensity terms [Gabor 1948].

Leith and Upatnieks suggested in 1962 an off-axis hologram setup, also called Leith-Upatnieks hologram. It is a modification of Gabor's original recording geometry that solved the twin-images problem [Leith 1972].

The major difference between inline and off-axis holography is that, rather than depending on the light directly transmitted by the object to serve as a reference wave, a separate reference wave is introduced (see figure 5.2). In addition, the reference is introduced with an offset angle, rather than being aligned with the propagation axis. The optical field measured by the array detector is used to compute the hologram which is linked to the object field by a Fourier or Fresnel transform depending on the setup.

To solve the zero-order intensity and the twin-images problem, a quadrature phase-shifting holography will be used in order to reconstruct the original complex object wave. This approach was first proposed by Gabor and Goss in the 1960s [Gabor 1966].

The initial optical field E is split and spread in two different paths, one passing

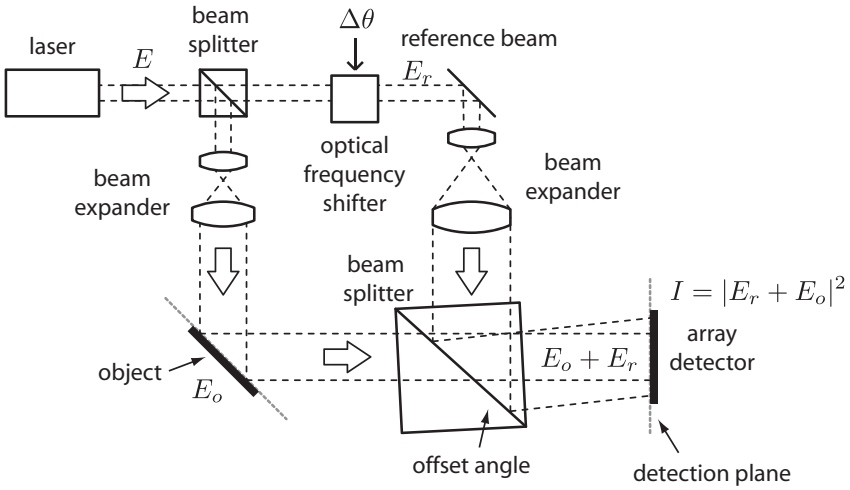

Figure 5.2: Off-axis holographic setup.

through the object creating the optical field E_o and the second which is the reference optical field E_r. The reference beam E_r is dynamically phase shifted with respect to the object field E_o. Four image acquisitions are performed while shifting the reference beam phase by $l\pi/2$ with $l = 0, 1, 2, 3$. This shift produces time-varying interferograms and the intensity $I(a, b, z)$ in the detector plane results from the interference of the object field with the $\Delta\theta$-shifted reference field:

$$I(a, b, z)_l = |E_o(a, b, z) + E_r(a, b, z)e^{2\pi i \Delta\theta_l}|^2 \tag{5.2}$$

where $\Delta\theta_l = l\pi/2$ and $l = 0, 1, .., L$, with $L = 4$.

Then, the object optical field E_o can be retrieved by demodulating I such as:

$$E_o(a, b, z) = \frac{1}{LE_r^*(a, b, z)} \sum_{l=0}^{L} I(a, b, z)_l e^{\frac{2\pi i l}{L}} \tag{5.3}$$

where E_r^* is the conjugate of E_r.

However, the equation (5.3) cannot be used directly since $E_r^*(a, b, z)$ is unknown. To reconstruct the original signal a complex hologram needs to be computed. For

$L = 4$ (i.e. 4 phases) the hologram is defined as:

$$\begin{aligned} H(a,b,z) &= \sum_{l=0}^{L-1}(i)^l I_l(a,b,z) \\ &= I_0(a,b,z) + iI_1(a,b,z) - I_2(a,b,z) - iI_3(a,b,z) \\ &= (I_0(a,b,z) - I_2(a,b,z)) + (I_1(a,b,z) - I_3(a,b,z))i \end{aligned} \tag{5.4}$$

where l is the image index and $i^2 = -1$. The hologram $H(a,b,z)$ is proportional to E_o (from Eq. (5.3)) and corresponds to the Fresnel transform of the image placed at $z = d$ from the camera (the object in figure 5.2). A simple image reconstruction when all coefficients of H are known consists in computing the inverse Fresnel transform.

Summarizing, for quadrature phase-shifting holography, two quadrature-phase holograms and two intensity values (namely the object field intensity and the reference field intensity) are needed.

5.2.3 Image Reconstruction from the Hologram

As discussed in the previous subsection, the image reconstruction from the total intensity field is performed in three steps: (1) compute the complex optical field from the real intensity measurements (equation (5.5)), (2) back-propagate the optical field H to the object plane and (3) the image reconstruction by multiplying the hologram H by a quadratic phase term $\exp\{\frac{i\pi}{\lambda z}a^2 + b^2\}$ which depends on the distance z between the object and the camera.

In Fourier holography the distance z between the object and the detection plane (without lens) is "assumed" infinite and the quadratic phase goes to zero; however in the Fresnel case, the distance z is finite and the quadratic phase is not insignificant. In the next two subsections we detail both cases and the respective image reconstructions process from the hologram $H(a,b,z)$.

5.2.3.1 Fresnel Hologram Case

For simplicity consider that $H(\omega,\nu,z)$ the hologram in the detector plane, and $E_o(a,b,0)$ the optical field in the object plane. In the Fresnel case the hologram and the object field are related by the Fresnel diffraction transformation which is quite

similar to the Fourier integral,

$$H(\omega,\nu,z)=\iint_{-\infty}^{\infty} E_o(a,b,0)\quad \underbrace{e^{\frac{i\pi}{\lambda z}(a^2+b^2)}}_{\text{quadratic phase}}\quad e^{-2\pi i(\omega a+\nu b)}da\ db \tag{5.5}$$

where λ is the coherent light wavelength.

The difference between the Fresnel integral and the Fourier integral is the quadratic phase factor $e^{\frac{\pi i}{\lambda z}(a^2+b^2)}$. The Fresnel transformation becomes a Fourier transformation if the distance z goes to infinity since the quadratic term tends to 1. In the Fresnel case the object is viewed as being the function $E_o(a,b,z)e^{\frac{\pi i}{\lambda z}(a^2+b^2)}$. The existence of a phase distribution across the object does not affect the intensity distribution, which allows us to have a good approximation of the bandwidth of the hologram.

In the next two chapters we will be interested in digital holographic microscopy, manipulating the discrete version of the hologram formation. Consider also square only images such that $n_a = n_b = n$. In the Fresnel digital holography, the hologram is linked to the optical field in the object plane via the following discrete transformation:

$$H[\omega,\nu,z]=\frac{1}{n}e^{-\frac{2\pi iz}{\lambda}}\sum_{a=0}^{n-1}\sum_{b=0}^{n-1}E_o[a,b,0]e^{-\frac{\pi i}{\lambda z}(a^2+b^2)}e^{-2\pi i\left(\frac{a\omega+b\nu}{n}\right)} \tag{5.6}$$

where λ is the coherent light wavelength and z is the distance between the detection and the object planes. In fact, (5.5) can be viewed as expressing the hologram field as the product of the quadratic-phase term and the Fourier transform of the modified object field. The difference between the Fresnel and the Fourier transforms lies entirely on the quadratic-phase factor, the Fresnel transform can also be computed with the fast Fourier transform (FFT) algorithm.

Finally, the object field amplitude can be estimated as:

$$\underbrace{E_o[a,b,0]}_{\text{image of interest}}=\frac{1}{n}e^{\frac{2\pi iz}{\lambda}}\sum_{\omega=0}^{n-1}\sum_{\nu=0}^{n-1}H[\omega,\nu,z]e^{\frac{\pi i}{\lambda z}(\omega^2+\nu^2)}e^{2\pi i\left(\frac{a\omega+b\nu}{n}\right)} \tag{5.7}$$

which is the general approach for DH image reconstruction when the complete hologram is known.

5.2.3.2 Fourier Hologram Case

The Fourier hologram can be obtained by using a fictitious lens of infinite size or without lens and placing the object and the detection plane at an infinite distance. The hologram field $H[\omega,\nu,z]$ and the object field are then related by a Fourier transform:

$$H[\omega,\nu] = \frac{1}{n}\sum_{a=0}^{n-1}\sum_{b=0}^{n-1} E_o[a,b]e^{-2\pi i\left(\frac{a\omega+b\nu}{n}\right)} \tag{5.8}$$

and, in this case, the image of the object can be estimated as:

$$\underbrace{E_o[a,b]}_{\text{image of interest}} = \frac{1}{n}\sum_{\omega=0}^{n-1}\sum_{\nu=0}^{n-1} H[\omega,\nu]e^{2\pi i\left(\frac{a\omega+b\nu}{n}\right)} \tag{5.9}$$

Note that, as described by the Whittaker-Shannon sampling theorem, the number of samples to be acquired in the detection plane depends on the bandwidth of the object field (object with fine details will require more samples, see 1.2.5).

5.2.4 From Fresnel to Fourier Domains

The radiation field propagates from the object to the detector plane in Fresnel diffraction conditions. Thus, the optical field in the object plane is linked to the field in the detector plane by a Fresnel transform, described in (5.6). The term $e^{\frac{i}{\lambda z}\pi(a^2+b^2)}$ is the quadratic phase factor describing the curvature in the detector plane of a wave emitted by a point source in the object plane.

In Figure 5.3 we illustrate how the curvature $c = e^{\frac{i\pi}{\lambda z}(a^2+b^2)}$ decreases as the object-detector distance z increases. The Fresnel diffraction occurs when $\pi(a^2+b^2)/\lambda z \geq 1$ and the Fourier diffraction occurs when $\pi(a^2+b^2)/\lambda z \ll 1$. In other words, when $z \to \infty$, then $e^{\frac{i\pi}{\lambda z}(a^2+b^2)} \to 1$, and hence the diffraction pattern described in (5.6) converges toward the Fourier transform. The Figure 5.3 illustrates the optical interpretation of spatial incoherence. Starting in the object plane the incoherence between $E_{z=0}$ and the field at inferior limit $E_{z=+0}$ is negligible. As the distance from the object increases, the diffraction pattern evolves toward the Fourier domain, and at the superior limit $z \to \infty$, the incoherence between the optical field $E_{z=0}$ and $E_{z=\infty}$ is maximal.

The object plane is the most coherent plane with the object image itself, and

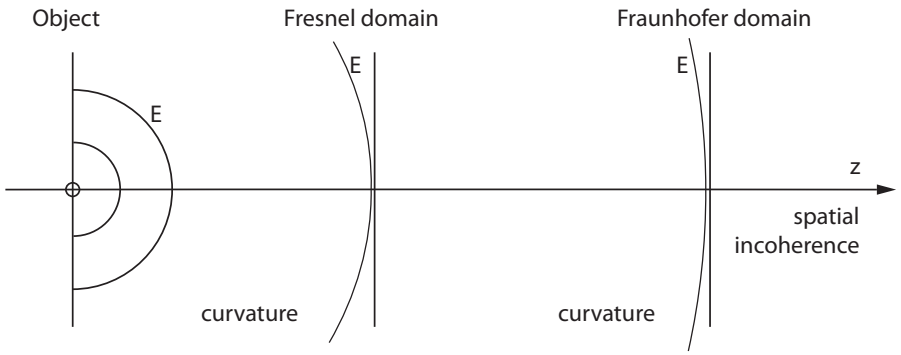

Figure 5.3: Radiation field propagation, from full coherence for a detector plane at $z = 0$ to complete incoherence at plane at $z \to \infty$. Fresnel and Fourier diffraction domains are defined according to the distance between the object and the detector plane.

the Fourier domain is the most incoherent plane. As illustrated in figure 5.3 the Fresnel domain is intermediate between a full coherence and a full incoherence to the object.

5.3 Coupling DHM With Compressed Sensing

In microscopy, several acquisition techniques allow to acquire high-resolution images with high frame-rates. However the acquisition of high-resolution images are time consuming and short acquisition time is required for dynamic screening. Digital holographic microscopy is a technique able to perform high-resolution imaging, yet limited by time consuming acquisitions setups. In this chapter we propose a method to address the sensing problem of DHM by using a compressed sensing approach.

In the previous sections we have introduced the basic principles of DHM and the conventional reconstruction scheme. In this section we describe our contribution which is to couple the compressed sensing framework to acquire and reconstruct DHM images. The main idea is to under-sample the Fresnel hologram and to use an algorithm based on the total variation minimization to reconstruct the image.

The classic image reconstruction in DHM with Fresnel measurements consists of back-propagating the optical field acquired by the camera to the object plane. It can be done by applying the inverse Fresnel transform described in (5.7). However if only a small number of Fresnel coefficients are acquired the image reconstruction is not possible using the classic scheme. We propose an image reconstruction algo-

rithm which follows a compressed sensing scheme with sparsity maximization and incomplete measurements as the data fidelity.

In other words, the incomplete linear measurements y correspond to incomplete coefficients of the hologram H, described in (5.6). Where the notation $y = \Phi E_o$ is equivalent to the selection of random coefficients of H. Thus, the optical field in the object plane E_o is linked to the field H in the detection plane by a Fresnel transform, expressed in the discrete case in (5.6). The signal reconstruction consists in solving an optimization problem that finds the candidate $\hat{E}_o$ (where $\hat{\cdot}$ denotes an estimator) of minimal complexity satisfying $y = \Phi E_o$ or $\| y - \Phi E_o \|_{\ell_2} \leq \delta$.

5.3.1 CS Reconstruction from Fresnel Measurements

We want to recover the intensity image of the object $E_o \in \mathbb{R}^N$ from a small number of measurements $y \in \mathbb{C}^M$ where $M \ll N$. Partial measurements in the detection plane, illustrated by the first step in Fig. 5.4, can be written as $y = \Phi E_o = H|_\Gamma$, where the sampling process ΦE_o represents a random undersampling with a uniform spatial distribution of H (the Fresnel transform of E_o). In other words, $y = H|_\Gamma$ corresponds to sample a subset Γ of all Fresnel coefficients H, such as $\Phi E_o = H|_\Gamma$. To find the best estimator $\hat{E}_o$ of the object of interest, we solve the following convex optimization problem [Candès 2006a]:

$$\hat{E}_o = \arg \min_{E_o \in \mathbb{R}^N} \| E_o \|_{TV} \quad \text{subject to} \quad y = \Phi E_o \tag{5.10}$$

This optimization leads to an iterative image reconstruction process, illustrated by the loop inside the dotted frame in Fig. 5.4. Explicitly, given a partial knowledge of the Fresnel coefficients $H|_\Gamma$, we seek a solution $\hat{E}_o$ with maximum sparsity (i.e. with minimal norm $\| E_o \|_{TV}$), and whose Fresnel coefficients $\hat{H}|_\Gamma$ match the observed subset $y = H|_\Gamma$ (as illustrated in Fig. 5.4). Since our test image is piecewise constant with relatively sharp edges (such as most microscopy images), it can be sparsely represented computing its gradient. In image processing, a suitable norm to constrain the gradient of an image was introduced as the Total Variation (TV) which approximates the ℓ_1 norm of the gradient magnitudes over the whole image:

$$\| E_o \|_{TV} = \sum_{a,b} \sqrt{\{E_o(a+1,b) - E_o(a,b)\}^2 + \{E_o(a,b+1) - E_o(a,b)\}^2} \tag{5.11}$$

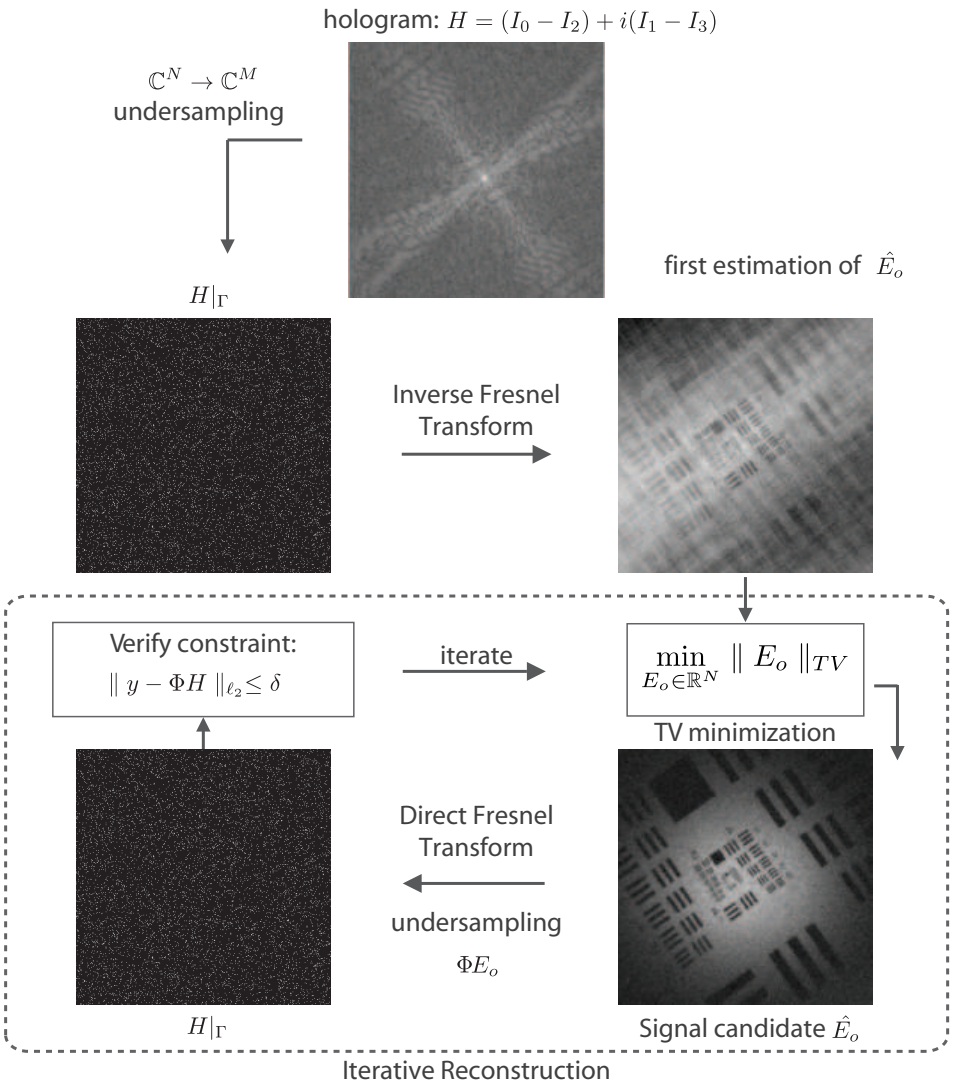

Figure 5.4: CS reconstruction scheme.

The incoherence property holds for the two basis adopted here, which are the Fresnel spectrum and the TV [Candès 2006b]. Moreover, uniform random measurements in the spectral domain satisfy the RIP condition [Candès 2008]. Hence for overwhelming percentage of Fresnel coefficients sets Γ with cardinality obeying $|\Gamma| = M \geq K \cdot S \log N$, for some constant K, for the sparsity S, for M measurements and a signal length N, the true object field $\hat{E}_o$ corresponds to:

$$\hat{E}_o = \arg \min_{E_o \in \mathbb{R}^N} \| E_o \|_{TV} \quad \text{subject to} \quad y = \Phi E_o \tag{5.12}$$

However, holographic measurements are corrupted with noise and the observed signal is not exactly sparse. In our experiments, the observations were described as noisy measurements $y = \Phi E_o + n$, where $n \in \mathbb{C}^M$ is a noise component with bounded energy $\| n \|_{\ell_2} \leq \varepsilon$. In this particular case, a better reconstruction can be achieved by relaxing the constraint $y = \Phi E_o$ and allowing an error δ at most proportional to the noise energy ε [Donoho 2006a]. Finally, solving the following problem performs the reconstruction of E_o with a controlled robustness to noise:

$$\hat{E_o} = \arg \min_{E_o \in \mathbb{R}^N} \| E_o \|_{TV} \quad \text{s.t.} \quad \| y - \Phi E_o \|_{\ell_2} \leq \delta \tag{5.13}$$

for some $\delta \leq C\varepsilon$, which depends on the noise energy.

5.3.2 Incoherent Sampling of Hologram Coefficients

The CS theory states that the design of the sampling process must enforce incoherence between the acquisition and the sparsity domains. This constraint has been formulated through several criteria, based on mutual coherence measures [Candès 2006b, Donoho 2006a], or matrix properties such as the *Restricted Isometry Property* (RIP, see section 1.3.2) conditions [Candès 2008].

Here the sampling process corresponds to linear projections of the signal in the Fresnel domain and the signal is sparse with respect to its total variation. For the Fresnel transform and for the Fourier transform, each projection contains global information about the whole signal. In our work we rely on the sufficient condition for the CS problem to be well conditioned, provided that ΦE_o must satisfies the RIP condition:

$$(1 - \delta_1)\| E_o \|_{\ell_2}^2 \leq \| \Phi E_o \|_{\ell_2}^2 \leq (1 + \delta_2)\| E_o \|_{\ell_2}^2 // (\delta_1, \delta_2) \in \mathbb{R}^+ \quad \text{and} \quad (\delta_1, \delta_2) \ll 1$$

This means that the sampling process ΦE_o must preserve the lengths of the signal of interest E_o. In [Candès 2008] it was shown that random acquisition in the Fourier domain, encoded by a matrix with 1s and 0s at random frequency locations verifies this incoherence property when combined with TV spatial constraints.

5.3.2.1 Reconstruction Algorithm

To solve the problem (5.13) we used NESTA, an algorithm proposed by Becker *et al.* in [Becker 2009] and discussed in subsection 1.3.3.2. NESTA is a first-order method for sparse recovery using an averaging of sequences of iterates to improve the convergence properties of standard gradient-descent algorithms. NESTA is based on the work of Nesterov [Nesterov 1983, Nesterov 2004, Nesterov 2005] which proposed smoothing techniques with improved gradient descent methods to derive first-order methods.

Becker *et al.* have extended nesterov's work to solve the compressed sensing problem. In [Becker 2009] the authors showed that NESTA algorithm can solve the total variation minimization with quadratic constraints such as:

$$\hat{x} = \arg\min_{x \in \mathbb{R}^N} \| x \|_{TV} \quad \text{s.t.} \quad \| y - \Phi x \|_{\ell_2} \leq \delta \tag{5.14}$$

with Φ modeling a uniform random undersampling in the Fourier domain. This is almost the same problem as (5.13) where the difference is the sampling domain.

The algorithm used to reconstruct the optical field in the object plane from holographic measurements (i.e. problem (5.13)) is an adaptation of NESTA. The main difference is that in our case the sampling domain is the Fresnel domain instead of Fourier. We note that similar to the Fourier sampling, the Fresnel sampling corresponds to a linear transformation. Other contributions to the algorithm such as a support constraint on the signal are explained in chapter 6.

5.3.2.2 Hermitian Symmetry

Based on the prior information that the signal to reconstruct is real, we can force the result from the Fourier transform to have the Hermitian symmetry. This can be obtained by restricting the sampling to the upper half-plane of the 2D Fourier transform. It can also be used to compress the signal since the even and odd parts are symmetric and then only one part needs to be measured. This method only concerns Fourier holography.

Definition A Hermitian matrix is a self-adjoint square matrix. For complex-valued matrices this means that the matrix is identical to its conjugate transpose. Two-dimensional discrete Fourier transforms of real-valued images provide Hermi-

NESTA	**Our approach**
Perform M random measurements y:	
$y = \Phi x$ $\Phi x \rightarrow$ models random undersampling in the Fourier domain $\Phi x \rightarrow$ linear transformation	$y = \Phi E_o$ $\Phi E_o \rightarrow$ models random undersampling in the Fresnel domain $\Phi E_o \rightarrow$ linear transformation
$\delta \rightarrow$ proportional to the noise on the Fourier coefficients	$\delta \rightarrow$ proportional to the noise on the Fresnel coefficients
$M \rightarrow$ depends on the mutual coherence of Fourier and TV	$M \rightarrow$ depends on the mutual coherence of Fresnel and TV.
solve the problem (5.14)	solve the problem (5.13)

Table 5.1: Main differences between NESTA and our approach.

tian matrices and are therefore entirely known with only half of the terms associated with the discrete frequencies used for the decomposition. This is a well known property largely exploited in several image processing algorithms. Such property can also be used to enforce the reconstruction of a real-valued image from a set of complex samples in the Fourier domain.

To force a Hermitian symmetry of the Fourier transform we can simply impose the even part to be the symmetric-conjugate of the odd part. This is exactly what is enforced on the data acquired with digital holographic microscopy. For all image reconstructions in this chapter we have forced the Fourier transform to have Hermitian symmetry, avoiding the acquisition of duplicate coefficients.

5.4 Experiments and Results

In this section we present two DHM setups used to acquire undersampled holograms. The optical setups were developed by the team of Michael Atlan from ESPCI ParisTech. We have tested the image reconstruction with a USAF target image placed in the object plane as described in figure 5.5. Then we have also modified the acquisition setup to place a mouse in the object plane and to observe the cerebral blood flow in-vivo. The setups were similar with some differences described in the following subsections.

5.4.1 Compressed DHM Setup for USAF Imaging

Taking into account the digital holographic principles we now present the DHM setup used to acquire the intensity images described in (5.2). The experimental

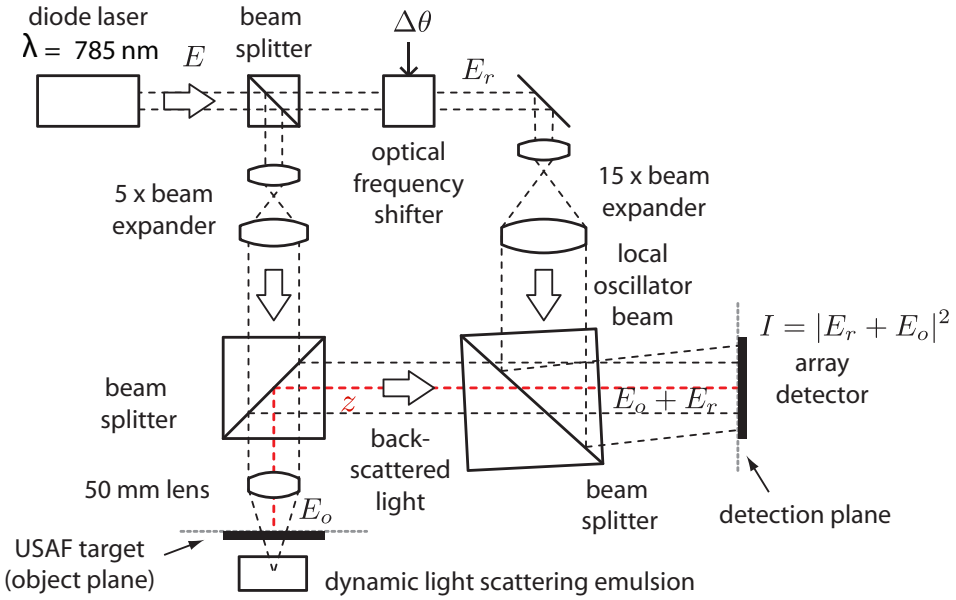

Figure 5.5: Sketch of the digital holographic microscopy experimental image acquisition setup.

DHM setup is sketched in Fig. 5.5. It consists of an off-axis, frequency-shifting digital holographic microscopy scheme [Atlan 2007, Gross 2007] such as described in subsection 5.2.1. The monochromatic optical field from a diode laser (dynamically backscattered by an intralipid emulsion) takes two paths i) one path illuminates an US Air Force (USAF) resolution target ii) one path beats against a separate local oscillator (LO) field detuned by $\Delta\theta/(2\pi) = 200\,\mathrm{Hz}$ and the two paths create a time-fluctuating interference pattern measured with a $N = 1024 \times 1024$ array detector. The diffracted object field map in the detector plane, resolved in quadrature (in amplitude and phase, see (5.2)) $H \in \mathbb{C}^N$ is calculated from a four-phase measurement [Atlan 2007] described in (5.5). The frequency detuning $\Delta\theta$ enables rejection of non fluctuating light components reflected by the target as well as noise reduction through signal accumulation.

The hologram H can be back-propagated numerically to the target plane with a inverse Fresnel transform when all measurements $H \in \mathbb{C}^N$ are available, as described in (5.6). By using the compressed sensing approach, the image can be reconstructed

by the method described in (5.13).

5.4.2 USAF Image Reconstruction

In Fig. 5.6 we illustrate some CS reconstruction results. A reconstruction of an off-axis image with the standard convolution method (eq. 5.7) is illustrated in Fig. 5.6a. The image reconstructed with holography uses all available measurements (4 phases $\times$ 10 accumulations $\times 1024^2 = 4.2 \times 10^7$ pixels). For the CS approach, Fresnel coefficients were undersampled randomly (after full acquisition by the CCD). Fig. 5.6b shows the CS reconstruction result from only 7% of the pixels used in the standard approach (4 phases $\times$ 10 accumulations $\times$ 0.07 $\times 1024^2 = 2.9 \times 10^6$ pixels). Fig. 5.6c illustrates the gradient of the image ∇E_o (sparsifying domain) and Fig. 5.6d illustrates the residual (Euclidean distance $|\hat{E}_o - E_o|$) from (a) the standard holographic reconstruction and (b) the CS reconstruction. The global normalized error is $\| \hat{E}_o - E_o \|_{\ell_2} = 0.05$ ($\hat{E}_o$ and E_o have unit norms). The content of the residual images is essentially due to the relaxation of the constraint for a perfect match between measures and estimations in the CS scheme, leading to some denoising effect, confirmed by the visual aspect on Fig. 5.6d showing essentially unstructured noise. Finally, Figs. 5.6e and 5.6f display magnified views from a central region of the images (a) and (b), illustrating the visual quality of the reconstruction.

5.4.3 Compressed DHM Setup for Biological Imaging

Now we present a similar experiment for biological imaging with compressed DHM. The experimental setup differs, however, the reconstruction algorithm used for the biological data is the same as the one used to reconstruct the USAF target.

The experimental setup is sketched in Fig. 5.7. It consists of an off-axis, frequency-shifting digital holographic microscopy scheme [Atlan 2007, Gross 2007]. The monochromatic optical field from a near infrared diode laser illuminates the skull of an adult mouse, anesthetized with a mixture of xylazine and ketamine (1 mg/kg IP, 10 mg/kg IP), positioned on a stereotaxic frame. Cranial skin and subcutaneous tissue were excised linearly over the sagittal suture and cortical bones were preserved. The backscattered field beats against a separate local oscillator (LO) field detuned by $\Delta\theta/(2\pi) = 30\,\mathrm{Hz}$ and creates a time-fluctuating interference pattern measured with a $N = 1024 \times 1024$ array detector. The diffracted object field map in the detector plane, resolved in quadrature (in amplitude and phase)

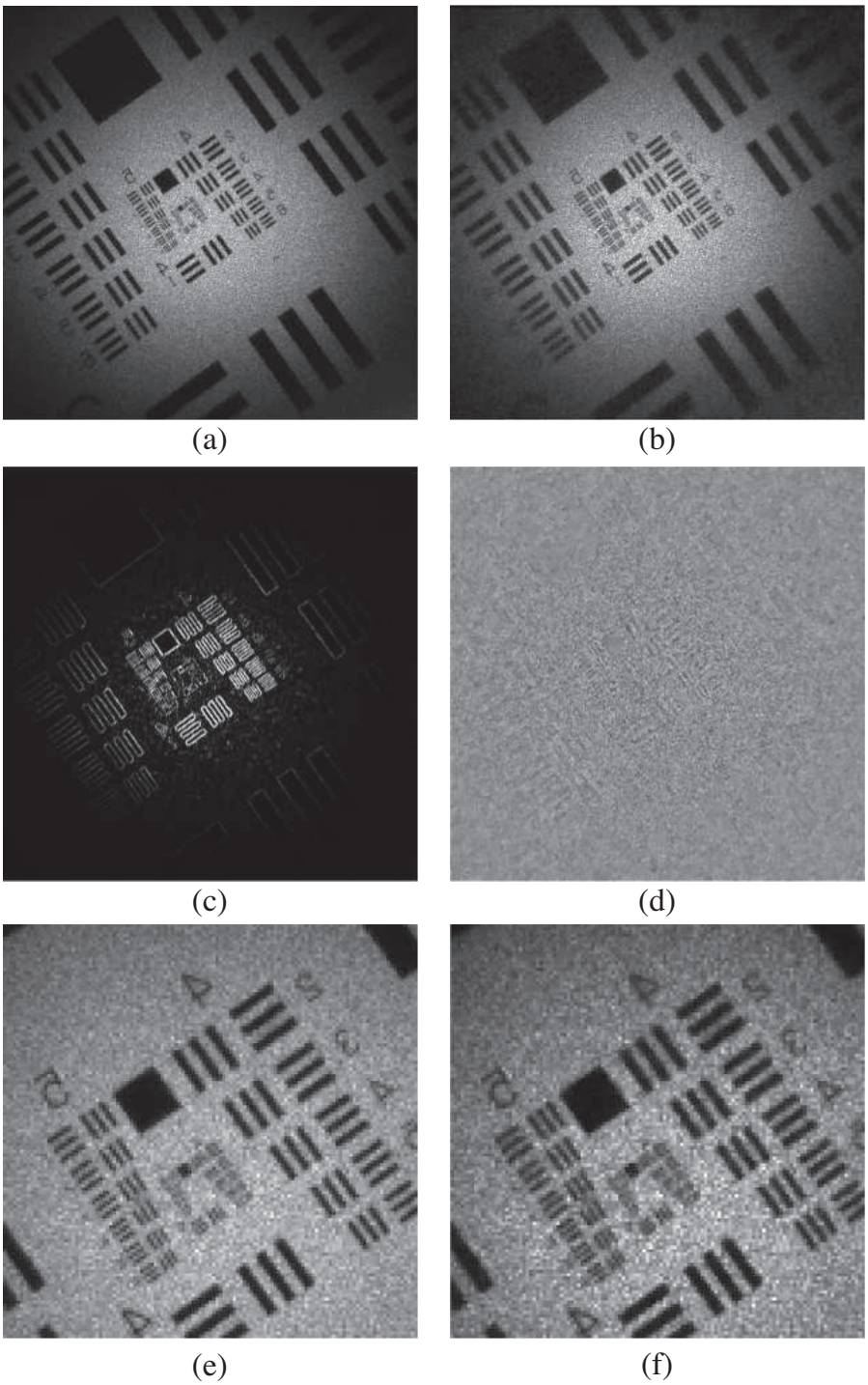

Figure 5.6: (a) Standard holography experiment, as described in Eq. (5.6). (b) CS reconstruction, using 7% of the Fresnel coefficients. (c) Gradient of (a). (d) Residual from (a) and (b). (e), (f) Magnified views from (a) and (b).

$H \in \mathbb{C}^N$ is calculated from a four-phase measurement [Atlan 2007]. The frequency detuning $\Delta\theta$ enables rejection of non fluctuating light components reflected by the preparation as well as speckle reduction through signal accumulation.

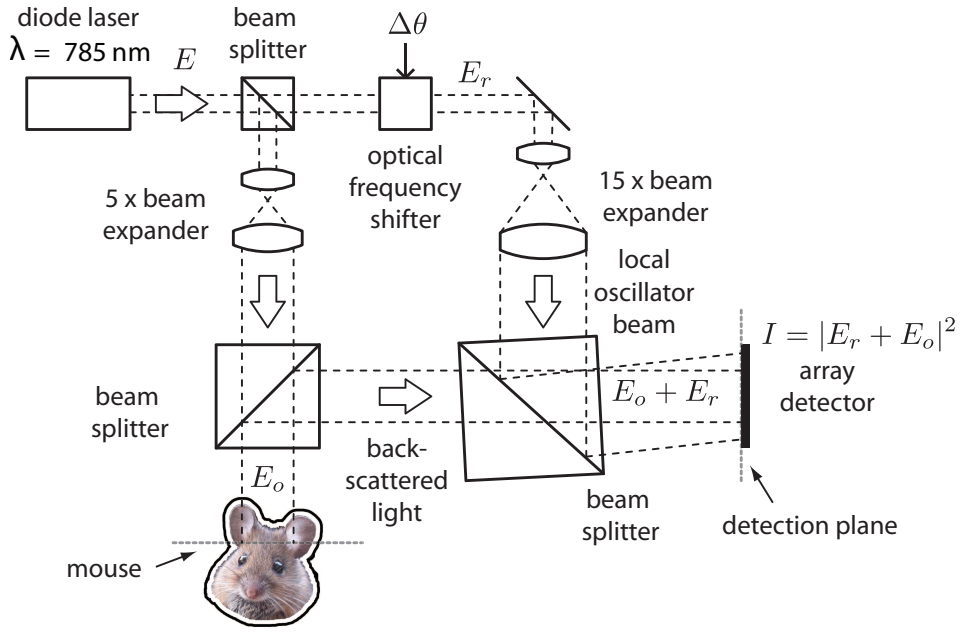

Figure 5.7: Sketch of the holographic microscopy experimental image acquisition setup.

5.4.4 Biological Image Reconstruction

In Fig. 5.8 we illustrate some CS reconstruction results. A reconstruction of an off-axis image with the standard convolution method described in (5.7) is illustrated in Fig. 5.8(a). The image reconstructed with holography used all available measurements (4 phases $\times$ 20 accumulations $\times 1024^2 = 8.4 \times 10^7$ pixels). For the CS approach, Fresnel coefficients were undersampled randomly. Fig. 5.8(b) shows the CS exact recovery such as described in (5.12) and Fig. 5.8(c) shows the CS recovery with the constraint relaxation such as described in (5.13). For both CS reconstruction we used only 7% of the pixels used in the standard approach (4 phases $\times$ 20 accumulations $\times$ 0.07 $\times 1024^2 = 5.8 \times 10^6$ pixels). Figs. 5.8(d)-(f) display magnified views from the central region of images (a-c), illustrating the quality of the reconstruction. Fig. 5.8(g) illustrates the gradient of the image ∇E_o, corresponding to the sparse domain. Finally, Figs. 5.8(h) and 5.8(i) illustrates the residual comparing standard holographic reconstruction (a) and CS reconstructions (b) and

(c). The global normalized error is $\| \hat{E}_o - E_o \|_{\ell_2} = 0.15$, $\hat{E}_o, E_o$ being normalized. This error in Fig. 5.8(i) is essentially due to the relaxation of the constraint for a perfect match between measures and estimations in the CS scheme, leading to some denoising effect, confirmed by the visual aspect of the residual image image Fig. 5.8(i) showing essentially unstructured noise.

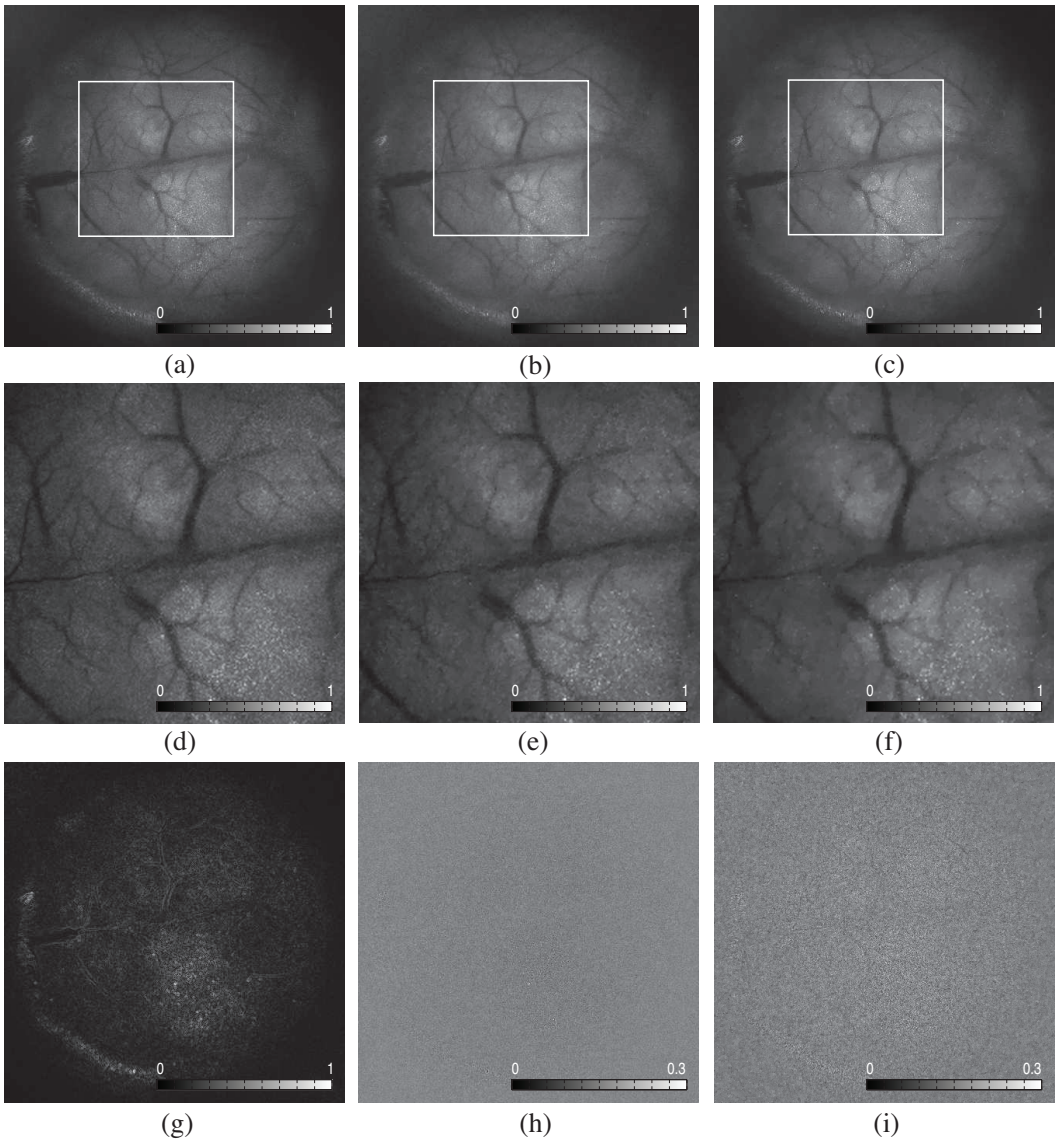

Figure 5.8: Mouse cerebral blood flow (CBF) imaged by digital holographic microscopy (a) Standard holographic reconstruction, as described in (5.7). (b) CS exact recovery, using 7% of the Fresnel coefficients acquired with holography, as described in (5.12). (c) CS recovery with denoising, as described in (5.13). (d-f) Magnified views from (a-c). (g) Gradient of (a). (h) Residual from |(a)-(b)|. (i) Residual from |(a)-(c)|.

5.4.5 Effect of Undersampling on CS Reconstructions

The minimum number of measurements required for CS imaging depends on the signal sparsity and the mutual coherence between the sparsity domain and the sampling domain such as described in subsection 1.3.2 by the equation (1.23). However, in practice the sparsity cannot be computed before the acquisition since the image is unknown. Thus, the number of measurements in our experiments was fixed empirically by pushing the undersampling to the limit, decreasing the number of measurements until the CS reconstruction fails. In experiments in subsections 5.4.2 and 5.4.4 the number of measurements was fixed above the empirical limit to guarantee that the image reconstruction works. Conversely, Fig. 5.9 displays an experience, on both USAF target and biological data, where the undersampling is too strong. The image reconstruction quality is then not satisfactory and we can see that the image reconstruction fails. The images in 5.9(a) result from the standard holographic reconstruction, the images 5.9(b) are CS reconstructions from 4% of the Fresnel coefficients acquired with holography, as described in (5.12), the images 5.9(c) are the residuals from |(a)-(b)| and finally the images 5.9(d) are SSIM maps between (a) and (b). These experiments showed that there is a critical threshold for the sampling rate, confirming the theory.

5.5 Conclusion

In this chapter, we have demonstrated the feasibility of a novel framework successfully employing compressed sensing principles for digital holographic microscopy. It combines iterative image reconstruction with quadrature-resolved random digital holography measurements of an optical field in a diffraction plane. Practical experiments on holographic microscopy images of the USAF target and of cerebral blood flow demonstrates that our CS approach enables image reconstruction from a very limited number of measurements. The proposed technique is expected to greatly improve microscopy applications, allowing the acquisition of high dimensional data with reduced acquisition time increasing imaging throughput and opening the door to fast and sample-friendly acquisition protocols.

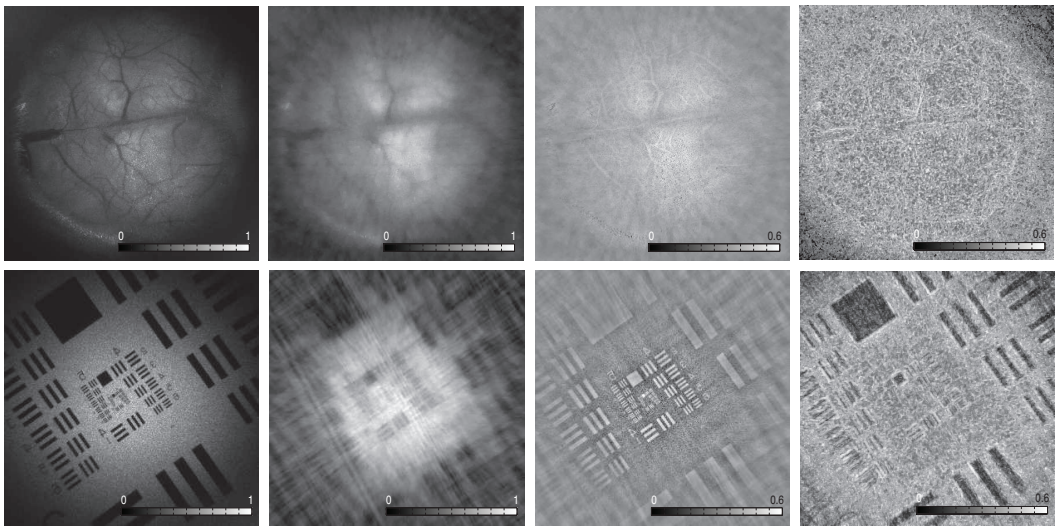

(a) (b) (c) (d)

Figure 5.9: (a) Standard holographic reconstruction, as described in (5.7). (b) CS exact recovery, using 4% of the Fresnel coefficients acquired with holography, as described in (5.12). (c) Residual from |(a)-(b)|. (d) Structural Similarity between images (a) and (b) SSIM=0.1355 (top) and SSIM=0.1653 (bottom). Here, the CS reconstruction is not satisfactory due to the number of samples being too low.

Chapter 6

One-Shot Off-Axis Compressed DHM in Low Light Conditions

This chapter reports a demonstration of off-axis compressed holography in low-light level imaging conditions. Different from the previous chapter 5, here the acquisition is performed in extremely low-light conditions and therefore with very noisy measurements. The acquisition protocol relies on a single exposure of a randomly undersampled diffraction map of the optical field, recorded in high heterodyne gain regime. CS-image reconstruction is further enhanced by introducing an off-axis spatial support constraint to the image estimation algorithm. We report accurate experimental recovering of holographic images of a resolution target in low-light conditions with a frame exposure of 5 μs, scaling down measurements to 9% of random pixels within the array detector.

Off-axis holography is well-suited to dim light imaging. Shot-noise sensitivity in high optical gain regime can be achieved with few simple setup conditions [Gross 2007]. Holographic measurements are made in dual domains, where each reordered pixel exhibits spatially dispersed (i.e. multiplexed) information from the object. The measurement domain and the image domain are "incoherent", which is a requirement for using compressed sensing (CS) sampling protocols [Candès 2004b]. In particular, CS approaches using frequency-based measurements can be applied to holography sampling the diffraction field in amplitude and phase. CS was used recently to improve image reconstruction in holography by increasing the number of voxels one can infer from a single hologram and canceling artifacts [Brady 2009, Denis 2009, Choi 2010]. CS was also used for image retrieval from undersampled measurements in millimeter-wave holography [Cull 2010] and off-axis frequency-shifting holography (see chapter 5).

[0]Based upon: M. Marim, M. Atlan, E. Angelini and J.-C. Olivo-Marin. *"Off-axis compressed holographic microscopy in low-light conditions"*, (Accepted in Optics Letters).

In this work, we describe an original acquisition and reconstruction protocol to achieve off-axis compressed holography in low-light conditions, from undersampled measurements. The main result presented in this chapter is an experimental demonstration of accurate image reconstruction from very few low-light holographic measurements. The acquisition setup consists of a frame exposed with the reference beam alone and subtracted to a frame exposed with light in the object channel, beating against the reference, to yield the holographic signal. This setup prevents any object motion artifact that would potentially occur with phase-shifting methods (see chapter 5). The CS image reconstruction algorithm relies on a total variation minimization constraint restricted to the actual support of the output image, to enhance image quality.

Contents

6.1 Introduction **128**
6.2 One-Shot Holography Setup **129**
6.3 Image Reconstruction With Bounded Support **131**
6.4 Noise Robustness and Results **133**
6.5 Conclusion **134**

6.1 Introduction

Digital holography (DH), as opposed to interferometry, requires information to be sampled in a reciprocal space. Hence sensing an object by holography consists in measuring hologram coefficients related to the frequency content. Digital holographic recordings are made in a diffraction plane of the image to assess. An integral transform is needed to turn measures of spatially dispersed information into the original imaging space. Hence, the image assessment in DH relies on sensing in a reciprocal space and a linear canonical transformation to compensate for spatial dispersion of the information.

The main result presented in this chapter is to provide accurate image reconstruction from very few low-light single shot holographic measurements. Moreover, we introduce a spatial support constraint during the sparsity maximization for a more accurate image reconstruction.

CS imaging has been tested experimentally with the linear measurements performed through innovative devices such as the single pixel architecture

[Takhar 2006], the off-axis frequency-shifting holography presented in chapter 5, or simply by native incoherent sampling such as Magnetic Resonance Imaging (MRI) [Lustig 2007], where measurements are naturally acquired in a dual Fourier domain. Here, we propose a new microscopy acquisition scheme successfully combining high speed low-light single-shot off-axis holography with a spectral support constraint, and a total variation minimization algorithm to reconstruct the image. Differently from the acquisition scheme presented in chapter 5, here the acquisition conditions are very noisy due to low-light single shot holography.

6.2 One-Shot Holography Setup

We consider the holographic detection of an object field E_o of small amplitude with a reference or local oscillator (LO) field E_r of much larger amplitude, to seek low-light detection conditions, using the Mach-Zehnder interferometer sketched in fig. 6.1. The main optical radiation comes from a single mode continuous laser at

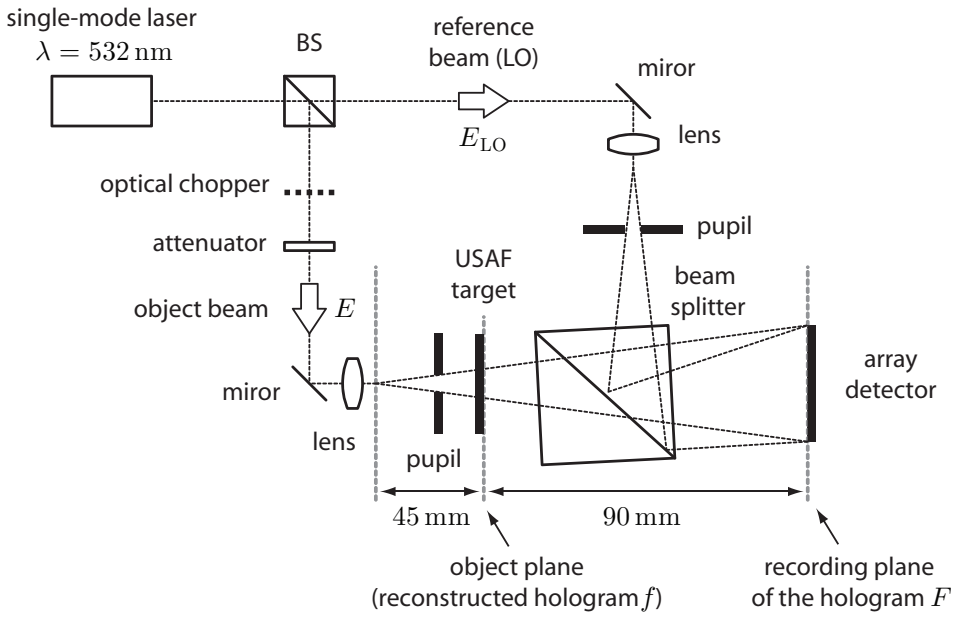

Figure 6.1: Sketch of the experimental one-shot holographic acquisition setup.

wavelength $\lambda = 532$ nm. Lenses with short focal lengths are used in both channels to create point sources. In the object channel, a negative U.S. Air Force (USAF) resolution target is illuminated in transmission. The amount of optical power in the object channel is tuned with a set of neutral densities. The interference pattern of

E_o beating against E_r corresponds to $I = |E_o + E_r|^2$. It is measured within the central region of a Sony ICX 285AL CCD array detector (gain $G_{\mathrm{CCD}} = 3.8$ photo-electrons per digital count, $N = N_a \times N_b$ elements, where $N_a = N_b = 1024$, pixel size $d_a = d_b = 6.7\,\mu$m, quantum efficiency ~ 0.6). The acquisition frame rate is set to 12 Hz and the exposure time to 5 μs. A mechanical chopper is used to switch the object illumination on-and-off from frame to frame. The recorded interference pattern takes the form:

$$I = |E_r|^2 + |E_o|^2 + E_o E_r^* + E_o^* E_r \tag{6.1}$$

where $*$ denotes the complex conjugate. In our setup we have $|E_o|^2 \ll |E_r|^2$. Let's define n and n_r, the number of photo-electrons released at each pixel, from light in the object and LO channel respectively, impinging on the detector. The reference beam intensity is adjusted so that the LO shines the detector to half saturation of the pixels' dynamic range, on average. This amounts to $\langle n_r \rangle / G_{\mathrm{CCD}} \sim 2000$ digital counts. The brackets $\langle \cdot \rangle$ denote the average over N pixels. Hence $\langle n_r \rangle = 7.6 \times 10^4$ e (photo-electrons) per pixel. In the object channel, three optical densities $D = 0$, $D = 0.5$, and $D = 1$, are set sequentially to reach very low $\langle n \rangle$ values. The average number of digital counts in 50 consecutive frames recorded in these conditions, while the LO beam is blocked, are reported in figs. 6.3(a)-(c). The detection benefits from a holographic (or heterodyne) gain $G_{\mathrm{H}} = \langle |E_o E_r^*| \rangle / \langle |E_o|^2 \rangle = (\langle n_r \rangle / \langle n \rangle)^{1/2}$, which ranges from $G_{\mathrm{H}} = 177$ ($D = 0$) to $G_{\mathrm{H}} = 563$ ($D = 1$). The spatial support of the signal term $E_o E_r^*$ is a compact region $\mathcal{R}$ of $P = 400 \times 400$ pixels. In such high gain regimes, the object field self-beating contribution $|E_o|^2$, spreads over a region twice as large as $\mathcal{R}$ along each spatial dimension, and can be neglected in comparison to the magnitude of $E_o E_r^*$ and $E_o^* E_r$ in eq. 6.1. In off-axis configuration, the term of interest $E_o E_r^*$ is also shifted away from $|E_o|^2$ and $E_o^* E_r$, which improves the detection sensitivity at the expense of spatial bandwidth. For the current setup, the ratio of available bandwidth between off-axis and on-axis holography is equal to $P/N \sim 16\%$. To cancel-out the LO flat-field fluctuations within the exposure time, a frame acquired without the object $I_0 = |E_r|^2$ is recorded. The difference of two consecutive frames $I - I_0 \simeq E_o E_r^* + E_o^* E_r$ yields a measure of the holographic signal $H = E_o E_r^*$. H which is proportional to the diffracted complex field E_o, will now be referred to as the optical field itself. Each measurement point on the array

detector $H(\omega, \nu)$, where $\omega = 1, ..., N$ and $\nu = 1, ..., N$, corresponds to a point in the Fresnel plane of the object. More precisely, the hologram H, computed from the intensity measurements I in the detection plane yields the field distribution in the object plane E_o via an inverse discrete Fresnel transform [Schnars 1994]:

$$E_o[a, b] = \frac{1}{n} e^{\frac{2\pi i z}{\lambda}} \sum_{\omega=0}^{n-1} \sum_{\nu=0}^{n-1} H[\omega, \nu] e^{\frac{\pi i}{\lambda z}(\omega^2+\nu^2)} e^{2\pi i(\frac{a\omega+b\nu}{n})} \tag{6.2}$$

where $i^2 = -1$, and (a, b), (ω, ν) denote pixel indexes in space and frequency. The quadratic phase factor depends on a distance z between the detection plane and the object plane. Standard holographic reconstruction, as illustrated in Figs. 6.3(d-f), consists in forming the intensity image of the object E_o from the measurements of H over the whole detection array, with eq. 6.2.

6.3 Image Reconstruction With Bounded Support

We want to recover E_o from a small number of measurements $H|_\Gamma = \Phi E_o$ in the detector plane, where $H|_\Gamma \subset H$. Φ is a $M \times N$ sensing matrix encoding the Fresnel transform (eq. 6.2) and the sampling of a subset Γ of M pixels, randomly distributed among the N pixels of the detection array. We want M to be as small as possible, to benefit from the best compression ratio M/N with respect to non-CS holography, and enhance the throughput savings parameter $1 - M/N$.

Since the target is piecewise constant with relatively sharp edges, its total variation provides a sparsity measure $\| E_o \|_{TV} < M \ll N$. The existence of a sparse representation means that E_o has at most $\| E_o \|_{TV}$ degrees of freedom. For a successful reconstruction we must perform at least $M > \| E_o \|_{TV}$ measurements, but much less than N.

However, when using an off-axis holography configuration, the image reconstructed from the hologram is shifted away from the center as illustrated in figure 6.2. There is no need to reconstruct the entire field of view since the image of interest is restrict to a small area. The CS-based image reconstruction can also be optimized since the number of measurements depends on the image size. In addition restricting the image reconstruction to this area (the square containing the object) leads to a total variation minimization restricted to a small area of 400^2 pixels and the reconstruction time approximately reduces by a factor two for a hologram with

1024^2 pixels.

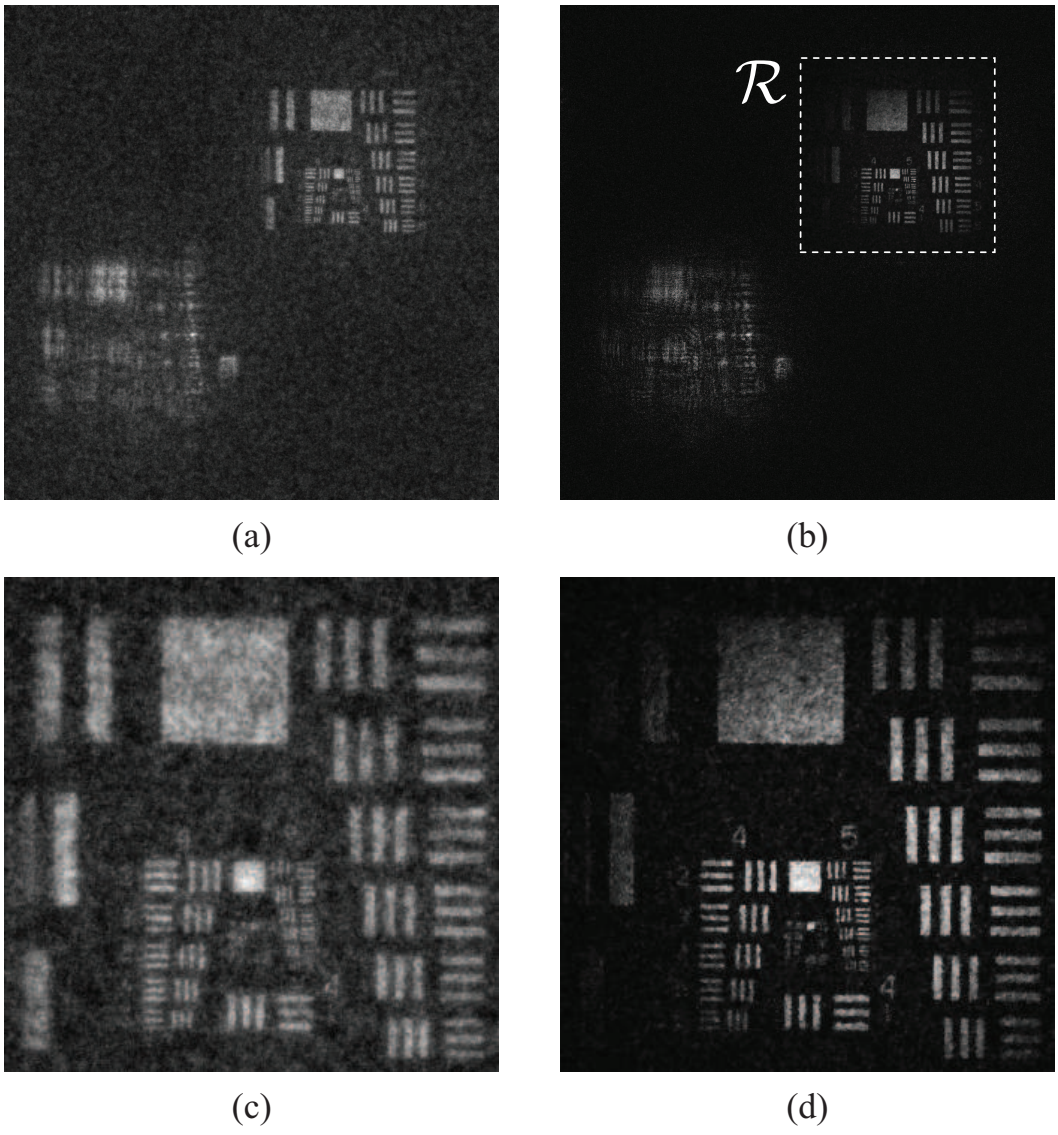

Figure 6.2: Compressed holographic reconstruction of E_o without support constraint (a). Reconstruction with TV minimization over the region $\mathcal{R}$ (b). In both cases, $\langle n \rangle = 2.4\,\mathrm{e}$ ($D = 0$) and $M/N = 9\%$. Magnified views over 330×330 pixels (c,d) of (a,b).

Therefore, given partial measurements $H|_\Gamma$, we seek an estimate $\hat{E}_o$ with maximum sparsity in a restricted support (i.e. inside the region $\mathcal{R}$) and whose Fresnel coefficients $\hat{H}|_\Gamma$ match the observations $H|_\Gamma$ within some error bound δ.

Then a constrained problem is expressed as:

$$\hat{E}_o = \arg\min_{E_o \in \mathcal{R}} \| E_o \|_{TV} \quad \text{s.t.} \quad \| H|_\Gamma - \Phi E_o \|_{\ell_2} \leq \delta \tag{6.3}$$

where δ is a constraint relaxation parameter introduced to better handle noisy measurements.

We note that $E_o \in \mathcal{R}$ corresponds to the image inside the spatial support and the bounds of $\mathcal{R}$ are illustrated in Fig. 6.2d by the white square. The sparsity measure $\| E_o \|_{TV}$ is then computed only on $\mathcal{R}$ giving a more accurate estimation of E_o since the signal outside $\mathcal{R}$ is not necessarily sparse (noisy/degraded replicate of the image in $\mathcal{R}$).

This restriction on the spatial support being constrained leads to a more accurate estimate of $\hat{E}_o$, actually reducing the number of relevant degrees of freedom to estimate, and hence the number of samples M required. For comparison purposes, CS reconstructions without and with support constraint from the same original frame are reported in fig.6.2. TV minimization over N pixels leads to the hologram magnitude map $\hat{E}_o$ reported in fig.6.2(a), while the same regularization constraint applied on $\mathcal{R}$ leads to the magnitude hologram reported in fig.6.2(b). Magnified views in figs. 6.2(c) and 6.2(d) show a clear increase in image sharpness with bounded spatial regularization.

6.4 Noise Robustness and Results

The image resolution is 1024 × 1024 pixels and the spatial constraint size is 400 × 400 pixels. Fig. 6.2 displays the CS reconstruction results with and without spatial constraints. Fig. 6.2(d) shows that the spatial support constraint allows a much better reconstruction, providing more details and sharpness than without the spatial support constraint in Fig 6.2(c). Moreover, the number of measurements can be significantly reduced from 14% of all pixels to 9% since it depends on the sparsity and E_o is more sparse with the spatial constraint. For more details on the CS reconstructions see magnified views (330 × 330 pixels) in Fig 6.2(e) and (f).

Fig. 6.3 illustrate the noise robustness and the denoising capability of the proposed CS reconstruction approach. For three different low-light conditions the CS reconstructions are capable of recovering the signal even for very low-light conditions (cs 3), while standard holography (holography 3) provides an unreadable

image, illustrated in 6.3 (d)-(f).

Standard Fresnel reconstruction from N pixels leads to the images reported in figs. 6.3 (d)-(f), recorded at $\langle n \rangle = (2.4, 0.75, 0.24)$ for figs.6.3 (d,e,f). CS image reconstructions of $\hat{E}_o$ with bounded TV regularization from the same data are reported in figs. 6.3 (g)-(i). Highly accurate image reconstruction is achieved, at compression rates of 9% in fig. 6.3(g), 13% in fig. 6.3(h), and 19% in fig. 6.3(i), i.e. from much less measurements than needed for Fresnel reconstruction.

6.5 Conclusion

In conclusion, we have presented a detection scheme for coherent light imaging in low-light conditions successfully employing compressed sensing principles. It combines a single-shot off-axis holographic scheme, to perform random measurements of an optical field in a diffraction plane, and an iterative image reconstruction enforcing sparsity on a bounded image support. Compressed off-axis holography is a powerful method to retrieve information from degraded measurements at high noise levels. We demonstrated single-shot imaging in high heterodyne gain regime at 5 μs frame exposure around one photo-electron per pixel in the object channel. In these conditions, throughput savings from 81% to 91% could be reached.

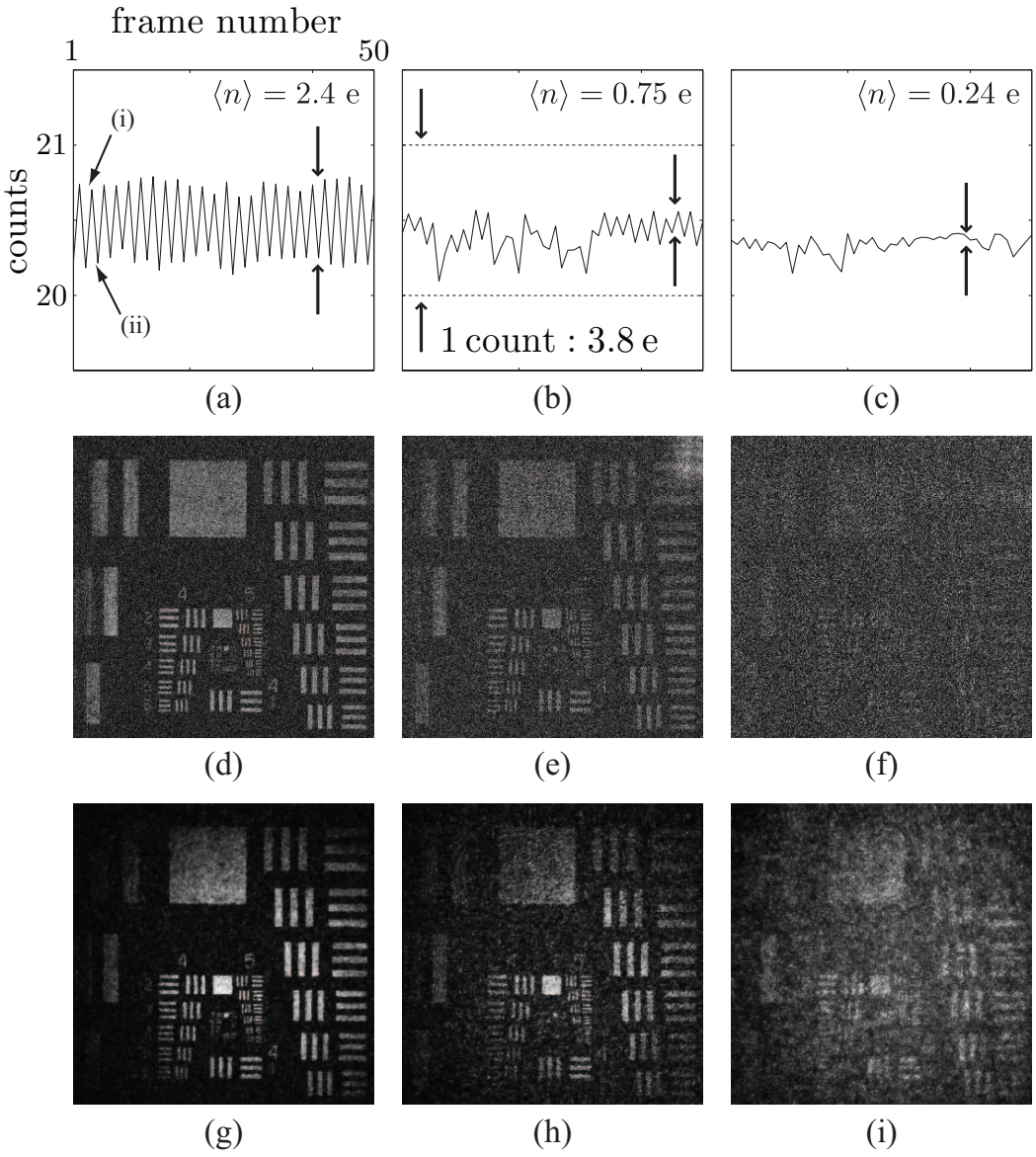

Figure 6.3: (a-c) Amount of digital counts in the object channel averaged over N pixels, for three different attenuations levels : $D = 0$ (a), $D = 0.5$ (b), $D = 1$ (c). The LO beam (reference beam) is turned off. The optical field E impinges onto the detector (i) and is blocked (ii) sequentially by the optical chopper, from one frame to the next. The horizontal axis represents the frame number, the vertical axis is the average number of counts per pixels. (d-f) Standard holographic reconstructions at $D = 0$ (d), $D = 0.5$ (e), $D = 1$ (f). (g-i) CS reconstructions at $D = 0$ with $M/N = 9\%$ (g), at $D = 0.5$ with $M/N = 13\%$ (h), and at $D = 1$ with $M/N = 19\%$ (i).

Conclusion and Perspectives

Optical microscopy remains limited by numerous problems, including the handling of noisy components during the image formation and acquisition and limited image acquisition frame rates. With regard to this specific limitation, it is necessary to ensure that the signal level relative to the noise is adequate when capturing accurate image information. A host of denoising methods have been developed to increase the signal-to-noise ratio, namely by modeling and removing the noise. However, most of them are post-processing techniques and require full data acquisition.

In a first place, the aim of this thesis was to investigate new sparsity-based image processing methods to address the denoising problem. Manipulating CS imaging approaches, we naturally transitioned from standard digital holographic microscopy to test acquisition protocols that use very few Fourier-based initial measurements. Indeed, holographic microscopy presents several advantages over traditional microscopy imaging techniques such as high-resolution three-dimensional recording of an object, precise quantitative reproduction of the object being imaged and a translucent image that allows the viewer to visualize both deep and superficial structures simultaneously. In addition, it is a label-free and non-invasive technique, avoiding photo-toxicity, unlike fluorescence imaging techniques.

The first part of this thesis consists in a CS-based denoising framework for biological microscopy imaging. Our approach is based on the total variation minimization for multiple CS reconstructions from incomplete and random measurements in the Fourier domain. We used different sampling matrices for multiple reconstructions to select different sets of Fourier coefficients. Using the total variation as a sparsity measure provides correlated reconstructions of the structures and objects and uncorrelated noise patterns. Thus, combining multiple reconstruction provides efficient noise reduction and structure enhancement. It turned out that the proposed approach compares well with traditional denoising methods while requiring less measures during acquisition.

We compared simple averaging and non-local averaging fusion methods for the multiple reconstructions. The non-local averaging takes advantage of image redundancy by averaging non-local similar patches, and provides better denoising quality. In addition, this work showed that if the proposed CS Fourier-based random acquisition setups were feasible in fluorescence microscopy, photobleaching effect could be significantly reduced.

This work can be extended in different directions. First, in order to improve the preservation of structural details in the objects, different sparsifying transforms can be applied. We have used the total variation, which enforces piecewise-constant object appearance. Also, sparsity transforms based on wavelet or texture dictionaries could be used. By using a quadratic norm in the fidelity term we optimize a Gaussian likelihood model for the signal which may be improved by using a measure taking into account the mixture of Gaussian and Poisson noise. Regarding the fusion of the multiple reconstructions, spatially-adaptive merging schemes could be tested to adapt to the local contents of the images. Finally, non-spatially uniform sampling patterns may be investigated to select the frequencies corresponding preferentially to signal than to noise.

In a second part, we focused on the optimization of DH microscopic acquisition. We built, together with Michael Atlan from the ESPCI, a DH detection setup for coherent light imaging in low-light conditions, that successfully employs compressed sensing principles. The image acquisition consists in a single-shot off-axis holographic scheme, which allows to perform random Fourier-type measurements of an optical field in a diffraction plane. This work demonstrates that compressed off-axis holography is a powerful method when it comes to retrieving structured information from degraded measurements at high noise levels. Indeed, we proposed a single-shot imaging in high heterodyne gain regime with a frame exposure of 5 μs. In these conditions, around one photo-electron per pixel was detected, and even with a high noise level, throughput savings from 81% to 91% could be reached with compressed sensing. We obtained significant improvements in image reconstruction by restricting the total variation minimization on a bounded image support. This gave a better reconstructed image quality from a reduced number on measurements. Finally, we used a programmable CMOS camera to perform a real random and undersampled acquisition in off-axis holography.

In addition to pursuing the development of CS-based holography setups, it is also

natural to envisage an extension to fluorescence microscopy. With reduced number of measurements provided by compressed sensing, fluorescence observations should benefit from higher frame-rates, longer observations and less photo-damage.

List of Publications

Journal Papers

1. Marcio Marim, Elsa Angelini, Jean-Christophe Olivo-Marin and Michael Atlan. *"Off-axis compressed holographic microscopy in low light conditions"*, (Accepted in Optics Letters).

2. Marcio Marim, Michael Atlan, Elsa Angelini and Jean-Christophe Olivo-Marin. *"Compressed sensing with off-axis frequency-shifting holography"*, Optics Letters, vol. 35, pp. 871-873, 2010.

International Conferences

1. Marcio Marim, Michael Atlan, Elsa Angelini and Jean-Christophe Olivo-Marin. *"Compressed Sensing Applications for Biological Microscopy"*, IEEE Workshop on Signal Processing Systems, SiPS, 2010.

2. Marcio Marim, Elsa Angelini and Jean-Christophe Olivo-Marin. *"Denoising in Fluorescence Microscopy Using Compressed Sensing with Multiple Reconstructions and Non-Local Merging"*, Int. Conference of the IEEE Engineering in Medicine and Biology Society, EMBS, 2010.

3. Marcio Marim, Michael Atlan, Elsa Angelini and Jean-Christophe Olivo-Marin. *"Compressed Sensing for Digital Holographic Microscopy"*, IEEE International Symposium on Biomedical Imaging, ISBI, 2010. Best Student Paper Award - ISBI 2010

4. Marcio Marim, Elsa Angelini and Jean-Christophe Olivo-Marin. *"Compressed Sensing in microscopy with random projections in the Fourier domain"*, IEEE International Conference on Image Processing, ICIP, pp. 2121-2124, 2009.

5. Marcio Marim, Elsa Angelini and Jean-Christophe Olivo-Marin. *"Compressed Sensing in Biological Microscopy"*, Proc. SPIE Wavelets XIII, vol. 7446, pp. 744605, 2009.

6. Marcio Marim, Elsa Angelini and Jean-Christophe Olivo-Marin.*"A Compressed Sensing approach for biological microscopic image processing"*, IEEE International Symposium on Biomedical Imaging, ISBI, pp. 1374-1377, 2009.

7. Marcio Marim, Elsa Angelini and Jean-Christophe Olivo-Marin. *"A Compressed Sensing Approach for Biological Microscopy Image Denoising"*, SPARS'09 - Signal Processing with Adaptive Sparse Structured Representations, 2009.

8. Marcio Marim, Bo Zhang, Jean-Christophe Olivo-Marin and Christophe Zimmer. *"Improving single particle localization with an empirically calibrated Gaussian kernel"*, IEEE International Symposium on Biomedical Imaging ISBI, 2008.

Appendix A

Random and Radial Undersampling in Holography With an Programable Camera

Here we present our most recent results for compressed sensing with random sampling. We designed an experimental optical setup testing and validating the concept of Compressed Sensing Imaging and most important, from a real undersampled data. As we have discussed before, the main limitation for a compressed sensing is to design the acquisition setup able to acquire randomly the incomplete transformed coefficients of the signal of interest. This appendix describes a simple setup which is able to do it and was specially designed to measure randomly, a subset of the frequency coefficients of an object using holography.

To realize the undersampling we used a CMOS programable camera, which has the random-pixel access ability. Indeed, the CMOS camera from *Vision Components* can read a restricted number of pixels beforehand defined. This functionality is not common on such devices there are not many cameras able to realize it. The proposed optical setup is quite simple but corresponds to an important concept proof of compressed sensing and successful reconstruction. We note that this work was conducted as part of an internship of Mathieu Baudin from École Central de Marseille.

The 8-bit camera measure the optical field in an off-axis setup and Fresnel domain. The Fresnel domain as discussed in the previous chapters is a frequency domain, less incoherent then the Fourier domain but sufficient incoherent to the spatial domain. The image reconstruction algorithm used consists to minimize the sparsity (measured by the total variation) with incomplete measurements in the Fresnel domain.

The optical setup is much less sophisticate than the setups described in chapter

5 and 6, however, it uses the same concept of fresnel holography imaging. The main idea of this experience is to prove that compressed sensing can be easily exploited using a programable CMOS with independent pixel access, without changes in the imaging setup but only in the way to acquire samples. Finally, the most important advantages of this kind of imaging system is the reduced data throughput which can be traduced by faster acquisitions, reduced data transfer, economy in storage, etc.

This appendix is organized in the following manner: we first introduce the experience and discuss the main difficulties in sections A.1 and A.2, then the reconstruction process and some results are presented in section A.3.

A.1 Introduction

The goal of this part of my thesis is to prove the feasibility of compressed sensing using a simple optical setup. The experiences we did here are quite simpler than those in the last chapters. However, here we have used a programable CMOS camera which is able to read independently a list of pixels. This ability is very useful for compressed sensing which is based on random and unstructured measurements.

The experience consists to record an hologram using a off-axis digital holographic setup, and later reconstructing the optical field from the object. The difference from traditional digital holography is that we want to acquire a very small part of the hologram which means measure only a small set of its all coefficients. Then, from the amplitude and phase of the optical wave arriving in the captor, we use a convex optimization algorithm to recover the original object field.

As indicated above, the wavefront reconstruction problem consist of two distinct parts, a detection step and an image reconstruction step. First, we focus on the first of theses steps. Since we use a laser, so coherent light, its is necessary to detect information about both amplitude and phase of the waves. However, using a real captor such as the CMOS used here, the only accessible information is the light intensity. The CMOS camera measure indeed the light intensity, therefore, the phase information is required and this is why we use interferometry, that is, a second wavefront which is mutually coherent with the one used to illuminate the object and with known phase and amplitude, is added to the unknown wavefront. The intensity of the sum of two complex fields then depends on both the amplitude

and the phase of the unknown field, thus if

$$E(x,y) = |\mathcal{E}(x,y)|e^{-j\phi(x,y)} \tag{A.1}$$

represents the wavefront to be reconstructed and if

$$E_{LO}(x,y) = |\mathcal{E}_{LO}(x,y)|e^{-j\psi(x,y)} \tag{A.2}$$

represents the reference wave with which $E(x,y)$ interferes, the intensity of the sum is given by

$$I(x,y) = |\mathcal{E}_{LO}(x,y)|^2 + |\mathcal{E}(x,y)|^2 + 2|\mathcal{E}_{LO}(x,y)||\mathcal{E}(x,y)|cos[\psi(x,y) - \phi(x,y)] \tag{A.3}$$

Accordingly with (A.3) the first two terms depend only on the intensities of the object field and the reference field and the third depends on their relative phase. Thus information about the amplitude and the phase of $E(x,y)$ is acquired with the hologram $I(x,y)$.

A.2 The Acquisition System

A.2.1 The Holographic Setup

The setup is composed by a Helium Neon (HeNe) laser with wavelength $\lambda = 632.8$ nanometers, 2 beam splitters (BS1 and BS2), 3 bi-concave lens (L1, L2, L3) and a bi-convex lens (L4) with focal distance ($f_1 = -50$cm, $f_2 = -100$cm, $f_3 = -25$cm and $f_4 = 50$cm), a mirror, an USAF target, some absorptive neutral density filters and a programable CMOS camera.

The components are fixed in an optical table such as illustrated in figure A.2 and photo A.2. The light beam emitted by the HeNe laser is divided in two beams by the first beam splitter BP1, and then expanded by the combination of two lens (L1 and L2). The beam is expanded by a factor 5 and then projected in the USAF target, reflecting and projected to the CMOS camera. In parallel, the reference beam is also expanded by L3 and L4 lens and recombined with the optical field coming from the object in the second beam splitter. The resultant beam is filtered by two absorptive neutral filters and before the final projection to the CMOS array detector. We use a slight rotation in the second beam splitter BP2 which forces the object optical field

and the reference optical field to be off-axis. The angle is controlled by the limit angle which can be previously computed.

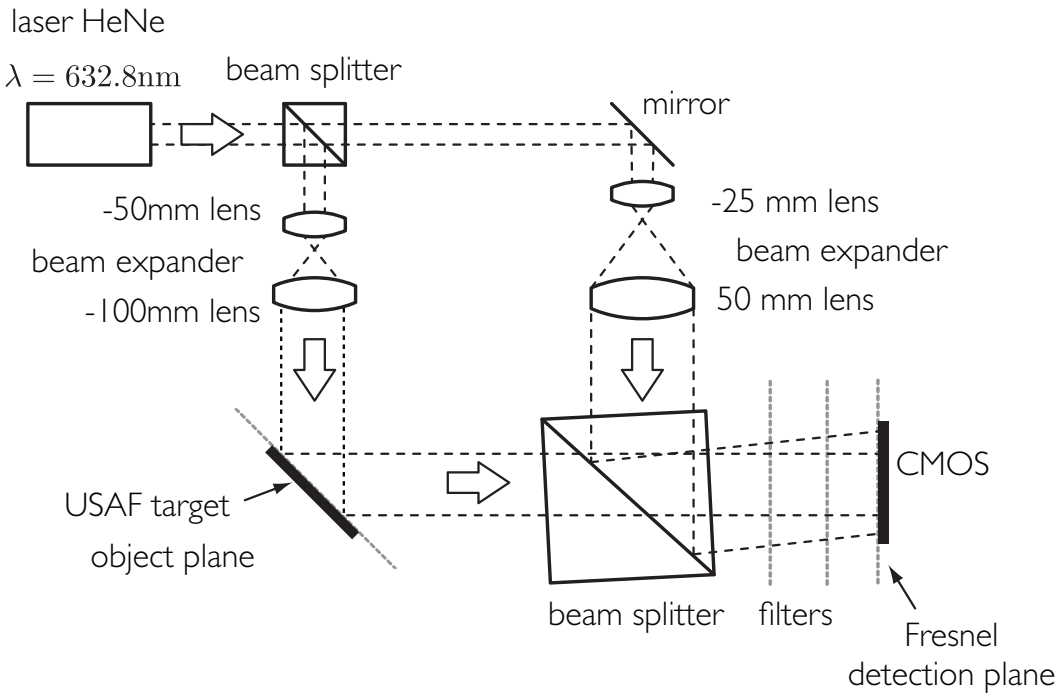

Figure A.1: Holographic setup with intelligent CMOS.

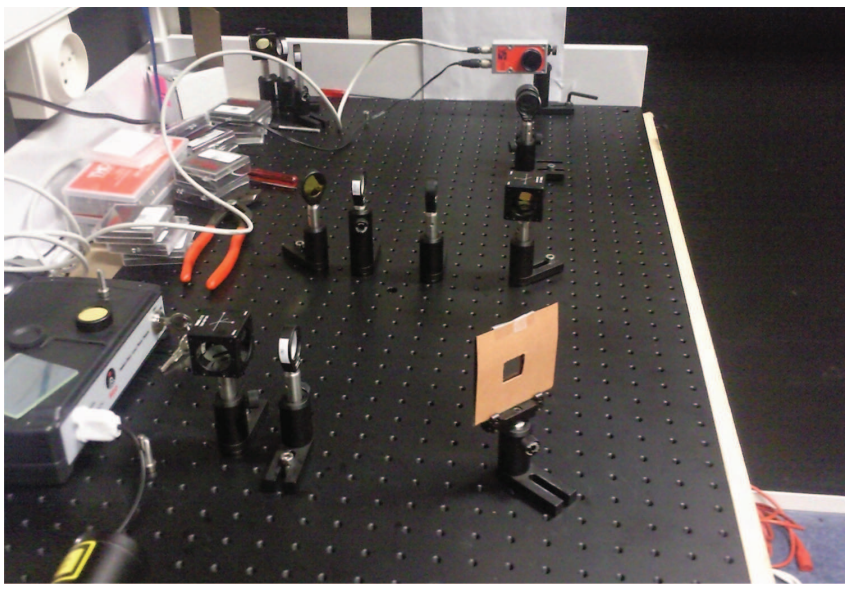

Figure A.2: Photo of the holographic setup with intelligent CMOS.

The optical intensity field accessed by the CMOS camera corresponds to Fresnel coefficients and the total incident field on the detection plane can be expressed as:

$$\begin{aligned} E(x,y) &= \mathcal{E}_r \exp\{-i\frac{\pi}{\lambda z_r}[(x-x_r)^2+(y-y_r)^2]\} \\ &\quad +\mathcal{E}_o \exp\{-i\frac{\pi}{\lambda z_o}[(x-x_o)^2+(y-y_o)^2]\} \end{aligned} \tag{A.4}$$

where λ is the coherent light wavelength. The corresponding intensity distribution of the diffraction pattern (interference between reference wave and object wave) in the detection plane corresponds to:

$$\begin{aligned} I(x,y) &= |\mathcal{E}_r|^2+|\mathcal{E}_o|^2 \\ &\quad \mathcal{E}_r\mathcal{E}_o^* \exp\{-i\frac{\pi}{\lambda z_r}[(x-x_r)^2+(y-y_r)^2]+i\frac{\pi}{\lambda z_o}[(x-x_o)^2+(y-y_o)^2]\} \\ &\quad \mathcal{E}_r^*\mathcal{E}_o \exp\{i\frac{\pi}{\lambda z_r}[(x-x_r)^2+(y-y_r)^2]-i\frac{\pi}{\lambda z_o}[(x-x_o)^2+(y-y_o)^2]\} \end{aligned} \tag{A.5}$$

The image reconstruction from the total intensity field measured has mainly two steps, the first one consists to compute the complex field from the real measurements, and the second one consists to back-propagate the field to the object plane. To compute the complex field the quadratic phase $\exp\{\frac{i\pi}{\lambda d}(x-x_r)^2+(y-y_r)^2\}$ is combined with $I(x,y)$.

A.2.2 The Programmable CMOS Camera

The CMOS camera we had used to measure the optical intensity is fabricated by Vision Components. It is a smart camera model VC4012nano (figure A.3), which is a programmable camera. The basic configurations of the camera is:

- 1/2.5" CMOS sensor
- resolution: 2592 x 1944 Pixel
- frame rate 11,6 fps
- high-speed shutter: 28,4 μs in steps of 43,7 μs
- low-speed shutter: up to 30 s adjustable integration time

It is absolutely not a plug-and-play camera, and the programming interface (API) is in practice not easy to use. The internal operating system "VCRT" of the

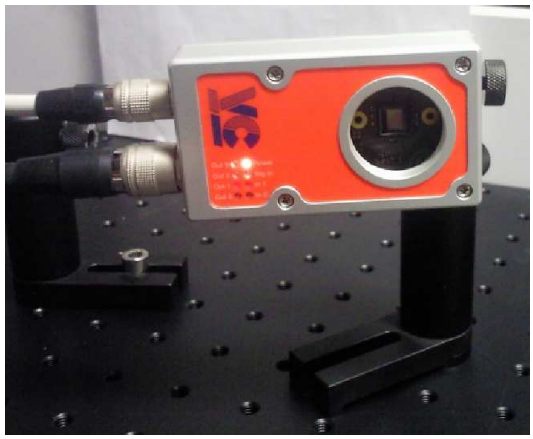

Figure A.3: Programmable CMOS camera.

VC4012nano is multitasking. This means that user interface commands can execute in parallel without stopping the inspection process. It has a video output onto a PC via 100 mega-bit Ethernet interface.

A.2.3 Preliminary Experiences

The first experience was the acquisition of the USAF target to test the camera, and to become familiar with the camera manipulation. In figure A.4 we show the USAF target imaged in a 5 megapixels resolution. The goal is to reconstruct the same image performing measures in the Fresnel domain with holography. In the next section we show examples of acquired holograms and the respective reconstructions.

A.3 The Image Reconstruction

The image reconstruction follow the same method used for compressed holography and we quickly recall how it works. Accordingly with the compressed sensing theory, if the signal is compressible (i.e. has a sparse representation), then if linear measurements are taken randomly (non-structured measurements) the original signal can be reconstructed with high probability. The setup proposed here perform indeed linear measurements and the CMOS camera can be programed to acquired a small set of pixels randomly chosen. As presented in [Candès 2005b] by E. Candès and J. Romberg, the reconstruction can also be achieved using a radial sampling (i.e. radial lines passing through the center of the image). We present also an image

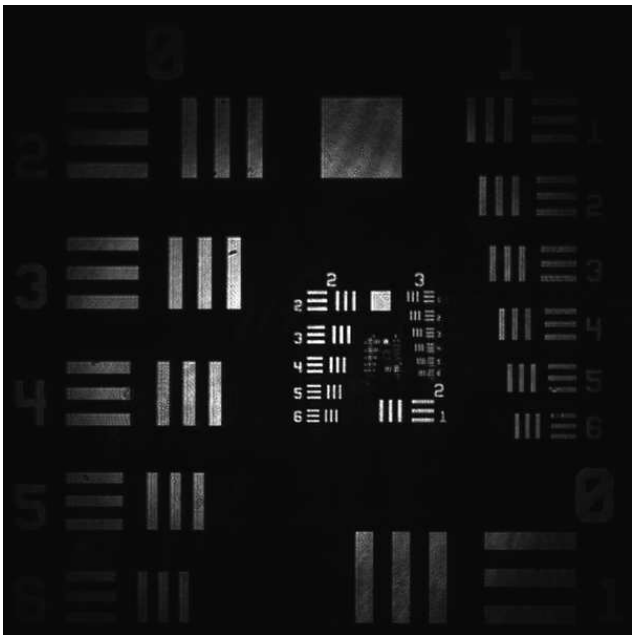

Figure A.4: US Air Force (USAF) target.

reconstruction using the radial sampling pattern.

As discussed before, the optical field in the object plane f is linked to the field F in the detection plane by a Fresnel transform, expressed in the discrete case as:

$$\begin{aligned} F &= \mathcal{F}(f) : \mathbb{C}^N \to \mathbb{C}^N \\ F_p &= \frac{1}{N} \sum_{n=1}^{N} f_n \, \mathrm{e}^{i\left(\alpha n^2 - 2\pi np/N\right)} \end{aligned} \tag{A.6}$$

where $n, p \in \{1, \ldots, N\}$ denote pixel indexes, $\alpha \in \mathbb{R}^+$ is the parameter of the quadratic phase factor $\mathrm{e}^{i\alpha n^2}$ describing the curvature in the detection plane of a wave emitted by a point source in the object plane. We illustrate in figure A.5 the complete hologram recorded with the CMOS camera.

F can be back-propagated numerically to the target plane with the standard convolution method when all measurements $F \in \mathbb{C}^N$ are available. In this case, the complex field in the object plane f is retrieved from a discrete inverse Fresnel transform of F; $f = \mathcal{F}^{-1}(F)$:

$$f_p = \frac{1}{N} \sum_{n=1}^{N} F_n \, \mathrm{e}^{-i\left(\alpha n^2 - 2\pi np/N\right)} \tag{A.7}$$

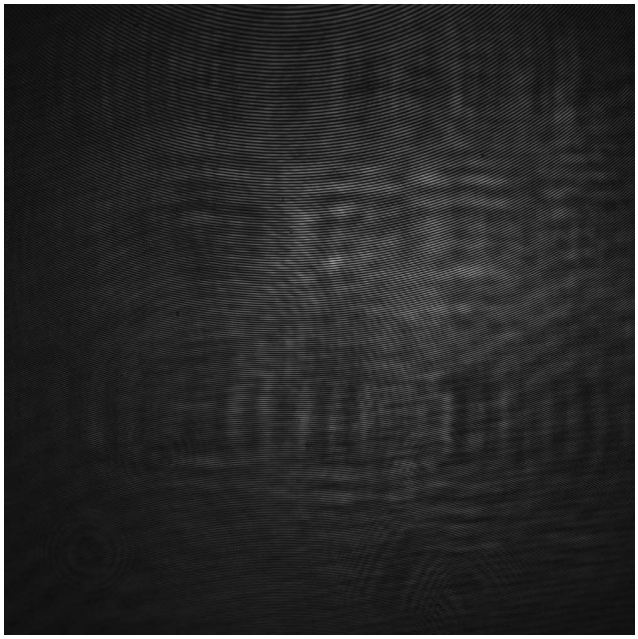

Figure A.5: Fresnel hologram measured with CMOS.

However, we want to recover the intensity image of the object $g = \{|f|^2 : f \in \mathbb{C}^N\}$ from a small number of measurements $F|_\Gamma \in \mathbb{C}^M$ where $M \ll N$. Partial measurements in the detection plane can be written as $F|_\Gamma = \Phi f$, where the sampling matrix Φ models a discrete Fresnel transform (A.6) and random sampling with a uniform spatial distribution of the measurements locations.

In CS, the signal reconstruction consists in solving a convex optimization problem that finds the candidate $\hat{g}$ ($\hat{\cdot}$ denotes an estimator) of minimal complexity satisfying $\hat{F}|_\Gamma = F|_\Gamma$, where $F|_\Gamma \subseteq F$ is a partial subset of measurements in the set Γ.

To find the best estimator $\hat{g}$ with a controlled robustness to noise, we solve the following convex optimization problem [Candès 2006a]:

$$\hat{g} = \arg\min_{g \in \mathbb{R}^N} \| \nabla g \|_{\ell_1} \quad \text{s.t.} \quad \| \hat{F}|_\Gamma - F|_\Gamma \|_{\ell_2} \leq \delta \tag{A.8}$$

for some $\delta \leq C\varepsilon$, which depends on the noise energy.

A.4 Results

The undersampled patterns are illustrated in figures A.7 and A.6. The random undersampling corresponds to the figure A.6 and the radial sampling in figure A.6. Both sets of measurements corresponds to 15% of all Fresnel coefficients. The reconstructions for these sets of measurements are in figures A.8b and A.8c, for the random and radial sampling respectively. We also show the reconstruction using all measurements (figure A.8a) such as conventional holography does.

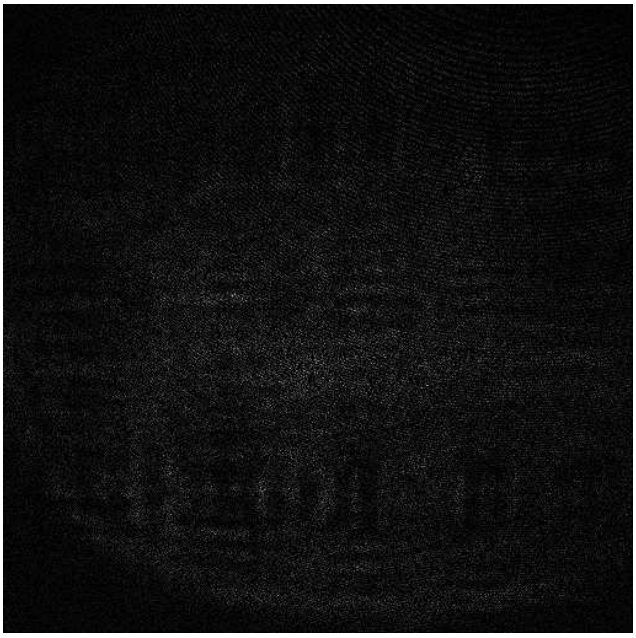

Figure A.6: Random pattern from undersampling.

A.5 Conclusion

In conclusion, we have demonstrated the feasibility of compressed sensing using digital holography and most important, from a real undersampling. We used a programmable CMOS camera to perform random and radial undersampling in the Fresnel domain. Using 15% of measurements with both radial and random pattern, we demonstrate that the image can be reconstructed without much loss of information compared to the reconstruction using all measurements. For future work, it should be useful if compressed sensing could be used in fluorescence microcopy or for general microscopy methods. However this problem should be solved differ-

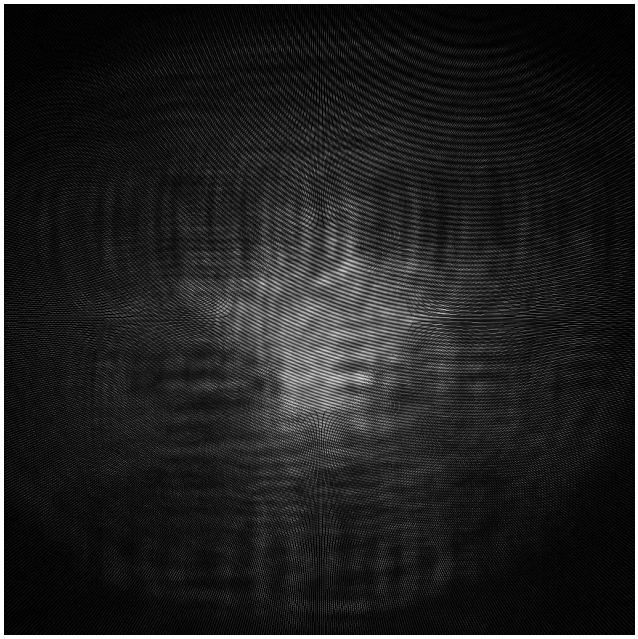

Figure A.7: Radial pattern from undersampling.

ently since the acquisition principle of holography can't be applied to conventional microscopy due to incoherent light.

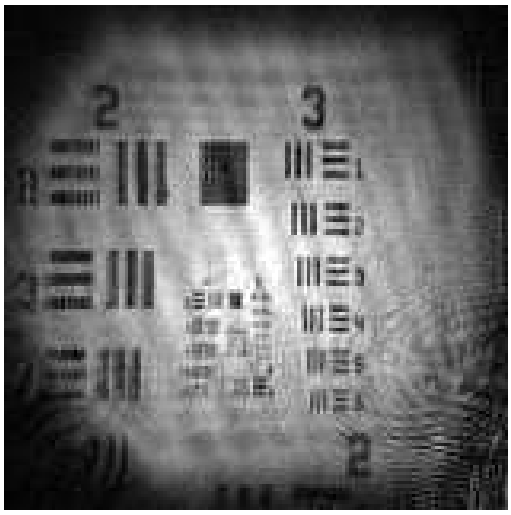

(a) Conventional Holography

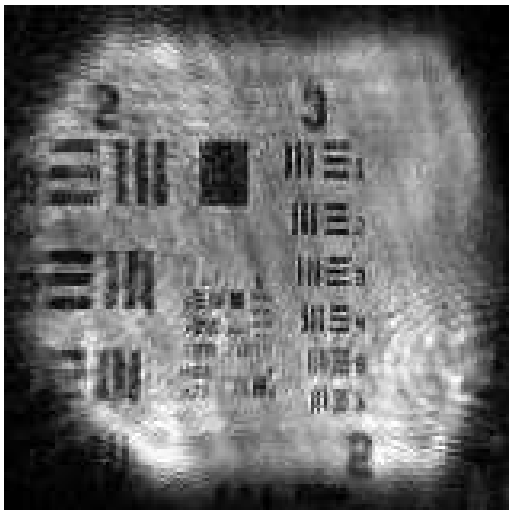

(b) CS with random sampling

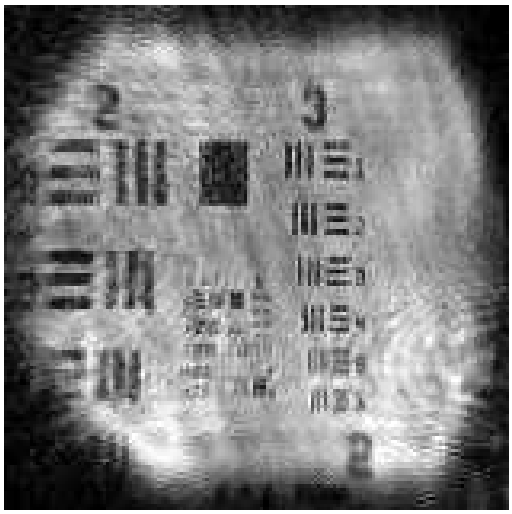

(c) CS with radial sampling

Figure A.8: Conventional digital holography and CS reconstruction with radial and random sampling from only 15% of measurements.

Appendix B

Reducing Photobleaching on Fluorescence Microscopy

We propose an application of compressed sensing on fluorescence microscopic images, as a powerful denoising method, enabling the reduction of photobleaching on images under reduced exposition times. Our denoising framework is based on the property of CS to efficiently reconstruct sparse signals with under-sampled acquisition rates, significantly below the Shannon/Nyquist theoretical bound. Similarly to recent experiments for MRI CS-based reconstruction [Lustig 2007], the acquisition protocol consists in measuring the image signal onto a random set of Fourier vectors [Candès 2006a], which is incoherent to the domain where the image is sparse. Indeed, the CS framework introduced by Candès [Candès 2006d] provides theoretical results and shows that if a signal is sparse (i.e. has a small number of non-zero coefficients) in some basis, then with high probability, uniform random projections of this signal onto an unstructured domain, where the signal is not sparse, contains enough information to optimally reconstruct this signal [Candès 2006d]. The incoherence property between the sparsity basis Ψ and the sampling basis Φ ensures that signals having sparse representations in Ψ must have a large support in the measurement domain described by Φ [Candès 2006b]. Random selections of basis functions in Φ are typically suitable since random vectors are, with very high probability, incoherent with any sparsity-encoding basis functions from Ψ, defining orthogonal domains [Donoho 2006b].

Contents

A.1 Introduction **144**

A.2 The Acquisition System **145**

[0]Based upon: M. Marim, E. Angelini and J.-C. Olivo-Marin.*"A Compressed Sensing approach for biological microscopic image processing"*, IEEE International Symposium on Biomedical Imaging, ISBI, pp. 1374-1377, 2009.

A.2.1 The Holographic Setup 145
A.2.2 The Programmable CMOS Camera 147
A.2.3 Preliminary Experiences 148
A.3 The Image Reconstruction 148
A.4 Results 151
A.5 Conclusion 151

B.1 Introduction

Here we propose an application of *Compressed Sensing* on fluorescence microscopic images, as a powerful denoising method, enabling the reduction of photobleaching on images under reduced exposure times. Our denoising framework is based on the property of CS to efficiently reconstruct sparse signals with under-sampled acquisition rates, significantly below the Shannon/Nyquist theoretical bound. Similarly to recent experiments for MRI CS-based reconstruction [Lustig 2007], the acquisition protocol consists in measuring the image signal onto a random set of Fourier vectors [Candès 2006a], which is incoherent to the domain where the image is sparse. Indeed, the CS framework introduced by Candès [Candès 2006d] provides theoretical results and shows that if a signal is sparse (i.e. has a small number of non-zero coefficients) in some basis, then with high probability, uniform random projections of this signal onto an unstructured domain, where the signal is not sparse, contains enough information to optimally reconstruct this signal [Candès 2006d]. The incoherence property between the sparsity basis Ψ and the sampling basis Φ ensures that signals having sparse representations in Ψ must have a large support in the measurement domain described by Φ [Candès 2006b]. Random selections of basis functions in Φ are typically suitable since random vectors are, with very high probability, incoherent with any sparsity-encoding basis functions from Ψ, defining orthogonal domains [Donoho 2006b].

In fluorescence microscopy, cellular components of interest in specimens such as proteins are typically labeled with a fluorescent molecule called a fluorophore such as green fluorescent protein (GFP) and can therefore be imaged with high specificity. Fluorophores lose their ability to fluoresce as they are illuminated through a process called photobleaching [Song 1995, Benson 1985]. In microscopy, observation of fluorescent molecules is challenged by the photobleaching, as these molecules are

slowly destroyed by the light exposure necessary to stimulate them into fluorescence. Loss of emission activity caused by photobleaching can be controlled by reducing the intensity or time-span of light exposure. At the same time, reducing the exposure time or intensity of the excitation also reduces the emission intensity but not the noisy acquisition components, leading to a decrease of the SNR. We propose to use the CS sampling and reconstruction framework to denoise and improve the SNR of microscopic fluorescence images acquired with shorter exposure times to reduce photobleaching.

B.1.1 Fluorescence Microscopy

Fluorescence emission occurs when an orbital electron of a molecule, atom or nanostructure relaxes to its ground state by emitting a photon after being excited to a higher quantum state by some type of energy. The figure B.1 illustrate the excitation and emission phenomenon. Let $h\nu$ represents the photon energy with h the

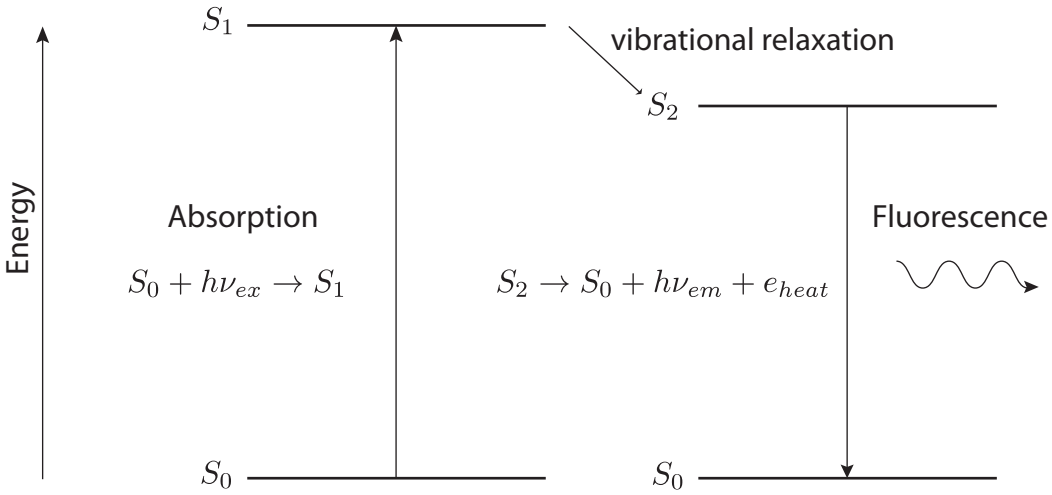

Figure B.1: Fluorescence photochemistry diagram.

Planck's constant and ν_{ex} the excitation light frequency. The S_0 level is the ground state and S_1 is the excited state after the photon absorption. After excitation and absorption the excited state S_1 can suffer from a vibrational relaxation and go to S_2 state still excited and finally, the S_2 state can relax by various competing pathways. It can release a non-radiative energy which may be dissipated as heat or vibrations. Fluorescence may occurs if relaxation from excited state S_2 to the ground state S_0 generating a less energetic photon $h\nu_{em}$. Excited organic molecules can also relax

via conversion to a triplet state which may subsequently relax via phosphorescence or by a secondary non-radiative relaxation step. This is discussed in the next subsection which is related to photo-damage. Fluorescence microscopy techniques have enabled numerous studies in biology by combining fluorescence and microscopy.

Fluorescence microscopy is a powerful technique for live-cell imaging, commonly used in biology. The specimen is illuminated with light at a specific wavelength which is absorbed by the fluorophores, causing them to emit light of longer wavelengths (with less energy, i.e. of a different color than the absorbed light). Before detection, the illumination light is separated from the emitted fluorescence through the use of a spectral emission filter.

The major part of fluorescence microscopes in use are epifluorescence microscopes which means that excitations and observations of the fluorescence are from above the specimen. Epifluorescence microscopes have become an important part in the field of biology, opening the doors for more advanced microscope designs, such as the confocal microscope [Pawley 1995] and the total internal reflection fluorescence microscope (TIRF) [Axelrod 2001, Axelrod 2008].

Fluorescence can be either endogenous (i.e. inherent to the cellular molecules) or, more commonly heterogeneous, introducing exogenous fluorescent molecules. Green fluorescent protein (GFP) [Chalfie 2000] technology has revolutionized live cell imaging as an auto-fluorescent molecule can be genetically encoded as a fusion with the cDNA of interest. Moreover, manipulating spectral variants of GFP and others fluorescent proteins enable multicolor imaging of living cells.

There are many other potential probes that can be introduced into cells like specific fluorescent lipid molecules and organelle-specific dyes. These probes are often cell-permeable and can simply be added to the culture medium.

When selecting an acquisition system for imaging living cells, one should consider the sensitivity of detection, the speed of acquisition, and the viability of the specimen. Light microscopy of living versus fixed samples is essentially a trade-off between acquiring images with a high signal-to-noise ratio and damaging the sample under observation, which is particularly critical in live-cell imaging.

In chapter 2 we discuss the signal-to-noise ratio limitations in microscopy and the cross-correlation with the photo-damage effect, which is discussed in Appendix B. We present results based on a compressed sensing framework to simultaneously improve on these limitations.

B.1.2 Photobleaching and Photodamage

Photobleaching occurs when a fluorophore permanently loses the ability to fluoresce due to photon-induced chemical damages [Axelrod 1976]. Upon transition from an excited singlet state to the excited triplet state, fluorophores may interact with another molecule to produce irreversible covalent modifications.

The most common photobleaching effect involves the interaction of the fluorophore with a combination of light and oxygen. Fluorophores and oxygen molecules react permanently destroying the fluorescence and yielding a free radical singlet oxygen species that can chemically modify other molecules in living cells. Photobleaching effects can be reduced by reducing the amount of illumination of fluorophores, which can be achieved by reducing the exposure time or by lowering the excitation energy level.

However, these techniques also reduce the measurable fluorescence signal, decreasing the signal-to-noise ratio and compromising the image quality. This central problem in fluorescence microscopy is also discussed in section 3.2 and an efficient solution is introduced in chapter B.

The figure B.2 displays an image sequence of fluoresceine with 200 frames, each one exposed 20 milliseconds. We can observe in this figure that image quality is degraded by photobleaching with decreasing fluorescence intensity.

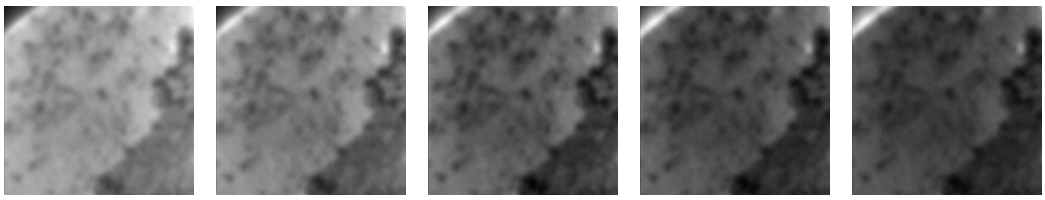

(a) frame 1 (b) frame 50 (c) frame 100 (d) frame 150 (e) frame 200

Figure B.2: Image sequence of fluoresceine. Images are exposed 20 milliseconds each (200 frames).

Photobleaching and SNR are cross-dependent, as illustrated in the graph B.3 where the blue curve shows the fluorescence intensity from the frame 1 to the 200, and the red curve shows the increase in the photobleaching effect along with, the SNR decreases along time. Intuitively, in the graph B.4 the red curve shows that the SNR should significantly increase if all images were accumulated. Indeed, by increasing the exposure time from 20 ms to 4000 ms, the SNR goes from 2dB to

17dB, but the fluorescence intensity goes from 0.64 to 0.10.

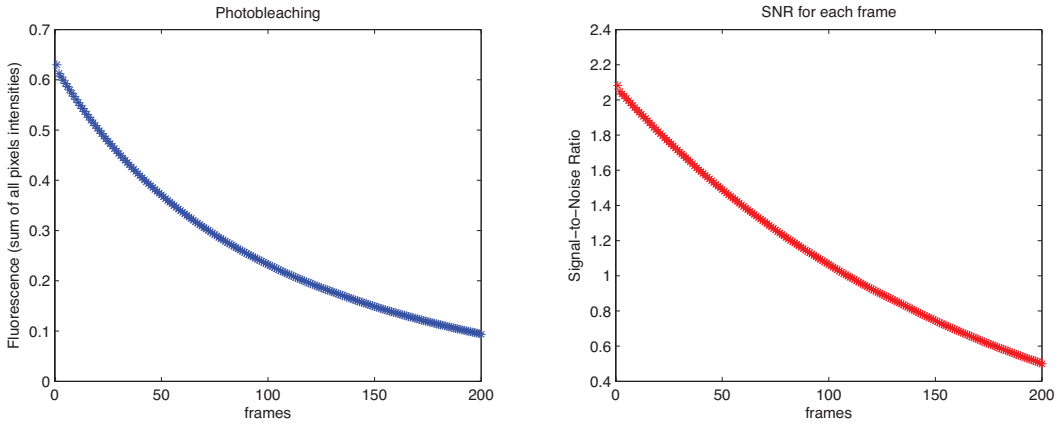

Figure B.3: Photobleaching and SNR profiles of the image sequence of fluoresceine.

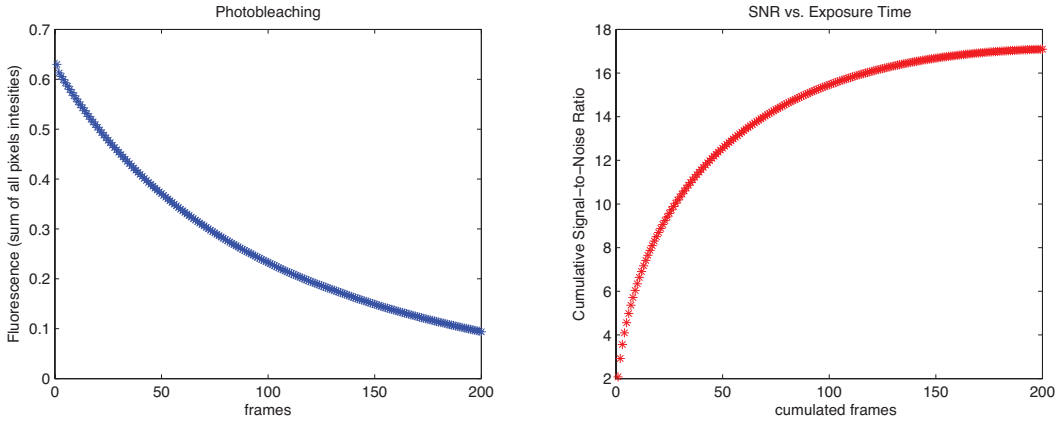

Figure B.4: Photobleaching curve of the image sequence of fluoresceine and SNR of accumulated frames (SNR vs. exposure time).

B.2 Methods

B.2.1 Reconstruction from Noisy Measurements

Considering that a signal x has a sparse representation in some basis Ψ, we want to recover the signal $x \in \mathbb{R}^N$ from noisy measurements $y = \Phi(x + n) \mid y \in \mathbb{R}^M$, the sampling matrix being defined by M vectors in Φ, with $M \ll N$. The presence of noise in the acquired signal might alter its sparsity in the domain Ψ. By optimally reconstructing a signal with explicit sparsity constraints, CS offers a theoretical

framework to remove non-sparse random noise components from a corrupted signal. Indeed, removing noise from $x + n$ will rely on the efficacy of Ψ on representing the signal x sparsely and the inefficacy on representing the noise n [Donoho 2006a]. The choice of the basis function Ψ is very important and depends directly on the kind of signal (or image) we want to recover and denoise using CS. If we make the assumption that the noise energy is bounded by a known constant $\| n \|_{\ell_2} \leq \varepsilon$, the transformed signal Ψx is sparse, and $\Phi \in \mathbb{R}^{MN}$ is a random matrix sampling x in the Fourier domain, the spatial signal x can be recovered nearly exactly using the following convex optimization:

$$\hat{x} = \arg \min_{x \in \mathbb{R}^N} \| \Psi x \|_{\ell_1} \text{ s.t. } \| y - \Phi x \|_{\ell_2} \leq \delta \tag{B.1}$$

for some small $\delta > \varepsilon$, where the operator Ψ is equivalent to compute the gradient, and hence the ℓ_1 norm of Ψx corresponds to the *Total Variation* (TV) of x, $\| \Psi x \|_{\ell_1} \Leftrightarrow \| \nabla x \|_{\ell_1} = \| x \|_{TV}$. In [Candès 2006c] it was shown that the solution $\hat{x}$ is guaranteed to be within $C\delta$ ($C \in \mathbb{R}^+$) of the original signal x.

$$\| \hat{x} - x \|_{\ell_2} \leq C\delta \tag{B.2}$$

We note here that this CS-based estimation framework, with noisy observations and TV spatial constraints [Candès 2005d], guarantees that no false component of $x + n$ with significant energy is created as it minimizes the ℓ_1 norm of $\hat{x}$, which is particularly high for the additive random noise components. More specifically, the TV-based spatial sparsity constraint, will lead to sharp edges and removal of noise components, resulting in an error:

$$\| \hat{x} - x \|_{\ell_2} \leq \alpha + \beta \tag{B.3}$$

where α reflects the desired error (responsible for noise removal) from the relaxation of the constrain δ in (B.1) and β reflects the undesired error from Fourier undersampling of the signal. If TV represents x efficiently and n inefficiently, the term β vanishes and $\alpha \to C\delta$.

In the context of microscopic images, noise models usually combine Poisson and Gaussian components, and the observation model commonly adopted is the

following:

$$\begin{aligned} I(x,y) = \quad & \zeta U_i(A(x,y)+\lambda_B)+V_i, \\ & U_i \sim \mathcal{P}(\lambda_i), \;\; V_i \sim \mathcal{N}(\mu,\sigma^2) \end{aligned} \tag{B.4}$$

where ζ is the overall gain of the detector, $A(x,y)$ is the object intensity, λ_B is the mean intensity of the background, U_i is a Poisson variable modeling the photon counting and V_i is a normal distribution with mean intensity μ and standard deviation σ, U_i and V_i are assumed mutually independent.

B.2.2 The Recovery Algorithm

As an alternative to image sampling and acquisition problems we focus on utilizing dual sparse and redundant representations in the CS framework for fluorescence microscopic image denoising.

The proposed CS-based denoising scheme consists in determining the shorter exposition time X necessary to obtain, with a set of combined CS restorations associated to a set of sampling matrices Φ_i, a target SNR level, corresponding to the SNR measured on the image exposed $T\ ms$. This scheme provides the potential advantage of requiring a single shorter acquisition time, limiting degradation of the biological material through photo-damage and photo-bleaching. We also exploit the fact that fluorescence signal $\Phi_i x$ should be strongly correlated for all sampling matrix Φ_i, while noisy sampling $\Phi_i n$ should not be.

Combining CS reconstructions of a single noisy image acquisition $x+n$, using different sampling matrices Φ_i, is performed as described below:

$$\hat{x}_i = \arg\min_{x\in\mathbb{R}^N} \| \Psi x \|_{\ell_1} \text{ s.t. } \| y_i - \Phi_i x \|_{\ell_2} \leq \delta \tag{B.5}$$

for $i = 1...K$.

The last step of the algorithm involves the combination of $\hat{x}_i$ by averaging to generate a final denoised image $\hat{x}$. The number of images combined will introduce a regularization on the final image. We show that averaging grater number of images recovered with CS reduces exponentially the TV, as illustrated in Figure B.5.

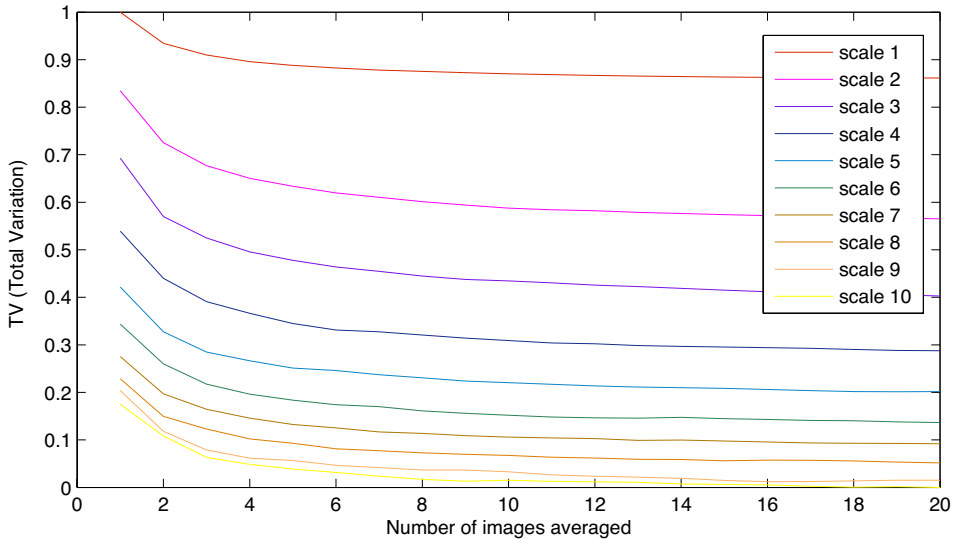

Figure B.5: TV versus number of images (Lymphocytes) recovered and combined for the 10 scales represented in Figure B.6.

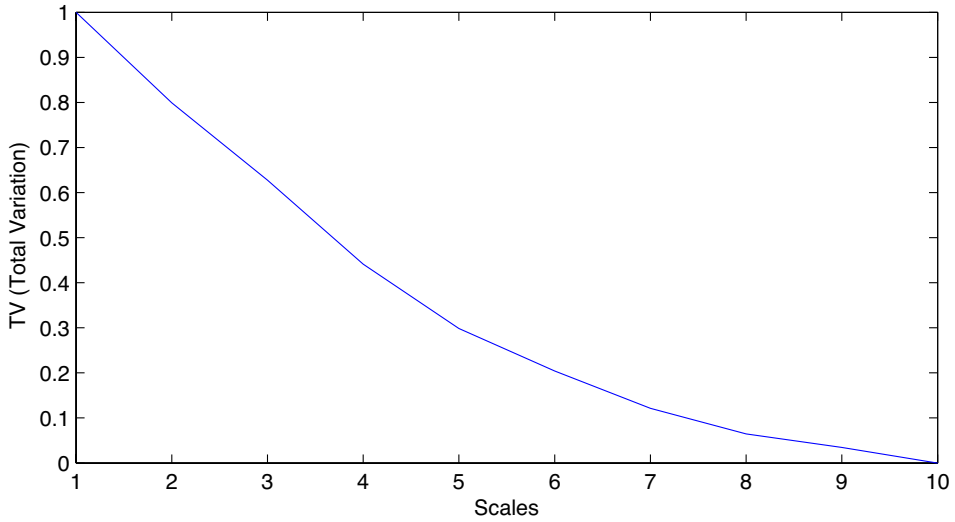

Figure B.6: TV versus scales for recovered images of Lymphocytes. Scales vary from a compression ratio exponentially increasing from $M = 30\%$ to $M = 0.3\%$.

B.3 CS and Scalability

With our working assumptions on the additive noise components, we propose to derive a series of CS reconstructions that will enable to separate noisy components from fluorescence signal reconstructions. The degree of freedom in this series of CS experiments in the choice of the sampling matrix Φ. Since the sparsity operator, TV, operates on the spatial domain, we chose to work with the orthogonal basis functions of random sampling in the Fourier domain. The degree of freedom for the choice of the Φ matrix, then becomes the number of random measurements M that is used. The CS theoretical framework states that the more measurements are used in the Φ domain, the closer is the reconstructed signal to the original measured signal. In the context of denoising (rather than estimation) we have a dual constraint on the noisy nature of the measurement and the risk to reconstruct these noisy components. Indeed, for a single CS experiment, the fluorescence signal will generate, from a set of random measures of structured Fourier values, a restored image with high values depicting a good estimation of the true signal. At the same time, purely random noisy component will be interpreted, from a set of undifferentiated Fourier values, as a structured combination of oscillating components, extrapolated over the spatial domain into patches, under the regularizing TV effect. Noise patches and fluorescence spatial localization will be directly related to M, the number of CS measurements acquired by Φ. We illustrate in Figure B.7 and B.8 how this number of measurements can be naturally viewed as a scale parameter, and in Figure B.6 how the TV decrease beyond scales. For Figure B.8, we cropped a background area from a fluorescence microscopic image, with pure noise signal, and performed CS reconstructions across scales (i.e. different numbers of measurements).

In the experiment on Figures B.7 and B.8, we observe that noise component is more uncorrelated than signal across scales while the spatial resolution of the signal component decreases. Increasing scale leads to a more difficult discrimination of signal and noise components.

We can make a connection here to the notion of multi-scale transforms which is discussed in [Lindeberg 1994]. These transforms were theoretically defined as linear transforms with a scale parameter controlling the ability of the transform to simplify the signal. We know from the sparsity constraint that strong true signals recovered by the CS framework will correspond to strong underlying components

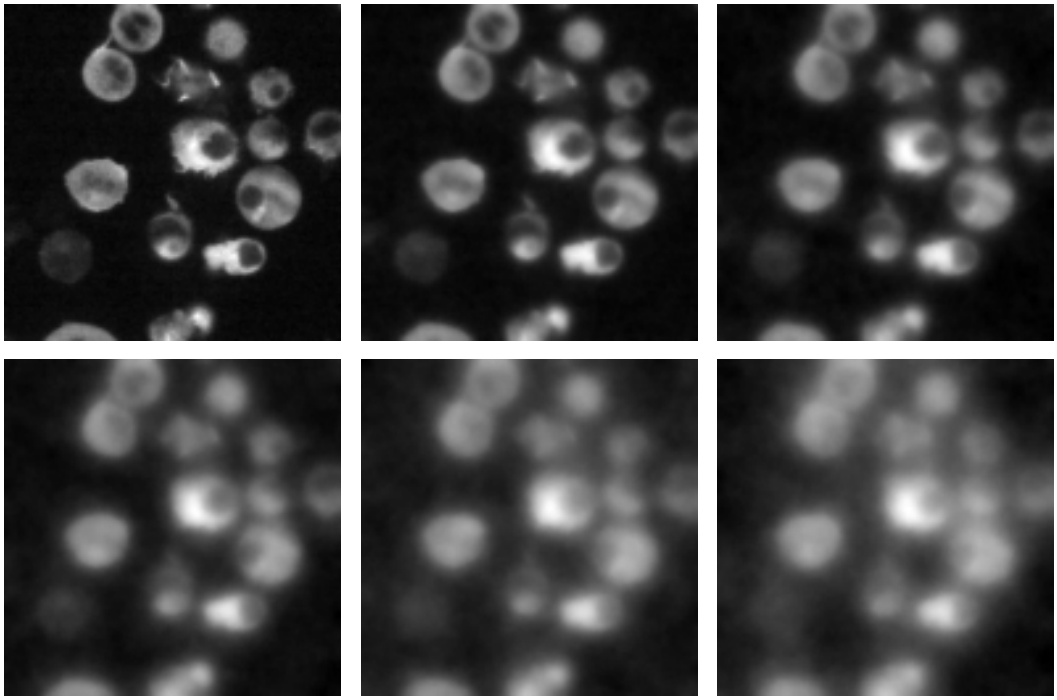

Figure B.7: Fluorescence microscopic image of Lymphocytes. Results from the same image recovered with six different numbers of measurements (i.e. 6 scales). Scales vary from a compression ratio exponentially increasing from $M = 30\%$ to $M = 0.3\%$.

in the context of noise estimation from a small set of measurements. Therefore, CS does not introduce false signal components and fits well in the framework of multi-scale transforms, as illustrated in Figure B.7.

Relaxing the constrain δ, which corresponds to the error allowed in (B.1), enables noise removal, or the appearance of patches which can present smooth edges. The difference between Figure B.8 top and bottom comes from the relaxation of the constraint $\delta_{bottom} > \delta_{top}$, increasing smoothness of the reconstructed images. The good news is that in both cases, if results from CS reconstructions of a pure noise signal are combined at different scales, the mean intensity returns a nearly homogeneous signal, as seen in Figure B.9. This observation clearly justifies the averaging operator introduced in section B.2.2 to remove noise from images.

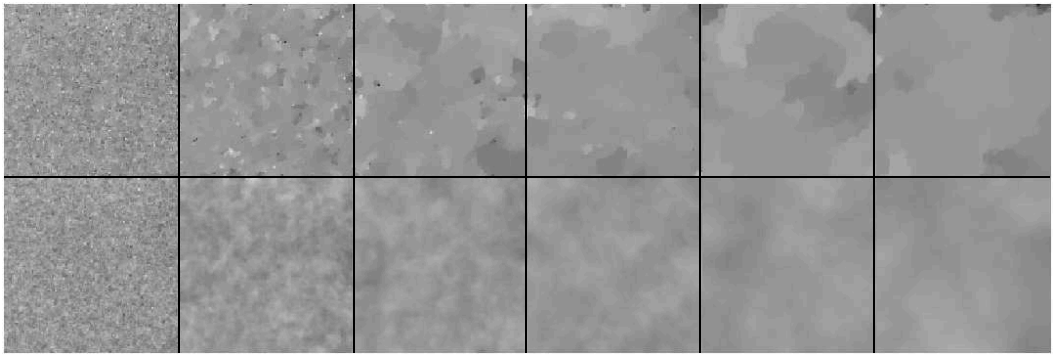

Figure B.8: Top: Pure noise signal extracted from a background patch of a microscopic image, recovered with six scales, (i.e. six different sizes of sample measurements). Scales vary exponentially from $M = 30\%$ to $M = 0.3\%$. Bottom: relaxing the constrain $\delta_{bottom} > \delta_{top}$.

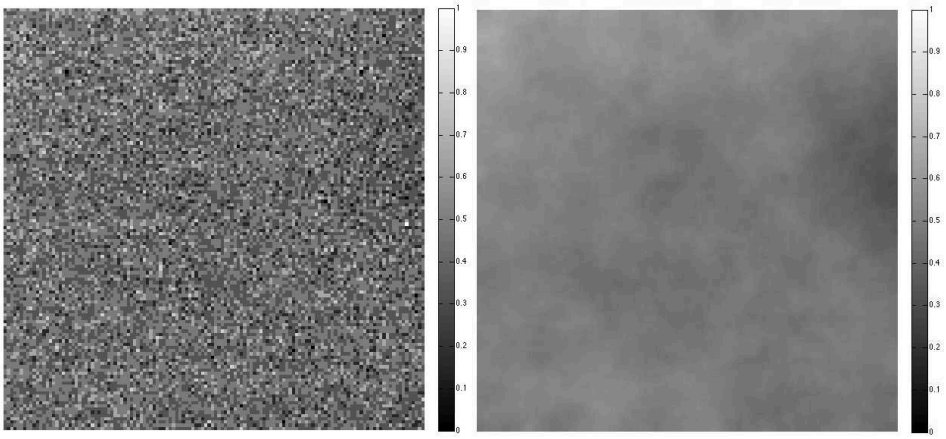

Figure B.9: Left: Pure noise image extracted from a microscopic image background. Right: Result obtained averaging 20 images recovered with different sets of measurements Φ_i for $(i = 1...20)$.

B.4 Photobleaching

Photobleaching is a process in which fluorochrome molecules undergo photo-induced chemical destruction upon exposure to light excitation and loose their fluorescence ability. Benson et al. in [Benson 1985] carried out an extensive study on the heterogeneous photobleaching rates, describing their experimental bleaching curve by a three-parameter exponential:

$$I_{(x,y,t)} = A_{(x,y)} + B_{(x,y)}e^{-kt} \tag{B.6}$$

for each pixel in an image. Where $I_{(x,y,t)}$ is the fluorescence intensity at pixel (x, y) at time t, the offset $A_{(x,y)}$ is attributed to the background fluorescence, $B_{(x,y)}$ is the fluorescence intensity which decays exponentially and k is the rate of photon absorption (s^{-1}).

To verify the real photobleaching effect we have acquired 200 fluorescein images exposed 20 ms, with a negligible time transition between two consecutive image acquisitions, resulting in a total exposition time of 2000 ms. In this experiment we can clearly observe the fluorescence intensity decreasing exponentially as described by (B.6) and confirmed in the experience illustrated in Figure B.10 and B.12. As a consequence of the fluorescence intensity decreases, the SNR also decreases as show in Figure B.11. Applying our CS-based method for denoising, we show that SNR can be highly improved while reducing photobleaching. Results on Figure B.11 show that the rate between original SNR and CS-recovered images SNR is ∼160%. Which means that still reaching an equivalent SNR, microscopic images could be acquired with a shorter exposition time, reducing photobleaching. The estimated final photobleaching improvement is illustrated in Figure B.12 by the green curve, computed from the model described in Equation B.6, fitting B and k values on the original images. Estimating the reduction of the exposition time necessary to achieve the same SNR as in the original data using the CS-based denoising scheme, we illustrate in Figure B.12 with the green curve that photobleaching can be highly reduced. The same result can also be visualized in Figure B.10.

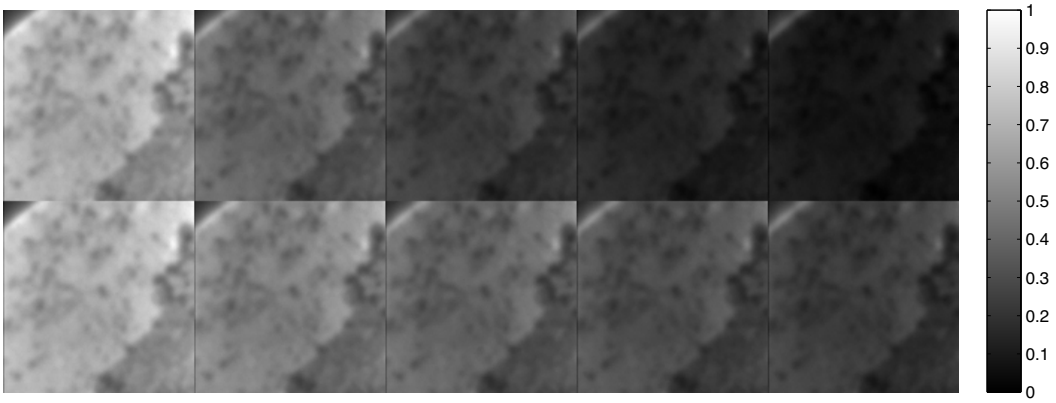

Figure B.10: Fluorescein images. Top: Six samples from the sequence of 200 images tagged with fluorescein. These images were acquired at $t = \{0, 500, 1000, 1500, 2000\}$ ms. Bottom: Supposed photobleaching resulted from 200 image acquisitions using CS denoising.

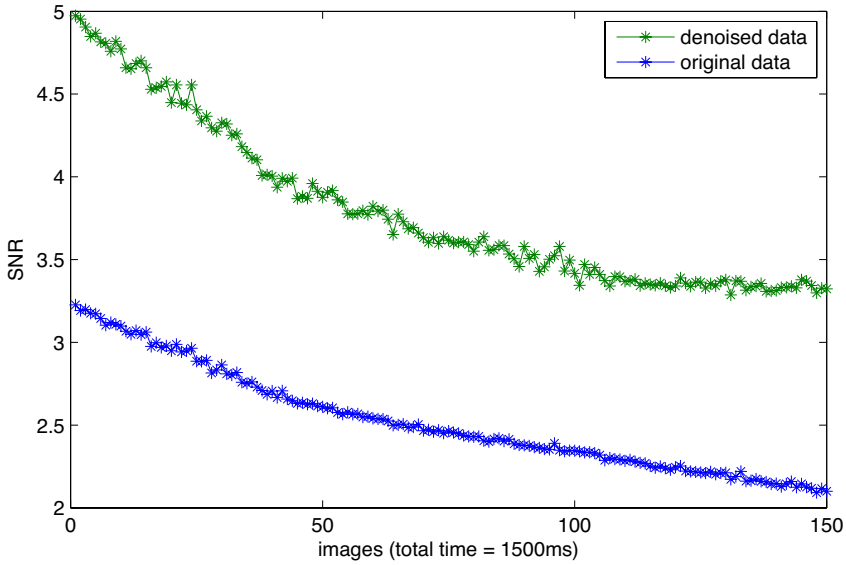

Figure B.11: SNR curves, we use a set of 150 fluorescein images acquired each 10 ms. The green line correspond to the SNR of images recovered with CS using the scheme proposed in Section B.2.2 and the blue line correspond to the SNR of the original set of images.

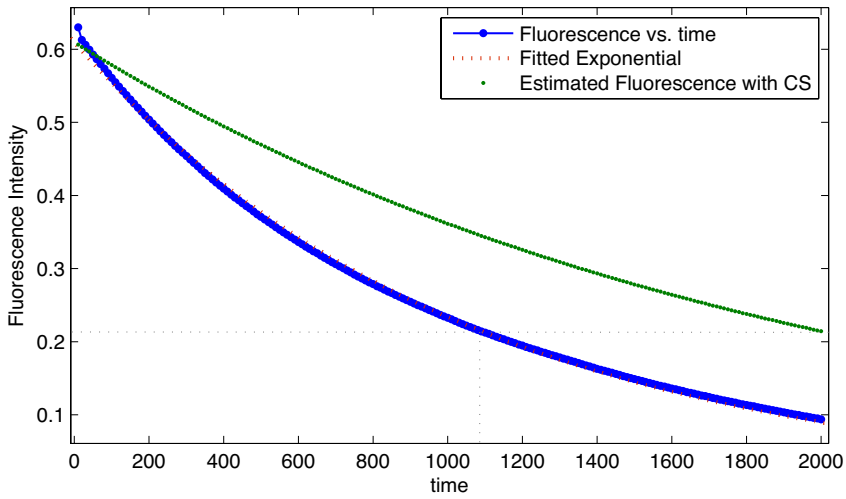

Figure B.12: Photobleaching curves, represented by the mean fluorescence intensity vs. time for original images of fluorescein (blue) and for images denoised with our proposed scheme (green). The red line corresponds to the exponential model fitted to the original data, setting specific values of B and k in Equation (B.6).

B.5 Conclusion

We introduced a CS-based image acquisition and denoising method exploiting multiple reconstructions with random Fourier projections. Our approach presents several advantages over traditional denoising methods, joining image acquisition, CS advantages and denoising in one framework. Through some practical experiments, we have shown that our method can significantly improve the SNR on fluorescent microscopic images and that photobleaching can be highly reduced with shorter exposition times. Such results open the gate to new mathematical imaging protocols, offering the opportunity to reduce exposition time along with photo-damage and photo-bleaching and help biological applications based on fluorescence microscopy.

Bibliography

[Aharon 2005] M. Aharon, M. Elad and A.M. Bruckstein. *The K-SVD Algorithm.* In Proceedings of SPARS'05, Rennes, France, 2005. 18, 20, 37, 49

[Aizu 1999] Yoshihisa Aizu and Toshimitsu Asakura. *Coherent Optical Techniques for Diagnostics of Retinal Blood Flow.* Journal of Biomedical Optics, vol. 4, no. 1, pages 61–75, 1999. 106

[Alizadeh 2003] F. Alizadeh and D. Goldfarb. *Second-order cone programming.* Math. Program., Ser. B, vol. 95, pages 3–51, 2003. 33

[Atlan 2006] M. Atlan, M. Gross, T. Vitalis, A. Rancillac, B. C. Forget and A. K. Dunn. *Frequency-domain, wide-field laser Doppler in vivo imaging.* Optics Letters, vol. 31, no. 18, pages 2762–2764, 2006. 106

[Atlan 2007] M. Atlan, M. Gross and E. Absil. *Accurate phase-shifting digital interferometry.* Optics Letters, vol. 32, pages 1456–1458, 2007. 106, 120, 121, 123

[Atlan 2008] M. Atlan, M. Gross, T. Vitalis, A. Rancillac, J. Rossier and A. C. Boccara. *High-speed wave-mixing laser Doppler imaging in vivo.* Optics Letters, vol. 33, no. 8, pages 842–844, 2008. 90

[Axelrod 1976] D. Axelrod, DE Koppel, J. Schlessinger, E. Elson and WW Webb. *Mobility measurement by analysis of fluorescence photobleaching recovery kinetics.* Biophysical journal, vol. 16, no. 9, pages 1055–1069, 1976. 159

[Axelrod 2001] Daniel Axelrod. *Total Internal Reflection Fluorescence Microscopy in Cell Biology.* Traffic, vol. 2, no. 11, pages 764–774, 2001. 158

[Axelrod 2008] D. Axelrod. *Total internal reflection fluorescence microscopy.* Methods in cell biology, vol. 89, pages 169–221, 2008. 158

[Bailey 1993] B. Bailey, D. L. Farkas, D. L. Taylor and F. Lanni. *Enhancement of axial resolution in fluorescence microscopy by standing-wave excitation.* Nature, vol. 366, no. 6450, pages 44–48r, November 1993. 77

[Baraniuk 2007] R. Baraniuk. *Compressive Sensing.* vol. 24(4), pages 118–121, July 2007. xiii, 84, 85, 86

[Becker 2009] Stephen Becker, Jérôme Bobin and Emmanuel Candès. *NESTA: A fast and accurate first-order method for sparse recovery.* Rapport technique, Caltech, 2009. 33, 34, 118

[Ben-Tal 2001] Aharon Ben-Tal and Arkadi Nemirovski. Lectures on Modern Convex Optimization: Analysis, Algorithms, and Engineering Applications (MPS-SIAM Series on Optimization). Society for Industrial Mathematics, August 2001. 35

[Benson 1985] D. Benson, J. Bryan, A. Plant, A. Gotto and L. Smith. *Digital Imaging Fluorescence Microscopy: Spatial Heterogeneity of Photobleaching Rate Constants in Individual Cells.* The Journal of Cell Biology, vol. 100, pages 1309–1323, 1985. 156, 166

[Berg 2008] E. Van Den Berg and M. P. Friedlander. *Probing the Pareto frontier for basis pursuit solutions.* SIAM Journal on Scientific Computing, vol. 31, pages 890–912, 2008. 33

[Betzig 2006] E. Betzig, G. H. Patterson, R. Sougrat, O. W. Lindwasser, S. Olenych, J. S. Bonifacino, M. W. Davidson, J. Lippincott-Schwartz and H. F. Hess. *Imaging intracellular fluorescent proteins at nanometer resolution.* Science, vol. 313, no. 5793, pages 1642–1645, 2006. 77

[Bloomfield 1983] P. Bloomfield and W. Steiger. Least absolute deviations: Theory, applications, and algorithms. Birkhauser, 1983. 22

[Bobin 2008] J. Bobin, J-L. Starck and R. Ottensamer. *Compressed Sensing in Astronomy.* IEEE Journal of Selected Topics in Signal Processing, vol. 2, pages 718–726, 2008. 85

[Boulanger 2008] J. Boulanger, J.-B. Sibarita, C. Kervrann and P. Bouthemy. *Non-parametric regression for patch-based fluorescence microscopy image sequence*

denoising. In Biomedical Imaging: From Nano to Macro, 2008. ISBI 2008. 5th IEEE International Symposium on, pages 748 –751, May 2008. 49

[Boulanger 2010] J. Boulanger, C. Kervrann, P. Bouthemy, P. Elbau, J.-B. Sibarita and J. Salamero. *Patch-based non-local functional for denoising fluorescence microscopy image sequences*. IEEE Transactions on Medical Imaging, vol. 29(2), pages 442–454, 2010. 44, 45

[Boyd 2004] S. Boyd and L. Vandenberghe. Convex optimization (chapter 11). Cambridge University Press, 2004. 34, 99, 100

[Brady 2009] David Brady, Kerkil Choi, Daniel Marks, Ryoichi Horisaki and Sehoon Lim. *Compressive Holography*. Optics Express, vol. 17, pages 13040–13049, 2009. 87, 127

[Buades 2005] A. Buades, B. Coll and JM. Morel. *A review of image denoising algorithms, with a new one*. SIAM J. Multiscale Model. Simul., vol. 4 (2), pages 490–530, 2005. 36, 44, 49, 68, 71

[Candès 2004a] E. Candès and J. Romberg. *Quantitative robust uncertainty principles and optimally sparse decompositions*. Found. of Comp. Math., 2004. Submitted. 1, 99

[Candès 2004b] E. Candès, J. Romberg and T. Tao. *Robust uncertainty principles: Exact signal reconstruction from highly incomplete frequency information*. IEEE Trans. Inform. Theory, 2004. Submitted. 1, 2, 33, 78, 127

[Candès 2005a] E. Candès and J. Romberg. *ℓ_1-Magic: Recovery of Sparse Signals via Convex Programming*. Rapport technique, Caltech, 2005. 33

[Candès 2005b] E. Candès and J. Romberg. *Practical signal recovery from random projections*. IEEE Trans. Signal Processing, 2005. Submitted. 148

[Candès 2005c] E. Candès, J. Romberg and T. Tao. *Stable signal recovery from incomplete and inaccurate measurements*. Communications on Pure and Applied Mathematics, 2005. Submitted. 99

[Candès 2005d] E. Candès and T. Tao. *The Dantzig selector: Statistical estimation when p is much larger than n*. Ann. Statist., 2005. 24, 30, 49, 99, 161

[Candès 2005e] E. Candès and T. Tao. *Decoding by linear programming.* IEEE Trans. Inform. Theory, vol. 51(12), pages 4203–4215, 2005. Submitted. 31, 99

[Candès 2006a] E. Candès. *Compressive sampling.* Int. Congress of Mathematics, vol. 3, pages 1433–1452, 2006. 49, 53, 78, 115, 150, 155, 156

[Candès 2006b] E. Candès and J. Romberg. *Sparsity and incoherence in Compressive Sampling.* Inverse Problems, vol. 23(3), pages 969–985, 2006. 29, 31, 116, 117, 155, 156

[Candès 2006c] E. Candès, J. Romberg and T. Tao. *Robust uncertainty principles: Exact signal reconstruction from highly incomplete frequency information.* IEEE Trans. Inform. Theory, vol. 52(2), pages 489–509, 2006. 33, 50, 99, 161

[Candès 2006d] E. Candès, J. Romberg and T. Tao. *Stable signal recovery from incomplete and inaccurate measurements.* Communications on Pure and Applied Mathematics, vol. 59(8), pages 1207–1223, August 2006. 155, 156

[Candès 2006e] E. Candès and T. Tao. *Near-optimal signal recovery from random projections: Universal encoding strategies?* IEEE Transactions on Information Theory, vol. 52, no. 12, pages 5406–5425, December 2006. 33, 99

[Candès 2008] E. Candès. *The restricted isometry property and its implications for Compressed Sensing.* Compte Rendus de l'Academie des Sciences, Paris, vol. Serie I, pages 346 589–592, 2008. 31, 32, 116, 117

[Chalfie 2000] M. Chalfie and D. Prasher. *Green fluorescent protein*, November 14 2000. US Patent 6,146,826. 158

[Chambolle 1997] A. Chambolle and P. L. Lions. *Image recovery via total variation minimization and related problems.* Numer. Math., vol. 76, pages 167–188, 1997. 23, 43

[Chan 1999] T. Chan, G. Golub and P. Mulet. *A nonlinear primal-dual method for total variation-based image restoration.* SIAM J. Sci. Comput., vol. 20, pages 1964–1977, 1999. 33

[Chan 2001] T. F. Chan, S. Osher and J. Shen. *The digital TV filter and nonlinear denoising.* IEEE Trans. on Im. Proc., vol. 10(2), pages 231–241, 2001. 30

[Chen 1998] S. Chen, D. Donoho and M. Saunders. *Atomic decomposition by basis pursuit.* SIAM J. Comput., vol. 20, no. 1, pages 33–61, 1998. 21, 24, 28, 32

[Choi 2010] Kerkil Choi, Ryoichi Horisaki, Joonku Hahn, Sehoon Lim, Daniel L. Marks, Timothy J. Schulz and David J. Brady. *Compressive holography of diffuse objects.* Appl. Opt., vol. 49, no. 34, pages H1–H10, 2010. 127

[Cohen 1999] M.L. Cohen, K.W. Schenck and S. H. Hemrick-Luecke. *5-Hydroxytryptamine(1A) receptor activation enhance norepinephrine release from the nerve in the rabbit saphepus vein.* Pharmacol Exp Ther., vol. 290, pages 1195–1201, 1999. 29

[Cull 2010] Christy Fernandez Cull, David A. Wikner, Joseph N. Mait, Michael Mattheiss and David J. Brady. *Millimeter-wave compressive holography.* Appl. Opt., vol. 49, no. 19, pages E67–E82, 2010. 127

[Davis 1994] G. M. Davis, S. Mallat and Z. Zhang. *Adaptive time-frequency decompositions.* SPIE J. of Opt. Engin., vol. 33, no. 7, pages 2183–2191, July 1994. 22

[Delpretti 2008] S. Delpretti, F. Luisier, S. Ramani, T. Blu and M. Unser. *Multiframe sure-let denoising of timelapse fluorescence microscopy images.* In Biomedical Imaging: From Nano to Macro, 2008. ISBI 2008. 5th IEEE International Symposium on, pages 149 –152, May 2008. 49

[Denis 2009] Loïc Denis, Dirk Lorenz, Eric Thiébaut, Corinne Fournier and Dennis Trede. *Inline hologram reconstruction with sparsity constraints.* Opt. Lett., vol. 34, no. 22, pages 3475–3477, 2009. 87, 127

[DeVore 1992] R.A. DeVore and B.J. Lucier. *Fast wavelet techniques for near-optimal processing.* IEEE Military Communications Conference, pages 48.3.1–48.3.7, 1992. 37, 49

[Donoho 1994] D. L. Donoho and I. M. Johnstone. *Ideal Spatial Adaptation via Wavelet Shrinkage.* Biometrika, vol. 81, pages 425–455, 1994. 18, 37, 38, 39, 40, 41

[Donoho 1995a] D. Donoho, I. Johnstone, G. Kerkyacharian and D. Picard. *Wavelet shrinkage: Asymptopia?* Journal of the Royal Statistical Society, Series B, vol. 57, pages 301–369, February 1995. (with discussion). 37

[Donoho 1995b] D. L. Donoho. *De-noising by Soft-Thresholding*. IEEE Trans. Inform. Theory, vol. 41, no. 3, pages 613–627, May 1995. 18, 37, 39

[Donoho 1995c] D. L. Donoho and I. M. Johnstone. *Adapting to unknown smoothness via wavelet shrinkage*. Journal of the American Statistical Association, vol. 90, pages 1200–1224, 1995. 37, 38, 40, 41

[Donoho 1995d] D. L. Donoho, I. M. Johnstone, G. Kerkyacharian and D. Picard. *Density Estimation by Wavelet Thresholding*. Rapport technique 426, Statistics, Stanford University, 1995. 37, 49

[Donoho 1998] D. L. Donoho and I. Johnstone. *Minimax estimation by wavelet shrinkage*. Ann. Statist., vol. 26, pages 879–921, 1998. 18, 37, 38

[Donoho 2001] D. L. Donoho. *Sparse Components of Images and Optimal Atomic Decompositions*. Constructive Approximation, vol. 17, no. 3, pages 353–382, January 2001. 28

[Donoho 2006a] D. Donoho, M. Elad and V. Temlyakov. *Stable Recovery of Sparse Overcomplete Representations in the Presence of Noise*. IEEE Trans. on Information Theory, vol. 52, pages 6–18, 2006. 31, 50, 117, 161

[Donoho 2006b] D. L. Donoho. *Compressed Sensing*. IEEE Trans. on Information Theory, vol. 52(4), pages 1289–1306, April 2006. 1, 2, 50, 78, 155, 156

[Duarte 2008] Marco Duarte, Mark Davenport, Dharmpal Takhar, Jason Laska, Ting Sun, Kevin Kelly and Richard Baraniuk. *Single-pixel imaging via compressive sampling*. IEEE Signal Processing Magazine, vol. 25(2), pages 83–91, Nov. 2008. 84

[Elad 2006] M. Elad and M. Aharon. *Image denoising via learned dictionaries and sparse representation*. In Conference on Computer Vision and Pattern Recognition, 2006. 18, 37, 49

[Fadili 2006] J. Fadili and J.L. Starck. *Sparse Representation-based Image Deconvolution by Iterative Thresholding*. In Astronomical Data Analysis ADA'06, 2006. 18

[Fadili 2009] J. Fadili, J.L. Starck and F. Murtagh. *Inpainting and zooming using sparse representations*. The Computer J, vol. 52(1), page 64, 2009. 18

[Fienup 1982] J. Fienup. *Phase retrieval algorithms: a comparison.* Applied Optics, vol. 21(15), pages 2758–2769, 1982. 91

[Gabor 1948] D. Gabor. *A new microscopic principle.* Nature, vol. 161, pages 777–778, 1948. 87, 107, 109

[Gabor 1966] D. Gabor and W. P. Goss. *Interference Microscope with Total Wavefront Reconstruction.* J. Opt. Soc. Am., vol. 56, no. 7, pages 849–856, Jul 1966. 109

[Gilboa 2006] Guy Gilboa, Nir Sochen and Yehoshua Y. Zeevi. *Texture Preserving Variational Denoising Using an Adaptive Fidelity Term.* IEEE Trans. on Image Processing, vol. 15(8), pages 2281–2289, 2006. 63

[Goodman 1996] Joseph W. Goodman. Introduction to fourier optics. McGraw-Hill International Editions, second edition édition, 1996. 90, 91, 92, 108, 109

[Gribonval 2003] R. Gribonval and M. Nielsen. *Sparse representations in unions of bases.* Information Theory, IEEE Transactions on, vol. 49, no. 12, pages 3320 – 3325, 2003. 21

[Gribonval 2005] R. Gribonval, R. Figueras i Ventura and P. Vandergheynst. *A simple test to check the optimality of sparse signal approximations.* Rapport technique, Infoscience | Ecole Polytechnique Federale de Lausanne [http://infoscience.epfl.ch/oai2d.py] (Switzerland), 2005. 21

[Gribonval 2007] R. Gribonval and M. Nielsen. *Highly sparse representations from dictionaries are unique and independent of the sparseness measure.* Applied and Computational Harmonic Analysis, vol. 22, no. 3, pages 335 – 355, 2007. 21

[Gross 2007] M. Gross and M. Atlan. *Digital holography with ultimate sensitivity.* Optics Letters, vol. 32, pages 909–911, 2007. 106, 120, 121, 127

[Gustafsson 2000] M. G. L. Gustafsson. *Surpassing the lateral resolution limit by a factor of two using structured illumination microscopy.* Journal Of Microscopy-Oxford, vol. 198, pages 82–87, 2000. 77

[Heintzmann 2006] R. Heintzmann and P. A. Benedetti. *High-resolution image reconstruction in fluorescence microscopy with patterned excitation.* Applied Optics, vol. 45, no. 20, pages 5037–5045, July 2006. 77

[Hell 1994] S. W. Hell and J. Wichmann. *Breaking the diffraction resolution limit by stimulated emission: stimulated-emission-depletion fluorescence microscopy.* Optics Letters, vol. 19, no. 11, pages 780–782, June 1994. 77

[Hell 1995] S. Hell and M. Kroug. *Ground-state depletion fluorescence microscopy, a concept for breaking the diffraction resolution limit.* Applied Physics B: Lasers and Optics, vol. 60 (5), pages 495–497, 1995. 77

[Herman 1993] Brian Herman and John J. Lemasters. *Optical Microscopy: Emerging Methods and Applications.* Academic Press, vol. Book Review, page 1791, 1993. 77

[Hildebrand 1970] B. P. Hildebrand. *General Theory of Holography.* J. Opt. Soc. Am., vol. 60, no. 11, page 1511, 1970. 108

[Hoebe 2007] R. Hoebe, C. Van Oven, T. Gadella Jr, P. Dhonukshe, C. Van Noorden and E. Manders. *Controlled light-exposure microscopy reduces photobleaching and phototoxicity in fluorescence live-cell imaging.* Nature Biotechnology, vol. 25, pages 249–253, 2007. xiii, 81, 82

[Hyvärinen 1999] A. Hyvärinen, P. Hoyer and E. Oja. *Sparse Code Shrinkage: Denoising by Nonlinear Maximum Likelihood Estimation.* Adv. Neural Inf. Process. Syst., vol. 11, pages 473–479, 1999. 37, 49

[Jackson 2009] C. Jackson, R. Murphy and J. Kovačević. *Intelligent Acquisition and Learning of Fluorescence Microscope Data Models.* vol. 18, pages 2071–2084, September 2009. xiii, 80

[Kalifa 2003] Jérôme Kalifa, Andrew Laine and Peter D. Esser. *Regularization in tomographic reconstruction using thresholding estimators.* IEEE Trans. Med. Imaging, vol. 22 (3), pages 351–359, 2003. 41

[Kindermann 2005] S. Kindermann, S. Osher and P. Jones. *Deblurring and denoising of images by nonlocal functionals.* Multiscale Modeling & Simulation, vol. 4 (4), pages 1091–1115, 2005. 43, 44

[Lee 1998] S. H. Lee and M. G. Kang. *Spatio-temporal video filtering algorithm based on 3-D anisotropic diffusion equation.* ICIP, vol. 3(2), pages 447–450, 1998. 44

[Leith 1972] E. N. Leith and J. Upatnieks. *Progress In Holography.* Physics Today, vol. 25, no. 3, pages 28–&, 1972. 109

[Liebling 2003] M. Liebling, T. Blu, É. Cuche, P. Marquet, C.D. Depeursinge and M. Unser. *Local Amplitude and Phase Retrieval Method for Digital Holography Applied to Microscopy.* In A.-M. Boccara, editeur, Proceedings of the SPIE European Conference on Biomedical Optics: Novel Optical Instrumentation for Biomedical Applications (ECBO'03), volume 5143, pages 210–214, Münich, Germany, June 22-25, 2003. 91

[Liebling 2004] M. Liebling, T. Blu and M. Unser. *Complex-wave retrieval from a single off-axis hologram.* J Opt Soc Am A, vol. 21, page 367, 2004. 90

[Liebling 2006] M. Liebling, A. S. Forouhar, R. Wolleschensky, B. Zimmermann, R. Ankerhold, S. E. Fraser, M. Gharib and M. E. Dickinson. *Rapid three-dimensional imaging and analysis of the beating embryonic heart reveals functional changes during development.* Developmental Dynamics, vol. 235(11), pages 2940–2948, 2006. 7

[Lindeberg 1994] T. Lindeberg. Scale-space theory in computer vision. The Kluwer International Series in Engineering and Computer Science, Dordrecht: Kluwer Academic, 1994. 57, 164

[Luisier 2010] F. Luisier, T. Blu and M. Unser. *Image Denoising in Mixed Poisson-Gaussian Noise.* IEEE Trans Image Process, 2010. 49

[Lustig 2005] M. Lustig, J. M. Santos, J. H. Lee, D. L. Donoho and J. M. Pauly. *Application of 'Compressed Sensing' for rapid MRI imaging.* In Proc. SPARS'05, Rennes, France, 2005. 83

[Lustig 2007] M. Lustig, D. Donoho and J. M. Pauly. *Sparse MRI: The application of compressed sensing for rapid MR imaging.* Magnetic Resonance in Medicine, vol. 58(6), pages 1182–1195, 2007. xiii, 49, 83, 84, 85, 90, 129, 155, 156

[Mallat 1993] S. Mallat and Z. Zhang. *Matching Pursuits with Time-Frequency Dictionaries.* IEEE Trans. Signal Processing, vol. 41, no. 12, pages 3397–3415, Dec. 1993. 22

[Mallat 1998] S. Mallat. A wavelet tour of signal processing. Academic Press, 1998. 38, 39

[Mallat 2009] S. Mallat. A wavelet tour of signal processing. Academic Press, 2009. 18

[Marcia 2009] Roummel Marcia, Zachary Harmany and Rebecca Willett. *Compressive Coded Aperture Imaging.* In SPIE Electronic Imaging, 2009. 86

[Minsky 1988] M. Minsky. *Memoir on inventing the confocal microscope.* vol. 10, pages 128–138, Scanning 1988. 77

[Moravec 2007] M. Moravec, J. Romberg and R. Baraniuk. *Compressed Sensing phase retrieval.* SPIE, Wavelets XII, vol. 6701, 2007. 91, 92

[Nesterov 1983] Y Nesterov. *A method of solving a convex programming problem with convergence rate O (1/k2).* Soviet Mathematics Doklady, vol. 27, no. 2, pages 372–376, 1983. 34, 118

[Nesterov 1994] Y. E. Nesterov and A. S. Nemirovski. *Interior Point Polynomial Methods in Convex Programming.* SIAM Publications, Philadelphia, 1994. 33

[Nesterov 2004] Yurii Nesterov. Introductory lectures on convex optimization: A basic course, volume 0. Kluwer Academic Publishers, 2004. 34, 118

[Nesterov 2005] Y Nesterov. *Smooth minimization of non-smooth functions.* Mathematical Programming, vol. 103, no. 1, pages 127–152, 2005. 34, 35, 118

[Nesterov 2007] Yurii Nesterov. *Gradient methods for minimizing composite objective function.* Rapport technique, Université Catholique de Louvain, 2007. 34

[Olivo-Marin 2002] Jean-Christophe Olivo-Marin. *Extraction of spots in biological images using multiscale products.* Pattern Recognition, vol. 35, no. 9, pages 1989–1996, may 2002. 49

[Olshausen 1997] B. A. Olshausen and D. J. Field. *Sparse coding with an overcomplete basis set: A strategy employed by V1?* Vision Research, vol. 37, page 3311–3325, 1997. 2

[Pati 1993] Y. C. Pati, R. Rezaifar and P.S. Krishnaprasad. *Orthogonal matching pursuit: Recursive function approximation with applications to wavelet decomposition.* In Proc. 27th Asilomar Conference on Signals, Systems and Computation, November 1993. 22

[Pawley 1995] James B. Pawley. Handbook of biological confocal microscopy. Plenum Press, 1995. 158

[Peyre 2010] G. Peyre, J. Fadili and J-L. Starck. *Learning the Morphological Diversity.* SIAM Journal of Imaging Science, vol. 3 (3), pages 646–669, 2010. 41

[Rappaz 2005] Benjamin Rappaz, Pierre Marquet, Etienne Cuche, Yves Emery, Christian Depeursinge and Pierre Magistretti. *Measurement of the integral refractive index and dynamic cell morphometry of living cells with digital holographic microscopy.* Opt. Express, vol. 13, no. 23, pages 9361–9373, 2005. 106

[Rose 2002] C. Rose and M. D. Smith. Mathematical statistics with mathematica, chapter 7.2c: k-statistics: Unbiased estimators of cumulants. Springer-Verlag, 2002. 15, 63

[Rudin 1992] L. Rudin, S. Osher and E. Fatemi. *Nonlinear Total Variation based Noise Removal Algorithms.* Physica D, vol. 60, pages 259–268, 1992. 23, 30, 34, 36, 41, 49

[Rudin 1994] L. Rudin and S. Osher. *Total Variation based image restoration with free local constraints.* In IEEE ICIP, pages 31–35, 1994. 23, 41, 43

[Rust 2006] Michael Rust, Mark Bates and Xiaowei Zhuang. *Sub-diffraction-limit imaging by stochastic optical reconstruction microscopy (STORM).* Nature Methods, vol. 3, pages 793–796, 2006. 77

[Schnars 1994] U. Schnars and W. Juptner. *Direct recording of holograms by a CCD target and numerical reconstruction.* Appl. Opt., vol. 33, pages 179–181, 1994. 131

[Shannon 1948] C. E. Shannon. *A Mathematical Theory of Communication, Part I.* Bell Sys. Tech J., vol. 27, pages 379–423, July 1948. 1

[Shannon 1949] C. E. Shannon. *Communication in presence of noise.* In IRE, 1949. 1

[Song 1995] L. Song, E. Hennink, T. Young and H Tanke. *Photobleaching Kinetics of Fluorescein in Quantitative Fluorescence Microscopy.* Biophysical Journal, vol. 68, pages 2588–2600, 1995. 156

[Starck 1998] J.-L. Starck, F. Murtagh and A. Bijaoui. Image processing and data analysis: The multiscale approach. Cambridge University Press, 1998. 41

[Stein 1981] C. M. Stein. *Estimation of the Mean of a Multivariate Normal Distribution.* Ann. Statist., vol. 9, pages 1135–1151, 1981. 41

[Takhar 2006] D. Takhar, J. N. Laska, M. B. Wakin, M. F. Duarte, D. Baron, S. Sarvotham, K. F. Kelly and R. G. Baraniuk. *A New Compressive Imaging Camera Architecture using Optical-Domain Compression.* In Proc. Computational Imaging IV at SPIE Electronic Imaging, San Jose, January 2006. SPIE. To appear. 129

[Taubman 2002] D.S. Taubman, M.W. Marcellin and M. Rabbani. *JPEG2000: Image compression fundamentals, standards and practice.* Journal of Electronic Imaging, vol. 11, page 286, 2002. 29

[Tibshirani 1996] R. Tibshirani. *Regression shrinkage and selection via the lasso.* J. R. Statist. Soc. B., vol. 58, pages 267–288, 1996. 33

[Turner 1966] L. Richard Turner, L. Richard Turner and L. Richard Turner. *Inverse of the Vandermonde matrix with applications.* Rapport technique, 1966. 17

[Vermot 2008] J. Vermot, S. E. Fraser and M. Liebling. *Fast fluorescence microscopy for imaging the dynamics of embryonic development.* HFSP Journal, vol. 2, no. 3, pages 143–155, 2008. 7

[Vidakovic 1999] Brani Vidakovic. Statistical modeling by wavelets. John Wiley & Sons, 1999. 41

[Wakin 2006a] M. Wakin, J. Laska, M. Duarte, D. Baron, S. Sarvotham, D. Takhar, K. Kelly and R. Baraniuk. *An Architecture for Compressive Imaging.* IEEE International Conference on Image Processing - ICIP, pages 1273–1276, 2006. 84

[Wakin 2006b] M. B. Wakin and R. G. Baraniuk. *Random Projections of Signal Manifolds.* In IEEE 2006 Int. Conf. Acoustics, Speech, Signal Processing (ICASSP), May 2006. to appear. 90

[Wang 2004] Z. Wang, A. Bovik, H. Sheikh and E. Simoncelli. *Image quality assessment: From error visibility to structural similarity.* IEEE Trans. on Image Processing, vol. 13, pages 600–612, 2004. 14, 71

[Wang 2009] Z. Wang and A. C. Bovik. *Mean Squared Error: Love it or Leave It?* IEEE Signal Processing Magazine, vol. 26, pages 98–117, 2009. 12, 14

[Wang 2010] Yu Wang, Xiangyang Ji and Qionghai Dai. *Fourth-order oriented partial-differential equations for noise removal of two-photon fluorescence images.* Opt. Lett., vol. 35, no. 17, pages 2943–2945, Sep 2010. 49

[Weickert 1998] J. Weickert, B.M. Ter Haar Romeny and M. Viergever. *Efficient and Reliable Schemes for Nonlinear Diffusion Filtering.* IEEE Trans. Image Processing, vol. 7, pages 398–410, 1998. 36, 49

[Wiaux 2009] Y. Wiaux, L. Jacques, G. Puy, A. M. M. Scaife and P. Vandergheynst. *Compressed sensing imaging techniques for radio interferometry.* In Monthly Notices of the Royal Astronomical Society, 2009. 86

[Wilson 1988] T. Wilson and A. R. Carlini. *Three dimensional ima- ging in confocal imaging systems with finite-sized detectors.* Journal of Microscopy, vol. 141, pages 51–66, 1988. 77

[Yang 2010a] J. Yang, J. Wright, T. Huang and Y. Ma. *Image super-resolution via sparse representation.* Trans. on Image Proc., vol. Accepted, 2010. 18

[Yang 2010b] Lei Yang, Richard Parton, Graeme Ball, Zhen Qiu, Alan H. Greenaway, Ilan Davis and Weiping Lu. *An adaptive non-local means filter for denoising live-cell images and improving particle detection.* Journal of Structural Biology, vol. 172, no. 3, pages 233 – 243, 2010. 45

[Yaroslavsky 1985] L. P. Yaroslavsky. Digital picture processing. an introduction. Springer Verlag, 1985. 43

[Yaroslavsky 1996] L. P. Yaroslavsky and M. Eden. Fundamentals of digital optics. Birkhäuser, 1996. 43

[Yu 2009] G. Yu and S. Mallat. *Sparse super-resolution with space matching pursuits*. In SPARS09, 2009. 18

[Yu 2010] G. Yu, G. Sapiro and S. Mallat. *Image enhancement via structured sparse model selection*. In IEEE International Conference on Image Processing (ICIP), 2010. 18

[Zhang 2007] Bo Zhang, J. M. Fadili, J.-L. Starck and J.-C. Olivo-Marin. *Multiscale Variance-Stabilizing Transform for Mixed-Poisson-Gaussian Processes and its Applications in Bioimaging*. IEEE International Conference on Image Processing ICIP, vol. 6, pages 233–236, november 2007. 49